Designing and Implementing a Variable Energy Neutron System to Search for Conventional Explosives

by

Zachary D. Whetstone

A dissertation submitted in partial fulfillment
of the requirements for the degree of
Doctor of Philosophy
(Nuclear Engineering and Radiological Sciences)
in The University of Michigan
2015

Doctoral Committee:

Professor Kimberlee J. Kearfott, Chair
Associate Research Scientist Marek Flaska
Associate Professor Sara A. Pozzi
Professor Edward D. Rothman

To my girlfriend, my fiancée, and my wife;
Kyla, your unending love and support has been an inspiration.
I cannot wait to start another new adventure with you.

ACKNOWLEDGMENTS

Although my name is on the dissertation, this project would not have been possible without assistance from a variety of sources. As such, I would like to personally acknowledge a number of people who were instrumental in my success. First, I must thank my parents for a lifetime of support and encouragement. Without them I would have never had such great opportunities to learn and grow. Also, a heartfelt thank you to my wife for her years of kind words, helpful advice, entertaining diversions, and eternal patience. Finally, thank you to my family and friends, whose constant presence made all these years a near constant joy.

On the academic side, I want to extend my deepest gratitude to my advisor, Professor Kim Kearfott, and committee member, Dr. Marek Flaska. Their guidance during both research and writing were vital to my work. I would also like to thank the Nuclear Engineering and Radiological Sciences Department at the University of Michigan, especially Peggy Gramer, for their support in completing this dissertation.

I also must thank Professor Sara Pozzi and the University of Michigan Detection for Nuclear Nonproliferation Group for access to their detectors, custom software, and technical assistance. Similarly, thank you to Dr. Michael Hartman, Bruce Pierson, Dr. Brian Kitchen, and Dr. Jeff Katalenich for providing advice and access to the deuterium-deuterium neutron generator at the University of Michigan Neutron Science Laboratory. Finally, I would like to recognize Dr. Adrienne Lehnert, whose work inspired my own, and Alexis Poitrasson-Rivière, for his assistance with the neutron detection hardware and MCNP PoliMi.

A portion of this research was performed under appointment to the Department of Homeland Security (DHS) Scholarship and Fellowship Program, administered by the Oak Ridge Institute for Science and Education (ORISE) through an interagency agreement between the U.S. Department of Energy (DOE) and DHS. ORISE is managed by Oak Ridge Associated Universities (ORAU) under DOE contract number DE-AC05-06OR23100. All opinions expressed in this paper are the authors' and do not necessarily reflect the policies and views of DHS, DOE, or ORAU/ORISE.

A portion of this research was performed under appointment to the Nuclear Nonproliferation International Safeguards Graduate Fellowship Program sponsored by the National Nuclear Security Administration's Next Generation Safeguards Initiative (NGSI).

TABLE OF CONTENTS

LIST OF FIGURES

LIST OF TABLES

LIST OF APPENDICES

ABSTRACT

Research was conducted to design an active neutron interrogation system to search for conventional explosives. The work began with a review of the current methods for explosives detection, with a particular focus on active neutron interrogation. The next step was to design a layered shield for an isotopic neutron generator that limited the influence of unattenuated neutrons at undesirable angles. The final shielding design was then adapted for neutron and gamma ray detector collimation in an active neutron interrogation system, and a modular shielding arrangement was proposed. Focus then shifted to improving the flexibility of the active neutron interrogation system via introduction of a method to reliably vary the energy from nearly monoenergetic sealed-tube deuterium-deuterium or deuterium-tritium neutron generators. This was accomplished through single neutron elastic scatter off a target of known composition, resulting in neutrons with predictable energies that can be adjusted through manipulation of the interrogation target location relative to the scatter target and neutron generator. This neutron elastic scatter system was optimized through the adoption of a neutron time-of-flight (TOF) method, where the hydrogen nuclei in the start detector (scatter target) also served as the scattering medium, signaling neutron scatter and allowing for discrimination of neutrons that did not interact in the scatter target. Laboratory measurements and simulations were performed to characterize the new variable energy neutron elastic scatter (VENES) system and evaluate its effectiveness in performing fast neutron resonance radiography. Preliminary investigations on the application of VENES to fast neutron analysis and neutron backscatter were also conducted to direct future work. There was a particular interest in combining all three active neutron

interrogation methods with the VENES system and proposed shield designs, allowing for investigations across multiple different neutron energies in the MeV range. The VENES system permits for reliable alteration of neutron energy in active interrogation systems, using relatively cheap, portable, and easily operated components that are either currently, or soon-to-be, commercially available. The improvements on current active neutron interrogation sources should result in its eventual adoption to a variety of applications.

CHAPTER 1: INTRODUCTION

Motivation

Conventional explosives present a serious security threat domestically and internationally. This situation results from the fact that relatively cheap and accessible materials can cause significant damage. Not only are lives and property at risk, but the economic and psychological consequences can also be severe. When searching, it is important to locate and identify all explosives before they can be used. Even a single undetected explosive can have grave consequences. Therefore, continued improvement of the explosives detection systems is critical.

There are several established methods to search for explosives, including trace chemical detection and the employment of canine units to search the air near objects of interest. These have both proven effective, but are generally deployed for spot-checking, not comprehensive investigation. Traditionally, x-ray machines have been used to search through a large number of objects relatively quickly for various types of contraband. Although efficient, this method has several drawbacks when searching specifically for explosives. As opposed to weapons, explosives can have their shape manipulated, allowing them to be disguised as innocuous objects. Additionally, dense, heavy materials can be used to shield the x-rays, obscuring the view within the objects being investigated.

Active neutron interrogation addresses all these issues. Conventional explosives have unique chemical compositions, which usually includes a high percentage of nitrogen compared to hydrogen, carbon, and oxygen. The distinctive ratios of these elements can be discovered during neutron interrogation through a variety of signatures, including characteristic neutron inelastic scatter gamma rays, elastically scattered source neutrons, or unattenuated transmission neutrons. These phenomena are not strongly affected by the shape of the material, rendering the disguising of explosives ineffective. Furthermore, compared to x-rays, neutrons can more easily penetrate dense shielding materials such as lead, providing a complimentary approach to more traditional screening methods.

Common features in all active neutron interrogation systems are the neutron source and detectors that identify the particles of interest, whether those are gamma rays, scattered neutrons, or unattenuated source neutrons. Improvements to these elements can potentially have far-reaching effects. The solutions presented in this thesis are not meant to stand alone as an entirely new method. Instead, they serve as general, yet significant, improvements to the active neutron interrogation systems that can be applied across a variety of different methods that search for conventional explosives.

Current State of the Art

Presently, there are several active neutron interrogation approaches to search for conventional explosives. In general, all of them require a neutron source be directed at the target and attempt to detect the relatively high concentration of nitrogen in common explosives. They can be differentiated based on what is ultimately detected. Thermal neutron analysis, fast neutron analysis, and pulsed fast/thermal neutron analysis methods take advantage of the gamma rays

that result from inelastic neutron scatters. Hydrogen, carbon, nitrogen, and oxygen, all of which maintain unique ratios in explosives, can be observed using these methods. Similarly, fast neutron scattering analysis attempts to identify the elemental fractions using neutron elastic scatter. Provided the user knows the initial energy of a source neutron and can determine its final energy after an elastic scatter, the mass of the target nuclei can be calculated and chemical composition inferred. As opposed to the other systems, neutron transmission measurements focus on neutrons that are not attenuated. Instead, the source neutrons pass through the target and interact with a detector. Based on the interaction probabilities of neutrons at different energies with various nuclei, it is possible to deduce the target's composition. Work on all three types of active neutron interrogation systems is ongoing, and attempts to combine the methods have had some success. A more in depth discussion of explosives detection methods, neutron sources, and active neutron interrogation can be found in Ch. 2.

Despite the increased penetration depth of neutrons compared to x-rays, and the ability to determine chemical composition of low-Z materials, active neutron interrogation has failed to find extensive deployment when searching for conventional explosives. X-ray systems, trace chemical detection, and canine assets are all extensively used at airports, seaports, and border crossings, but neutron interrogation systems have not advanced much beyond occasional field tests. The systems have yet to prove themselves efficient and cost effective enough to replace the currently installed systems. Some of the main disadvantages are the large, complicated, expensive accelerators used as neutron sources, as well as the insufficiently low count rate abilities and energy resolution of neutron detectors. However, if these challenges can be overcome with easily implemented and deployable solutions, widespread active neutron interrogation and its promise of effective material discrimination will be closer to reality.

Proposed Improvements

This research focuses on several improvements to active neutron interrogation systems. The first improvement is a novel, compact shield design for both the neutron source and any detectors used in the system. Discussed in Ch. 3, the shield effectively collimates an isotropic fast neutron source, allowing for unattenuated neutrons to emerge from the shield opening at a specific solid angle, forming a beam of a desired size and shape. This limits the flux at other angles, reducing the dose to personnel and restricts the number of neutrons that could interact in the environment and contribute unwanted signal in a detector. In Ch. 4, the shield design is further refined and applied to a detector to constrict its field of view, reducing the undesirable particles detected and improving the system's signal. Additionally, modular implementation of the design is discussed, which allows for altering the shield and permits portability and adaptability based on the desired application.

The second part of the dissertation focuses on the development of a methodology to reliably and precisely reduce the energy of neutrons from a monoenergetic deuterium-deuterium (D-D) or deuterium-tritium (D-T) source, providing flexibility to the user. The initial idea, as investigated in Ch. 5, involves elastically scattering source neutrons of known energy off a target nucleus of known mass. The interrogation object is placed at a specific angle relative to the scatter target. Assuming a single elastic scatter, it is possible to determine the final energy of the neutron given its mass, initial energy, mass of the scatter nucleus, and angle of scatter.

Ch. 6 further refines the idea by adopting time-of-flight (TOF) measurement techniques to discriminate undesirable neutrons, resulting in development of the novel variable energy neutron elastic scatter (VENES) system. The VENES system, which was tested in the laboratory, uses two organic scintillator detectors, one near the source and another separated by some

distance and offset at a predetermined angle. Some neutrons emitted from the source will elastically scatter off a hydrogen nucleus in the first detector. In addition to serving as a scatter target, the pulse created when the neutrons scatter acts as a start signal. If the neutrons also interact in the second detector, generating another pulse, TOF can be used to confirm the neutron's energy and neglect neutrons that may have multiply-scattered or interacted somewhere else in the environment before finding their way to the second detector. By altering the angle of the second detector relative to the first, and using TOF to discriminate multiple neutron scatters and other types of interactions, a fraction of the neutrons emitted from the monoenergetic fusion source can have their energy reliably varied by the user. The VENES system can be applied to active neutron interrogation, particularly when searching for conventional explosives. When probing a target, the energy can be adjusted based on the interrogation object's scatter cross sections, density, thickness, and other properties that affect neutron attenuation. The neutron energy can be aligned based on resonance inelastic scatter peaks to search for characteristic gamma rays, encourage neutron elastic scatter, or influence neutron transmission measurements.

To evaluate the effectiveness of the VENES system, further laboratory measurements were performed in Ch. 7, placing several different materials, including an explosive surrogate, between the scattered D-D neutrons and the stop detector. The measured transmission count rates were used to benchmark Monte Carlo simulations and evaluate application of the VENES system to fast neutron resonance radiography. Successful identification of the approximate atom fractions for all simulated materials demonstrated the utility of the VENES system for active neutron interrogation.

In Ch. 8, the promising results encouraged preliminary investigation in to alternative explosives detection applications. Simulations of both fast neutron analysis and fast neutron

scattering analysis were performed using the VENES system as the neutron source. Additionally, implementation of previously developed source and detector shields were evaluated. The results helped direct future work and eventual possible deployment of the VENES system.

Finally, Ch. 9 summarizes the benefits of the VENES system: such as ease of use, portability, and low comparative costs to similar neutron sources, and contrasts that against the relatively low count rate inherent in a system dependent on neutron elastic scatter.

Evaluation Methods

There are two primary types of analysis performed in this dissertation. Much of the original design and evaluation, for both the shield and VENES system, were done using Monte Carlo N-Particle Transport Code (MCNP)[1]. This limited the time and resources required to build and test the designs and allowed for quick comparison between a large variety of choices. Preliminarily, the simulations were kept relatively simple, often neglecting environmental objects such as ground and air in order to avoid obscuring the underlying interactions of interest. Although there is always some uncertainty present in simulations, this minimalist approach helped limit it by reducing the complexity of the models. As a result, many of the early values obtained, particularly from the more basic simulations, provide relative results, not absolute.

As research continued, the simulations began to incorporate more realistic models. These included source and detector housings, realistic source energy distributions, and approximated detector response functions. This provided more accurate simulations and allowed for more in depth analysis of the VENES system's capabilities. Care was always taken to minimize statistical uncertainty and, when appropriate, randomized uncertainty was introduced to the simulated

[1] computer code Monte Carlo N-Particle Transport version 5 (Los Alamos National Laboratory, Los Alamos, NM 87545, 2006).

results to determine the susceptibility of VENES measurements to undisclosed systematic uncertainties.

Whenever possible, laboratory measurements were performed. This served to confirm the simulated results and provide even more realistic values. Using a D-D generator and two liquid scintillators, the viability of elastic scatter to reliably change a source neutron's energy was established. Further laboratory measurements investigated the application of the VENES system to searching for conventional explosives via neutron transmission.

CHAPTER 2: A REVIEW OF CONVENTIONAL EXPLOSIVES DETECTION USING ACTIVE NEUTRON INTERROGATION

Abstract

Conventional explosives continue to be a serious threat. They are relatively easy to obtain or create and have the potential to cause massive harm to people and property. There are several tools employed by law enforcement to try to detect explosives before they are used, but they can be subverted if the correct precautions are taken. Active neutron interrogation, a rapidly evolving field, is an alternative to these other detection techniques. There are several different methods proposed that use active neutron interrogation to search for explosives: Fast Neutron Analysis, Thermal Neutron Analysis, Pulsed Fast/Thermal Neutron Analysis, Neutron Elastic Scatter, and Fast Neutron Radiography. These methods vary based on neutron energy and the radiation they detect. A thorough review of the basic principles behind active neutron interrogation and an investigation of each type of active neutron interrogation, complete with the advantages and disadvantages, was conducted and will be presented.

Introduction

A quick, accurate method of finding hidden explosives is a high priority in national security. Relatively small amounts of explosive materials in airport luggage or landmines can cause injury or death to individuals and destruction of property. Various detection methods from

different fields of science, including vapor detection and x-ray screening, have been employed in order to identify explosive materials (Hussein and Waller, 1998; Steinfeld and Wormhoudt, 1998; Singh and Singh, 2003; Moore, 2004; Moore, 2007). However, it has been only during the last 25 years or so that neutron interrogation has become a viable method of identifying potential explosive materials (Gozani et al., 1989). This chapter will review the advantages and disadvantages of neutron interrogation as a means of explosives detection as well as provide a brief overview of the various types of neutron sources and related information. Then several techniques that use neutrons to identify explosives will be discussed in greater depth. These will include thermal neutron analysis, fast neutron analysis, pulsed fast/thermal neutron analysis, neutron elastic scatter or fast neutron scattering analysis, and fast neutron radiography.

The explosives interrogation methods that do not involve neutrons all have drawbacks that limit their effectiveness. Many methods, including the use of canines, ion mobility spectrometry, and chemiluminescence search for trace amounts of explosives in the air (Furton and Myers, 2001; Ewing et al., 2001; Jimènez and Navas, 2004). Unfortunately, if the explosives are properly handled and sealed, these techniques will be unable to identify the material. There are also detection methods that involve the use of x-ray transmission or photon scatter to investigate targets (Singh and Singh, 2003; Faust, 2002; Strom and Callerame, 2004; Tang and Hussein, 2004). However, these photons can be shielded using high atomic number materials, which would allow anything behind the shielding to remain undetected (da Silva and Crispim, 2001). Furthermore, although densities and atomic numbers can be approximated using these methods, they cannot be specifically determined (Harding, 2004). This allows for confusion when examining objects. A harmless material with physical properties similar to that of an

explosive will trigger a false alarm. More importantly, depending on the orientation of materials inside the object, it is still possible that explosive material could be misidentified as harmless.

There have been many specific methods proposed that use a neutron source to search for explosives, but the active interrogation techniques these systems employ are generally the same. In passive interrogation, the system does not interact with the target and only uses information that can be obtained without invasive measures, such as when a canine unit sniffs the air around the outside of a target. With an active interrogation system, the explosives detection system is actually interacting with the target, such as by directing neutrons towards it, in order to obtain information more quickly. Each of the systems discussed in this chapter requires neutrons to interact with the materials of interest in some specific target. Depending on the concentration and neutron interaction cross sections of the atoms present in the target, the neutrons have a greater or lesser chance of interacting and releasing radiation (Lehnert and Kearfott, 2010). Radiation associated with these neutron interactions includes characteristic x-rays, gamma rays, inelastically scattered neutrons, and elastically scattered neutrons (Buffler and Tickner, 2010). The active neutron interrogation systems have detectors set up to record one or more types of secondary radiation. The signal is then processed by the equipment and analyzed either by a computer or a person. This assists the operator in determining whether the target needs to be investigated further to see if the materials within it are either illegal or dangerous.

The major advantage of neutron based explosives detection systems is that it is hard to shield neutrons, which pass through iron and lead with very little attenuation. This is a benefit compared to many other systems, most notably those based on x-rays and gamma rays directed at the target, which can be shielded by middle- to high-atomic number, dense materials. If such materials are placed between the source and explosive, the explosive may not be detected.

However, neutrons, which are better shielded by light nuclei, pass through high-atomic-number materials and reach the explosive. Another disadvantage of x-rays and gamma rays are that they can only broadly discriminate between organic and inorganic materials while neutrons are effective at differentiating between various types of organic material based on their chemical composition (Liu et al., 2008).

The fact that neutrons are more difficult to shield with high-z materials may make them advantageous for detecting explosives, but it also causes them to be a hazard to work with. Neutrons can deliver a potentially harmful radiation dose to nearby personnel if the individuals are not properly protected. The difficulty of attenuating neutrons requires either significant shielding or large stand-off distances. Either option contributes to an expanded system footprint. This can make implementation for luggage inspection at airports and cargo inspection at shipping yards, both places where floor space is at a premium, complicated. Similarly, neutron sources used in land mine detection would necessitate shielding, which adds to the weight to the system and limits its portability. Furthermore, the additional shielding material adds to the system cost. When implementing on a large scale, these costs can be significant.

Another disadvantage of neutron interrogation is the potential for materials activation. When high energy neutrons interact with certain nuclei, it is possible they will undergo a reaction and leave the target nucleus in an excited state. Eventually this nucleus will move to a stable nuclear state and release radiation. This may happen almost immediately after the neutron interacts with the nucleus, or it may be delayed, such as with activated silicon and phosphorous (Vourvopoulos and Womble, 2001). Due to the fact that the materials being interrogated are largely unknown, it is impossible to anticipate what interactions will occur and the amount of activation induced. Therefore, it is necessary to strike a balance between having a high enough

neutron flux to obtain a clear signal, while keeping it low enough to minimize the risk due to activation.

A final disadvantage is the novelty of the systems proposed. Research and development is continuing in the field of active neutron interrogation in a number of areas, but there has yet to be a system that has found widespread deployment. This means data and benchmarks are either being generated in a lab or at one or two trial locations. Conversely, metal detectors and x-ray screening, for example, have been used for decades in airports, courthouses, and other public areas around the world. They are mature, robust technologies with a proven track record. Any new approach must provide a distinct advantage or address a unique need to be considered for wide-scale adoption. Active neutron interrogation may be a viable alternative to other explosives detection techniques, but its pros and cons must be weighed carefully when compared to competing technologies.

Basic Principles of Neutron-based Explosives Interrogation

Neutron sources

There are four basic types of compact neutron sources. The first is a radioactive material that spontaneously and continuously releases neutrons as it decays to a stable state. An example of this would be ^{252}Cf, which has a neutron energy spectrum with a most probable energy of 0.8 MeV and average energy of 2.1 MeV. Another neutron source type pairs two nuclides: one alpha-emitting, and another that absorbs the emitted alpha particle and then releases a neutron. These sources include plutonium beryllium (PuBe), americium beryllium (AmBe), and americium lithium (AmLi). Due to the variability of the alpha particle energy, the resultant neutron energy spectra are quite broad and dependent on the alpha source (Knoll, 2010). A third

neutron source depends on a high energy photon to excite a nucleus resulting in the release of a neutron. The two nuclides that typically undergo this reaction are ^{9}Be and ^{2}H. The minimum photon energy for these reactions is 1.67 and 2.23 MeV, respectively. Typical sources of gamma rays include ^{226}Ra, ^{124}Sb, ^{72}Ga, ^{140}La, and ^{24}Na. An advantage of neutron sources that use high energy photon excitation is that the resulting energy of the neutron is dependent on the energy of the incident gamma ray. If a monoenergetic photon source is used, a nearly monoenergetic neutron source will be obtained. However, the photoneutron interaction probability is relatively low. Therefore, a high activity gamma ray source must be used, which will create a large gamma ray background (Knoll, 2010).

All of these types of neutron sources are easy to operate and require no equipment other than shielding. The associated major drawback is that they are constantly decaying and there is no way to turn them off. Therefore, when the neutron source is unshielded, it presents a constant hazard to nearby personnel, even when it is not being used. Furthermore, the radioactive material can expose unknowing individuals to a constant radiation dose if it is lost or stolen. The sources themselves present possible risks for terrorism when coupled with conventional explosives to create radiological dispersive devices.

Neutron generators are a viable alternative that enable reactions that lead to the creation of neutrons. They allow for timed neutron pulses, can be turned off and thus are easier to transport, and have high neutron fluxes (Aleksandrov et al., 2005). One example of such a generator is the deuterium-tritium (D-T) neutron generator. When a D-T generator is turned on, deuterium (^{2}H) ions are accelerated across a maximum voltage difference of around 90 kV into a tritium (^{3}H) target. The deuterium and tritium undergo a fusion reaction to form an alpha particle (^{4}He) and a neutron whose average initial energy is near 14.1 MeV (Knoll, 2010). A deuterium-

deuterium (D-D) neutron generator works in the same way, except in this case deuterium ions are accelerated towards a deuterium target. When the two particles go through a fusion reaction, the product is ^{3}H and a neutron with an average energy of about 2.5 MeV. In both cases, if the generator is off, the deuterium is not directed towards the tritium or deuterium and no neutrons are created. This makes it ideal for interrogation applications and reduces the risk of accidental exposure from the unshielded source. Several compact D-T and D-D generators have been designed specifically for active neutron interrogation applications (Chichester et al., 2007). For both radioisotopes that release neutrons and neutron generators, the energy of the neutron is dependent on the atom that is decaying or the reaction taking place. Both of these types of sources tend to have very specific neutron energies that cannot be easily adjusted. Large accelerators, which are costly and relatively complicated, can be used to impart the incoming deuterium ion with more energy than required to initiate fusion, resulting in some of the excess energy being transferred to the resultant neutron in the D-D or D-T reaction (Hall et al., 2006; Lanza, 2007). Alternatively, the neutrons can be passed through a moderating material so that they lose energy through multiple interactions with nuclei of low atomic mass. This will generally lower the average energy of the neutron to the thermal range around 0.025 eV, but cannot reliably reduce a significant number of neutrons to any other energy.

All of the neutron sources have their own advantages and disadvantages, which are summarized in Table 1. It is up to the system designer to decide which best suits his or her needs while adequately limiting the potential dose to any operators or the nearby public.

Neutron source collimation

Regardless of the type of neutron source, the distribution of neutrons is either isotropic or nearly isotropic. This is not ideal for the application of neutron interrogation where the operator

is interested in neutrons interacting in a target within a specified solid angle. If the source were unshielded and neutrons were released isotropically to interact with the surrounding environment, products of the interactions, either scattered neutrons or associated gamma rays, could end up being directed towards the detector and counted by the detection system. These additional interactions in the detector create noise and the signal from the materials being investigated may be lost or obscured. Furthermore, the additional neutrons provide a health hazard to anyone near the source. Shielding can be used to limit the isotropic neutron source, reduce the unwanted interactions, and protect nearby personnel and the public (Reda 2011, Whetstone and Kearfott 2011). Such shielding, applied to either radioactive sources or neutron generators, is never completely effective so there will still be some neutrons that escape the collimation and interact within the environment. In the case that additional shielding is too heavy or has too large of a footprint, another option is to use associated particle imaging (API).

Associated particle imaging

Without bulky collimation, it is very hard to determine if a detected gamma ray or neutron is the result of neutrons scattering in the environment or within the target. Additionally, even if it can be determined that the neutron interacted in the target, it is unknown whether the secondary radiation is a result of a single interaction or several, based on the detector signal alone. The incident neutron may undergo interactions within the target and change its energy before scattering out or creating a prompt gamma ray. This can lead to much uncertainty within the system. One way to correct this is to use associated particle imaging (API) (Beyerle et al., 1990; Chichester et al., 2005). This system includes a either D-T or D-D fusion source. When the interaction occurs in the source and creates an energetic neutron, the associated charged ^{4}He or ^{3}He nuclei, respectively, moves in the opposite direction due to conservation of momentum and

is detected. The time and angle at which the charged particle is detected signals the time of creation and resultant incident angle of the neutron. If the neutron is not directed toward the target, any secondary radiation detected is ignored by the system (Sudac et al., 2007). If, on the other hand, the initial neutron is directed at the target, then the time until the secondary prompt gamma ray or scattered neutron interacts within the detector is used to determine if the neutron interacted only once. If so, it is counted by the system. Otherwise, it is neglected. The total time of flight (TOF) of the neutron can also be used to determine its energy. The additional information helps to reduce sources of uncertainty in the explosives detection system. Portable neutron imaging devices have been developed with yields of at least 1 x 10^8 neutrons per second and weighing 12 kg, which could prove useful for many explosives detection scenarios (Chichester et al., 2007).

Explosives detection methods

In order to find explosives, active neutron interrogation methods rely on identifying the signature chemical makeup that most explosive materials possess. Many of the commonly used explosives have high nitrogen content (Gozani, 1994). This relatively large amount of nitrogen, compared to other elements common in explosives, such as hydrogen, carbon, and oxygen, is what neutron based detection systems look for (Buffler and Tickner, 2010). The abnormally high nitrogen content is used as a flag when searching for explosives. Some of the explosives that can be detected are trinitrotoluene (TNT), cyclotrimethylenetrinitramine (RDX), ammonium nitrate, composition 4 (C-4), pentaerythritol tetranitrate (PETN), and Semtex 1A (Gozani and Strellis, 2007; Sudac et al., 2008). Unfortunately, not all explosives are rich in nitrogen, such as triacetone triperoxide (TATP), which has been used by several terrorist groups, including shoe bomber Richard Reid in 2001 (Dubnikova et al., 2002). Furthermore, many other items of

concern, such as guns and knives, would go undetected by all active neutron interrogation methods besides neutron transmission. Additionally, benign materials, such as rubber, silk, and nylon, may have high nitrogen content which could trigger false alarms (Cinausero et al., 2004).

Although they are unable to detect all types of explosives, systems employing the various active neutron interrogation methods can be used in a wide array of applications. Their ability to detect both small and bulk explosives means they can be deployed to search automobiles and cargo containers. They can also be used for baggage and freight inspection at airports (Runkel et al., 2009). There is also ongoing research exploring usage of these systems to search for land mines and roadside improvised explosive devices (IEDs). Narcotics and chemical agents, which are additional contrabands of interest to border security, also contain relatively high nitrogen levels or specific carbon to oxygen ratios and can be readily identified using neutron interrogation (Vourvopoulos and Womble, 2001; Gozani and Strellis, 2007).

Neutron-based Explosives Interrogation Systems

There are several different types of active neutron interrogation methods, each with its unique advantages and disadvantages. The various methods are summarized in Table 2. The system designer must decide what elements he or she wants to search for and how high their associated neutron flux can be, then determine the best method to fit these requirements. The section will review such systems.

Thermal neutron analysis (TNA)

Thermal neutron analysis (TNA) takes advantage of the characteristic radiation released by activated nuclei (Gozani et al., 1989). In this method, thermal neutrons, with energy around 0.025 eV, are used. While some of these passing through the object do so without interaction,

others are absorbed through a characteristic (n, γ) reaction with nuclei within the target. The new nuclei created in the absorption process are placed in an excited state. In order for the nuclei to move to a stable state, they release a gamma ray with a characteristic energy dependent on the nuclei absorbing the neutrons. By using a spectroscopic gamma ray detector, the relative amounts of each of these elements can be determined by looking for these unique characteristic energy peaks in the gamma ray spectra. Generally, a high peak at nitrogen's characteristic energy is used separately, or in conjunction, with other flags to signal the presence of suspicious material.

The theory of TNA for explosives detection has been around since the 1980s and several systems have been designed to use it to search for explosives (Davies et al., 1987, Gozani et al., 1989, Brown and Gozani, 1997, McFee et al., 1998). TNA primarily searches for nitrogen and hydrogen, because when these nuclei absorb a thermal neutron, they emit a 10.8 and 2.2 MeV gamma ray, respectively (Buffler, 2004). Originally developed as a means to detect most solid explosives, TNA has also been applied to the detection of drugs, liquid explosives, and buried land mines due to its ability to also detect chlorine (Brown and Gozani, 1997; McFee et al., 1998). More recently, the relative amounts of hydrogen, carbon, and nitrogen were determined for various samples when placed in a beam of thermal neutrons from a research reactor (Im et al., 2006). A "small parcel explosive detection system" was created which employed TNA to scan packages. In tests, the system was able to determine 0.1 – 1.0 L of concealed liquid explosives and chemical weapons threats 90% of the time and provided false alarms 1% of the time with measurement times of 60 s. Also, the system was able to distinguish between live and inert explosive ordinances 100% of the time employing measurement times of 60 s (Shaw et al., 2005).

A pulsed TNA device is being developed which uses graphite to moderate the neutrons of a pulsed D-T generator until they reach thermal energies. Once the thermal neutron flux is sufficiently characterized, it should be possible to determine the chemical makeup of materials and detect explosives using multiple thermal neutron pulses. Additionally, the detectors will also have the ability to detect fast neutrons, which will allow the system to search for fissionable materials once the thermal neutrons induce fission (Favalli and Pendersen, 2007).

TNA has proved an effective detection method. It is employed in a commercial system for determining the location of anti-tank mines (Clifford et al., 1999; Clifford et al., 2007) and more recently, land mines and other explosive remnants containing as little as 20 g of hydrogen (Brooks et al., 2012). Although the cost and time required to use TNA for demining is increased compared to more conventional methods, it can be justified for more complicated situations such as important infrastructure and industrial areas (Cinausero et al., 2004). It was shown that replacing a ^{252}Cf source and moderator with a D- T source and moderator improved the TNA method for landmine detection both for deeper mines and when the system is not directly over the mine (Haslip et al., 2001).

Fast neutron analysis (FNA)

One improvement to the previous method is to increase the energy of the neutrons in a technique known as fast neutron analysis (FNA) (Gozani, 1994). Instead of relying on thermal neutron absorption like TNA, FNA exploits the inelastic scatter of fast neutrons off characteristic nuclei such as nitrogen, oxygen, and carbon. The ratio of these three elements in explosives is quite specific (Buffler, 2004). For an inelastic collision, when the fast neutron is incident on the nucleus, a new, lower energy neutron is emitted and is accompanied by a characteristic gamma ray. The cross sections for inelastic scatter vary by nuclei as well as neutron energy and are

generally smaller than capture cross sections for thermal neutrons, meaning fewer interactions per unit flux (Buffler, 2004). A collimated beam of fast neutrons is typically directed at the target. By comparing the relative numbers of detected characteristic gamma rays, an operator or automated computer program can make a determination as to whether the target constitutes a threat. If the characteristic gamma rays are detected in ratios similar to conventional explosives, a red flag is raised and the package can be examined more thoroughly. As an example, FNA was used in a prototype system that was remotely controlled and employed a D-T generator and high-purity germanium detectors to interrogate vehicles for IEDs (Koltick et al., 2007).

Furthermore, researchers have investigated FNA for use in conjunction with coded aperture imaging to examine airport luggage and cargo containers. Coded aperture imaging works by placing shielding material over specific parts of the detector. Gamma rays interact with the detector after having passed through the unshielded part of the aperture. Given the pattern of the interactions on the detector and the configuration of the aperture, it is possible to determine the distribution of the source within a volume (Lanza and Zhang, 1999). Instead of a narrow beam of neutrons, this method uses a field of fast neutrons that interact throughout the item of interest simultaneously. The neutrons undergo an inelastic scattering interaction within the target and create characteristic gamma rays. Theoretically, by using coded aperture imaging, the system is able to determine the location of the interaction and therefore, the elemental makeup of specific regions within the target. The method is able to determine the mass of a sucrose sample to within 7% and determine its molar ratio of carbon to oxygen to within 4%, but needs further investigation for use in high background and three-dimensional applications (Accorsi and Lanza, 2001).

This method has an advantage over TNA because more of the elements present in explosives emit characteristic gamma rays during FNA. For TNA, the process usually just looks for high nitrogen content and hydrogen, but with FNA, the signal also includes information about the concentration of oxygen and carbon, which have unique concentrations relative to one another and nitrogen in explosives. Therefore, the additional information gained through FNA can be used to eliminate some of the false alarms associated with TNA (Singh and Singh, 2003).

One major drawback to this method is the large background noise associated with FNA (Gozani, 1994). The fast neutrons, once scattered, can interact within the gamma ray detectors and distort the gamma ray signal coming from the target. It is possible to shield these neutrons, but the detector efficiency must be sacrificed. One way to limit the fast neutron background is to use associated particle imaging. This method has allowed for preliminary detection of underwater TNT (Sudac et al., 2011). Another option is to use a pulsed beam of fast neutrons, as described in the next sub-section.

Pulsed fast neutron analysis (PFNA) and pulsed fast/thermal neutron analysis (PFTNA)

To reduce the background signal in FNA, the fast neutrons are released in short pulses in an approach termed pulsed fast neutron analysis (PFNA). Gamma rays traveling at the speed of light move about seven times faster than the neutrons used in PFNA, in which 8 and 14 MeV neutrons have velocities of 3.9 and 5.2 cm ns^{-1}, respectively (Gozani, 1995). Releasing the neutrons in short pulses allows for any gamma rays that are created during an inelastic collision to reach the detector before the scattered neutrons that accompany them. The gammas rays from the target are counted first, and when the neutrons interact later within the detector and create additional gamma rays, the system discriminates and neglects them. Recently, hydrogen, carbon, and oxygen concentrations were determined in a variety of materials of interest using a 14 MeV

PFNA source and a $LaBr_3$:Ce detector (Naqvi et al., 2013). Additionally, Compton cameras have been investigated for use in PFNA to determine the elemental compositions at a localized point within the target (Farahmand et al., 2007). Compton cameras, originally used with gamma ray astronomy and medical imaging, detect the Compton scatter of a photon on one plane of a detector, and the photoelectric absorption of the same photon on another. Given the angle of scatter and final energy of the photon, the incident angle of the photon can be determined. With enough events, the source of the photons can be determined (Todd et al., 1974).

After the fast neutrons interact in the target, some of them become thermalized through multiple interactions (Buffler, 2004). These thermal neutrons can then be absorbed in the nitrogen nuclei, just like in TNA, and release characteristic prompt gamma rays which are then recorded. Fast/thermal neutron analysis (FTNA) takes advantage of the already preset thermal neutrons to obtain more information about the object being interrogated. FTNA, combining the principles of PFNA and TNA, performs the equivalent of two separate interrogations at once, looking for both characteristic neutron absorption and neutron inelastic scatter gamma rays. Furthermore, the neutron generator can be cycled in such a way to allow for neutron thermalization between pulses. This is known as pulsed fast/thermal neutron analysis (PFTNA). In this case, the target is hit with fast neutrons for about 10 μs and the gamma rays from the inelastic fast neutron collisions are detected, similar to PFNA. The generator is turned off for 90 μs while the neutrons from the initial pulse thermalize within the target. Some of these thermalized neutrons are absorbed by nitrogen, hydrogen, and chlorine nuclei in the target and characteristic gamma rays are released. This cycle is repeated for a set number of times. Finally, the sample is allowed to sit for an extended time period while any characteristic gamma rays from previously activated nuclei with slightly longer half-lives, such as silicon or phosphorous,

are released (Vourvopoulos and Womble, 2001). The combination of multiple detection techniques in PFTNA assists in determining the composition of the target. The relative amounts of carbon, oxygen, and nitrogen can be obtained with PFNA; the presence of nitrogen, hydrogen, and chlorine in the target can be determined with TNA; and by looking for delayed gamma rays, silicone and phosphorous can also be detected. This in turn helps the operator make a more accurate determination of the unknown material within a package and assess whether or not it is a threat.

Many advances have been occurring in the fields of FTNA and PFTNA. Preliminary tests have shown the ability of an FTNA detection system to correctly determine gamma ray signatures of nitrogen rich targets as small as 3.8 L when compared to inert targets (Brewer et al., 2012). A handheld PFTNA system was developed and tested using a 14.1 MeV D-T neutron generator that determined the elemental content of packages in field demonstrations (Womble et al., in 2001). It correctly verified the carbon to oxygen and nitrogen to oxygen ratios to within a few percent for C-4, TNT, and RDX explosives. Also, the use of PFTNA was investigated for the interrogation of larger objects, such as cargo containers (Vourvopoulos and Womble, 2001), while other researchers have attempted to design a CsI(Tl) detector that will be able to provide a multi-color picture of the object during PFTNA (Evans et al., 1999). Using PFTNA, researchers have shown it is possible to find 2 kg of cocaine hidden behind 85 cm of cement (Dokhale et al., 2001). More recently, a PFNA system was deployed in an airport in Houston, Texas. It uses a Van de Graaff accelerator to obtain neutron pulses on the order of several nanoseconds for TOF information and is able to obtain three dimensional images of airplane cargo containers (Strellis et al., 2009). Finally, artificial neural networks have been applied to help in identifying explosives from gamma ray spectra (Nunes et al., 2002).

Fast neutron scattering analysis (FNSA) or neutron elastic scatter (NES)

Another detection technique is fast neutron scattering analysis (FNSA) or neutron elastic scatter (NES). Many explosives have a chemical signature that is high in nitrogen and also contains carbon, oxygen, and hydrogen. All of these elements have a relatively low atomic mass, which allows for a neutron to transfer a substantial amount of energy during an elastic collision. In elastic collisions, when the neutron interacts with a nucleus it immediately transfers energy as it bounces off. If the initial energy of the neutron is known, and if both the neutron's scattering angle and scattered energy are determined by detectors, then the mass of the nucleus can be calculated (Buffler, 2004). The common elements in explosives have nuclei with different masses. Therefore, by using this method the relative amounts of each element can be determined based on the energy and angle of scatter of the detected neutrons.

The benefit of this technique is that for most nuclides, the probability of elastic scatter is larger than either inelastic scatter or neutron capture. This allows for a stronger signal at lower flux, reducing the activation and required shielding. This method requires the ability to determine the energy of a scattered neutron, but the energy discrimination for neutron detectors is not nearly as good as gamma ray detectors. However, NES does show promise. Experimentally, it was shown that atom fractions of a small sample between 0.2 and 0.8 kg could be determined (Buffler et al., 2001). Also, computer simulations were run that helped characterize the scattering of fast neutrons in explosive materials (Lehnert and Kearfott, 2011b). If this detection method can be further improved, it would allow for explosives detection in airports or when searching for land mines (Brooks et al., 2004).

Neutron transmission/Fast Neutron Radiography

Because neutrons attenuation varies based on neutron energy and the materials they are passing through, their transmission through a target reveals some unique information about the elemental makeup. Using a ^{252}Cf source, it is possible to search for nitrogen and oxygen in the target. Both of these elements have neutron absorption resonances and the energy spectrum of the transmitted neutrons will show a decrease at these resonance energies compared to a sample that contained no nitrogen or hydrogen (Gokhale and Hussein, 1997). Also, looking at the ratio of fast neutron transmission to gamma ray transmission can help provide an idea as to the type of material in a target air cargo container (Eberhardt et al., 2005). This method allows for the determination of the density of materials as well as their class of composition: organic, glass or ceramic, or metal.

One of the advantages of neutron transmission is that it does not require a strong source because it is looking for neutrons that do not interact in the target. Since neutrons tend to have a relatively low interaction probability, most of them will pass through the target and contribute a signal to the system (Gokhale and Hussein, 1997; Sowerby and Tickner, 2007). However, neutron transmission cannot identify as many elements as some other active neutron interrogation methods and traditionally only determined high concentrations of certain elements, such as nitrogen.

More recent advances in neutron transmission, known as fast neutron radiography, have shown promise. By combining neutron and gamma ray transmission, fast neutron/gamma ray radiography can determine the average composition of an unknown target material. This is either accomplished using separate compact D-D or D-T sources for the neutrons and a ^{60}Co source for the gamma rays, or a high energy accelerator that pulses both particles (Sowerby and Tickner,

2007). Alternatively, a variable-energy, quasi-monoenergetic neutron source can be employed to interrogate the target through fast neutron resonance radiography. By having a variety of source neutron energies, it is possible to take advantage of multiple attenuation resonances to differentiate between hydrogen, carbon, nitrogen, and oxygen (Overley, 1985). This can be achieved either through a broadband pulsed spectrum neutron generator and TOF measurements or kinematic reactions in an accelerator where neutron energy is dependent on the incident deuterium energy and the neutron emission angle (Lanza, 2007). One such broadband pulsed time-of-flight system that was developed initially had an explosives detection rate of 88% with a false alarm rate of 2%, which was improved to 93% and 3.4%, respectively (Overley et al., 1997; Overley et al., 2005). Additionally, the creation of a novel integrative detector that uses a plastic fiber scintillator screen has enhanced fast neutron energy discrimination via improved TOF measurements (Mor et al., 2009). The kinematic method has also shown promise in simulations, but proven difficult in practice due to excessive secondary gamma ray contamination from the neutron source (Raas et al., 2005). Both fast neutron resonance radiography methods also require relatively complicated accelerators and implementation (Sowerby and Tickner, 2007).

Alternative and combined technologies

Many of the previously discussed methods of neutron interrogation have been adapted and applied to landmine detection. Several groups have looked at the ability of hydrogen rich explosives to thermalize fast neutrons and backscatter them (McFee et al., 2003; Datema et al., 2003; Brooks et al., 2004). When scanning a location for a possible landmine with a neutron flux, the higher concentration of backscattered neutrons from hydrogen in the landmine indicates its presence. Several detectors have been designed specifically for this application and shown some success (Fioretto et al., 2004; Bom et al., 2004; Elsheikh et al., 2012).

Recently, several explosives detection systems have been designed or built that incorporate both the more traditional x-ray inspection systems and active neutron interrogation systems (Valković et al., 2007; Carasco et al., 2008; Al-Bahi et al., 2013). A system has already been deployed for field testing in the port of Rijeka in Croatia which uses x-ray images to determine any suspicious objects within a large cargo container. If an object raises concern, then a D-T neutron source is used to interrogate that particular area. It uses "tagged" neutrons with an API to determine the time between creation of the initial neutron and the detection of FNA characteristic gamma rays (Carasco et al., 2008). In a different study, it was shown that by looking at the FNA peaks for oxygen and carbon as well as the neutron transmission peak, the explosive Semtex 1A was distinguished from other organic materials, provided the density of the target was known (Sudac et al., 2008).

Another system under development aims to combine any number of interrogation techniques to obtain information. This method could use TNA, FNA, and NES in conjunction with gamma ray transmission to obtain information about the target and then compare that information to a library of threat templates that have already been analyzed and stored in its memory (Dunn et al., 2007). A different system is trying to use a cylindrical inertial electrostatic device, which is capable of creating D-T and D-D neutrons and 80 keV x-rays as a line-like source. By combining line source TNA and PFNA with x-ray interrogation, the system hopes to decrease scan time and false alarm rates associated with neutron beams (Wu et al., 2007). A different experiment, first simulated with a Monte Carlo numerical code, found that observing the slowing down of fast neutrons by hydrogen; the scattering of fast neutrons by carbon, nitrogen, and oxygen; and the Compton scattering of gamma rays due to the object's density, provide three useful indicators as to the composition of the object (Hussein et al., 2005).

Development is continuing on a portable active neutron interrogation system that utilizes D-T and D-D generators for TNA and FNA, with comparisons of laboratory benchmark measurements to Monte Carlo simulations (Alfonso et al., 2013). Combining signals from fast and inelastic neutron scatter is also being investigated (Lehnert and Kearfott, 2011a, Lehnert et al., 2012).

Although systems designed to search for illicit nuclear material is beyond the scope of this work, the active neutron interrogation methods discussed here can also be applied to that mission. When irradiating a target to search for conventional explosives, the neutrons may also stimulate the release of characteristic radiation from special nuclear material. If the system is properly calibrated, these signatures can be detected as well (Valković et al., 2007; Mihalczo and Mullens, 2012; Alfonso et al., 2013). This dual use encourages increased deployment while minimizing the cost and expense of fielding multiple systems.

Feasibility of explosives detection using neutrons

In a published review the National Academy of Sciences suggested that the x-ray screening systems already in place at airports were currently sufficient for explosives detection and recommended that a working prototype pulsed neutron system for luggage interrogation not be constructed (National Research Council, 2002). The abilities of the system were no better than the x-ray method, while the cost and size made implementation impractical. However, the report does suggest further laboratory research so as to be prepared for any new explosives detection challenges that may arise. It has been suggested by Buffler (2004) that the use of a fast neutron interrogation system may be better suited for application as a second or third tier screening device. Only after a possible threat had been identified by x-ray screening would the package be interrogated. Therefore, each package would have more time to be examined, which would lead

to better results. Also, the number of systems, and hence the price of implementing them, could be reduced as the number of packages screened would not be as large.

Conclusion

Advances in active neutron interrogation steadily continue. Various aspects of the systems, such as neutron generators, electronics, signal acquisition, and analysis algorithms, are improving (Gozani and Strellis, 2007). Furthermore, the cost and size of neutron and gamma ray detectors will continue to decline. This allows for cheaper and expanded deployment of neutron interrogation-based explosives detection systems.

For further improvement, several of the methods can be combined. If PFTNA can be combined with FNSA, both the inelastically and elastically scattered neutrons contribute a signal. This is a more efficient use of the neutron source, and as a result, fewer neutrons would be needed to determine if a target is a threat. These methods could be used in conjunction with non-nuclear based devices to reduce the required neutron flux further. This would increase the throughput of the system while reducing the amount of activation and potential dose. Additionally, the lower neutron flux would require less shielding, reducing the weight and size of the system.

Active neutron interrogation systems are an interesting alternative to other explosives detection methods. Their unique approach allows for detection of explosives that other systems may miss due to high density shielding or disguised contraband. However, they cannot detect all explosives or other illegal items, such as guns and knives. As the technology continues to improve, active neutron interrogation should be further explored as a possible replacement detection method or solution to new, unique problems.

Tables

Table 2.1: Summary of types of neutron sources, with advantages and disadvantages for use in active neutron interrogation systems for conventional explosives.

Neutron source	Examples	Advantages	Disadvantages
Fission	^{252}Cf	Small	Can't be turned "off"
		Relatively inexpensive	Not monoenergetic
(α, n)	Am/Be, Pu/Be	Small Relatively inexpensive	Can't be turned "off" Not monoenergetic
Photonuclear	^{9}Be or ^{2}H	Can be nearly monoenergetic	Photon source can't be turned off
	with ^{24}Na, ^{28}Al, or ^{38}Cl	Small Relatively inexpensive	High gamma ray background
Fusion generator	D-D, D-T	Can be nearly monoenergetic	Expensive
		Can be turned off	Associated electronics make it larger than other sources

Table 2.2: Summary of active neutron interrogation methods, including their advantages and disadvantages for conventional explosives detection.

Active neutron interrogation method	Advantages	Disadvantages
Thermal Neutron Analysis (TNA)	Detects nitrogen and hydrogen	Does not detect carbon or oxygen
	Higher interaction probability than FNA	
Fast Neutron Analysis (FNA)	Detects nitrogen, carbon, and oxygen	High neutron background
	Neutron moderation not required	Relatively low fast neutron interaction cross section
Pulsed Fast/Thermal Neutron Analysis	Detects hydrogen, carbon, nitrogen, oxygen, chlorine, silicone, and phosphorous	Lower interaction probability than NES
	Low neutron background compared to TNA and FNA	
Neutron Elastic Scatter (NES)	Higher interaction probability than neutron absorption	Determination of final neutron energy is difficult
	In theory, can detect all low atomic number elements	Can only detect low atomic mass nuclides
	Low neutron background	
Neutron transmission/Fast Neutron Radiography	Lower flux necessary since transmission is likely	Requires neutrons of various energies

References

Accorsi, R., Lanza, R.C., 2001. Coded aperture fast neutron analysis: latest design advances. Application of Accelerators in Research and Industry – Sixteenth Int'l Conf., *AIP Conf. Proc.,* 576, 491 – 494.

Al-Bahi, A.M., Soliman, A.Y.A, Hassan, M.H.M., Mohamed, N.M.A., 2013. Concept design of an illicit material detection system. *J. Radioanal. Nucl. Chem.*, Online Publication, October, 2013, 1-6.

Aleksandrov, V.D., Bogolubov, E.P., Bochkarev, O.V., Korytko, L.A., Nazarov, V.I., Polkanov, Y.G., Ryzhkov, V.I., Khasaev, T.O., 2005. Application of neutron generators for high explosives, toxic agents, and fissile material detection. *Appl. Radiat. Isotopes,* 63 (5-6), 537-543.

Alfonso, K., Marshal, E., King, M., Strellis, D., Gozani, T., 2013. MCNP simulation benchmarks for a portable inspection system for narcotics, explosives, and nuclear material detection. *IEEE T. Nucl. Sci.*, 60 (2), 520-527.

Beyerle, A., Hurley, J.P., Tunnel, L., 1990. Design of an associated particle imaging system. *Nucl. Instrum. Meth. A*, 299 (1-3), 458-462.

Bom, V.R., Datema, C.P., van Eijk, C.W.E., 2004. The status of the Delft University Neutron Backscatter Landmine Detector (DUNBLAD). *Appl. Radiat. Isotopes,* 61 (1), 21- 25.

Brewer, R.L., Dunn, W.L., Heider, S., Matthew, C., Yang, X., 2012. The signature-based radiation-scanning approach to standoff detection of improvised explosive devices. *Appl. Radiat. Isotopes*, 70 (7), 1181-1185.

Brooks, F.D., Drosg, M., Buffler, A., Allie, M.S., 2004. Detection of anti-personnel landmines by neutron scattering and attenuation. *Appl. Radiat. Isotopes,* 61 (1), 27-34.

Brooks, F.D., Drosg, M., Smit, F.D., Wikner, C., 2012. Detection of explosive remnants of war by neutron thermalisation. *Appl. Radiat. Isotopes*, 70 (1), 119 – 127.

Brown, D.R., Gozani, T., 1997. Thermal neutron analysis technology. SPIE Conference on Physics-Based Technologies for the Detection of Contraband, *Proc. SPIE*, 2936, 85-94.

Buffler, A., 2004. Contraband detection with fast neutrons. *Radiat. Phys. Chem.*, 71(3-4), 853-861.

Buffler, A., Brooks, F.D., Allie, M.S., Bharuth-Ram, K., Nchodu, M.R., 2001. Material classification by fast neutron scattering. *Nucl. Instrum. Meth. B*, 173 (4), 483-502.

Buffler, A., Tickner, J., 2010. Detecting contraband using neutrons: challenges and future directions. *Radiat. Meas.*, 45 (10), 1186 – 1192.

Carasco, C., Perot, B., Bernard, S., Mariani, A., Szabo, J-L., Sannie, G., Roll, Th., Valkovic, V., Sudac, D., Viesti, G., Lunardon, M., Bottosso, C., Fabris, D., Nebbia, G., Pesente, S., Moretto, S., Zenoni, A., Donzella, A., Moszynski, M., Gierlik, M., Batsch, T., Wolski, D., Klamra, W., Le Tourneur, P., Lhuissier, M., Colonna, A., Tintori, C., Peerani, P., Sequeira, V., Salvatoj, M., 2008. In-field test of EURITRACK tagged neutron inspection system. *Nucl. Instrum. Meth. A*, 588 (3), 397 – 405.

Chichester, D., Lemchak, M., Simpson, J., 2005. The API 120: A portable neutron generator for the associated particle technique. *Nucl. Instrum. Meth. B,* 241 (1-4), 753-758.

Chichester, D.L., Simpson, J.D., Lemchak, M., 2007. Advanced compact accelerator neutron generator technology for active neutron interrogation field work. *J. Radioanal. Nucl. Ch.*, 271 (3), 629-637.

Cinausero, M., Lunardon, M., Nebbia, G., Pesente, S., Viesti, G., Filippini, V., 2004. Development of a thermal neutron sensor for humanitarian demining. *Appl. Radiat. Isotopes*, 61 (1), 59 – 66.

Clifford, E., Ing, H., McFee, J., Cousins, T., 1999. High rate counting electronics for a thermal neutron analysis land mine detector. SPIE Conference on Penetrating Radiation Systems and Applications, *Proc. SPIE*, 3769, 155-166.

Clifford, E.T.H., McFee, J.E., Ing, H., Andrews, H.R., Tennant, D., Harper, E., Faust, A.A., 2007. A militarily fielded thermal neutron activation sensor for landmine detection. *Nucl. Instrum. Meth. A*, 579 (1), 418 – 425.

da Silva, A.X., Crispim, V.R., 2001. Use of thermal neutron tomography for the detection of drugs and explosives. *Radiat. Phys. Chem.*, 61 (3-6), 767-769.

Datema, C.P., Bom, V.R., Eijk, C.W.Ev., 2003. Monte Carlo simulations of landmine detection using neutron backscattering imaging. *Nucl. Instrum. Meth. A*, 513 (1-2), 398-402.

Davies, J.A., Hart, P.A., Wood, G.A., 1987. The determination of tin in explosive materials by thermal neutron activation analysis. *J. Radioanal. Nucl. Ch.*, 111 (1), 71 – 79.

Dokhale, P.A., Csikai, J., Oláh, A., 2001. Investigations on neutron-induced prompt gamma ray analysis of bulk samples. *Appl. Radiat. Isotopes*, 54 (6) , 967 – 971.

Dubnikova, F., Kosloff, R., Zeiri, Y., Karpas, Z., 2002. Novel approach to the detection of triacetone triperoxide (TATP): its structure and its complexes with ions. *J. Phys. Chem. A*, 106 (19), 4951 – 4956.

Dunn, W.L., Banerjee, K., Allen, A., van Meter, J., 2007. Feasibility of a method used to identify targets that are likely to contain conventional explosives. *Nucl. Instrum.Meth. B*, 263 (1), 179 – 182.

Eberhardt, J.E., Rainey, S., Stevens, R.J., Sowerby, B.D., Tickner, J.R., 2005. Fast neutron radiography scanner for the detection of contraband in air cargo containers. *Appl. Radiat. Isotopes*, 63 (2), 179 – 188.

Elsheikh, N., Viesti, G., ElAgib, I., Habbani, F., 2012. On the use of a (^{252}Cf – ^{3}He) assembly for landmine detection by the neutron back-scattering method. *Appl. Radiat. Isotopes*, 70 (4), 643 – 649.

Evans, R.J., Jupp, I.D., Lei, F., Ramsden, D., 1999. Design of a large-area CsI(Tl) photo-diode array for explosives detection by neutron-activation gamma-ray spectroscopy. *Nucl. Instrum. Meth. A*, 422 (1-3), 900-905.

Ewing, R.G., Atkinson, D.A., Eiceman, G.A., Ewing, G.J., 2001. A critical review of ion mobility spectrometry for the detection of explosives and explosive related compounds. *Talanta*, 54 (3), 515-529.

Farahmand, M., Boston, A.J., Grint, A.N., Nolan, P.J., Joyce, M.J., Mackin, R.O., D'Mellow, B., Aspinall, M., Peyton, A.J., van Silfhout, R., 2007. Detection of explosive substances by tomographic inspection using neutron and gamma-ray spectroscopy. *Nucl. Instrum. Meth. B*, 261 (1-2), 396 – 400.

Faust, A.A., 2002. Detection of explosive devices using x-ray backscatter radiation. SPIE Conference on Penetrating Radiation Systems and Applications IV, *Proc. SPIE*, 4786, 17-28.

Favalli, A., Pedersen, B., 2007. Design and characterization of a pulsed neutron interrogation facility. *Radiat. Prot. Dosim.*, 126 (1-4), 74 – 77.

Fioretto, E., Barbui, M., Giangrandi, S., Cinausero, M., Prete, G., Nebbia, G., Viesti, G., 2004. Neutron back-scattering sensor for the detection of land mines. *Nucl. Instrum. Meth. B*, 213, 457-459.

Furton, K.G., Myers, L.J., 2001. The scientific foundation and efficacy of the use of canines as chemical detectors for explosives. *Talanta*, 54 (3), 487-500.

Gokhale, P., Hussein, E., 1997. A Cf-252 neutron transmission technique for bulk detection of explosives. *Appl. Radiat. Isotopes*, 48 (7), 973-979.

Gozani, T., 1994. Novel applications of fast neutron interrogation methods. *Nucl. Instrum. Meth. A*, 353 (1-3), 635-640.

Gozani, T., 1995. Understanding the physics limitations of PFNA - the nanosecond pulsed fast neutron analysis. *Nucl. Instrum. Meth. B*, 99 (1-4), 743-747.

Gozani, T., Ryge, P., Shea, P., Seher, C., Morgado, R.E., 1989. Explosive detection system based on thermal neutron activation. International Carnahan Conference on Crime Prevention, *IEEE AES Magazine*, 4 (12), 17 - 20.

Gozani, T., Strellis, D., 2007. Advances in neutron based bulk explosives detection. *Nucl. Instrum. Meth. B*, 261 (1-2), 311 – 315.

Hall, J.M., Rusnak, B., Shen, S., Fitsos, P.J., 2006. High-energy neutron imaging developments at LLNL. *Lawrence Livermore National Laboratory: ESC Annual Report (FY05)*.

Harding, G., 2004. X-ray scatter tomography for explosives detection. *Radiat. Phys. Chem.*, 71 (3-4), 869-881.

Haslip, D., Cousins, T., Andrews, H., Chen, J., Clifford, E., Ing, H., McFee, J., 2001. DT neutron generator as a source for a thermal neutron activation system for confirmatory land mine detection. Hard X-Ray and Gamma-Ray Detector Physics III, *Proc. SPIE*, 4507, 232-242.

Hussein, E.M.A., Desrosiers, M., Waller, E.J., 2005. On the use of radiation scattering for the detection of landmines. *Radiat. Phys. Chem.*, 73 (1), 7 – 19.

Hussein, E.M.A., Waller, E.J., 1998. Review of one-side approaches to radiographic imaging for detection of explosives and narcotics. *Radiat. Meas.*, 29 (6), 581 – 591.

Im, H., Cho, H., Song, B.C., Park, Y.J., Chung, Y., Kim, W., 2006. Analytical capability of an explosives detection by a prompt gamma-ray neutron activation analysis. *Nucl. Instrum. Meth. A*, 566 (2), 442-447.

Jimènez, A.M., Navas, J.M., 2004. Chemiluminescence detection systems for the analysis of explosives. *J. Hazard. Mater.*, 106 (1), 1-8.

Knoll, G.F., 2010. Radiation Detection and Measurement, 4th ed. (Wiley, Hoboken, NJ), pp. 19-22.

Koltick, D., Kim, Y., McConchie, S., Novikiv, I., Belbot, M., Gardner, G., 2007. A neutron based vehicle-borne improvised explosive device detection system. *Nucl. Instrum. Meth. A*, 261 (1-2), 277-280.

Lanza, R., 2007. Nuclear techniques for explosive detection: current prospects and requirements for future development. *Proceedings of an IAEA Technical Meeting: combined devices for humanitarian demining and explosives*, *November 13-17, 2006*.

Lanza, R.C., Zhang, L., 1999. CAFNA, Coded aperture imaging for fast neutron analysis: application to contraband and explosive detection. Fifteenth Int'l Conf. on the Applications of Accelerators in Research and Industry, *AIP Conf. Proc.*, 475, 678 – 681.

Lehnert, A.L., Kearfott, K.J., 2010. The detection of explosive materials: review of considerations and methods. *Nucl. Technol.*, 172 (3), 325 – 334.

Lehnert, A.L., Kearfott, K.J., 2011a. Preliminary identification of flags for a novel algorithm-based approach for explosives detection using neutron interrogation for a simulated idealized cargo container scenario. *Nucl. Instrum. Meth. A*, 638 (1), 201 – 205.

Lehnert, A.L., Kearfott, K.J., 2011b. Simplified simulation of fast neutron scattering for an explosives detection application. *Nucl. Sci. Eng.*, 168 (3), 278 – 286.

Lehnert, A.L., Flaska, M., Kearfott, K.J., 2012. D-D neutron-scatter measurements for a novel explosives-detection technique. *Nucl. Instrum. Meth. A*, 693, 195-202.

Liu, Y., Sowerby, B.D., Tickner, J.R., 2008. Comparison of neutron and high-energy X-ray dual-beam radiography for air cargo inspection. *Appl. Radiat. Isotopes*, 66 (4), 463 – 473.

McFee, J., Faust, A., Andrews, H.R., Clifford, T., Ing, H., Cousins, T., Haslip, D., 2003. The feasibility of neutron moderation imaging for land mine detection. *P. Soc. Photo-opt. Ins.*, 4 (3), 209-240.

McFee, J.E., Cousins, T., Jones, T., Brisson, J.R., Jamieson, T., Waller, E., LeMay, F., Ing, H., Clifford, E.T.H., Selkirk, B., 1998. A thermal neutron activation system for confirmatory nonmetallic land mine detection. SPIE Conference on Detection and Remediation Technologies for Mines and Minelike Targets III, *Proc. SPIE*, 3392, 553-564.

Mihalczo, J., Mullens, J., 2012. Nuclear material identification system with imaging and gamma-ray spectrometry for plutonium, highly enriched uranium, high explosives, and other materials. *Oak Ridge National Laboratory - Global Nuclear Security Technology Division: ORNL/TM-2012/22*.

Moore, D.S., 2004. Instrumentation for trace detection of high explosives. *Rev. Sci. Instrum.*, 75 (8), 2499 – 2512.

Moore, D.S., 2007. Recent advances in trace explosives detection instrumentation. *Sens. Imaging*, 8 (1), 9 – 38.

Mor, I., Vartsky, D., Bar, D., Feldman, G., Goldberg, M.B., Katz, D., Sayag, E., Shmueli, I., Cohen, Y., Tal, A., Vagish, Z., Bromberger, B., Dangendorf, V., Mugai, D., Tittelmeier, K., Weierganz, M., 2009. High spatial resolution fast-neutron imaging detectors for pulsed fast neutron transmission spectroscopy. J. Instrum., 4, P05016.

Naqvi, A.A., Al-Matouq, F.A., Khiari, F.Z., Isab, A.A., Raashid, M., Khateeb-ur-Rehman, 2013. Hydrogen, carbon and oxygen determination in proxy material samples using a LaBr3:Ce detector. *Appl. Radiat. Isotopes*, 78, 145-150.

Nunes, W.V., Silva, A.Xd., Crispim, V.R., Schirru, R., 2002. Explosives detection using prompt-gamma neutron activation and neural networks. *Appl. Radiat. Isotopes*, 56 (6), 937-943.

Overley, J.C., 1985. Determination of H, C, N, O content of bulk materials from neutron-attenuation measurements. *Int. J. Appl. Radiat. Is.*, 36 (3), 185-191.

Overley, J.C., Chmelik, M.S., Rasmussen, R.J., Schofield, R.M.S., Sieger, G.E., Lefevre, H.W., 2006. Explosives detection via fast neutron transmission spectroscopy. *Nucl. Instrum. Meth. B*, 251 (2), 470-478.

Overley, J., Chmelik, M., Rasmussen, R., Sieger, G., Schofield, R., Lefevre, H., 1997. Results of tests for explosives in luggage from fast-neutron time-of-flight transmission measurements. SPIE International Conference Neutrons in Research and Industry, *Proc.SPIE*, 2867, 219-222.

National Research Council, 2002. Summary -- Assessment of the Practicality of Pulsed Fast Neutron Analysis for Aviation Security. The National Academies, Washington, D.C.

Raas, W.L., Blackburn, B., Boyd, E., Hall, J.M., Kohse, G., Lanza, R., Rusnak, B., Watterson, J.I.W., 2005. Neutron resonance radiography for explosives detection: technical challenges. *Nuclear Science Symposium Conference Record, 2005 IEEE*, (1), 129-133.

Reda, A.M., 2011. Monte Carlo simulations of a D-T neutron generator shielding for landmine detection. *Radiat. Meas.*, 46 (10), 1187 – 1193.

Runkle, R.C., White, T.A., Miller, E.A., Caggiano, J.A., Collins, B.A., 2009. Photon and neutron interrogation techniques for chemical explosives detection in air cargo: a critical review. *Nucl. Instrum. Meth. A*, 603 (3), 510 – 528.

Shaw, T.J., Brown, D., D'Arcy, J., Liu, F., Shea, P., Sivakumar, M., Gozani, T., 2005. Small threat and contraband detection with TNA-based systems. *Appl. Radiat. Isotopes*, 63 (5-6), 779 – 782.

Singh, S., Singh, M., 2003. Explosive detection systems (EDS) for aviation security. *Signal Process.*, 83 (1), 31-55.

Sowerby, B.C., Tickner, J.R., 2007. Recent advances in fast neutron radiography for cargo inspection. *Nucl. Instrum. Meth. A*, 580 (1), 799-802.

Steinfeld, J.I., Wormhoudt, J., 1998. Explosive detection: a challenge for physical chemistry. *Annu. Rev. Phys. Chem.*, 49 (1), 203 -232.

Strellis, D., Gozani, J., Stevenson, J., 2009. Air cargo inspection using pulsed fast neutron analysis. *International Topical Meeting on Nuclear Research Applications and Utilization of Accelerators*, *Vienna, Austria, May 4-8, 2009*.

Strom, D.J., Callerame, J., 2004. "Imaging and identification technologies for homeland security", in: Brodsky, A., Johnson, R.H. Jr., Goans, R.E. (Eds.), *Public Protection from Nuclear, Chemical, and Biological Terrorism: The 2004 Health Physics Society Summer School*. Medical Physics Publishing, Madison, Wisconsin, pp. 49 – 68.

Sudac, D., Blagus, S., Valkovic, V., 2007. The limitation of associated alpha particle technique for contraband container inspections. *Nucl. Instrum. Meth. B*, 263 (1), 123 – 126.

Sudac, D., Matika, D., Valkovic, V., 2008. Identification of materials hidden inside a sea-going cargo container filled with an organic cargo by using the tagged neutron inspection system. *Nucl. Instrum. Meth. A*, 589 (1), 47 – 56.

Sudac, D., Vlakovic, V., Nad, K., Obhodas, J., 2011. The underwater detection of TNT explosive. *IEEE T. on Nucl. Sci.*, 58 (2), 547 – 551.

Tang, S., Hussein, E.M.A., 2004. Use of isotopic gamma sources for identifying anti-personnel landmines. *Appl. Radiat. Isotopes*, 61 (1), 3-10.

Todd, R.W., Nightingale, J.M., Everett, D.B., 1974. A proposed γ camera. *Nature,* 251, 132 – 134.

Valković, V., Sudac, D., Blagus, S., Nađ, K., Obhođaš, J., Vekić, B., G., Pesente, S., 2007. Fast neutron inspection of sea containers for the presence of "dirty bomb". *Nucl. Instrum. Meth. B*, 263 (1), 119-122.

Vourvopoulos, G., Womble, P.C., 2001. Pulsed fast/thermal neutron analysis: a technique for explosives detection. *Talanta*, 54 (3), 459 – 468.

Whetstone, Z.D., Kearfott, K.J., 2011. Use of multiple layers of repeating material to effectively collimate an isotropic neutron source. *Nucl. Technol.*, 176 (3), 395 – 413.

Womble, P.C., Campbell, C., Vourvopoulos, G., Paschal, J., Gácsi, Z., Hui, S., 2001. Detection of Explosives With the PELAN System. Application of Accelerators in Research and Industry – Sixteenth Int'l Conf., *AIP Conference Proceedings*, 576, 1069 – 1072.

Wu, L., Miley, G.H., Momota, H., Shrestha, P.J., 2007. An integrated broad area coverage fusion neutron/x-ray interrogation unit. *Fusion Sci. Technol.*, 52 (4), 1096 – 1100.

CHAPTER 3: USE OF MULTIPLE LAYERS OF REPEATING MATERIAL TO EFFECTIVELY COLLIMATE AN ISOTROPIC NEUTRON SOURCE

Abstract

This research was conducted to determine the optimal way to shield a compact, isotropic neutron source into a beam for active interrogation neutron systems. To define the restricted emission angle and to protect nearby personnel when standoff distances are limited, shielding materials were added around the source. Due to limited space in many locations where active neutron interrogation is employed, a compact yet effective design was desired. Using the Monte Carlo N-Particle Transport Code, several shielding geometries were modeled. Materials investigated were polyethylene, polyethylene enriched with ^{10}B, water, bismuth, steel, nickel, Inconel 600, tungsten, lead, and depleted uranium. Various simulations were run testing the individual materials and combinations of them. It was found that at a standoff distance of 1.5 m from the source, the most effective shielding configuration is a combination of several layers of polyethylene and steel. Without any shielding, the dose is 3.71×10^{-15} Sv per source particle. With a shielding consisting of multiple layers of steel totaling 30 cm thick, interspersed with several layers of polyethylene totaling 20 cm thick, the dose drops to 3.68×10^{-17} Sv per emitted neutron at π radians opposite the shield opening. The layered shielding approach is more effective at reducing dose equivalent and neutron fluence than shields made out of single

continuous layers of the same material and thicknesses. Adding boron to the polyethylene and substituting tungsten for steel would make the shielding more effective, but add mass and cost.

Introduction

Compact neutron sources are used for a variety of active neutron interrogation techniques, including special nuclear material detection (Hall et al., 2007), explosives detection at ports and border crossings (Lehnert and Kearfott, 2010), and landmine detection (Clifford et al., 1999; Cinausero et al., 2004). In general, the neutron sources used are isotropic. However, many of the applications could benefit from a narrow neutron beam instead of an isotropic source.

There are many options for an active interrogation neutron source, including, but not limited to: spontaneous fission sources such as ^{252}Cf; sources that pair two isotopes, one alpha emitting and the other that absorbs the alpha particle and emits a neutron, including plutonium beryllium, americium beryllium, and americium lithium; photoneutron sources containing ^{9}Be and ^{2}H; and portable accelerators that create neutrons through deuterium-deuterium (D-D) and deuterium-tritium (D-T) fusion reactions (Knoll, 2010). In all of these cases, the neutrons are released with an isotropic or nearly isotropic angular distribution. This is not a desirable feature for most active neutron interrogation systems for a variety of reasons, including safety and signal interpretation.

In the case of neutron elastic scatter, if the angle of approach of the neutrons is unknown, the information gathered by the active neutron interrogation system cannot be properly analyzed due to an unknown incidence angle (Buffler, 2004; Lehnert and Kearfott, 2011). Furthermore, the neutrons created in the source that are not initially directed at the target may interact with

other objects within the vicinity of the source. The scattered neutrons or their secondary radiation could interact in the system's detectors and create an undesired signal that makes determination of the materials within the target more difficult. Additionally, active neutron interrogation systems search for illicit materials within a larger object. If the source is not shielded, then the neutrons will hit a large cross section of the target all at once. If contraband is detected, it can be difficult to determine its exact location. Finally, the large neutron fluxes associated with these systems pose a radiation health risk for personnel or civilians near the source.

The problems associated with active neutron interrogation discussed above can be mitigated by using appropriate materials to selectively shield the neutron source. An isotropic source can be shielded such that a majority of the neutrons emitted at a specified angle are unattenuated. Most of the neutrons emitted at other angles are scattered, usually multiple times, within the shielding material. They are either eventually absorbed within the shield or exit it at lower energies. It is desirable to collimate neutron sources into a beam in active neutron interrogation systems. Fewer neutrons scattering in the environment contribute to a cleaner signal in the detector and a reduced dose to nearby personnel. Furthermore, a well collimated beam allows the operator to know the incidence angle of the neutrons and systematically work the neutron beam over the target while investigating specific target volumes.

The purpose of this research was to determine the optimal shielding to allow for 14.1 MeV D-T source neutrons to emerge from the shielding at one angle unattenuated, while limiting the emissions of neutrons at all other angles. Although there are a number of possible sources that can be used in active neutron interrogation, the D-T source has seen widespread use (Pesente et al., 2004; Aleksandrov et al., 2005; Wu et al., 2007; Carasco et al., 2008). As opposed to fission sources, alpha-neutron sources, and photoneutron sources, a D-T generator can be turned

off and will stop emitting neutrons, which is a desirable safety feature. Additionally, the energy of D-T neutrons is higher than the average energy of any of the other sources. Therefore, any shielding designs appropriate for D-T generators can be scaled for lower energy neutrons produced by other sources.

It is not very difficult to shield neutrons if size and mass of the shielding is not an issue. If enough moderating material is placed between the source and the area of interest, the neutron fluence can be reduced to appropriate levels. However, in many instances where active neutron interrogation is used, such as airports, border crossings, and shipping ports, space is at a premium. In the case of landmine detection, the entire system, including shielding, must be portable. As a result, large, stationary neutron shields are not appropriate. Instead, an alternative shielding arrangement must be found that is more compact and effective.

Shielding fast neutrons, compared to other forms of ionizing radiation, has presented a unique challenge from the near beginning of the nuclear age to the present time (Fermi and Zinn, 1957; Studenski and Kearfott, 2007). Due to their lack of charge, neutrons tend to pass through materials with relative ease. This makes them ideal for searching for hidden contraband. However, this also means neutron shielding must be approached differently than other types of ionizing radiation. For neutrons with energy near 14 MeV, medium to high atomic number materials; such as iron, nickel, and lead, have higher attenuation cross sections compared to low atomic number materials; such as hydrogen, carbon, and oxygen (Shultis and Faw, 1996). For neutrons in the keV – MeV range, elastic scatter is the primary interaction with low atomic number elements, and a likely interaction with medium to high atomic number elements. Conservation of energy and momentum show that, on average, a neutron will lose more energy per elastic collision with lighter nuclei than it will with heavier nuclei. As neutrons lose energy,

the capture cross sections of most nuclei increase, which makes neutron capture more likely. Therefore, an effective method of neutron attenuation is through multiple elastic collisions with light nuclei. Hence, lighter nuclides are commonly used for shielding neutrons. However, iron and other similar elements have large attenuation cross sections and should not be entirely discounted. Each type of material has its own advantages and disadvantages when it comes to shielding neutrons, but if they are combined, the best properties of both materials can be employed.

Using layers of materials to shield neutrons was first proposed by Morrison (Morrison, 1957). Repeating layers of hydrogenous material and higher atomic number material work to slow and absorb neutrons, then shield any secondary gamma rays created. Additional research was done to Morrison's proposed design by Greene and Thomas in 1969 (Greene and Thomas, 1969), which was then expanded upon by Maruyama and Bouts in 1972. Several different shielding configurations were set up and tested in a lab. The materials tested included steel, polyethylene, borated wood, and borated polyethylene. A neutron source was set up on the opposite side of the shielding from a neutron detector. After taking measurements, the ideal shielding design was found to include polyethylene and steel with 5 cm of polyethylene close to the source in order to reduce activation of the steel, then 25 cm of steel, then 5 cm of polyethylene, an additional 5 cm of steel, 5 more cm of polyethylene, and finally 5 cm of steel, for a shield thickness of 50 cm. Each of these measurements required setting up and deconstruction of heavy materials, which would be time-consuming and limit the number of configurations that could be tested. Now, with advanced simulation methods, it is possible to try a much larger variety of materials and shielding combinations in order to find an optimal configuration.

Neutron shielding materials can then be used to make an isotropic source appear more like a neutron beam. Constructing a "beam" of neutrons is important in medical neutron therapy (Lundberg, 1973; Brahme, 1984; Mollon, 1987) and has also been considered for active neutron interrogation as well (Kearfott, 2008). The prevalence of isotropic neutron sources coupled with the difficulty in attenuating neutrons makes obtaining a monodirectional beam difficult. Additionally, since active neutron interrogation systems tend to be deployed in areas with limited space, the shielding size and mass is another important factor to consider.

In this paper, several new shielding configurations for D-T generators are discussed and their neutron shielding effectiveness is examined. Also, data are presented that show that the layered shielding approach is effective at maintaining a beam of unattenuated neutrons at the shield opening while significantly reducing the neutron flux at all other angles.

Materials and Methods

Due to the extended time required and high cost involved with testing so many shielding variations, real measurements in a laboratory could not be performed. Instead, the shielding design optimizations were performed as simulations in a Monte Carlo radiation transport computer program. The program used was the Monte Carlo N-Particle Transport Code (MCNP)[1]. A post processing computer code was written and executed in a commercially available mathematics parser[2] to extract data from the MCNP output, which was then collected and graphed in a commercially available spreadsheet[3] for analysis and comparison.

[1] computer code Monte Carlo N-Particle Transport version 5 (Los Alamos National Laboratory, Los Alamos, NM 87545, 2006).

[2] computer program MATLAB (The MathWorks, Inc., Natick, MA 01760-2098, 2006).

[3] computer program Microsoft Excel (Microsoft Corp., Redmond, WA 98052, 2007).

Several materials were tested in the simulations: water; polyethylene; borated polyethylene; steel; nickel; Inconel 600, a nickel alloy; tungsten; lead; bismuth; and depleted uranum. Water, polyethylene, and borated polyethylene were chosen because of their ability to moderate and absorb neutrons. Materials with medium to heavy elements, such as steel and tungsten, were chosen because they were listed as effective, dense materials for shielding neutrons (Shultis and Faw, 1996; Hussein, 2003). The chemical composition and density of all materials tested can be found in Table 3.1. The use of some of the medium to higher atomic number materials could lead to neutron activation and was investigated (Hussein, 2003). In one arrangement, lead was used as an additional outside layer to attenuate any secondary gamma rays that may escape the shielding.

All of the shielding arrangements were a variation on the same design. The materials were arranged in a cylinder, 100 cm in length, with a typical radius of 66 cm. An isotropic 14.1 MeV neutron point source was placed at the center of the cylinder. One end of the cylinder had a hole in it 50 cm deep, with a radius of 16 cm. The shielding consisted of layers 5 cm thick. Each layer could have its material varied independently. The solid angle of the unattenuated neutron beam is about 1.14 steradians, which is equivalent to a cone subtending and angle of just over 35°. The solid angle was designed to meet the specifications of active neutron interrogation research being performed in the investigators' facility (Lehnert and Kearfott, 2011).

An example of the shielding can be seen in Figs. 3.1, 3.2, and Appendix A. It was surrounded on all sides by air. Several different arrangements of the materials were tested. Each specific arrangement is referred to as a geometry. A list of all the geometries simulated can be found in Table 3.2, while Fig. 3.3 gives a visual representation of geometries 1 - 14. Geometry 4 contains the same materials and thickness that were determined as optimal by Maruyama and

Bouts (1972). Geometries 11 – 14 were tested as alternatives to this design. They still consist of several alternating layers, however, the thickness of the large steel layer in the center was varied and additional alternating layers of steel and polyethylene were added to the outside in order to determine if Maruyama and Bouts' design was the best solution. Geometries 15 – 23 have the same layered design as geometry 11, however, various other materials are substituted in for the steel or polyethylene in order to test their shielding effectiveness.

Two different metrics were used to evaluate the effectiveness of each shielding geometry. The first was to simulate the neutron and photon dose equivalent received at several points around the shielding. In order to do this, five spheres were constructed in MCNP, each with a radius of 25 cm. They were placed 1.5 m from the source at specific angles relative to the opening of the shielding. The sphere directly in front of the shielding is considered to be at 0 radians. The next four were placed at $\pi/4$ radians, $\pi/2$ radians, $3\pi/4$ radians, and π radians. This configuration can be seen in Fig. 3.4. The dose at each of the 5 points was estimated by multiplying the estimated neutron and photon fluence at a point at the center of each of the spheres by dose conversion factors found in ICRP Publication 51 (1987) and ICRU Report 47 (1992). The fluence at a point was found using the F5 tally in MCNP. A large enough number of particle histories was run in order to keep statistical uncertainty below 5%.

The second method used for evaluating the various shielding geometries was to examine the estimated energy dependent neutron and photon fluence at the various angles. The F1 tally in MCNP 5 was used to determine the energy of each particle crossing the surface of a sphere in the simulation in order to estimate fluence. The same spheres as before were used, but in this case their interior was set to a vacuum and particles entering the sphere were counted. The energy spectra for the neutrons and photons passing through the spheres were generated, then

normalized by the width of their energy bin, and graphed. The neutron and photon fluence through each of the spheres was estimated for geometries 0, 1, 3, 4, and 6 – 22. However, since the purpose of the shielding is to allow unattenuated neutrons to emerge from the opening while attenuating neutrons emitted at all other angles, and the photon dose turned out to be so low, only the normalized neutron fluence was plotted.

In order to limit statistical uncertainty within the spectra, a large number of histories were run for each simulation. The number of histories was determined so that uncertainty within each energy bin was below 10%. However, in many cases, the uncertainty was below 5%. The number of histories required to limit uncertainty was a function of the number of neutrons that were simulating crossing the surface of the spheres. As such, the number of histories ran for a simulation varied depending on the effectiveness of the shielding.

The mass of each geometry was calculated using the density and volume of each of the layers. Only the materials listed were taken into account. No support structure or construction materials were included in the calculation.

There were concerns that the large neutron flux would activate some of the shielding materials to the point where their use would be impractical due to the imparted radioactivity and the complications that would create. Although full activation analysis is beyond the scope of this work, several simulations were run in MCNP to estimate the order of magnitude of the activation rate. To do this, an F4 tally, which provides the flux averaged over a cell, was calculated for each layer of steel in geometry 11. A multiplication function within MCNP was used to multiply this flux by the energy dependent (n,γ), (n,p), (n,2n), and (n,α) cross sections for each naturally occurring isotope of iron, manganese, and chromium. The number of new isotopes created by a particular reaction with a specific isotope can be determined by the differential equation,

$$\frac{dN_n}{dt} = N_i \sigma \varphi - \lambda_n N_n , \tag{3.1}$$

where N_n is the number of new nuclei, N_i is the number of initial nuclei, σ is the reaction cross section for the initial nuclei, φ is the neutron flux, λ_n is the decay constant of the new nuclei, and t is time. The equation can be solved for the number of new nuclei as a function of time:

$$N_n(t) = \frac{N_i \sigma \varphi}{\lambda_n}\left(1 - e^{-\lambda_n t}\right). \tag{3.2}$$

Therefore, the activity of the new nuclei, A_n, is:

$$A_n(\lambda_n, t) = N_i \sigma \varphi \left(1 - e^{-\lambda_n t}\right). \tag{3.3}$$

The maximum activity as $\lambda_n t$ approaches infinity is then:

$$A_{\max} = N_i \sigma \varphi . \tag{3.4}$$

The F4 tally with the multiplication function provides an estimate of $\sigma\varphi$ per source neutron within the cell. The reaction rates for each isotope were then multiplied by their relative abundance within steel and the total number of atoms for each layer. Finally, this was multiplied by the generator's neutron production rate, which was estimated to be 2 x 10^8 neutrons per second. This provided the number of new radioactive isotopes at a given time. λ_n is already

known, allowing for an estimate of the maximum activity for each isotope. The maximum activities for each isotope in each steel layer were then summed to determine the total maximum activity. For these calculations, the steel was assumed to have 2% manganese and 20% chromium by weight, in order to account for steel alloys with relatively high amounts of each of these elements.

The same process and assumptions were repeated for the tungsten and nickel in geometries 10 and 16, assuming no additives to those shielding materials. For geometry 10, it should be noted that the MCNP library used did not have cross section data available for ^{180}W. Therefore, it was estimated that the interaction probability of ^{180}W was equal to the largest interaction probability of the other isotopes in a given layer. Furthermore, after the interaction with the neutron, some of the new nuclei were isotopes that possessed a metastable state. It was not clear how often a reaction would cause a nucleus to go to a metastable state instead of a ground state, so the conservative estimate was made to assume it occurred for every reaction. For example, ^{184}W absorbed a neutron and became ^{185m}W, which decayed to ^{185}W, which then decays by beta emission to ^{185}Re, a stable nucleus. It was assumed that for every ^{184}W nucleus that absorbs a neutron, there were two decays. Additionally, if any new nucleus formed and decayed to another unstable nucleus, the decay of the progeny nucleus was also accounted for in the activity estimate. It was possible that a single reaction could contribute 3 or more decays due to metastable states and unstable progeny.

Finally, in order to investigate the effectiveness of the shielding and the neutron beam intensity, the simulated neutron flux emerging from the opening of the shielding was examined for geometry 11. Within MCNP, the neutron flux at varying radial distances from the centerline of the opening were estimated. Planes were constructed parallel to the shielding surface that

contained the opening. Rings 5 cm thick were then constructed on the plane, creating a bull's-eye design with the centerline of the opening passing through the center of the bull's-eye. Neutrons passing through each ring were counted and their energy was tallied. This was done at the shielding surface, 25 cm, 50 cm, 100 cm, and 150 cm from the opening surface. The shielding was simulated in a vacuum to focus entirely on the shielding materials' performance.

Results

The dose equivalent at each of the five points surrounding the shielding was estimated for both photons and neutrons for geometries 1 – 10 and can be found in Table 3.3. Due to photon attenuation within the shielding, the neutron dose is much higher than photon dose, and is the primary concern. Lead around the outside of the shielding is unnecessary, while adding over 3,000 kg to the mass of the shielding, and will not be evaluated further as an exterior photon shield. Moreover, the shielding made entirely of water, geometry 2, was not as effective at reducing dose as the shielding made of polyethylene, geometry 1, and therefore was not further investigated.

The relative neutron fluence for each of these geometries at the opening of the shielding, 0 radians, is shown in Fig. 3.5. There is a visible peak for all the spectra around 14 MeV. However, there are also a large number of neutrons with energy below 1 MeV due to multiple scattering events. The relative fluence at $\pi/4$ radians is also shown in Fig. 3.6. The sphere used to determine the fluence is outside the solid angle defined by the shielding opening, and therefore gives a good idea of how effective the shielding is. There is still a peak around 14 MeV for all the spectra, but the number of neutrons has decreased over two orders of magnitude for every geometry except for 0, which is air, and 3, which is less than 6 cm of steel. There are also more

lower energy neutrons than were present at 0 radians. Finally, Fig. 3.7 gives the relative neutron fluence at $3\pi/4$ radians. Out of all the spheres, the neutrons must travel the furthest through the shielding material to reach this sphere. The peak near 14 MeV is depressed between three and four orders of magnitude for all geometries except 0 and 3, when compared to the spectra at 0 radians. There are also a large number of low energy neutrons, but fewer than compared to the spectra at 0 or $\pi/4$ radians.

It is understood that the neutron flux, as simulated, is not a continuous spectra, but rather a series of binned counts. However, it was difficult to show multiple histograms on a single figure, so a scatter plot was used instead. Be aware that all these spectra represent histograms with the points representing the left edge of each bin.

According to the simulations, the layered shielding is effective. Even though the same thicknesses of each material were used, geometry 4 was more effective at reducing dose than either geometry 8 or 9, where there were no repeating layers. Therefore it is important to see if geometry 4, which was based on Maruyama and Bouts' design (1972), is the best layering arrangement. Geometries 11 – 14 are all variations on the layering theme. The doses estimated outside the shielding for geometry 4 and geometries 11 – 14 can be found in Table 3.4. The dose for geometry 11 is the lowest of the five shielding configurations. Figs. 3.8, 3.9, and 3.10 are the relative energy dependent neutron fluences for air, geometry 4, and geometries 10 – 14 at 0, $\pi/4$, and $3\pi/4$ radians, respectively. As with the other spectra, there is a peak around 14 MeV at 0 radians, but it is suppressed by several orders of magnitude at $\pi/4$ and $3\pi/4$ radians.

Geometry 11 proved to reduce dose equivalent and neutron flux as effectively as geometry 4, but its design had more polyethylene and less steel, which reduced the weight. Geometries 15 – 22 were all variations on this design. Different materials were switched in for

either the steel or polyethylene. The dose estimates outside the shielding are compiled in Table 3.5, with geometry 11 also included for reference. Geometries 16 – 18 had lower total dose equivalents at all 5 points around the shielding than geometry 11, while all other geometries had larger dose equivalents. At 0 and $\pi/4$ radians, geometry 16 was the lowest with about a 28% reduction in dose equivalent at $\pi/4$ radians. At $\pi/2 - \pi$ radians, the lowest dose equivalent was for geometry 18, which was nearly a 50% reduction relative to geometry 11.

The results of the simulations can be found in Fig. 3.11a and b for 0 radians, 3.12a and b for $\pi/4$ radians, and 3.13a and b for $3\pi/4$ radians. At 0 radians, the relative neutron fluences are about the same as geometry 11. Geometry 18 has a slightly increased neutron fluence below 6 MeV and mildly decreased fluence above. At $\pi/4$ radians, the various relative fluences again are all very similar with all of them showing a decreased number of 14.1 MeV neutrons when compared to geometry 0. At higher energies, it appears geometry 15 is the highest of the fluences and geometry 18 is the lowest. In Fig. 3.13a and b, the fluences become slightly more differentiated. Geometries 15, 20, and 21 are clearly higher than the other geometries, while above several MeVs, geometries 18 and 19 appear to have the lowest relative fluence. It should also be noted that geometry 19, which included depleted uranium, had some neutrons that exceed 14.1 MeV in all of its fluences.

The mass of each geometry is given in Table 3.6, with geometry 10 having the maximum mass of 17,800 kg and geometry 3 the minimum mass of 352 kg.

The results of the activation estimates for steel, nickel, and tungsten were calculated using MCNP. The maximum activation of the steel was estimated to be 6.0×10^7 Bq or 1.6 mCi. The maximum activation for the nickel was estimated to be 1.2×10^8 Bq or 3.3 mCi. Finally, the maximum activation for the tungsten shielding was 2.0×10^9 Bq or 55 mCi.

The simulated neutrons emerging from the opening of geometry 11 were tallied in MCNP. The average energy for the neutrons passing through each ring was estimated. The results for the plane at the shielding surface, 25 cm, 50 cm, 100 cm, and 150 cm can be seen in Fig. 3.14. In an attempt to quantify the neutron beam intensity, the neutron count, normalized by the area of each ring, was then multiplied by the average neutron energy for each ring. These values can be seen in Fig. 3.15.

Discussion

The various neutron shielding designs are very effective in attenuating not only neutrons, but also photons. The dose equivalent for photons was significantly lower than for neutrons for every geometry tested. In shielding geometries that used dense, mid to high atomic number materials such as steel, lead, and tungsten, the photon dose was nearly two orders of magnitude less than the neutron dose equivalent. However, even geometries comprised entirely of hydrogenous materials had a photon dose equivalent one order of magnitude less than the neutron dose equivalent. This is fortunate. It means that when building neutron shielding structures such as these, an exterior lead layer to attenuate secondary photons will not be needed. The main concern for dose is from the neutrons. If those can be properly handled, then the photon dose should already be under control.

It was also interesting to note that geometries 8 and 9 provided higher doses at angles other than 0 radians when compared to geometry 4. They all used the same amount of materials, 15 cm of polyethylene and 35 cm of steel, however, when they are layered intermittently, they actually provide more of a shielding benefit than when they are separated. Due to the large relative mass of high atomic number materials contrasted to the low mass of a neutron, the

energy lost by the neutron in an elastic scatter with a higher atomic number material is minimal. By employing multiple layers of the low atomic number and mid to high atomic number materials, the neutrons will pass through one or more layers of moderating material and have a chance of being slowed and absorbed. If they are not absorbed, they will also pass through several layers of higher atomic number scattering material. The neutrons that interact in these materials will be scattered through the shielding materials and have additional opportunities to be slowed and absorbed by the moderating material. By causing the neutrons to pass through the moderating material multiple times via scattering off mid- to high-atomic-number materials, the size of the shielding structure can be reduced.

It should be noted that although the dose equivalent for geometry 9 is larger than geometry 4 everywhere except at 0 radians, the neutron dose equivalent a $\pi/2 - \pi$ radians was actually lower. The larger gamma ray dose equivalent made the total dose equivalent larger for geometry 9 than geometry 4, which is most likely the result of neutron capture within the polyethylene and outer layers of steel that are not sufficiently shielded. Borated polyethylene may reduce the number of neutrons absorbed in the steel and reduce the gamma ray dose equivalent.

An awareness of cost versus benefit is important when examining the data. The borated polyethylene in geometry 7 helped to reduce the dose by 8.0%, compared to geometry 4. This is due to the large neutron capture cross section of ^{10}B. Owing to the increased cost of obtaining borated polyethylene, the relatively small benefit must be weighed against the higher price. The layers of tungsten and polyethylene were the most effective at reducing dose, so it would make an ideal choice. However, tungsten is much more expensive and could be very costly when buying the large amounts needed for this shielding application.

Figs. 3.5 and 3.8 show that the neutrons emerging from the shielding opening are mostly in the energy range of 14 MeV. The amount of lower energy neutrons fall off between two to three orders of magnitude. There is a large peak near the thermal neutron energy range. This is because some neutrons not originally emitted at 0 radians interacted in the shielding material, were slowed down, but not absorbed. They were then able to exit the shielding and pass through the sphere. The addition of ^{10}B to the polyethylene helped to reduce the number of low energy neutrons, but there were still some present. Depending on the application, energy discrimination or time-of-flight measurements may be able to help keep track of and neglect the low energy neutrons (Buffler, 2004). If only neutrons of a specific energy are examined, this will help eliminate some of the noise in the system.

Neutrons that are initially directed at or are scattered towards the sphere at $\pi/4$ radians must first travel through the shielding material. Comparing Fig. 3.6 to Fig. 3.5 and Fig. 3.9 to Fig. 3.8 gives a good idea at how effective the shielding is. There is no longer a peak of neutrons at 14 MeV. The spectra show that most of the neutrons at this location have a lower energy. This corresponds to what was seen in Tables 3.3 – 3.5. As the point of interest moves further from the shield opening, the neutrons have to travel through more material and the dose equivalent and neutron fluence both decrease quickly. The neutron spectrum for the sphere at $3\pi/4$ radians further confirms this. With even more shielding material to pass through, the neutron fluence is reduced even further. This would be the ideal place for personnel or detectors to be, because it is the most shielded location.

The layered shielding design, originally proposed by Maruyama and Bouts and adapted for study here, was effective at shielding the neutrons at angles other than 0 radians. It reduced dose rate surrounding the shielding compared to geometry 1, a pure polyethylene shield, and

geometries 8 and 9, which contained the same thicknesses of steel and polyethylene but were not layered. The relative neutron energy spectra of geometry 4 was very similar to the other steel and polyethylene layered shielding arrangements, geometries 11 – 14, even though the layers were arranged differently. Geometry 11 also was more effective at reducing dose than geometry 4 and it contained less steel, so it was lighter. Geometry 11 is a better configuration than geometry 4 and was investigated further.

Several other materials were tested using the pattern of layering seen in geometry 11. Geometries 19, 20, and 21, which replaced steel with depleted uranium, lead, and bismuth, respectively, were not as effective as geometry 11. Additionally, the spectrum for the depleted uranium had a small amount of neutrons above 14.1 MeV, which was a result of induced fissions and other neutron interactions. These higher energy neutrons are less than ideal, because even after multiple collisions, they could still have a relatively high energy and cause confusion within any data obtained. In geometry 22, water replaced the polyethylene in geometry 11. This substitution proved less effective. Polyethylene is a better moderating material and absorbs more slow neutrons when doped with ^{10}B.

Geometries 16 – 18 were more effective at reducing neutron fluence around the shield than geometry 11. Furthermore, the dose equivalent was reduced by nearly 50%. Geometry 16 replaced the steel in geometry 11 with nickel. Geometry 17 was similar to geometry 16, but instead of pure nickel, the nickel alloy Inconel 600 was used, which was less effective. Geometry 18 also used pure nickel, but the inner layers of polyethylene and nickel were switched. The neutron spectra at 0 and $\pi/4$ radians showed the neutron fluence for geometry 16 was similar to geometry 11, but at lower energies, geometry 18 had a higher relative fluence, while at energies above 6 MeV or so, the fluence for geometry 18 was decreased. At $3\pi/4$ radians, both geometry

16 and 18 had spectra that were smaller than geometry 11. This variation in neutron fluence can be seen in the dose equivalent estimates as well. The total dose equivalent for geometry 16 was lower at 0 and $\pi/4$ radians, while geometry 18 had a slightly lower dose equivalent at $\pi/2$, $3\pi/4$, and π radians. Switching the layer of nickel and polyethylene in geometry 18 changes the average energy of the neutrons emerging near the shield opening, which increases the dose equivalent. Away from the shield opening, however, the neutrons must pass through a layer of moderating material within the large nickel layer, allowing for the scattered neutrons to be slowed further. The lowered neutron energy equates to a larger interaction probability, which increases shielding effectiveness.

Another interesting observation from the simulations is that geometry 15, a homogenously mixed shielding which was comprised of polyethylene and steel atoms, is significantly less effective at shielding neutrons than the layered design. The spectra at $\pi/4$ and $3\pi/4$ radians is larger than geometry 11, which has the same atomic ratio and total density as geometry 15. Also, the dose equivalent at all locations simulated is significantly higher than geometry 11. At $3\pi/4$ radians, there is over an order of magnitude difference between the two shielding configurations. This, combined with geometries 8 and 9's simulations show the layered design is most effective.

The mass of the shielding geometries differs greatly. The pure polyethylene, geometry 1, is the lightest, while the combination of tungsten and polyethylene, geometry 10, is the heaviest. Depending on the application, the mass of the shield may be of importance. If the active neutron interrogation system is meant to be mobile, then steel and tungsten, although effective shields, may not be ideal. If transportation of the shield is important, then water, which is relatively light,

may be a better choice because it is available and can be accessed in most locations; therefore it does not need to be shipped.

The activation of the shielding materials may be of some concern. The estimated maximum activity of geometry 11 was 6.0 x 10^7 Bq, while geometry 16 was estimated to be 1.2 x 10^8 Bq. Geometry 10 had a higher maximum activity of 2.0 x 10^9 Bq, but a large fraction of that was due to isotopes with half-lives of 5.15 and 98.4 seconds. If left to set for 20 minutes or so after the source has been turned off, the activity of the tungsten shielding will drop by an order of magnitude. Furthermore, it should be realized that the activity within the shielding is distributed throughout the shielding material. There will be significant self-attenuation of photons within the steel, nickel, and tungsten, which will reduce potential dose. Also, geometric attenuation will minimize this even further. The eventual disposal of the shielding material could be a challenge because some of the newly formed nuclei have half-lives that are fairly long. Since only a few materials were simulated and only rough estimates were made using MCNP, this is a topic that will require further investigation in future work.

The effectiveness of the shielding is a combination of limiting neutrons at undesirable angles and insuring a compact beam of high energy neutrons is directed where desired. Figure 3.14 shows the average energy of neutrons leaving the shielding surface that contains the opening for geometry 11. At the surface of the shielding, the average energy peaks at 15 – 20 cm and there is a smaller peak at 65 – 70 cm from the centerline of the shield opening. This corresponds to the edge of the opening at 16 cm and the edge of the shielding at 66 cm. The increase is most likely due to the inner and outer layers of polyethylene absorbing thermal neutrons; therefore, the remaining neutrons have a higher average energy. The average energy at 25, 50, 100, and 150 cm only have 1 peak each, which becomes less distinct, but has a larger

magnitude, and shifts out the further the surface is from the shielding. This indicates a broadening of the neutron beam as it moves away from the shielding. Figure 3.15 takes the average energy of each ring and multiplies it by the normalized number of neutrons passing through each ring. These plots show the shielding efficiency and beam broadening. The beam intensity is much greater towards the centerline of the opening and drops off quickly. The beam does broaden as the isotropically released neutrons move further away from the shielding, but the beam still maintains most of its strength. Of course, the shielding design could be changed so that the opening was smaller or larger depending on the application and the desired beam width at a given distance.

It is difficult to choose one ideal shielding configuration because the requirements may change with each application. However, geometry 11 is a good compromise. The layered materials are effective at attenuating the neutrons, while maintaining a neutron "beam." The steel used is not nearly as expensive as tungsten, and furthermore, the mass of geometry 11 is less than the mass of the shielding based on a design by Maruyama and Bouts (1972), while maintaining a very similar neutron energy spectrum and a slightly lower dose equivalent around the source. Another option would be either geometry 16 or 18. The nickel is more effective than steel, and its mass and cost fall between that of steel and tungsten. Geometry 18 is slightly lighter than 16 and the dose equivalent is less at $\pi/2 - \pi$ radians, but it is greater a $0 - \pi/4$ radians. The choice of geometry would have to account for where the operator and other personnel would be located. Shielding could be further improved if borated polyethylene was substituted for the regular polyethylene, but that would add cost to the configuration.

Conclusions

The ability to shield isotropic neutron sources can be helpful in active neutron interrogation. The shielding around the source limits the number of neutrons interacting in the environment while still allowing for a narrow beam of unattenuated neutrons. This decreases the amount of unwanted secondary radiation interacting in the system's detectors and distorting its signal. It also reduces potential dose to nearby personnel and limits activation concerns. Because active neutron interrogation is often used in areas where space is limited, an effective, compact neutron shielding is necessary.

Layering of various materials, like in geometries 4 and 11, which had a 5 cm thick inner layer of polyethylene, followed by a thicker layer of steel, and then several alternating 5 cm thick layers of polyethylene and steel, improves neutron shielding and reduces dose equivalent. The mid to high atomic number material serves multiple purposes. Firstly, it can be used to shield any gamma rays created when neutrons are absorbed. Additionally, the material can reflect neutrons back through the moderating material and slightly reduce the neutron energy every collision.

There are many options for shielding neutrons. Each active neutron interrogation system is different and has different requirements. If space is limited, but the budget is higher, then perhaps layers of borated polyethylene and tungsten would be the preferred shielding method. However, if cost is the limiting factor, then maybe more common and less expensive materials like steel and polyethylene would be better choices. And if weight were an issue, then a pure polyethylene shield may be most effective. It is up to the designer to determine what is best for that particular scenario.

This work is not meant to offer solutions to all neutron source shielding applications. There are limitless combinations of materials and shielding configurations that could be tested. It

is up to the user to determine which shielding properties are most important to him or her. Hopefully, the shielding materials and evaluations methods discussed in this paper can act as a starting point when selecting high energy neutron shielding for portable or limited space applications.

Figures

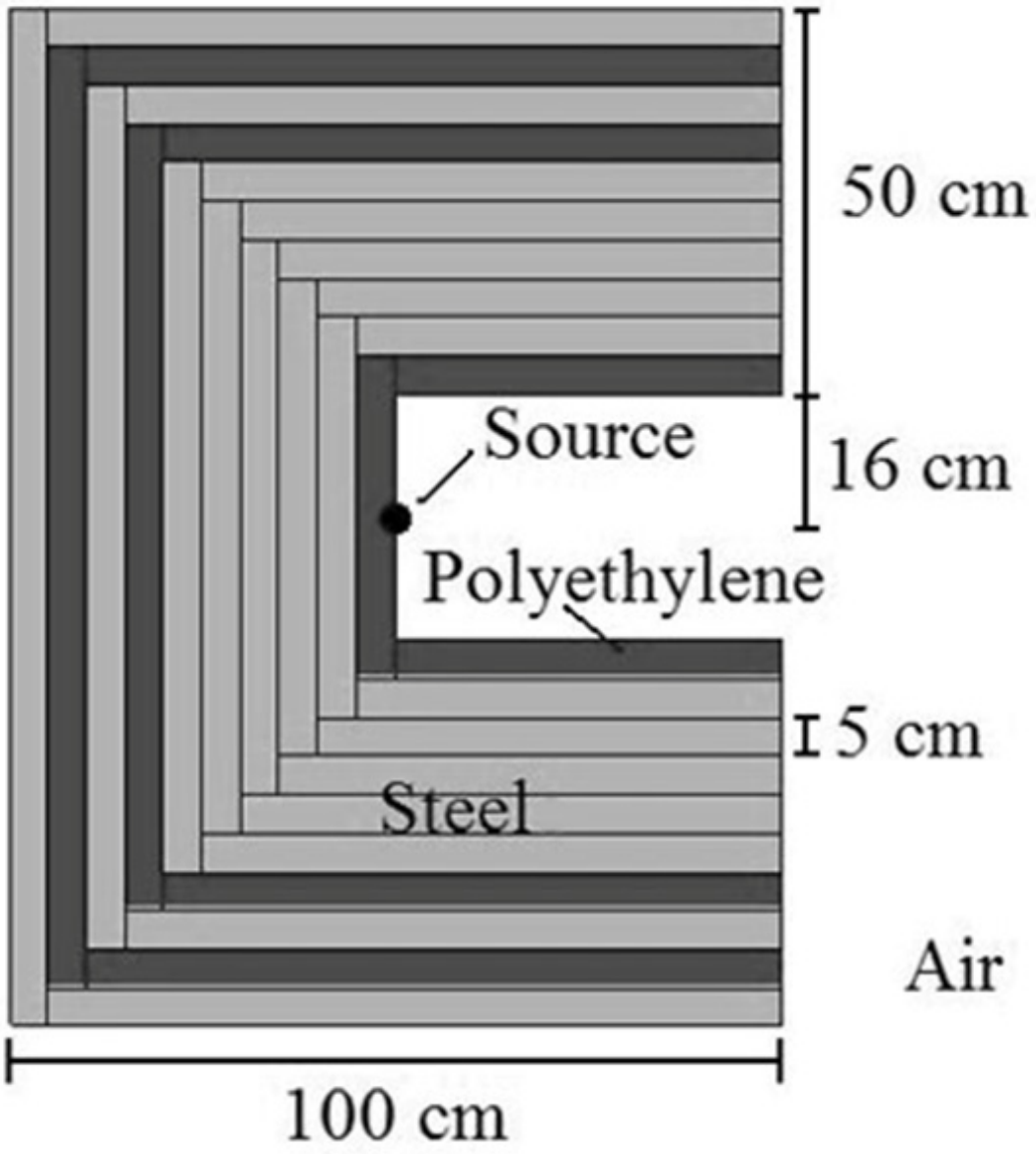

Fig. 3.1: An example of how the shielding is assembled in MCNP, in this case it is geometry 4. Pictured is a cross section through the center of the shielding. Neutrons emerge unattenuated through the opening on the right side of the shielding, creating a beam, while the neutron fluence in all other directions is significantly more limited due to all of the shielding material.

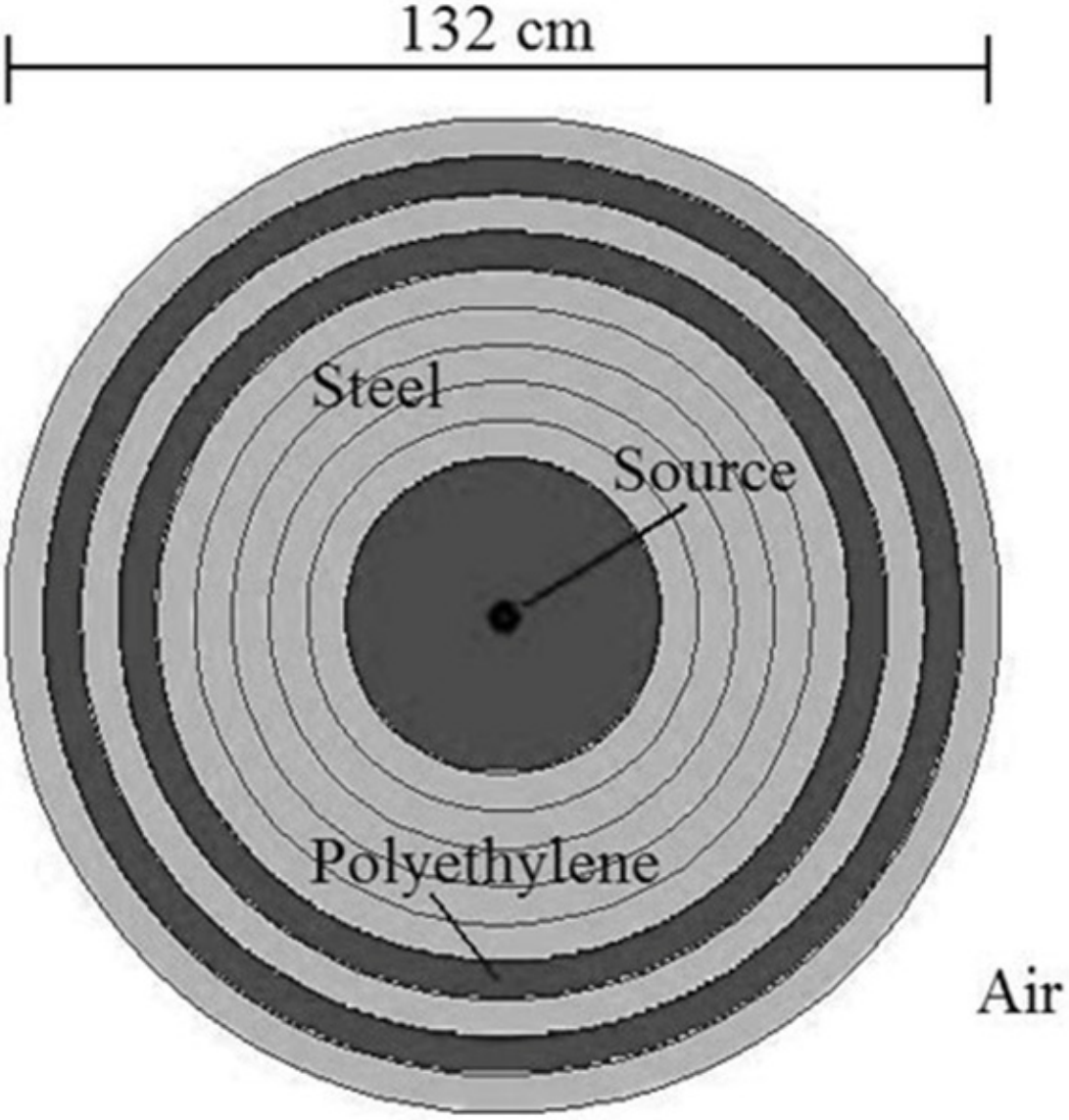

Fig. 3.2: A cross section across the center of the geometry 4 shielding through its width, looking down the barrel.

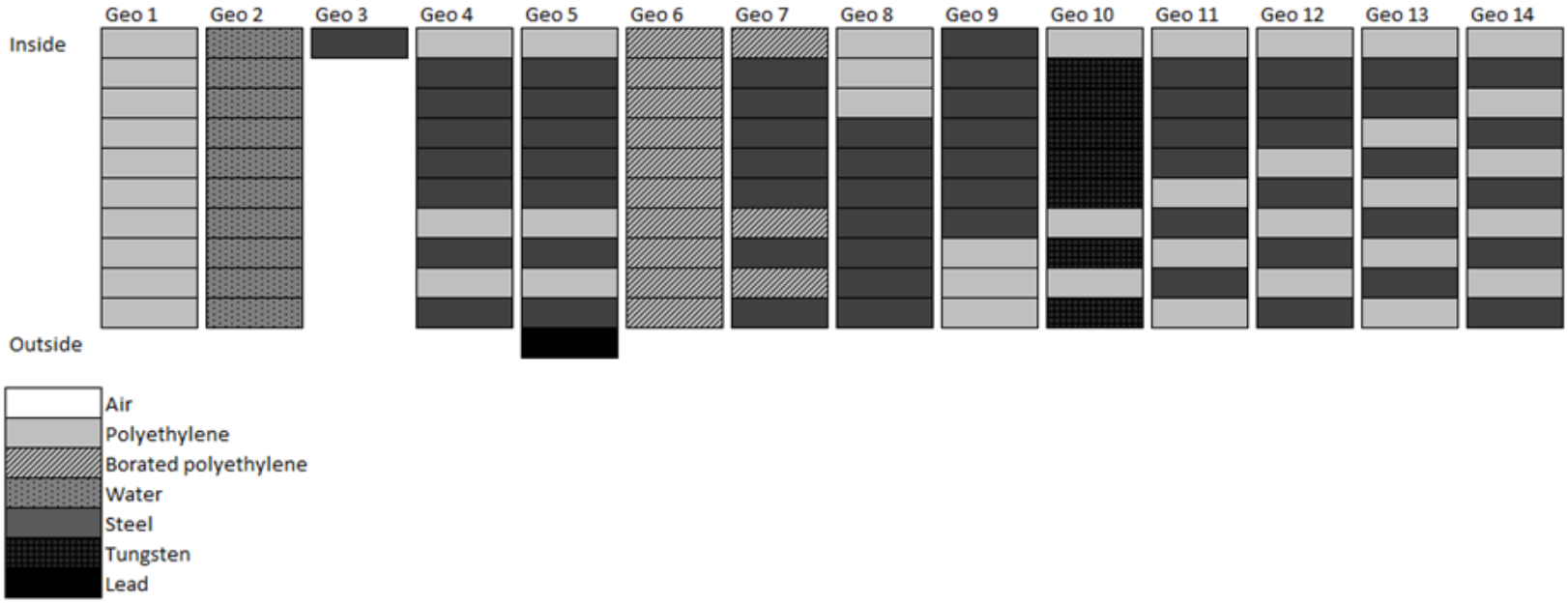

Fig. 3.3: A visual representation of geometries 1 – 14. Each 5 cm thick layer of material is represented by one block with the center of the configuration at the top and the outside at the bottom.

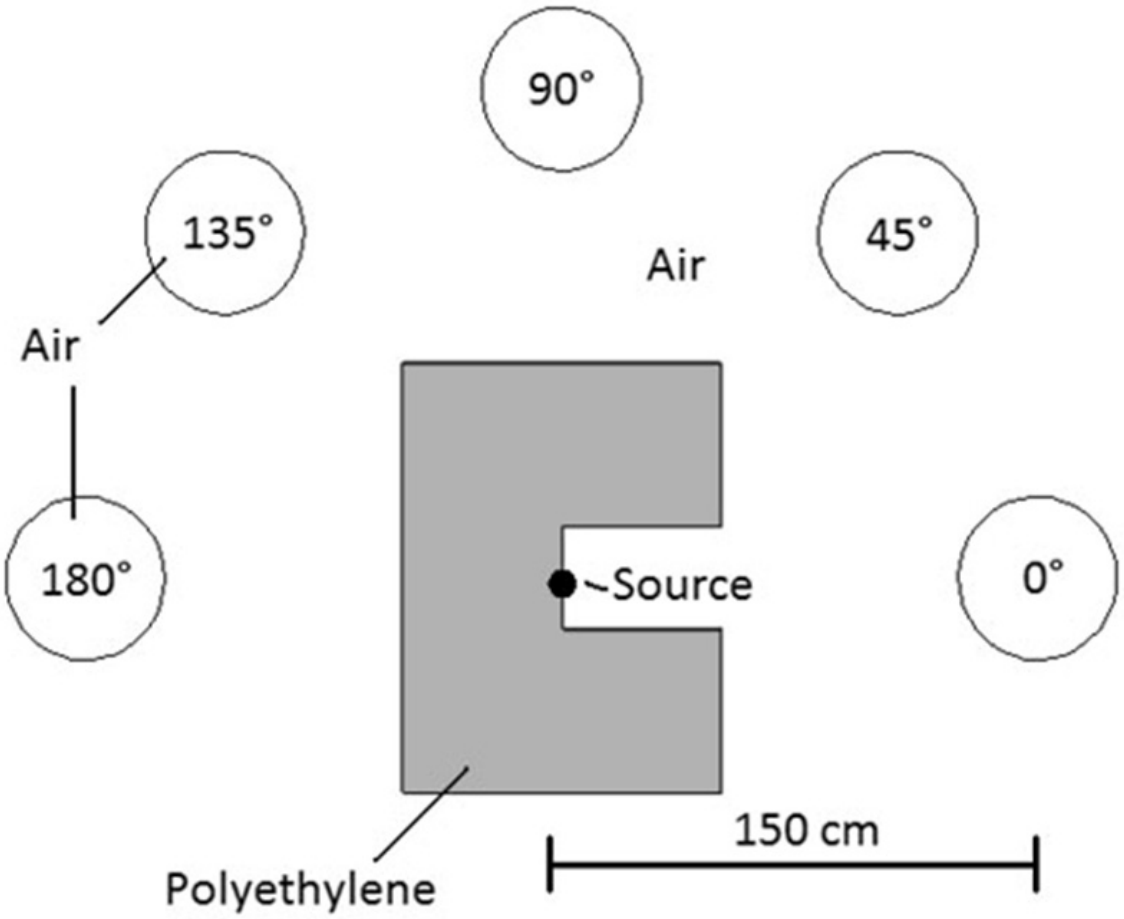

Fig. 3.4: The arrangement used in the MCNP simulations to estimate dose and relative neutron fluence at several points around the shielding. Geometry 1 is pictured. An F1 tally is used to determine the energy of neutrons that cross the surface of the spheres surrounding the shielding in order to estimate the energy dependent fluence of neutrons and photons at various points around the material.

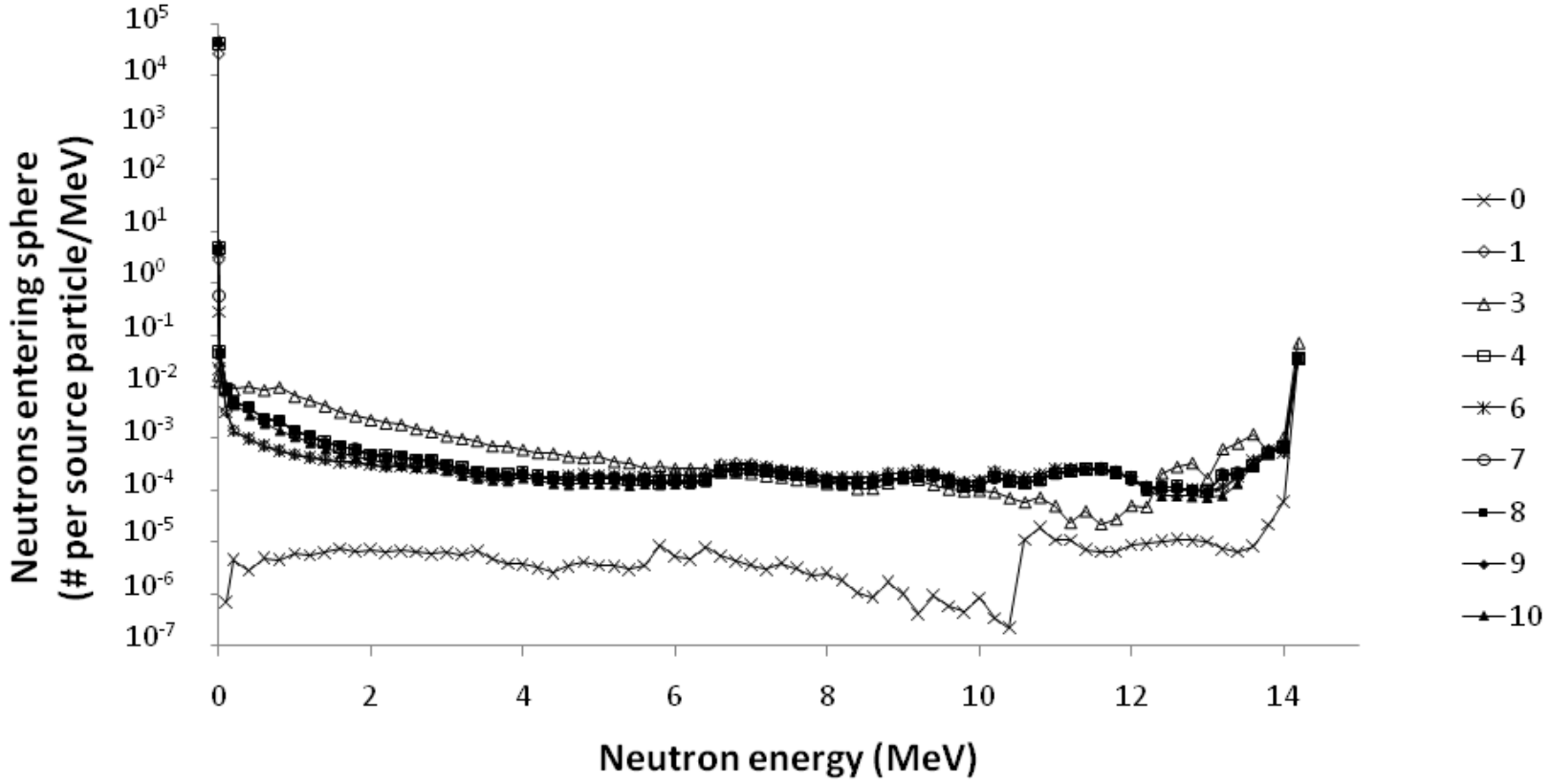

Fig. 3.5: A comparison of the normalized relative neutron fluence through the sphere located at 0 radians versus energy for geometries 0 - 10. There is a large peak of neutrons around 14 MeV, the original energy of the source.

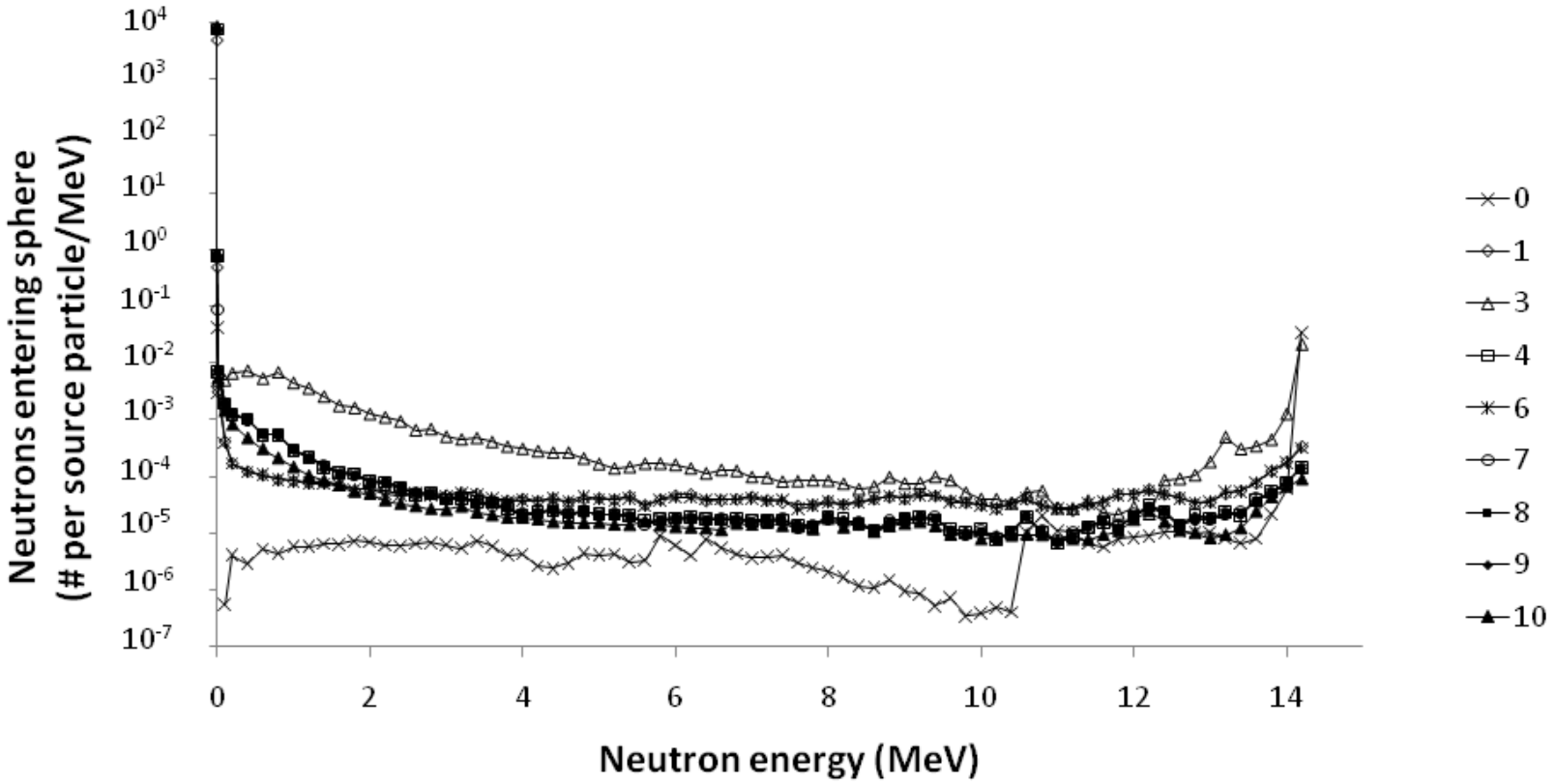

Fig. 3.6: A comparison of the normalized relative neutron fluence through the sphere located at π/4 radians versus energy for geometries 0 - 10. The peak of neutrons near 14 MeV has been reduced by about two orders of magnitude for many of the shielding arrangements tested.

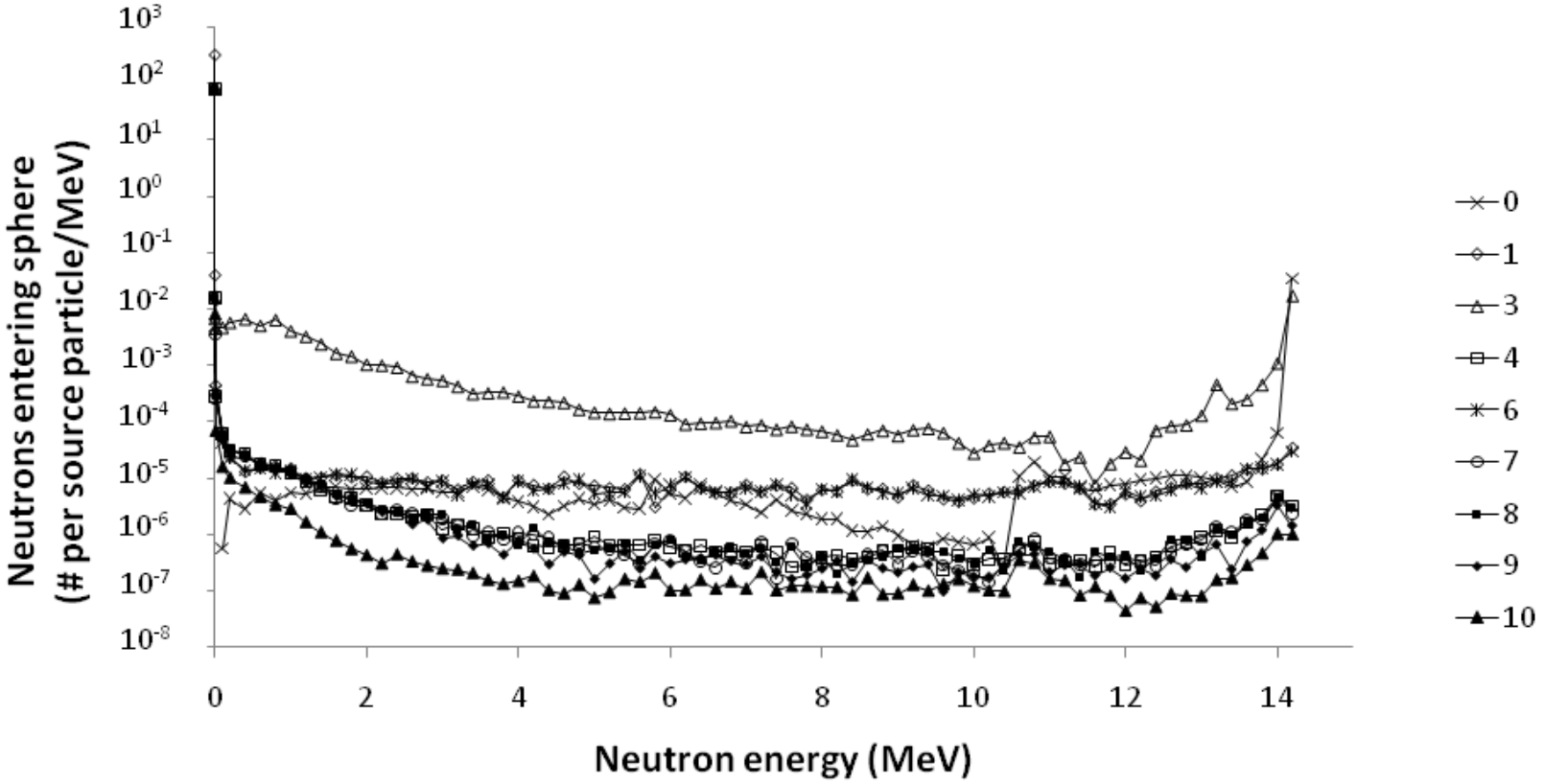

Fig. 3.7: A comparison of the normalized relative neutron fluence through the sphere located at π/4 radians versus energy for geometries 0 - 10. The peak of neutrons near 14 MeV has been further reduced to about three – four orders of magnitude less for many of the shielding arrangements tested.

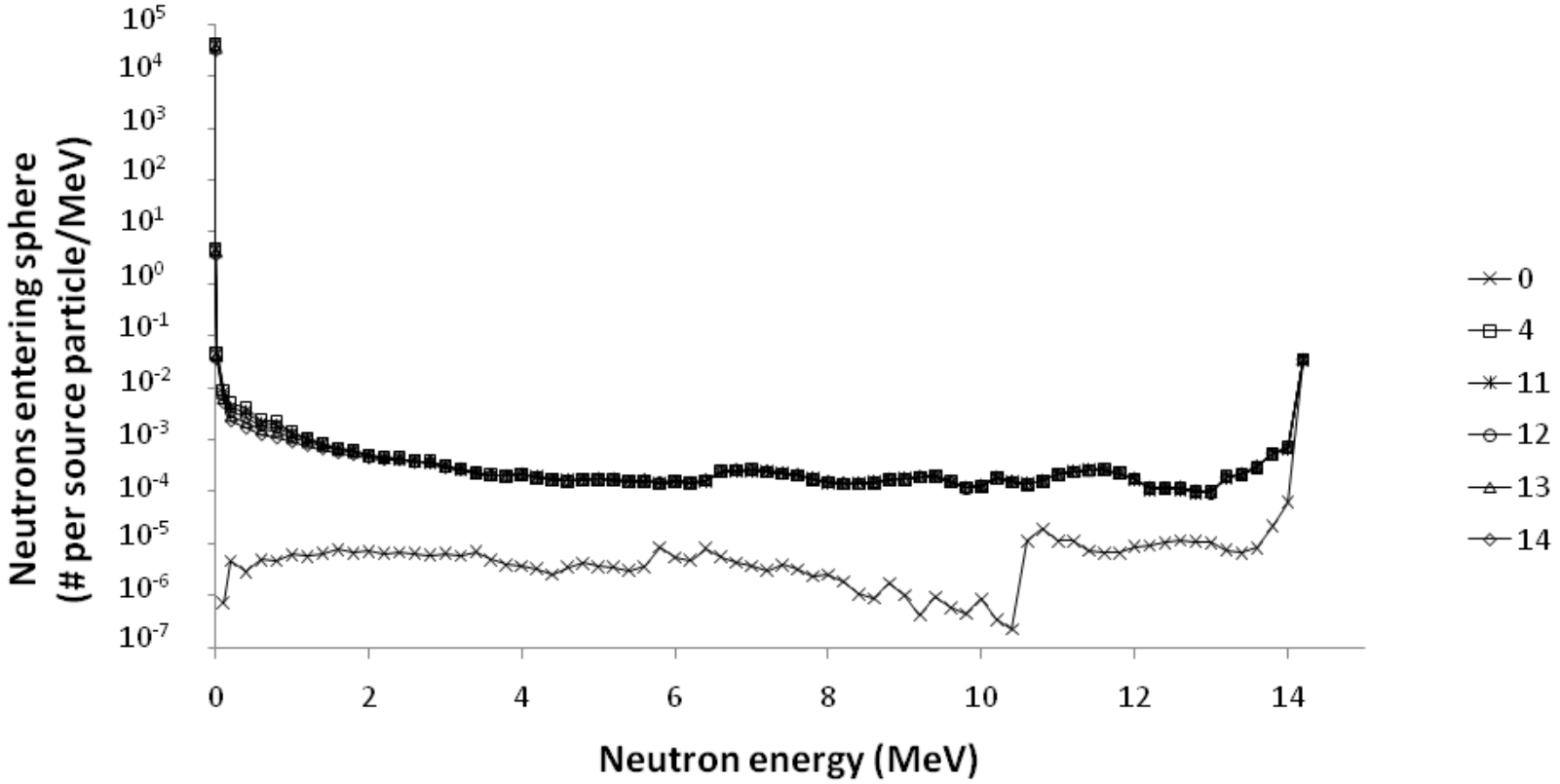

Fig. 3.8: A comparison of the normalized relative neutron fluence through the sphere located at 0 radians versus energy for geometries 0, 4, and 11 – 14. Again, there is a large peak of neutrons around 14 MeV, the original energy of the source.

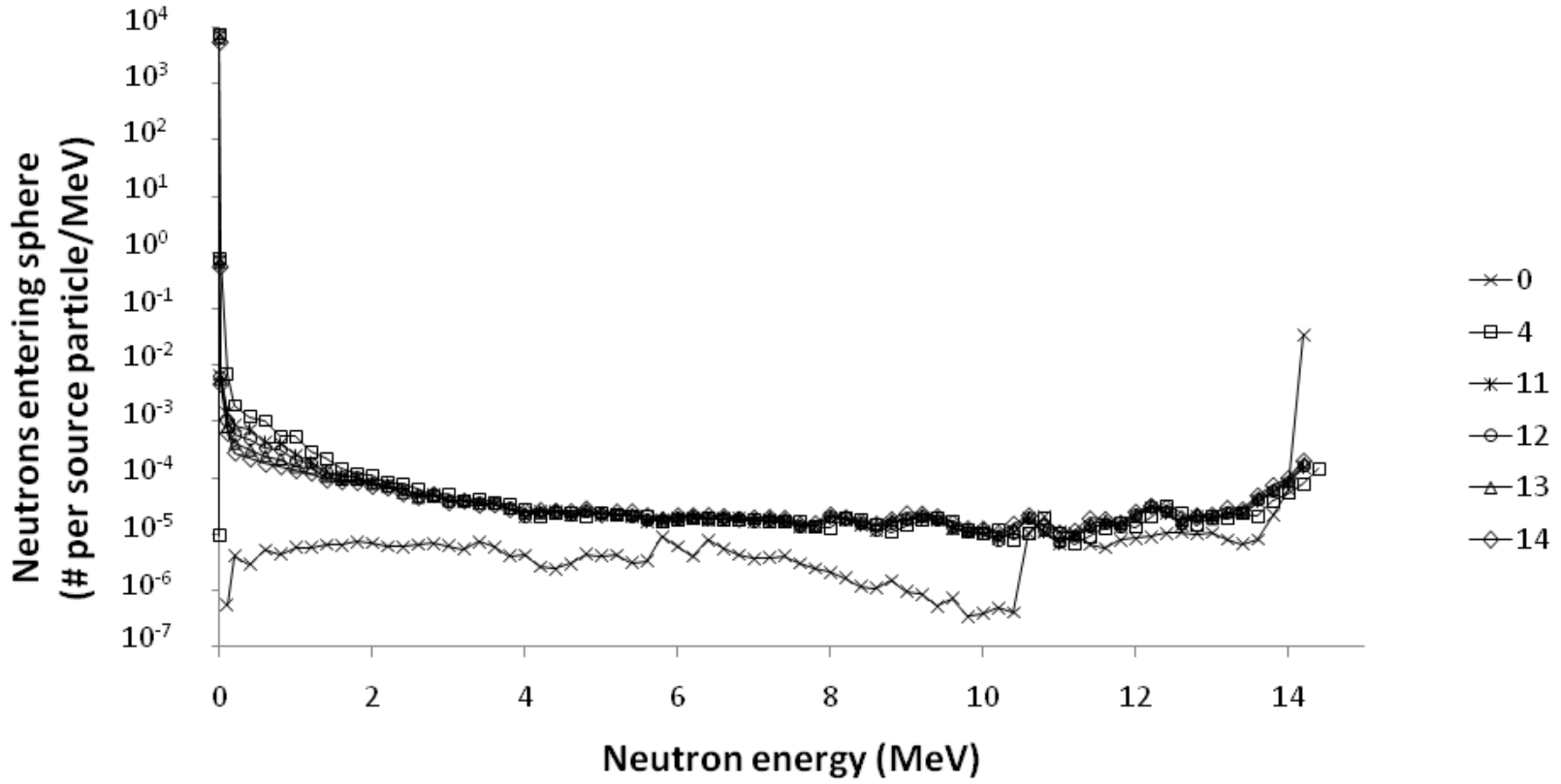

Fig. 3.9: A comparison of the normalized relative neutron fluence through the sphere located at π/4 radians versus energy for geometries 0, 4, and 11 – 14. The peak of neutrons near 14 MeV has been reduced by about two orders of magnitude for all of the shielding arrangements tested, when compared to geometry 0, air.

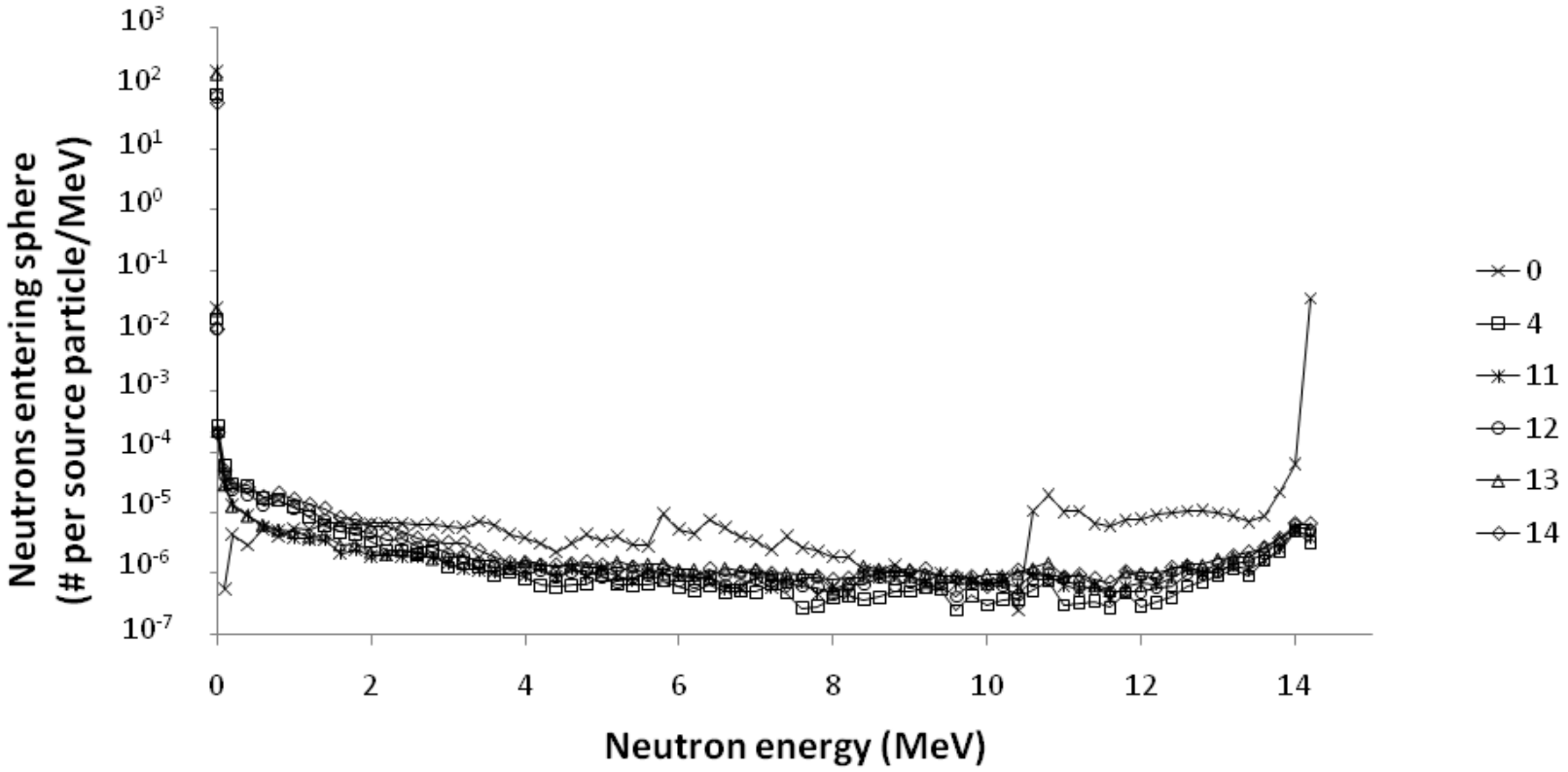

Fig. 3.10: A comparison of the normalized relative neutron fluence through the sphere located at 3π/4 radians versus energy for geometries 0, 4, and 11 – 14. Again, the peak of neutrons near 14 MeV has been reduced by about three – four orders of magnitude for all of the shielding arrangements tested. The spectra of geometries 11 – 14 are very similar to geometry 4, while the shielding materials are less massive.

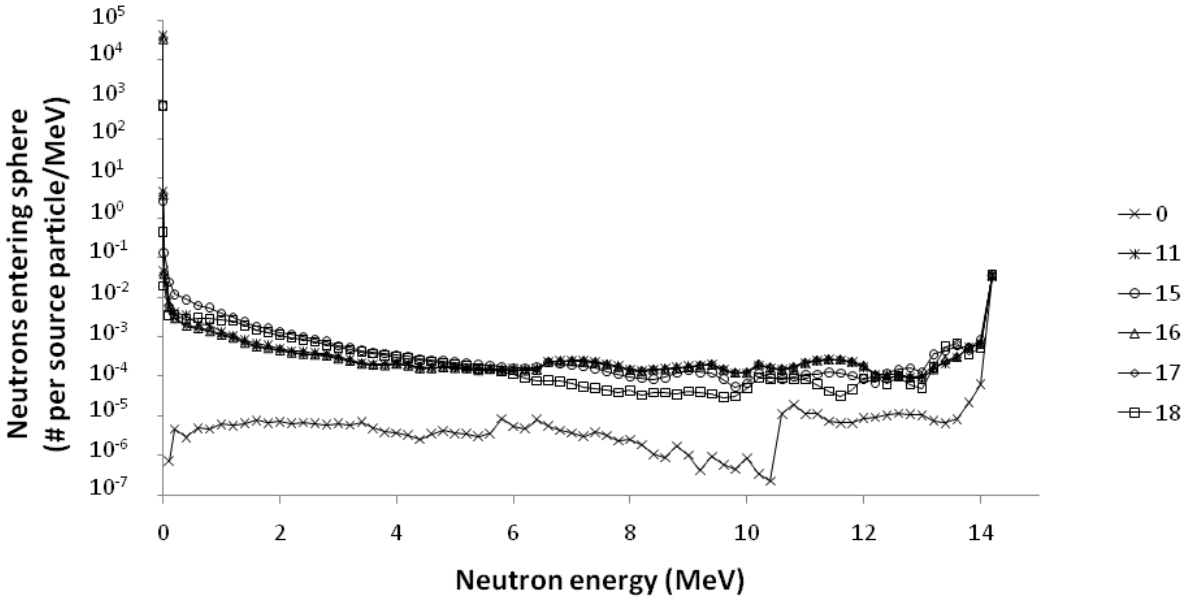

a)

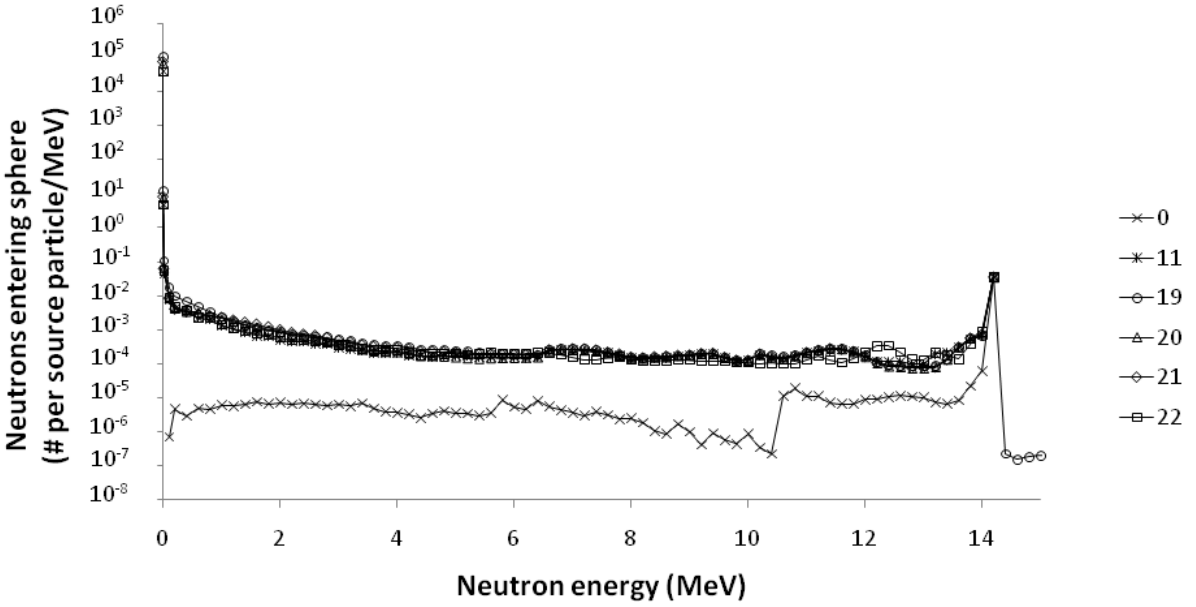

b)

Fig. 3.11: A comparison of the normalized relative neutron fluence through the sphere located at 0 radians versus energy for geometries a) 0, 11, and 15 – 18 and b) 0, 11, and 19 – 22. The peak near 14 MeV is present for all geometries.

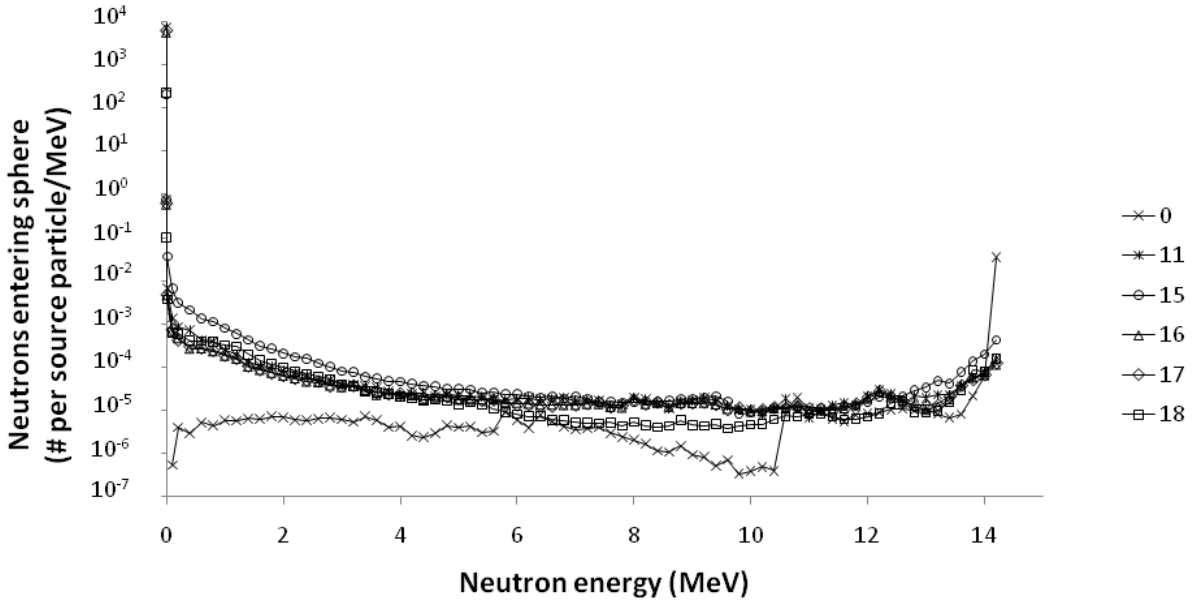

a)

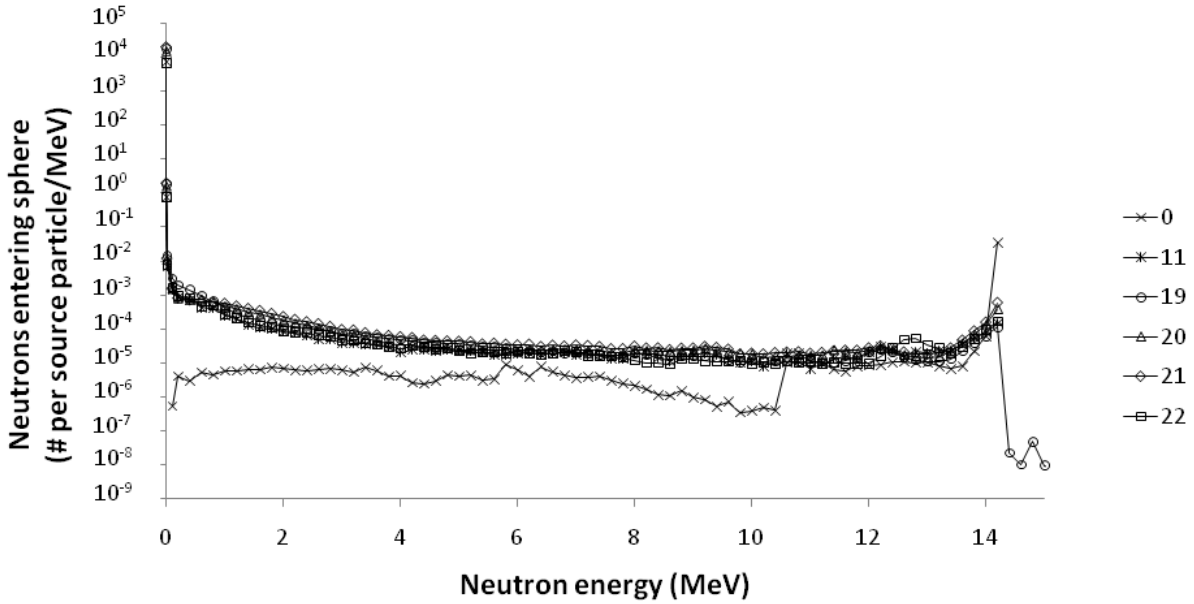

b)

Fig. 3.12: A comparison of the normalized relative neutron fluence through the sphere located at π/4 radians versus energy for geometries a) 0, 11, and 15 – 18 and b) 0, 11, and 19 – 22. The magnitude of the peak near 14 MeV has once again been reduced outside the solid angle of the shielding opening.

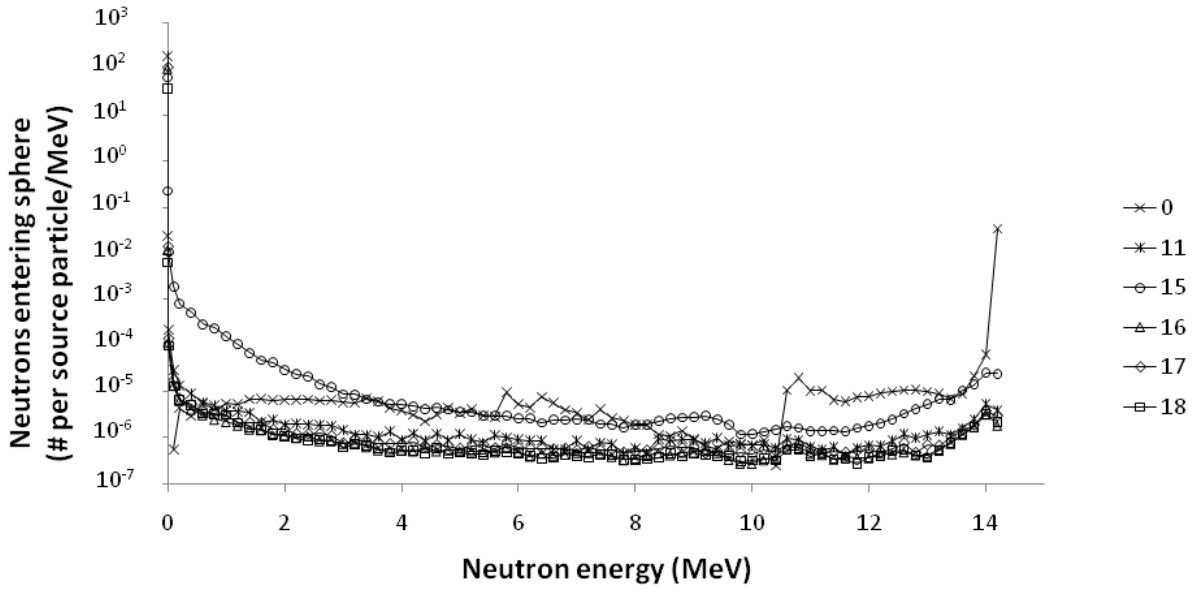

a)

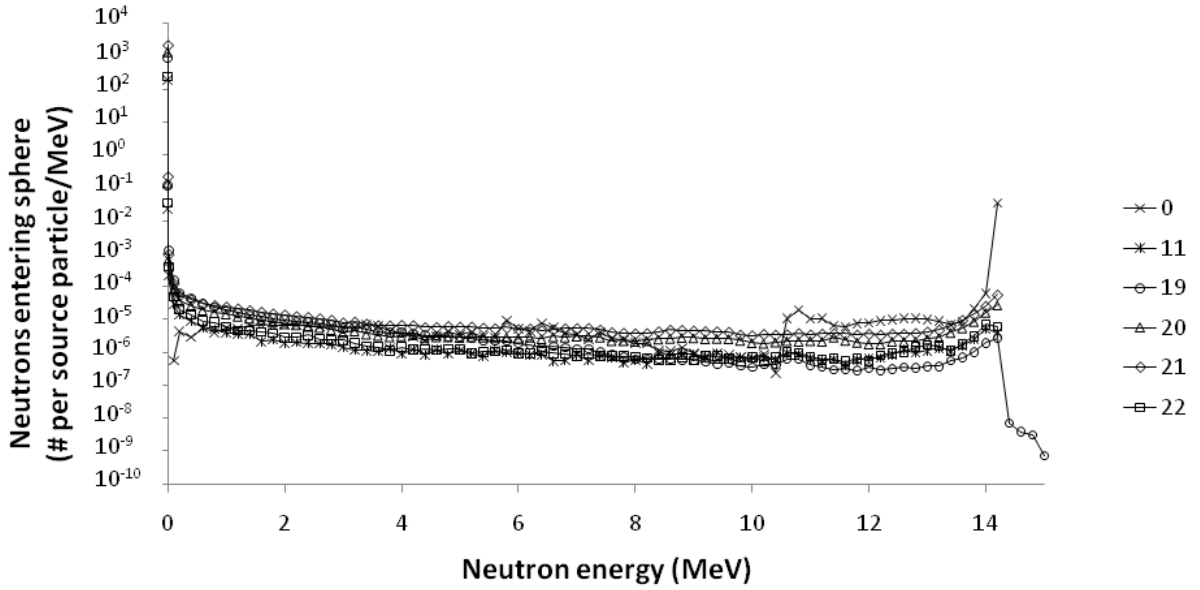

b)

Fig. 3.13: A comparison of the normalized relative neutron fluence through the sphere located at 3π/4 radians versus energy for geometries a) 0, 11, and 15 – 18 and b) 0, 11, and 19 – 22. The peak near 14 MeV, for all geometries, has been reduced by several orders of magnitude when compared to the unshielded source, geometry 0.

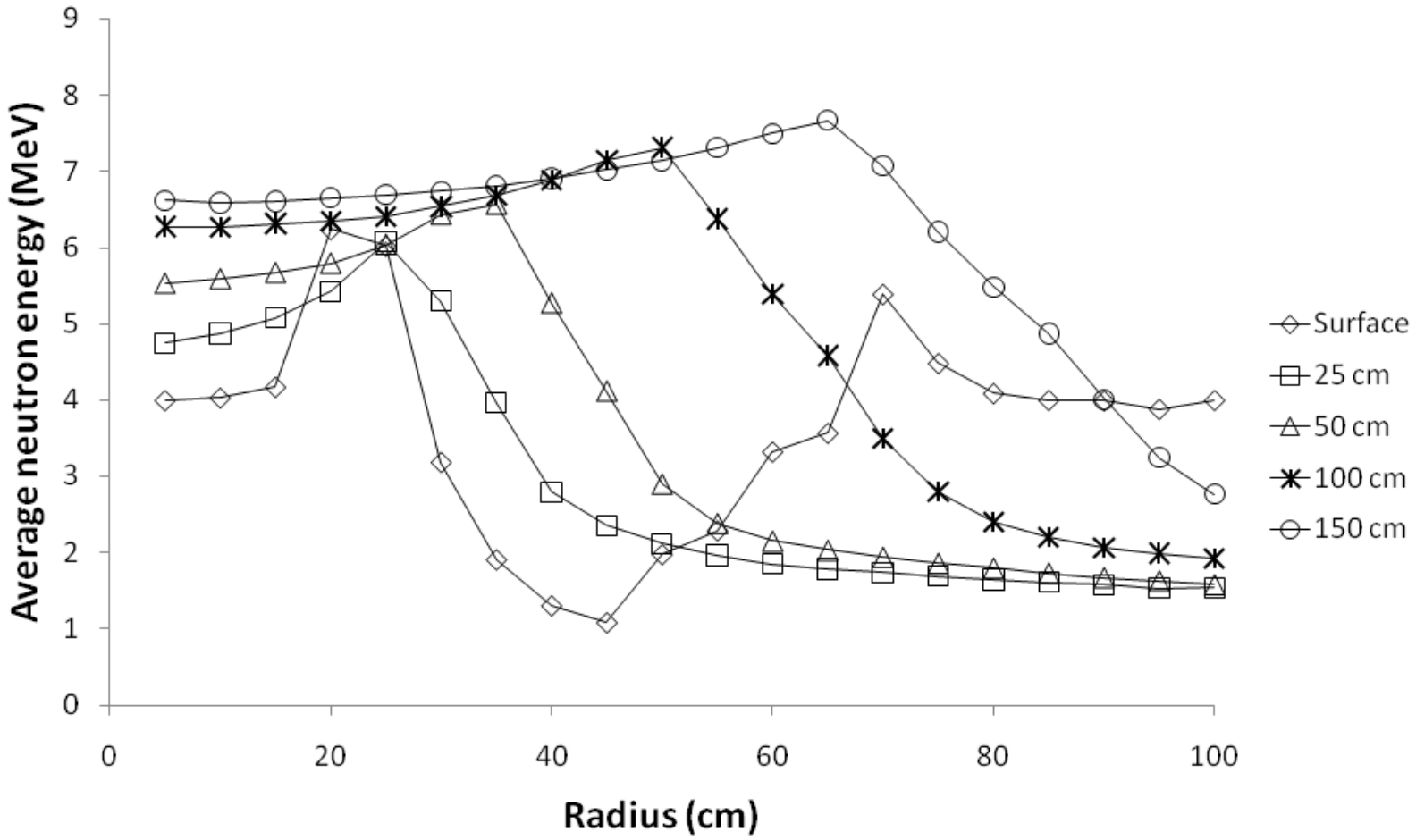

Fig. 3.14: The average energy of neutrons at various distances from the centerline of the shield opening for geometry 11. The neutron energies were recorded at 0, 25, 50, 100, and 150 cm from the shielding surface that contained the opening.

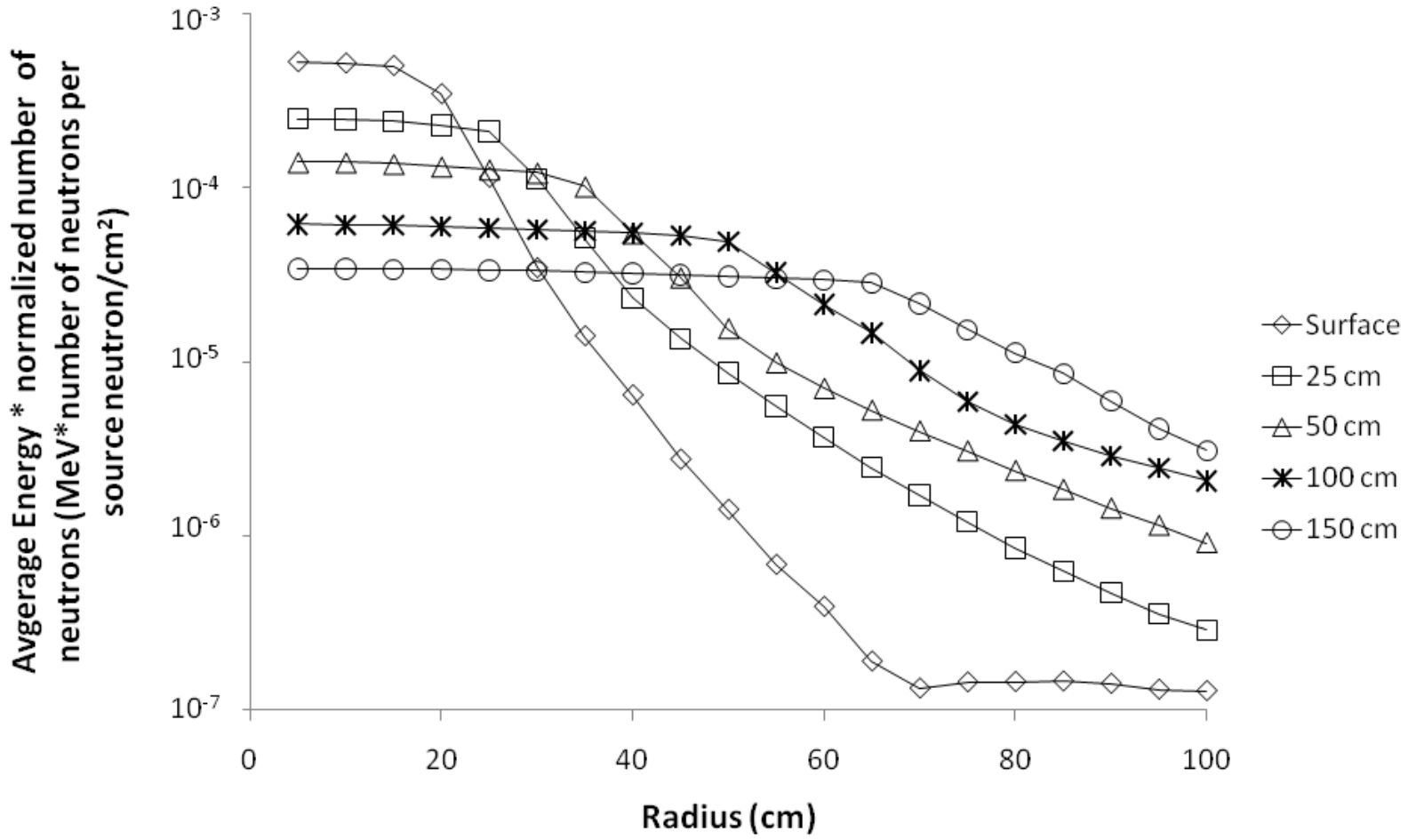

Fig. 3.15: An estimation of how the relative neutron beam intensity varies based on distance from the shielding surface for geometry 11. The beam intensity was determined by multiplying the average energy of neutrons crossing a plane at varying distances from the beam centerline by the relative number of neutrons crossing the plane at that radial distance.

Tables

Table 3.1: A description of the materials simulated.

Material	Elemental makeup (relative abundance)	Elemental makeup (weight %)	Density (kg m^{-3})
Air		C (0.001), N (0.755), O (0.231), Ar (0.013)	1.2
Polyethylene	H (4), C (2)		940
Borated polyethylene	H (4), B (0.18), C (1.82)		940
Water	H (2), O (1)		1,000
Steel/polyethylene mixture		H (1.36), C(8.34), Fe (90.30)	4,630
Steel		C (0.2), Fe (99.8)	7,860
Inconel 600		Ni (72.0), Cr (16.835), Fe (9.0), Mn (1.0), Cu (0.5), Si (0.5), C (0.15), S (0.00015)	8,430
Nickel	Ni (1)		8,910
Lead	Pb (1)		11,340
Bismuth	Bi (1)		9,780
Tungsten	W(1)		19,250
Depleted uranium	^{234}U (0.000018), ^{235}U (0.0024), ^{238}U (0.997582)		19,100

Table 3.2: A listing of all the material configurations simulated.

Geometry	Description
0	Air (no shielding)
1	50 cm thick polyethylene shielding surrounding the source
2	50 cm thick water shielding surrounding the source
3	5.98 cm thick shielding of 1018 steel surrounding the source
4	Alternating layers of steel and polyethylene starting from the inside with: 5 cm polyethylene, 25 cm steel, 5 cm polyethylene, 5 cm steel, 5 cm polyethylene, 5 cm steel
5	Same as geometry 4, but with an added layer of 5 cm of lead on the outside
6	Geometry 1 enriched with 3% ^{10}B by weight
7	Geometry 4 enriched with 3% ^{10}B by weight
8	15 cm thick of polyethylene on the inside of the shielding with 35 cm thick of steel outside of that
9	35 cm thick of steel on the inside of the shielding with 15 cm thick of polyethylene outside of that
10	Alternating layers of tungsten and polyethylene starting from the inside with: 5 cm polyethylene, 25 cm tungsten, 5 cm polyethylene, 5 cm tungsten, 5 cm polyethylene, 5 cm tungsten
11	Alternating layers of steel and polyethylene starting from the inside with: 5 cm polyethylene, 20 cm steel, 5 cm polyethylene, 5 cm steel, 5 cm polyethylene, 5 cm steel, 5 cm polyethylene
12	Alternating layers of steel and polyethylene starting from the inside with: 5 cm polyethylene, 15 cm steel, 5 cm polyethylene, 5 cm steel, 5 cm polyethylene, 5 cm steel, 5 cm polyethylene, 5 cm steel
13	Alternating layers of steel and polyethylene starting from the inside with: 5 cm polyethylene, 10 cm steel, 5 cm polyethylene, 5 cm steel, 5 cm polyethylene, 5 cm steel, 5 cm polyethylene, 5 cm steel, 5 cm polyethylene
14	Alternating layers of steel and polyethylene with every 5 cm for a total thickness of 50 cm
15	A mixture of polyethylene and iron with the same proportions as are present in Geometry 11
16	Same as geometry 11, but with nickel replacing the steel
17	Same as geometry 11, but with the nickel alloy Inconel 600 replacing the steel
18	Same as geometry 16, but with the inner 5 cm layers of nickel and polyethylene switched
19	Same as geometry 11, but with depleted uranium replacing the steel
20	Same as geometry 11, but with lead replacing the steel
21	Same as geometry 11, but with bismuth replacing the steel
22	Same as geometry 11, but with water replacing the polyethylene

Table 3.3: A summary of the neutron and photon dose estimates at various points surrounding the shielding for various shielding geometries. The values are in units of 10^{-17} Sv per source neutron.

		Geometry										
		0	1	2	3	4	5	6	7	8	9	10
0 radians	Neutron Dose	3.71	5.33	5.27	2.94	5.92	5.92	5.27	5.84	5.53	9.69	5.62
	Photon Dose	0.000425	0.0242	0.0301	0.0379	0.0340	0.0340	0.0120	0.0214	0.0273	0.0357	0.0278
	Total Dose	3.71	5.35	5.30	2.98	5.96	5.96	5.28	5.86	5.56	9.73	5.65
π/4 radians	Neutron Dose	3.71	0.336	0.411	1.09	0.338	0.338	0.316	0.324	0.403	1.13	0.203
	Photon Dose	0.000444	0.0121	0.0153	0.0147	0.00504	0.00489	0.00513	0.00252	0.00531	0.00883	0.00275
	Total Dose	3.72	0.349	0.426	1.11	0.343	0.343	0.321	0.327	0.409	1.14	0.206
π/2 radians	Neutron Dose	3.72	0.111	0.164	0.941	0.0254	0.02048	0.103	0.0245	0.265	0.0233	0.00646
	Photon Dose	0.000429	0.00977	0.0125	0.0133	0.00140	0.000149	0.00382	0.000190	0.000192	0.0121	0.0000285
	Total Dose	3.72	0.121	0.176	0.954	0.0268	0.0206	0.107	0.0247	0.265	0.0353	0.00649
3π/4 radians	Neutron Dose	3.71	0.0517	0.0841	1.24	0.0117	0.00925	0.0469	0.0109	0.201	0.00869	0.00250
	Photon Dose	0.000423	0.00725	0.00954	0.0189	0.000727	0.0000343	0.00280	0.0000857	0.000114	0.0113	0.0000102
	Total Dose	3.71	0.0589	0.0936	1.26	0.0124	0.00929	0.0497	0.0109	0.201	0.0200	0.00251
π radians	Neutron Dose	3.72	0.178	0.261	1.54	0.0355	0.0265	0.164	0.0338	0.388	0.0268	0.00710
	Photon Dose	0.000437	0.0119	0.0150	0.0223	0.00224	0.000260	0.00464	0.000279	0.000265	0.0128	0.0000232
	Total Dose	3.72	0.190	0.276	1.57	0.0377	0.0267	0.168	0.0341	0.388	0.0396	0.00712

Table 3.4: A summary of the neutron and photon dose estimates at various points surrounding geometries 4 and 11 - 14. The values are in units of 10^{-17} Sv per source neutron.

		Geometry				
		4	11	12	13	14
0 radians	Neutron Dose	5.92	5.84	5.74	5.64	5.52
	Photon Dose	0.0340	0.0338	0.0335	0.0334	0.0338
	Total Dose	5.96	5.87	5.78	5.67	5.56
π/4 radians	Neutron Dose	0.338	0.302	0.272	0.249	0.244
	Photon Dose	0.00504	0.00510	0.00496	0.00515	0.00553
	Total Dose	0.343	0.307	0.277	0.254	0.250
π/2 radians	Neutron Dose	0.0254	0.0235	0.0285	0.0303	0.0376
	Photon Dose	0.00140	0.00161	0.000829	0.00121	0.000824
	Total Dose	0.0268	0.0251	0.0294	0.0316	0.0384
3π/4 radians	Neutron Dose	0.0117	0.00841	0.0130	0.0109	0.0175
	Photon Dose	0.000727	0.000919	0.000366	0.000658	0.000369
	Total Dose	0.0124	0.00933	0.0134	0.0116	0.0179
π radians	Neutron Dose	0.0355	0.0343	0.0390	0.0448	0.0531
	Photon Dose	0.00224	0.00252	0.00130	0.00188	0.00127
	Total Dose	0.0377	0.0368	0.0403	0.0467	0.0544

Table 3.5: A summary of the neutron and photon dose estimates at various points surrounding the shielding for geometries 11 and 15 - 22. The values are in units of 10^{-17} Sv per source neutron.

		Geometry								
		11	15	16	17	18	19	20	21	22
0 radians	Neutron Dose	5.84	7.60	5.57	5.62	6.26	6.93	6.42	6.58	5.88
	Photon Dose	0.0338	0.0383	0.0302	0.0325	0.0343	0.0358	0.0194	0.0181	0.0368
	Total Dose	5.87	7.64	5.60	5.65	6.29	6.97	6.44	6.60	5.92
π/4 radians	Neutron Dose	0.302	0.733	0.216	0.231	0.259	0.477	0.497	0.601	0.331
	Photon Dose	0.00510	0.00613	0.00381	0.00428	0.00309	0.00432	0.00282	0.00301	0.00547
	Total Dose	0.307	0.739	0.220	0.235	0.262	0.482	0.500	0.604	0.336
π/2 radians	Neutron Dose	0.0235	0.223	0.0139	0.0170	0.0133	0.0541	0.0713	0.118	0.0302
	Photon Dose	0.00161	0.00257	0.000596	0.000816	0.000438	0.000743	0.00103	0.00143	0.00189
	Total Dose	0.0251	0.226	0.0145	0.0178	0.0137	0.0548	0.072	0.119	0.0321
3π/4 radians	Neutron Dose	0.00841	0.131	0.00499	0.00615	0.00465	0.0238	0.0307	0.0547	0.0108
	Photon Dose	0.000919	0.00159	0.000312	0.000441	0.000225	0.000631	0.000969	0.00139	0.00112
	Total Dose	0.00933	0.132	0.00530	0.00659	0.00487	0.0244	0.0316	0.0561	0.0119
π radians	Neutron Dose	0.0343	0.336	0.0197	0.0251	0.0187	0.0852	0.111	0.184	0.0438
	Photon Dose	0.00252	0.00375	0.000977	0.00134	0.000682	0.000988	0.00140	0.00182	0.00292
	Total Dose	0.0368	0.340	0.0206	0.0264	0.0193	0.0862	0.112	0.186	0.0467

Table 3.6: An estimate of the mass of each of the shielding geometries. No support structure or construction materials were accounted for when calculating the mass, only the materials listed in Table 3.1.

Geometry	Mass (kg)
0	0
1	1,250
2	1,330
3	352
4	7,520
5	10,850
6	1,250
7	7,520
8	9,360
9	5,780
10	17,800
11	6,140
12	6,750
13	5,520
14	6,270
15	6,140
16	6,880
17	6,540
18	6,760
19	14,100
20	8,600
21	7,500
22	6,180

References

Aleksandrov, V.D., Bogolubov, E.P., Bochkarev, O.V., Korytko, L.A., Nazarov, V.I., Polkanov, Y.G., Ryzhkov, V.I., Khasaev, T.O., 2005. Application of neutron generators for high explosives, toxic agents, and fissile material detection. *Appl. Radiat. and Isotopes*, 63 (5-6), 537-543.

Brahme, A., 31 July 1984. Neutron collimator. U.S. Patent No. 4,463,266.

Buffler, A., 2004. Contraband detection with fast neutrons. *Radiat. Phys. Chem.*, 71(3-4), 853-861.

Carasco, C., Perot, B., Bernard, S., Mariani, A., Szabo, J-L, Sannie, G., Roll, Th., Valkovic, V., Sudac, D., Viesti, G., Lunardon, M., Bottosso, C., Fabris, D., Nebbia, G., Pesente, S., Moretto, S., Zenoni, A., Donzella, A., Moszynski, M., Gierlik, M., Batsch, T., Wolski, D., Klamra, W., Le Tourneur, P., Lhuissier, M., Colonna, A., Tintori, C., Peerani, P., Sequeira, V., Salvatoj, M., 2008. In-field test of EURITRACK tagged neutron inspection system. *Nuc. Instrum. and Methods in Physics Research A*, 588 (89), 397-405.

Cinausero, M., Lunardon, M., Nebbia, G., Pesente, S., Viesti, G., Filippini, V., 2004. Development of a thermal neutron sensor for humanitarian demining. *Appl. Radiat. and Isotopes*, 61 (1), 59-66.

Clifford, E., Ing, H., McFee, J., Cousins, T., 1999. High rate counting electronics for a thermal neutron analysis land mine detector. *Penetrating Radiation Systems and Applications*, 3769, 155-166.

Fermi, E., Zinn, W.H., 24 Sept. 1957. Neutronic reactor shield. U.S. Patent No. 2,807,727.

Greene, D., Thomas, R.L., 1969. The attenuation of 14 MeV neutrons in steel and polyethylene. *Phys. Med. Biol.*, 14 (1), 45-54.

Hall, J.M., Asztalos, S., Biltoft, P., Church, J., Descalle, M-A, Luu, T., Manatt, D., Mauger, G., Norman, E., Petersen, D., Pruet, J., Prussin, S., Slaughter, D., 2007. The nuclear car wash: neutron interrogation of cargo containers to detect hidden SNM. *Nuc. Instrum. and Methods in Physics Research B*, 261 (1-2), 337-340.

Hussein, E.M.A., 2003. Handbook on Radiation Probing, Gauging, Imaging and Analysis, Volume II: Applications and Design, (Kulwer Academic Publishers, Norrwell, MA), pp. 689-692.

International Commission on Radiation Protection (ICRP), 1987. Data for use in protection against external radiation. Oxford: ICRP Publication 51.

International Commission on Radiation Units and Measurements (ICRU), 1992. Measurement of dose equivalents from external photon and electron radiations. Bethesda, MD: ICRU Report 47.

Kearfott, K.J., 29 July 2008. Neutron irradiative methods and systems. U. S. Patent No. 7,405,409.

Knoll, G.F., 2010. Radiation Detection and Measurement, 4th ed. (Wiley, Hoboken, NJ), pp. 19-22.

Lehnert, A.L., Kearfott, K.J., 2010. The detection of explosive materials: review of considerations and methods. *Nucl. Technol.*, 172 (3), 325-334.

Lehnert, A.L., Kearfott, K.J., 2011. Simplified simulation of fastneutron scattering for an explosives detection application. *Nucl. Sci. Eng.*,168 (3), 278-286.

Lundberg, D.A., 25 Dec. 1973. Neutron beam collimators. U. S. Patent No. 3,781,564.

Maruyama, T., Bouts, C.J., 1972. Attenuation of 15 MeV neutrons in multilayer shields composed of steel, polyethylene and borated materials. *Phys. Med. Biol.*, 17 (3), 420-424.

Mollon, L., 17 Feb. 1987. Neutron absorbing panel. U. S. Patent No. 4,644,171.

Morrison, P., 18 June 1957. Radiation shield. U.S. Patent No. 2,796,529.

Pesente, S., Nebbia, G., Lunardon, M., Viesti, G., Sudac, D., Nađ, K., Blagus, S., Valković, V., 2004. Detection of hidden explosives by using tagged neutron beams with sub-nanosecond time resolution. *Nuc. Instrum. and Methods in Physics Research A*, 531 (3), 657-667.

Shultis, J.K., Faw, R.E., 1996. Radiation Shielding. (Prentice-Hall, Inc., Upper Saddle River, NJ), pp. 282-290.

Studenski, M.T., Kearfott, K.J., 2007. Design and simulation of a neutron facility. *Health Phys*., 92 (2 Suppl), S37-44.

Wu, L., Miley, G.H., Momota, H., Shrestha, P.J., 2007. An integrated broad area coverage fusion neutron/x-ray interrogation unit. *Fusion Sci .and Technology*, 52 (4), 1096-1100.

CHAPTER 4: LAYERED SHIELDING DESIGN FOR AN ACTIVE NEUTRON INTERROGATION SYSTEM

Abstract

The use of source and detector shields in active neutron interrogation can improve detector signal. In simulations, a shielded detector with a source rotated $\pi/3$ radians relative to the opening decreased neutron flux roughly three orders of magnitude. Several realistic source and detector shield configurations were simulated. A layered design reduced neutron and secondary photon flux in the detector by approximately one order of magnitude for a deuterium-tritium source. The shield arrangement can be adapted for a portable, modular design.

Introduction

There have been several active neutron interrogation methods proposed to detect explosives and narcotics (Cinausero et al., 2004; Clifford et al., 1999; Lehnert and Kearfott, 2010; Whetstone and Kearfott, 2014). The analyzed signal consists of one or more emitted radiation types, including characteristic x-rays, gamma rays, and inelastic and elastically scattered neutrons (Lehnert and Kearfott, 2011a). The various active neutron interrogation systems then have detectors set up to record one or more of these secondary radiations to obtain a signal. The signal is investigated and a determination of whether or not the materials within the target are either illegal or dangerous can be made.

In such systems, a neutron source is required, many of which are approximately isotropic.

Because the interpretation of the detector signal may be dependent on the neutron's incident angle when it interacts in the target, this is not a desirable feature for most active neutron interrogation systems (Buffler, 2004; Lehnert and Kearfott, 2011a). Furthermore, neutrons that are not initially directed at the target may interact with other objects in the room, creating secondary radiation and adding noise to the system.

By designing the shield for an isotropic source with a single opening, a limited neutron beam can be created. The neutrons emitted towards the opening have an unattenuated path towards the target, while many neutrons emitted at other angles are scattered and eventually absorbed within the shield (Whetstone and Kearfott, 2011). Similarly, the detectors used in an active interrogation system can be shielded so that radiation emerging from the area of interest will be preferentially detected over that from other angles. This is sometimes referred to as "collimation", although it could be argued that the term is better applied to photon shielding rather than neutron shielding. The increased complexity of neutron interactions in materials precludes the efficacy of producing a clean beam when compared to what is possible for photons. Using both source and detector shields creates a cleaner signal for both photons and neutrons, improving determination of the target's composition for a variety of methods.

The shield designs employed in this work were similar to those presented previously for shielding a deuterium-tritium (D-T) source (Whetstone and Kearfott, 2011) and based upon much earlier work (Greene and Thomas, 1969; Maruyama and Bouts, 1972). After evaluating several designs, two were chosen for further exploration. The neutron source shields were 0.5 m thick and consisted either of polyethylene or alternating layers of steel and polyethylene. The polyethylene is a moderator to slow and absorb neutrons. Steel shields the neutrons and secondary gamma rays.

For neutrons in the multiple MeV range, the iron atoms in steel have larger scatter cross sections than low atomic number materials (Shultis and Faw, 1996). However, due to the large relative mass of middle atomic number materials contrasted to the low neutron mass, the energy lost by the neutron in an elastic scatter with iron is minimal, thus requiring many interactions to slow the neutron. By having multiple layers of the low- and middle-atomic number materials, the neutrons will have many chances to scatter and pass through moderating material to lose energy or be absorbed.

In addition to collimating the detector, it is also desirable to limit any radiation entering the detector that is not the result of a single scatter within the target, such as neutrons or gamma rays that scattered multiple times first in the target or in the surrounding environment. If the radiation ends up being directed towards a detector after it scatters, it may contribute an undesirable signal. To further compound matters, gamma rays can interact in neutron detectors and neutrons can interact in gamma ray detectors, which will also lead to poor signal quality.

The layered technique used to shield the neutron source by Whetstone and Kearfott (2011) can be applied to detectors, only in a reverse order. Any neutrons that are not coming from the target area will have to pass through shielding, where they can be scattered, slowed, or absorbed by the polyethylene and steel, reducing the probability of entering the detector. The steel will also shield the detector from gamma rays. The result is a detector with a limited field of view focused on the area of interest.

The purpose of this work was to extend the layered steel and polyethylene design to use with a detector in a D-T active neutron interrogation system. An examination was also conducted on how the combined source and detector shields affected the neutrons and photons entering the detector. Additional discussion on modular implementation of the design is included.

Materials and Methods

Monte Carlo N-Particle 5 (MCNP 5)[1] was used to perform multiple simulations to determine neutron transmission. The shielded detector was suspended in air with an isotropic neutron source placed 1.0 m from the shield center and rotated 0, $\pi/6$, $\pi/3$, and $\pi/2$ radians about the opening. The neutron energies simulated were 14.1, 12.0, 10.0, 8.0, 6.0, 4.0, 2.5, and 1.0 MeV. For each energy and source position, an F4 tally, representing the flux averaged over the cell, was estimated for neutrons in the detector volume. The number of histories performed ensured <5% statistical uncertainty.

A shield previously developed for a D-T neutron source (Whetstone and Kearfott, 2011), was adapted for use with the detector by reversing the layering. The layer of shield closest to the detector was 0.05 m polyethylene, followed by 0.05 m steel, 0.05 m polyethylene, 0.05 m steel, 0.05 m polyethylene, 0.20 m steel, and, finally, 0.05 m polyethylene on the outside. The detector was modeled after a 0.127 m radius, 0.127 m long EJ-309 liquid scintillator[2], commonly used for fast neutron measurements (Kaplan et al., 2013, Dolan, et al., 2014). The 0.50 m thick, 0.127 inner radius, 0.50 m long shield, shown in Fig. 4.1, is open at one end to allow unattenuated radiation to approach the detector. Material compositions are in Table 4.1.

The combined source and detector shields were also simulated in a generic, more realistic environment that included walls, ceiling, floor, ground, and an interrogation object, shown in Fig. 4.2. The 0.634 m radius source shield is either the layered design from Whetstone and Kearfott (2011) or strictly polyethylene. The shield barrel has a radius of 0.134 m instead of 0.160 m presented previously (Whetstone and Kearfott, 2011), providing a $\pi/6$ steradian solid

[1] computer code Monte Carlo N-Particle Transport version 5 (Los Alamos National Laboratory, Los Alamos, NM 87545, 2006).

[2] EJ-309 liquid scintillator (Eljen Technology, Sweetwater, TX 79556).

angle from the source to the inner shield edge. To approximate a neutron transmission measurement, the barrels of the two shields are parallel to the ground and facing each other with the source 1.873 m from the detector face. A 0.40 m radius, 0.30 m long water cylinder placed between the source and the detector represents an interrogation target. It is several mean free paths thick for D-T neutrons and wide enough that all unattenuated neutrons from the source shield opening will pass through. The source and center of the detector are 0.85 m above the 0.15 m thick concrete floor resting on soil. The walls and ceiling of the 5.50 x 6.00 m, 2.35 m tall room are 0.15 m thick concrete. Several simulations were run with various shield configurations named arrangements 1-6, and one configuration with no shields, referred to as air. The specific layering schemes can be seen in Fig. 4.3. Only 14.1 MeV D-T neutrons were studied as the shield design could be adopted with modification for the less energetic deuterium-deuterium neutrons. An F4 tally determined the energy-dependent neutron flux averaged over the detector volume. Another F4 tally evaluated the effectiveness of the various shielding arrangements to minimize the secondary gamma ray background. The number of histories simulated for each arrangement was varied so the statistical uncertainty of each histogram bin was below 10%. Generally it was significantly lower.

The neutron flux for the realistic arrangement was also investigated with the source and detector offset $\pi/2$ radians in the horizontal plane, meeting the requirements of neutron elastic scatter or pulsed fast neutron analysis measurements (Buffler, 2004; Lehnert and Kearfott, 2011b, Gozani, 1994). In this case, source neutrons cannot pass through the target unattenuated and reach the detector. They must interact in the target or environment, or pass through both source and detector shielding before entering the detector. The neutron target was changed from a disc of water to a 0.25 m radius sphere of liquid nitrogen, with a density of 0.808 g cm^{-3}, to

yield a more obvious scattered neutron spectrum. Relative to Fig. 4.2, the source and its shield were rotated about the center of the target $\pi/2$ radians counterclockwise and moved back from the target an additional 0.15 m to allow space for both the source and detector shields. The source was 1.15 m from the target center. The detector/shield locations and dimensions remained unchanged. An example MCNP input file can be found in Appendix A. Each arrangement was again simulated, with the source and detector shield from arrangement 1 now referred to as arrangement 7, arrangement 2 as 8, etc. A modified arrangement 5, with the shield openings aligned, was chosen to compare to the rotated simulations. Arrangement 5 was considered a compromise, using polyethylene in the source shield to minimize mass and reduce the generation of secondary gamma rays, while the detector shield still employed layered polyethylene and steel to shield both neutrons and gamma rays. The only modification to arrangement 5 was to move the source and shield back 0.15 m and change the scatter target to match arrangements 7-12.

Results

The averaged detector neutron flux from the simulated sources at various energies and angles can be found in Fig. 4.4. The largest flux was at 0 radians relative to the shield opening and the smallest was at $\pi/3$ radians. The flux difference between the two was estimated to be roughly three orders of magnitude for all neutron energies, both with the steel and polyethylene layered shield and the shield that contained only polyethylene.

The results for the aligned system simulated in a room can be seen in Fig. 4.5 and 4.6. It should be noted that spectral data are generally displayed in the form of histograms. However, in order to display multiple data sets in a single figure, it was decided to use scatter plots instead, where the upper right corner of each bin is represented by a data point. Furthermore, the energy

between data points was varied in the lower region of the spectrum to more accurately reflect the variation in the flux. Therefore, it was necessary to normalize the simulated bin counts by the width of the bin. The units on the y-axis of the spectra are particles cm^{-2} MeV^{-1} per source particle.

The spectra from D-T neutrons entering the detector were very similar, regardless of the detector and source shield. Only the simulation with no shield, labeled air, showed a flux spectrum approximately one order of magnitude greater for all energies. The peak to background ratio for the shielded arrangements were all similar and ranged between 21 and 36 when taken from 4 to 12 MeV. The air arrangement, with no shield material, had ratios between 7 and 19.

The secondary photon spectra showed a greater variability with shield arrangement. Again, the largest overall flux was the simulation without shielding, while the lowest flux was seen for arrangements 3 and 5 at higher energies, and arrangement 2 for lower energies. The flux difference between shielded configurations was just over an order of magnitude between 6 and 7 MeV and got progressively smaller at lower energies. The photon spectra were shown for energies up to 7 MeV to account for the most prominent gamma rays associated with inelastic neutron scatter off carbon, nitrogen, and oxygen, all of which are present in the air, with oxygen also in the interrogation target and carbon in the shielding material. The gamma rays of concern are carbon: 4.43 MeV, nitrogen: 2.31, and oxygen: 6.13 MeV, all seen in the simulations. An estimate of the peak to background ratio at all three energies was performed to better understand the characteristic gamma ray behavior of the various arrangements, with results in Table 4.2.

As seen in Fig. 4.7, when rotated $\pi/2$ radians, a large decrease in the 14.1 MeV neutrons was observed in arrangements 7 – 12. The simulated detector neutron flux of arrangements 7 – 12 was normalized by the flux of the modified arrangement 5 and displayed in Fig. 4.8. For

arrangements 7, 9, 11, and 12, which all included source shields, the ratios at 14.1 MeV are below 0.001. The ratios for arrangements 8 and 10, which had no source shields, were below 0.06. Large peaks at 12.6 MeV, with magnitudes between 1.2 and 0.7 are visible in all spectra.

The gamma ray spectra for the various rotated arrangements, seen in Fig. 4.9, had a magnitude and shape similar to the aligned spectra. An estimate of the peak to background ratio was again performed, with results in Table 4.3.

Discussion

Simulations

As seen in Fig. 4.4, both shielding arrangements, as a function of position, produce spectra having the same order of magnitude and basic shape. Even though the source was further from the shield opening, the thickness of shielding material was actually less than at $\pi/3$ radians, due to the cylindrical form. In general, this correlated to the relative counts at each position in both shields. The layered and polyethylene shield designs were similarly effective at reducing neutron flux at all angles. The order of magnitude drop in neutron flux from 0 to $\pi/6$ radians, and even larger drop from $\pi/6$ to $\pi/3$ radians, demonstrate efficient detector collimator design.

In the simulations, there was a wider spread in neutron flux at $\pi/2$ radians for both the layered and strictly polyethylene designs. As expected, closer inspection revealed that the lower energy neutron sources tended to have a lower total flux than the higher energy sources. High energy neutrons are less likely to be scattered or absorbed in the shield, so there is a greater number of them that reach the detector. Interestingly, this trend was reversed when the neutron source was at $\pi/3$ radians. Although the data points are more tightly packed, the highest energy sources had lower fluxes while low energy sources had higher fluxes. This was most likely the

result of the average neutron path length through the shield being longer at $\pi/3$ radians than at $\pi/2$. This extra material allowed for an accumulation of multiply scattered lower energy neutrons while the higher energy neutrons passed through with fewer interactions and a smaller buildup factor. At $\pi/2$ radians, the same phenomenon was not observed because there was not enough shield material for the lower energy neutrons to undergo significant buildup. Similar effects can be seen in Veselkin et al. (1969) and Shin et al. (1997). This theory is further supported by comparing the 1 MeV neutron flux at $\pi/3$ and $\pi/2$ radians for the polyethylene and layered shield designs. In both instances, the total neutron flux is actually larger at $\pi/3$ radians, even though the amount of attenuating material is greater. The same does not hold true for the higher energy neutron fluxes.

The simulated neutron energy spectra from neutron transmission, seen in Fig. 4.5, reveal no significant differences among designs. Large disparities between spectra were not anticipated because the source shield opening was directly aligned with the detector shield opening. The spectra is dominated by neutrons that were emitted from the source and traveled through the shield opening, possibly after one or more scattering events, towards the detector. For all arrangements, there is a peak at 14.1, then the spectra drops by over an order of magnitude and rises up to 10^8 times as the energy approaches thermal. Even in arrangements 2 and 4, having no source shield, the spectra are similar. The air arrangement, however, was consistently at least an order of magnitude greater than the shielded simulations and had a smaller peak to background ratio, validating the effectiveness of the detector shields at minimizing multiply scattered neutrons.

When the source was rotated about the target $\pi/2$ radians in the horizontal plane, there were some interesting results. As seen in Fig. 4.7, when combined with collimation, the new

alignment significantly suppresses the 14.1 MeV peak in arrangements 7-12. Both arrangement 5 and air maintain a large D-T peak due to a lack of shield material between the source and detector. In Fig. 4.8, when the energy dependent neutron fluxes of arrangements 7-12 were normalized by the flux of modified arrangement 5, a peak at 12.6 MeV resulting from single elastic scatter in the nitrogen target was clearly visible. The peaks have a magnitude ranging from 1.2 to 0.75. Arrangements 7, 9, 11, and 12, which included source shields, had peak ratios near 0.75 with similar spectra shapes. At higher energies, the ratios fell below 0.001, a three order of magnitude drop in source neutrons entering the detector.

Despite signal noise, the simulation demonstrates a clear method of neutron energy adjustment. All that is required is an elastic scatter target of known atomic mass, a neutron source with a constant energy, and proper shielding to limit the detector field of view. This would allow for active interrogation with neutrons of controllable and variable energies.

The photon spectra for both the aligned and rotated arrangements varied significantly. The smallest spectra with aligned shields (arrangements 2, 3, and 5) have no steel in the source shield, eliminating many of the photons generated. Arrangement 4 also has no steel. However, more secondary photons from neutron interactions in the room are evident due to decreased attenuation in the polyethylene detector shield.

Furthermore, as seen in Tables 4.2 and 4.3, the characteristic carbon gamma ray peak-to-background ratio is greatest for arrangements 2, 5, and 9, where the large carbon content of the polyethylene shields creates a sizeable 4.43 MeV gamma ray peak. For the water interrogation target, arrangement 3 had the largest peak to background ratio for characteristic oxygen gamma rays at 6.13 MeV. When the detector and shield were rotated $\pi/2$ radians, the carbon and oxygen peak-to-background ratios were generally smaller because the gamma rays had to pass through

more shielding material. Arrangement 7, which had the steel and polyethylene layered shield for both the source and detector, provided the greatest peak-to-background ratio for the 2.31 MeV characteristic nitrogen gamma rays. With the large amounts of steel present, the arrangement effectively limited the detector field of view.

Proposed shielding design

The addition of a source and detector shield to an active neutron interrogation system helps minimize undesired neutrons and photons entering the detector. When the source and detector shield openings are facing each other, the relative arrangement of steel and polyethylene around the source does not have a significant effect on neutron flux in the detector. Although steel in the source shield has been shown to reduce the neutron flux and total dose around an isotropic neutron source (Whetstone and Kearfott, 2011), by removing it, the total detected secondary gamma ray flux can be significantly reduced. However, a larger characteristic carbon gamma ray peak will be present, which could be a problem for some measurements. Similarly, the use of steel in the detector shield does not appear to meaningfully change the detector's neutron spectra.

When the detector is rotated $\pi/2$ radians, layers of steel around both the source and detector minimize environmental neutron interactions and secondary gamma rays entering the detector. This allows for cleaner signals from the target of interest. When used properly, steel can improve the performance of an active neutron interrogation system by effectively collimating the source and detector.

Appropriate collimation reduces the system footprint. The use of multiple separate layers provides an easy method to break down and reconstruct the system, facilitating portability. This can be accomplished by using a rectilinear shield design, seen in Fig. 4.10. Each layer can

consist of a preferred material in two “L” shaped pieces that fit together in an open-ended box. One end can be closed using a shielding cap with the other left open to allow for neutrons to emerge unattenuated. Additional layers fit flush against previous layers until the desired shield thickness is achieved. As seen in Fig. 4.11, the modular shield design can employ overlapping, interlocking pieces, adding structural stability and eliminating the emergence of unattenuated neutrons at joints or between layers. The modular construction also allows for simple adjustment and adaptability by changing, removing, or adding layers depending on the application.

In all interrogation systems, the most important consideration is a signal with minimal noise. The shield design proposed in this paper offers a novel method for both material arrangement and implementation to help produce a cleaner detector signal.

Conclusions

The use of source and detector shielding can greatly increase the effectiveness of active neutron interrogation systems. The source shield limits unattenuated neutrons entering the surrounding area and, combined with the detector shield, reduces the number and energy of secondary photons and scattered neutrons entering the detector by an order of magnitude. The limited field of view provides a cleaner signal without sacrificing detector efficiency for the area of interest. The simulations show the similarities and differences between shield designs that employ either polyethylene or alternating layers of steel and polyethylene.

Depending on the application, the source and detector shields can be used separately or combined, with or without steel, to enhance an active neutron interrogation system. The proposed modular shield component designs allow for easy construction, transportation, disassembly, and modification. The shield designs presented are viable options for active neutron

interrogation and deserve consideration for new detection systems.

Figures

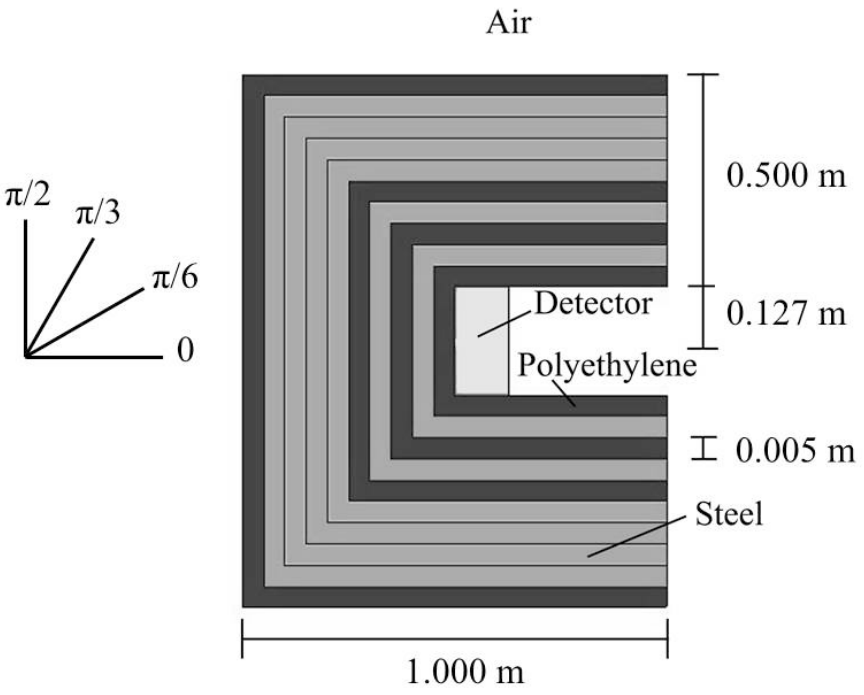

a)

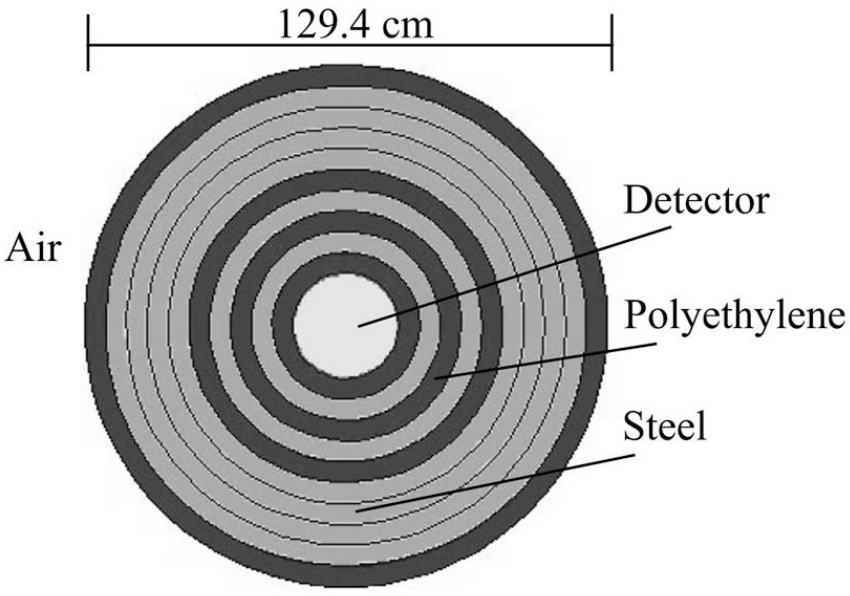

b)

Fig. 4.1: A cutaway a) side view and b) down the barrel of the detector shield. This represents the layered steel and polyethylene design.

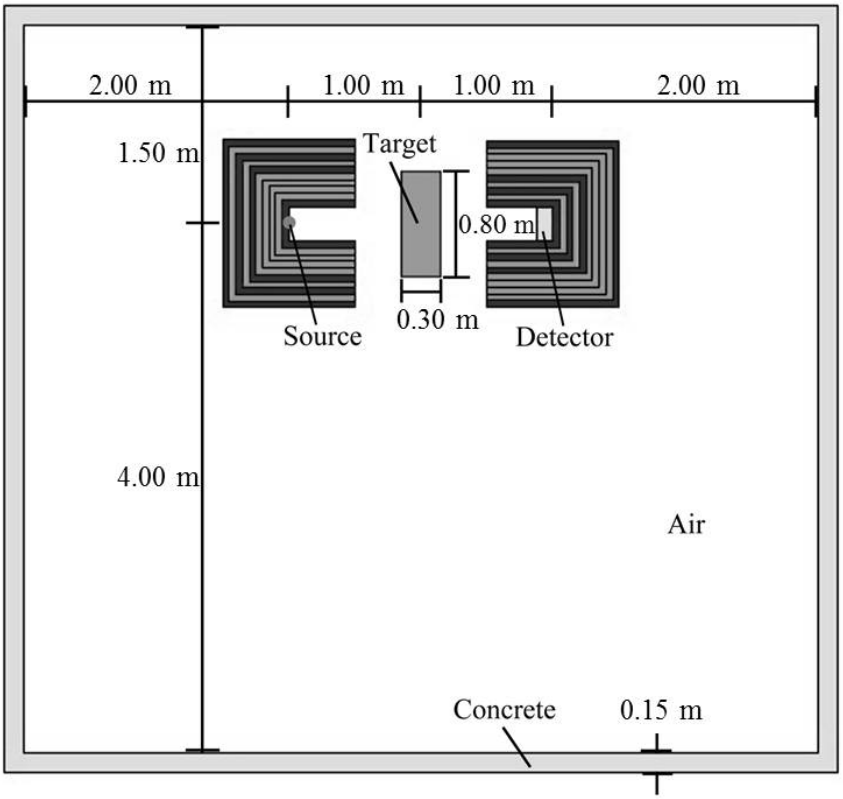

a)

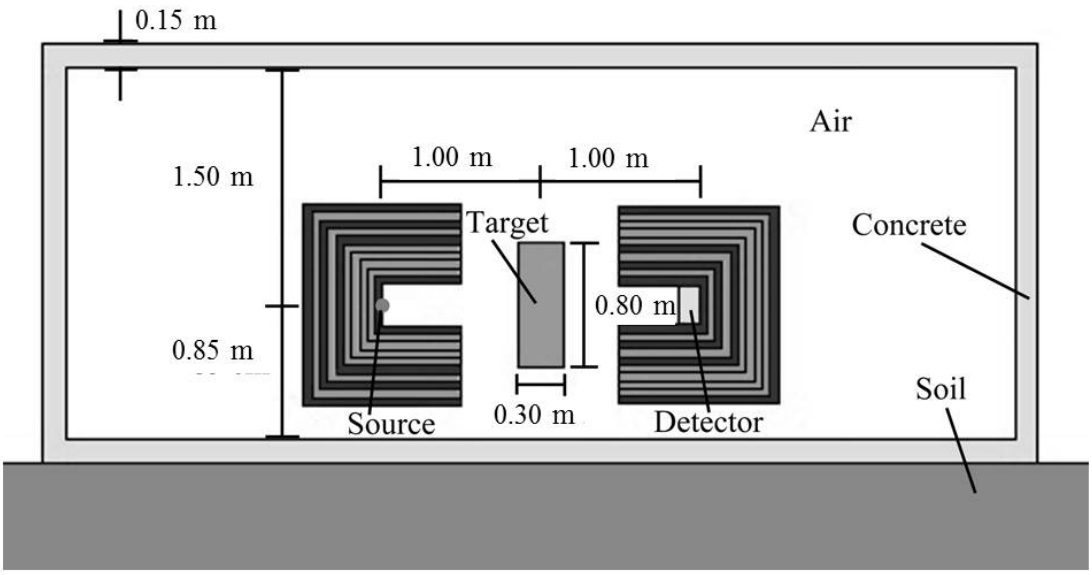

b)

Fig. 4.2: A a) top-down and b) side view of the simulated room with the detector, source shield, and water target arrangement.

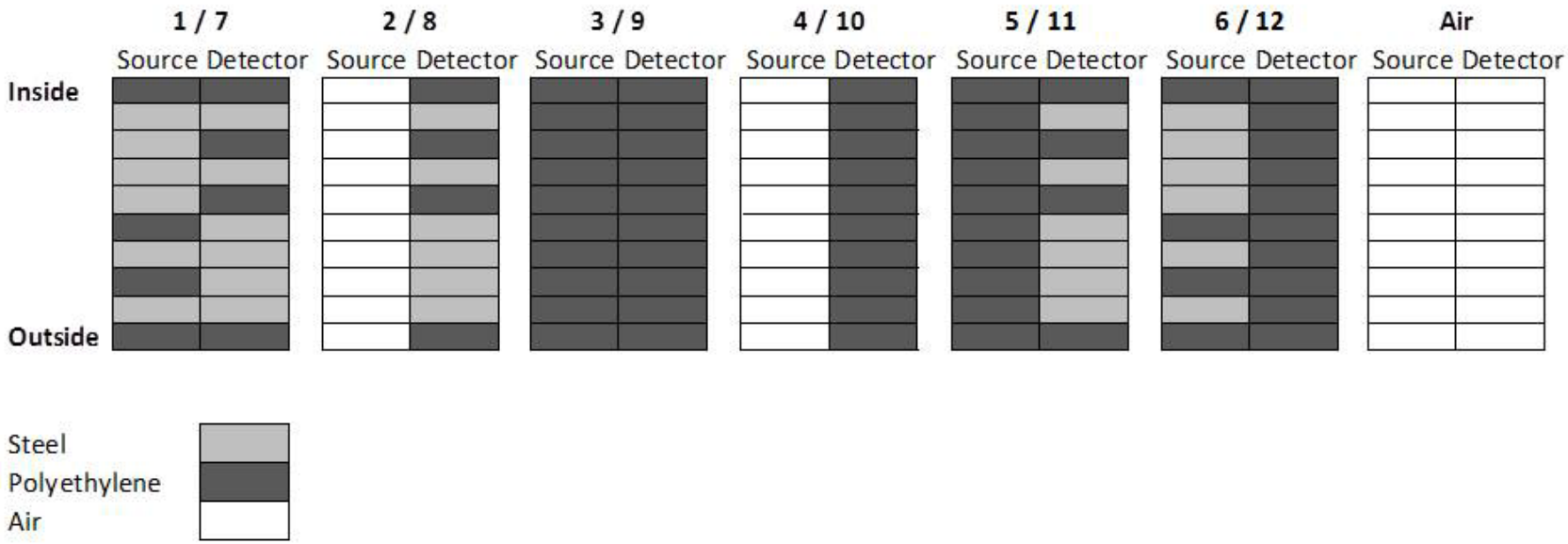

Fig. 4.3: A graphical representation of the various shield arrangements simulated in the realistic environment. Each layer is 0.05 m thick.

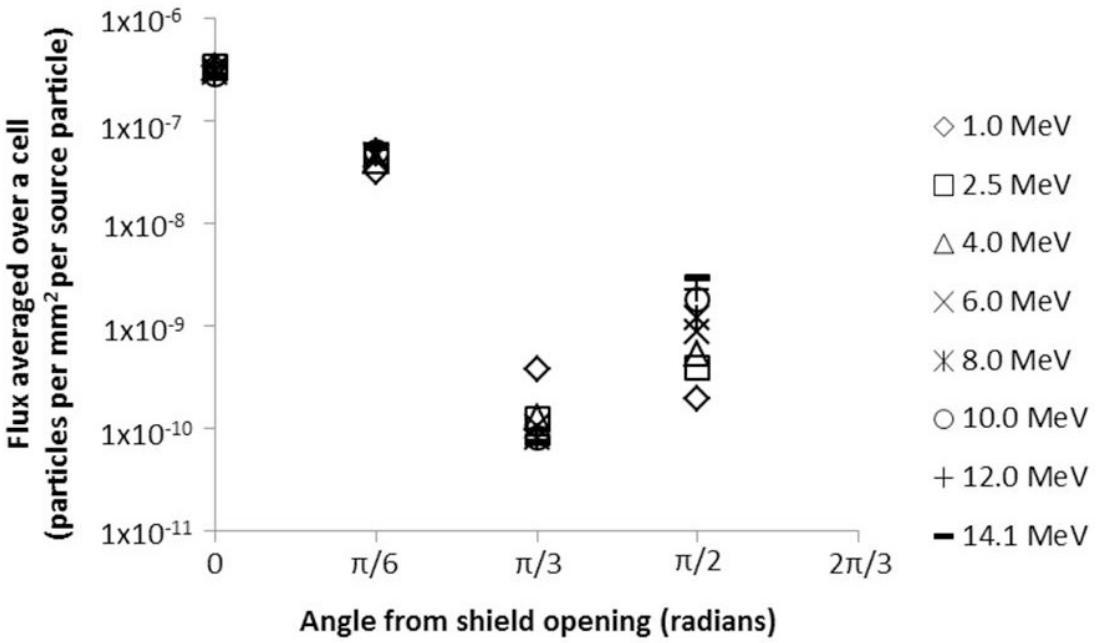

a)

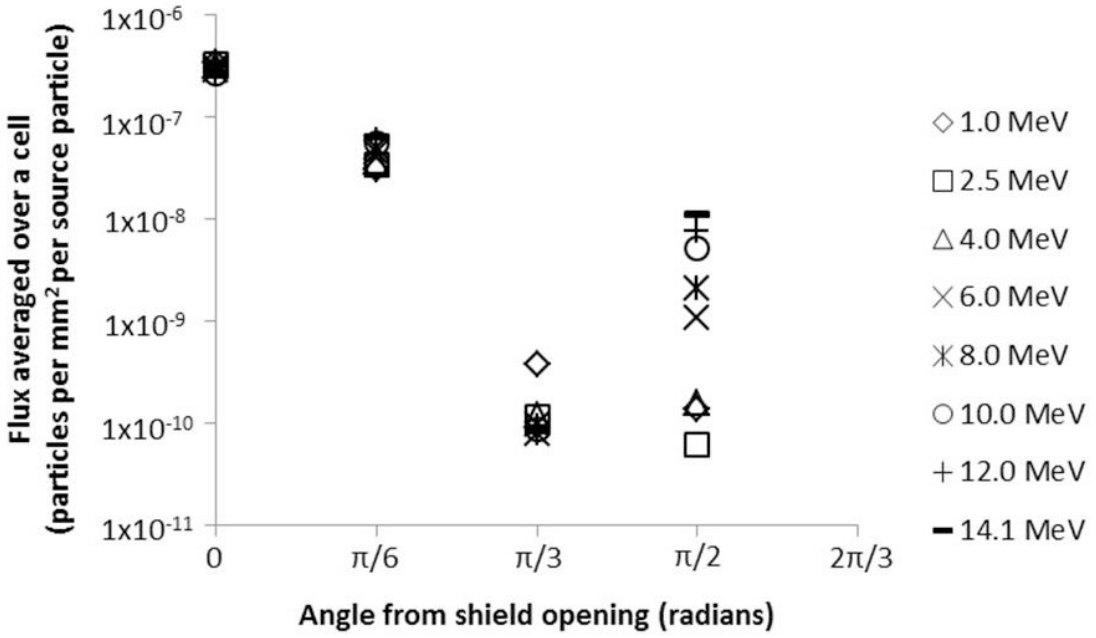

b)

Fig. 4.4: The neutron flux for a variable energy neutron source at different locations around the a) layered polyethylene and steel and b) pure polyethylene detector shields.

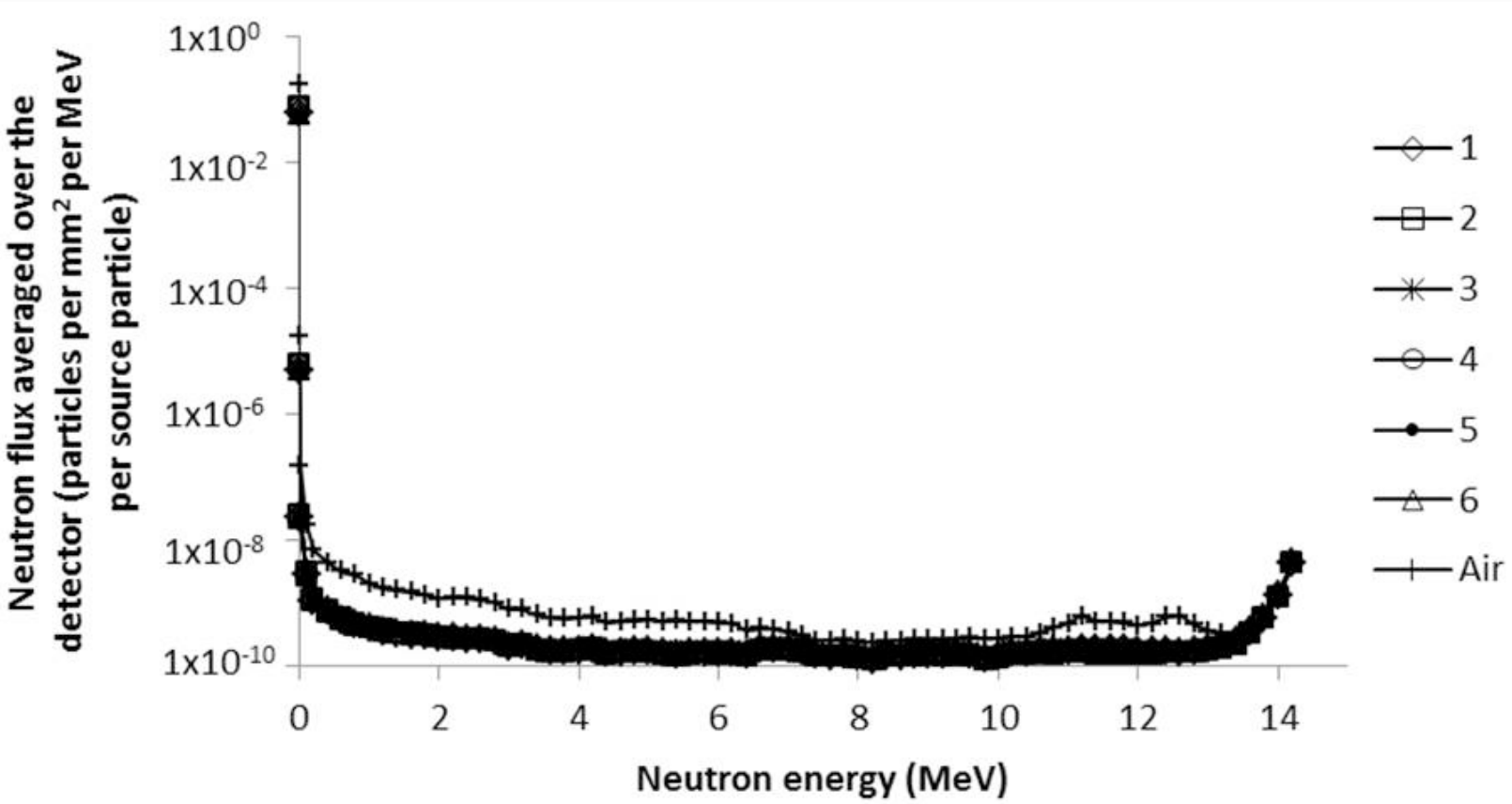

Fig. 4.5: The detector neutron energy spectra for various aligned source and detector shield arrangements.

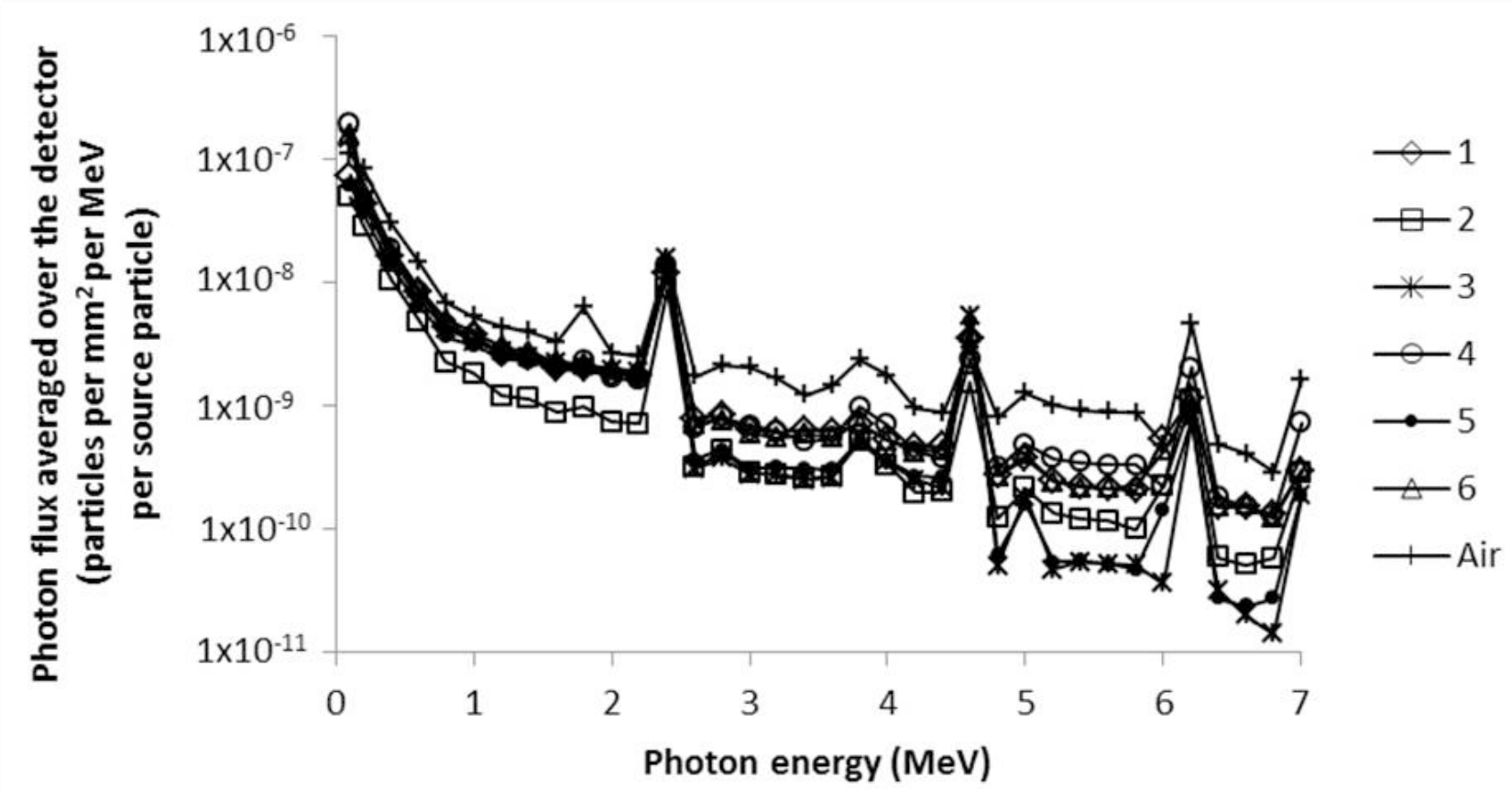

Fig. 4.6: The detector gamma ray energy spectra for various aligned source and detector shield arrangements.

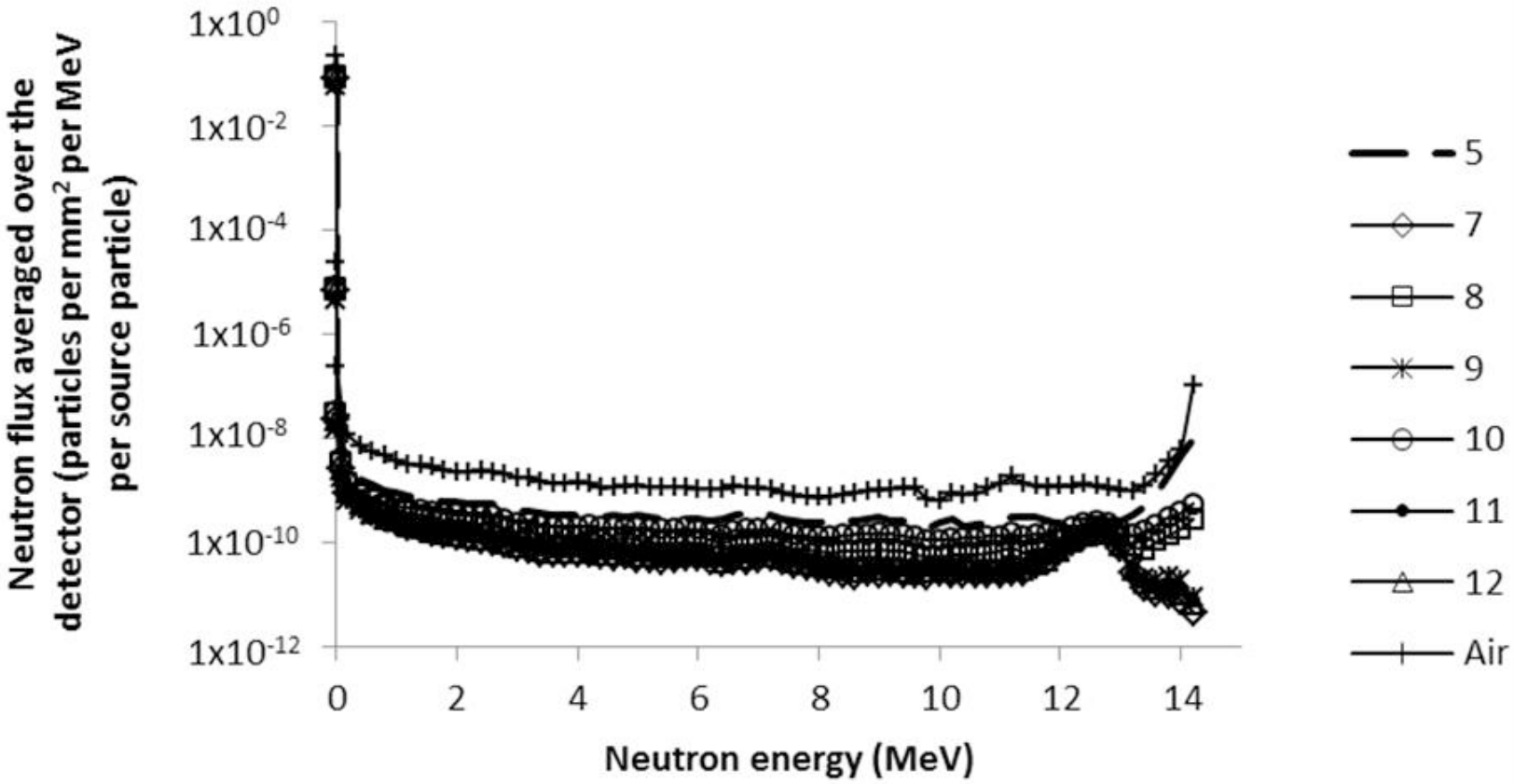

Fig. 4.7: The detector neutron energy spectra for the rotated source and detector shield arrangements.

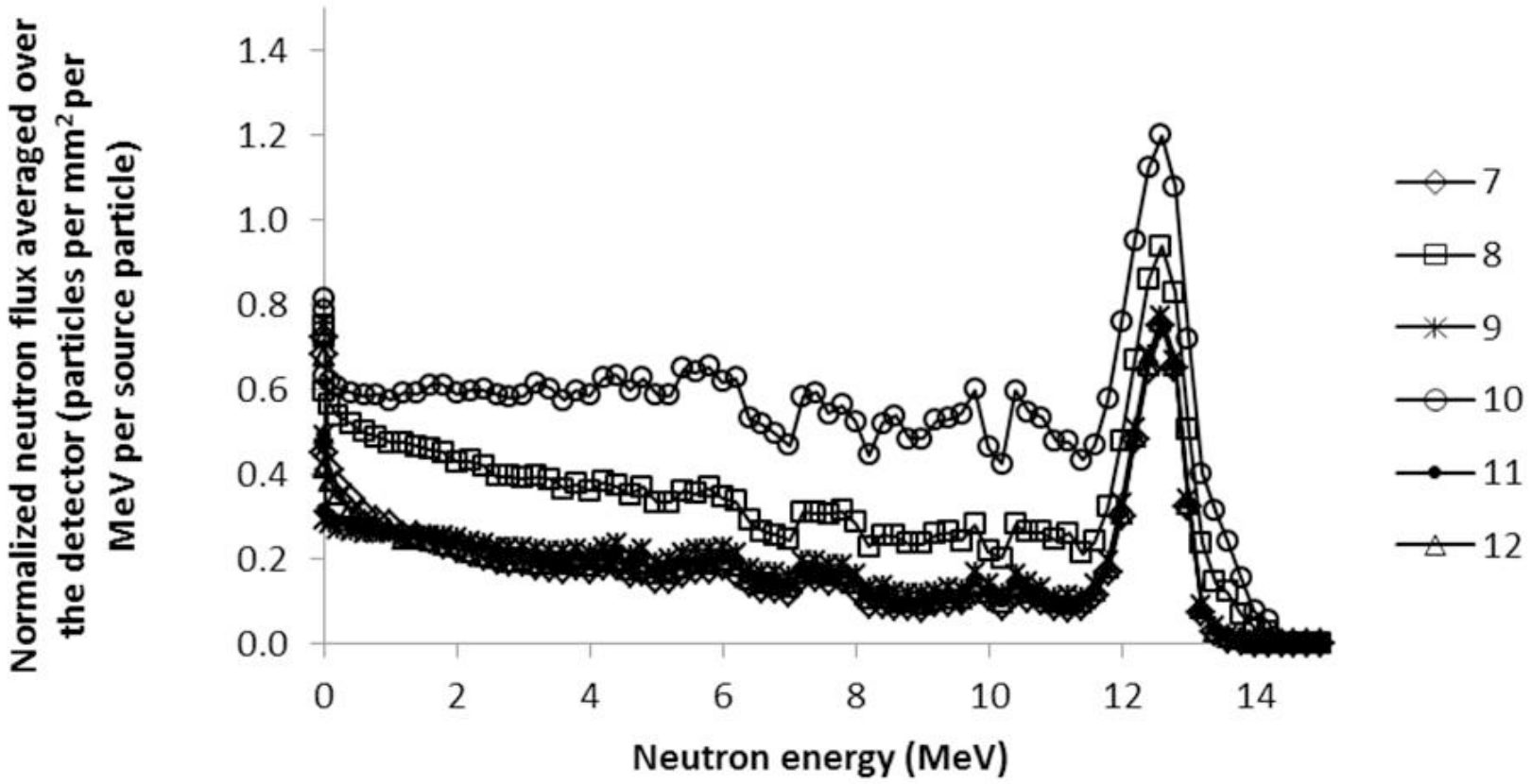

Fig. 4.8: Arrangements 7– 12, normalized by the spectra from a modified arrangement 5. There is a noticeable increase at 12.6 MeV, which is correlated to the elastic scatter of 14.1 MeV neutrons off the nitrogen target at $\pi/2$ radians.

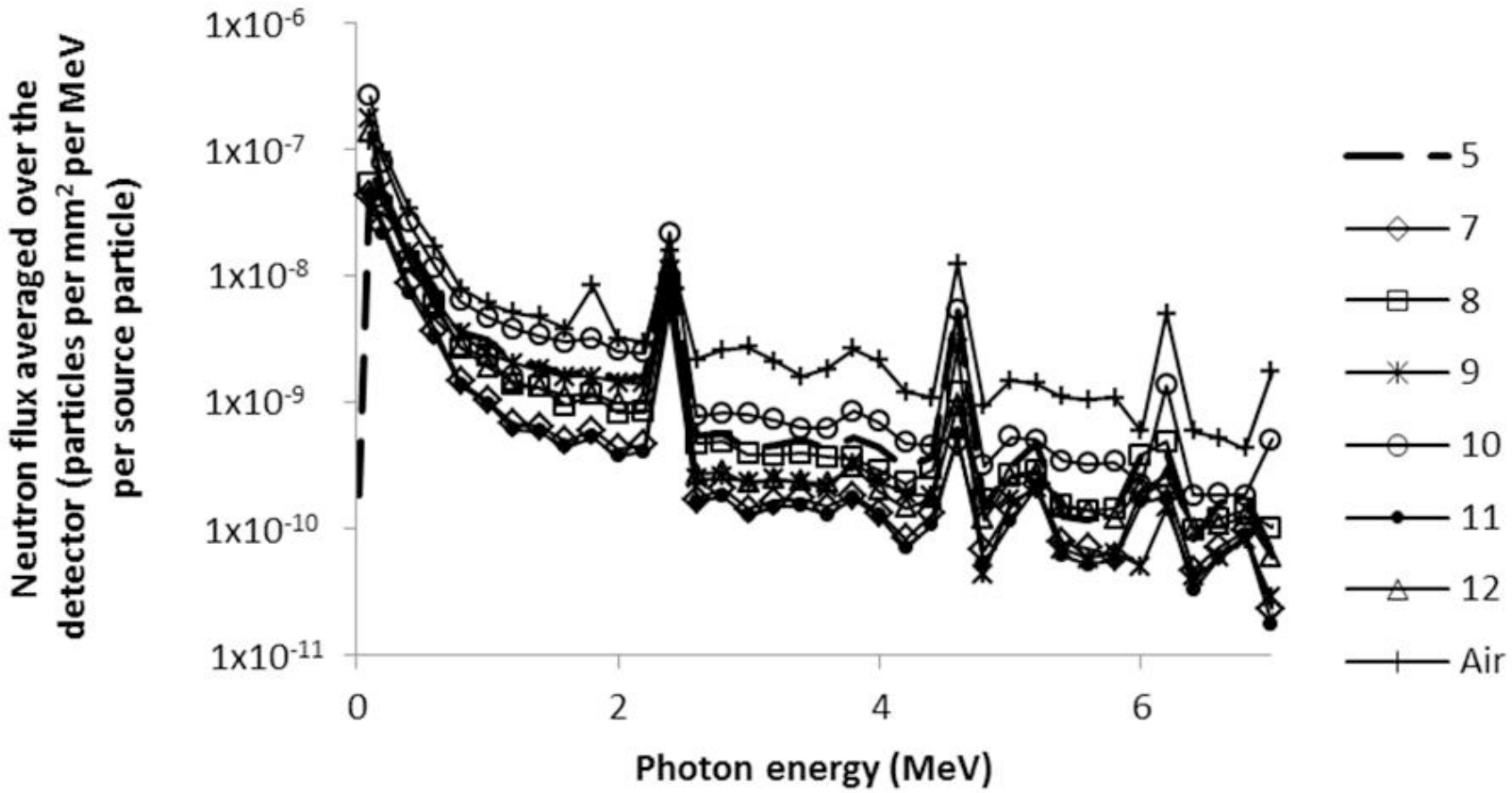

Fig. 4.9: The detector gamma ray energy spectra for the rotated source and detector shield arrangements.

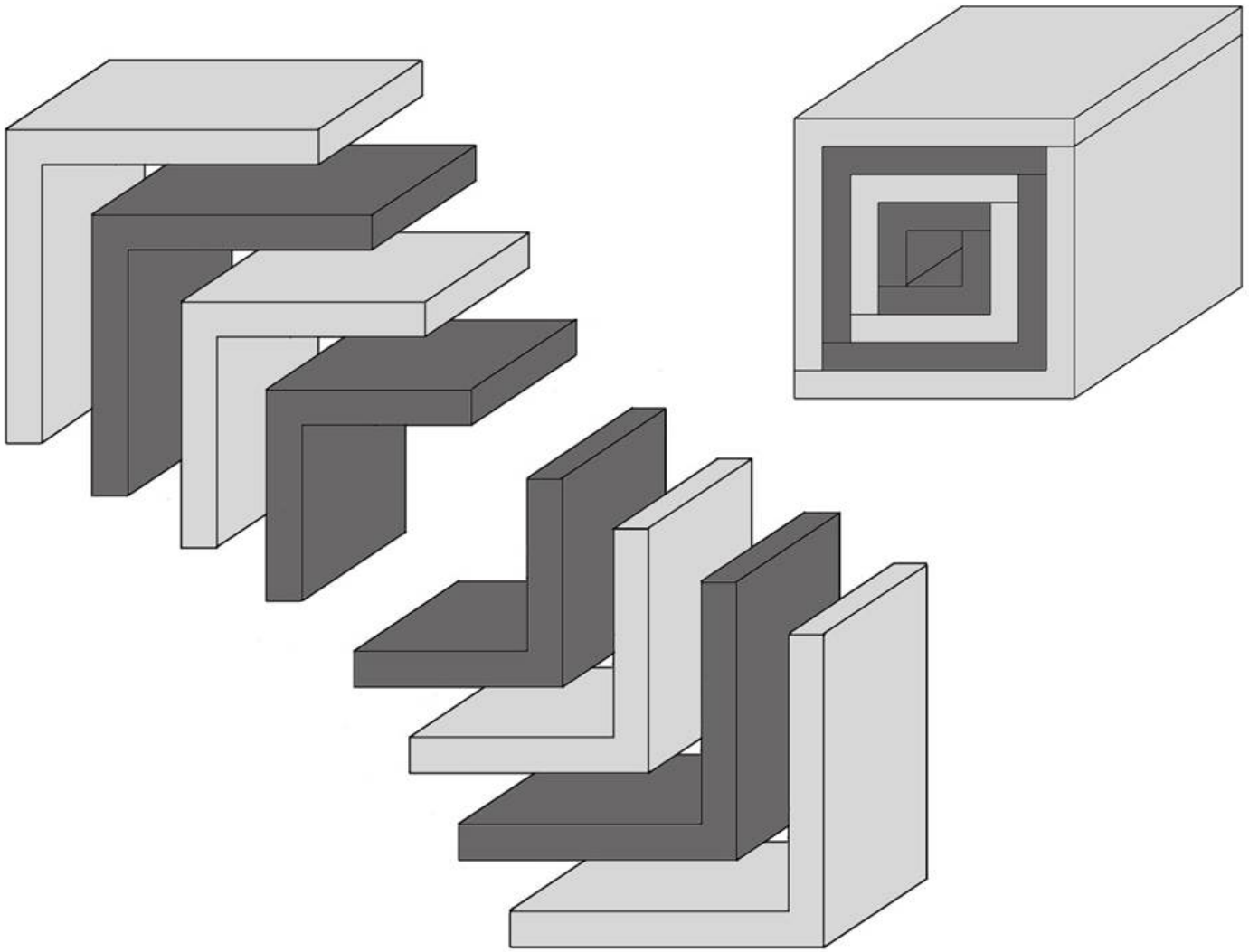

Fig. 4.10: An example of how the modular shielding could be constructed so that there were no continuous seams between layers. The "L" shaped pieces form a rectilinear box which can then be capped at one end to create either a source or detector shield.

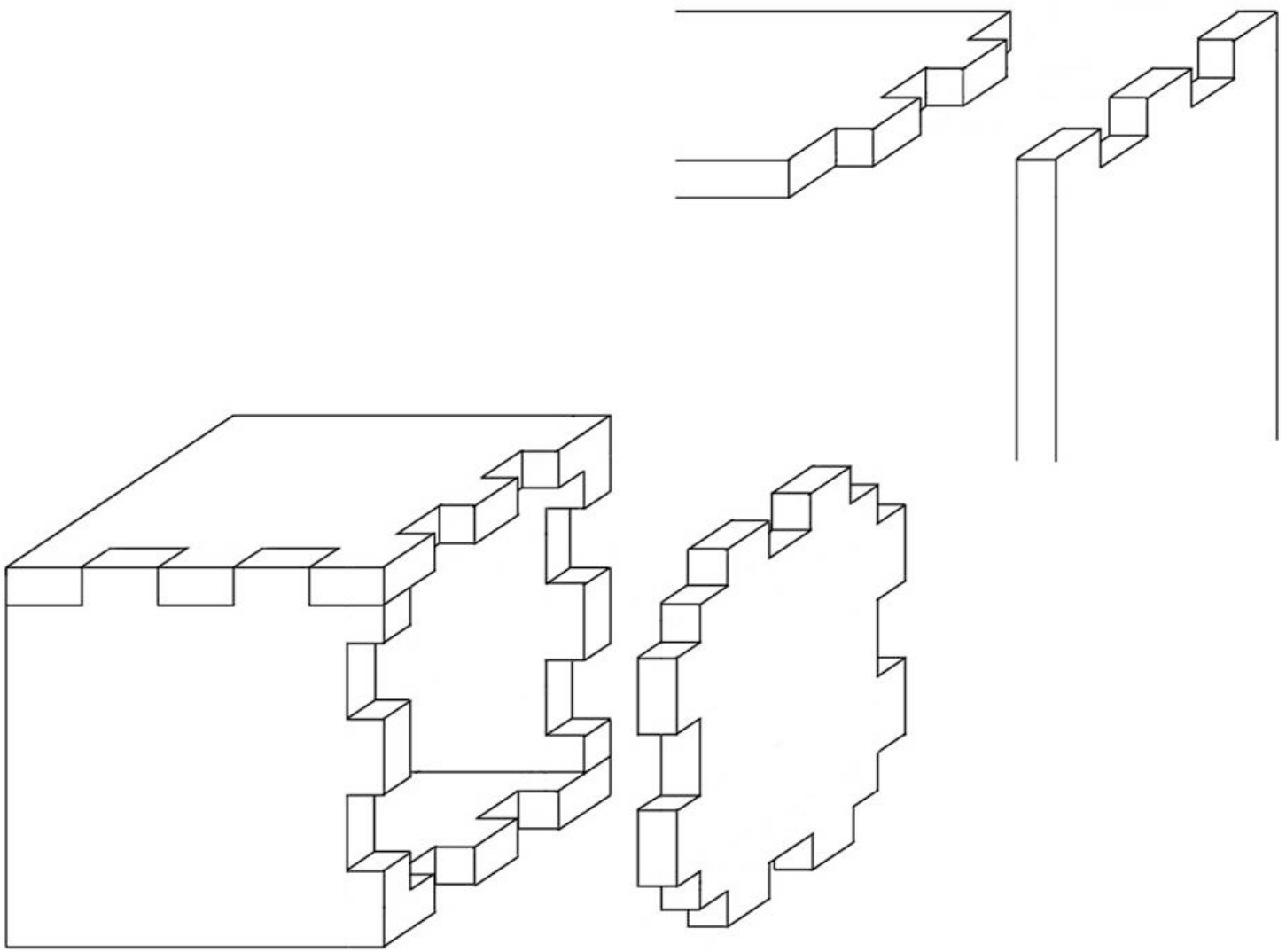

Fig. 4.11: An example design for the various shield pieces so that they fit together more securely and limit the size and length of cracks at seams.

Tables

Table 4.1: A description of materials simulated.

Material	Elemental makeup (relative abundance)	Elemental makeup (weight %)	Density (kg m^{-3})
Air (McConn et al., 2011)		C (0.001), N (0.755), O (0.231), Ar (0.013)	1.2
Polyethylene	H (4), C (2)		940
Water	H (2), O (1)		1,000
Steel		C (0.2), Fe (99.8)	7,860
EJ-309	H(5), C(4)		960
Nitrogen	N(1)		810
Soil (Eckerman and Ryman, 1993)	H (0.2938), C (0.0187), O (0.5045), Al (0.0259), Si (0.1354), K (0.0143), Fe (0.0027)		1,750
Concrete (McConn et al., 2011)		H (0.56), O (49.81), Na (1.71), Mg (0.26), Al (4.57), Si (31.51), S (0.13), K (1.92), Ca (8.29), Fe (1.24)	2,080

Table 4.2: Peak-to-background ratio for characteristic gamma rays in simulated D-T shielding arrangements with the source and detector shield openings aligned.

Photon energy (MeV)	Peak-to-background ratio for each arrangement						
	1	2	3	4	5	6	Air
2.31	9.2 ± 0.2	17.3 ± 0.4	14.2 ± 0.2	12.0 ± 0.1	12.8 ± 0.3	10.7 ± 0.3	7.0 ± 0.1
4.43	9.4 ± 0.3	9.5 ± 0.4	39.9 ± 1.7	7.1 ± 0.2	29.9 ± 1.5	11.1 ± 0.5	3.6 ± 0.1
6.13	3.3 ± 0.1	7.9 ± 0.5	22.3 ± 1.6	10.1 ± 0.4	9.2 ± 0.6	3.7 ± 0.2	9.5 ± 0.2

Table 4.3: Peak-to-background ratio for characteristic gamma rays in simulated D-T shielding arrangements with the shielded detector rotated $\pi/2$ radians relative to the source.

Photon energy (MeV)	Peak-to-background ratio for each arrangement							
	7	8	9	10	11	12	Air	Modified 5
2.31	24.6 ± 0.6	13.4 ± 0.2	13.6 ± 0.3	13.3 ± 0.2	19.1 ± 0.5	18.8 ± 0.4	6.1 ± 0.1	13.9 ± 0.2
4.43	4.9 ± 0.2	5.1 ± 0.1	23.5 ± 1.5	13.7 ± 0.4	6.9 ± 0.3	6.5 ± 0.3	12.4 ± 0.4	21.6 ± 0.6
6.13	1.8 ± 0.1	2.0 ± 0.1	3.2 ± 0.4	6.6 ± 0.3	1.8 ± 0.2	1.7 ± 0.1	8.5 ± 0.4	1.8 ± 0.1

References

Buffler, A., 2004. Contraband detection with fast neutrons. *Radiat. Phys. Chem.*, 71 (3-4), 853 – 861.

Cinausero, M., Lunardon, M., Nebbia, G., Pesente, S., Viesti, G., Filippini, V., 2004. Development of a thermal neutron sensor for humanitarian demining. *Appl. Radiat. Isotopes* 61 (1), 59 – 66.

Clifford, E., Ing, H., McFee, J., Cousins, T., 1999. High rate counting electronics for a thermal neutron analysis land mine detector. Penetrating Radiation Systems and Applications, *Proc. SPIE*, 3769, 155 – 166.

Dolan, J.L., Marcath, M.J., Flaska, M., Pozzi, S.A., Chichester, D.L., Toanin, A., Peerani, P., 2014. Active-interrogation measurements of fast neutrons from induced fission in low-enriched uranium. *Nucl. Instrum. Methods Phys. Res. A,* 738, 99 – 105.

Eckerman, K.F., Ryman, J.C., 1993. External exposure to radionuclides in air, water, and soil. Oak Ridge National Laboratory, Report No. EPA-402-R-93-081.

Gozani, T., 1994. Novel applications of fast neutron interrogation methods. . Nucl. Instrum. *Methods Phys. Res. A,* 353 (1-3), 635 – 640.

Greene, D., Thomas, R.L., 1969. The attenuation of 14 MeV neutrons in steel and polyethylene. *Phys. Med. Biol.,* 14 (1), 45 – 54.

Kaplan, A.C., Flaska, M., Enqvist, A., Dolan, J.L., Pozzi, S.A., 2013. EJ-309 pulse shape discrimination performance with a high gamma-ray-to-neutron ratio and low threshold. *Nucl. Instrum. Methods Phys. Res. A*, 729, 463 – 468.

Lehnert, A.L., Kearfott, K.J., 2010. The detection of explosive materials: review of considerations and methods. *Nucl. Technol.*, 172 (3), 325 – 334.

Lehnert, A.L., Kearfott, K.J., 2011a. Preliminary identification of flags for a novel algorithm-based approach for explosives detection using neutron interrogation for a simulated idealized cargo container scenario. *Nucl. Instrum. Methods Phys. Res. A*, 638 (1), 201 – 205.

Lehnert, A.L., Kearfott, K.J., 2011b. Simplified simulation of fast neutron scattering for an explosives detection application. *Nucl. Sci. Eng.,* 168 (3), 278 – 286.

Maruyama, T., Bouts, C.J., 1972. Attenuation of 15 MeV neutrons in multilayer shields composed of steel, polyethylene and borated materials. *Phys. Med. Biol.,* 17 (3), 420 – 424.

McConn Jr., R.J., Gesh, C.J., Pagh, R.T., Rucker, R.A., Williams III, R.G., 2011. Compendium of material composition data for radiation transport modeling. Pacific Northwest National Laboratory, Report No. PNNL-15870.

Shin, K., Kotegawa, H., Sakamoto, Y., Nakane, Y., Nakashima, H., Tanaka, S., Uwamino, Y., Bani, S., Hirayamai, H., Tanaka, S., 1997. Point isotropic build-up factors of medium energy neutrons for concrete, iron and a double iron followed by concrete. *Radiat. Prot.*, 71 (4), 269 – 278.

Shultis, J.K., Faw, R.E., 1996. Radiation Shielding. (Prentice Hall, Upper Saddle River, NJ), pp. 282-290.

Veselkin, A.P., Egorov, Y.A., Netecha, M.E., Pankrat'ev, Y.V., Piskunov, V.I., 1969. Buildup of moderated neutrons in reactor shielding. *Atomnaya Énergiya*, 26(3), 269 – 278.

Whetstone, Z.D., Kearfott, K.J., 2011. Use of multiple layers of repeating material to effectively collimate an isotropic neutron source. *Nuc. Technol.*, 176 (3), 395 – 413.

Whetstone, Z.D., Kearfott, K.J., 2014. A review of conventional explosives detection using active neutron interrogation. *J. Radioanal. Nucl. Ch.*, 301 (3), 629 – 639.

CHAPTER 5: A METHOD FOR USING NEUTRON ELASTIC SCATTER TO CREATE A VARIABLE ENERGY NEUTRON BEAM FROM A MONENERGETIC NEUTRON SOURCE

Abstract

There are a variety of sources that can be used for active neutron interrogation. Currently, however, only complicated, expensive accelerators can provide monoenergetic neutrons across a range of energies. This work describes preliminary investigation into the design of a compact, portable source that can reliably vary neutron energy. If feasible, such a system could be of significant benefit to active neutron interrogation for contraband detection. The proposed method uses elastic neutron scatter at a specific angle to reliably reduce the neutron energy of a deuterium-deuterium (D-D) or deuterium-tritium (D-T) fusion neutron source. The research focuses on D-T Monte Carlo simulations, both in idealized and more realistic scenarios, and a small experiment using a D-D source, a boron triflouride (BF_3) neutron detector, and a water scatter target. Systematic uncertainty of the method is also analyzed. The idealized scenarios showed promise and encouraged future work, but the more realistic simulations highlighted the need for discrimination of multiply scattered neutrons, either through a pulsed generator or associated particle imaging.

Introduction

Active neutron interrogation can employ various methods of neutron generation and be applied to several different methods of contraband detection. The search for explosives and

narcotics can be performed using pulsed fast neutron analysis (PFNA) and neutron elastic scatter (Buffler, 2004; Lehnert and Kearfott 2010; Lehnert and Kearfott, 2012; Strellis et al., 2009; Whetstone and Kearfott, 2014). Neutron transmission and fast neutron radiography, which utilize neutrons that do not interact in a target, can be employed to investigate the elemental composition of a target (Overley et al., 2006; Sowerby and Tickner, 2007). Neutron energy plays a strong role in the performance of explosives detection methods of various types (Hsu and Kearfott, 1999).

One drawback to active neutron interrogation is that the user is limited in choices for a neutron source. Large accelerators, although more versatile, are expensive, complicated, and occupy a large area. This is not ideally suited to many applications, including anything mobile or at locations such as airports or border crossings where space is limited and costs need to be controlled. Smaller, portable neutron sources are also available, but they too have issues. High energy photon sources, when paired with ^{9}Be or ^{2}H, can generate neutrons through a (γ,n) reaction (Knoll, 2010). The photon energy dictates the energy of the released neutron, potentially allowing for a near-monoenergetic source. However, photonuclear sources require a high gamma ray flux that may impede measurements and, unless a large accelerator is used to create photons, the practical maximum energy of the neutrons is limited to about 1 MeV. Small fission and radioisotope sources such as ^{252}Cf and plutonium-beryllium, respectively, release neutrons over a range of energies (Knoll, 2010). Unfortunately, all of these compact source types cannot be turned off and present a hazard if lost or stolen.In contrast, fusion sources, such as deuterium-deuterium (D-D) and deuterium-tritium (D-T) generators, are compact, can be powered on and off, and have relatively high energy nearly-monoenergetic spectra around 2.5 and 14.1 MeV, respectively. This makes them the sources of choice for many active neutron interrogation

applications (Aleksandrov et al., 2005). Unfortunately, in both cases, the resulting neutron energy is fixed, limiting the user to only two choices, even if a different energy is more ideal. A portable, tunable neutron source that could be turned off and minimized photon background could find use in many active neutron interrogation applications.

There are many benefits to a tunable neutron source. First, it would allow the user to set the neutron energy in such a way as to take advantage of natural resonance peaks in materials of interest. Traditional explosives and narcotics have unique nitrogen, oxygen, and carbon ratios. All three of these elements have distinct, strong, neutron interaction peaks in the 1 – 15 MeV range (Raas et al., 2005). A neutron source that could change its energy reliably and easily would allow for more thorough measurements at lower fluence. Another benefit would be that lower neutron energies would require less shielding and provide less dose to any personnel in the area.

Theory

The proposed compact, tunable active neutron interrogation system uses either a monoenergetic D-D or D-T neutron source and takes advantage of neutron elastic scatter to reliably reduce the energy of the neutrons. The system, which includes previously designed radiation shielding for the source and detector (Whetstone and Kearfott, 2011; Ch. 4), utilizes a scattering target directly in front of the source and a detector separated by some distance and offset at a predetermined angle. Some of the neutrons emitted by the source will have a single elastic interaction with a nucleus in the scatter target and be directed towards the detector. In this case, it is possible to calculate the neutron's remaining energy. Knoll (2010) provides an equation to determine the energy of the recoil nucleus in the laboratory system, E_R, given the initial energy of the source neutron in the laboratory system, E_n, the angle of scatter in the center

of mass coordinate system, Θ, the mass of the scatter nucleus, m_s, and the mass of the neutron, m_n:

.

$$E_R = \frac{2m_s m_n}{(m_s+m_n)^2}(1-\cos\Theta)E_n. \quad (5.1)$$

Assuming a completely elastic scatter, the energy of the scattered neutron in the laboratory system, E_n', is

$$E_n' = E_n\left[1-\frac{2m_s m_n}{(m_s+m_n)^2}(1-\cos\Theta)\right]. \quad (5.2)$$

Solving for Θ yields

$$\Theta = \cos^{-1}\left[1-\frac{(m_s+m_n)^2}{2m_s m_n}\left(1-\frac{E_n'}{E_n}\right)\right]. \quad (5.3)$$

Using trigonometry to convert the neutron scattering angle from the center of mass coordinate system, Θ, to the laboratory reference system, ψ, gives

$$\tan\psi = \frac{\sin\Theta}{\cos\Theta+\frac{m_n}{m_s}}. \quad (5.4)$$

Substituting Eq. 5.3 for Θ, applying trigonometric identities, and solving for ψ yields an equation that provides the appropriate scatter angle in the laboratory system as a function of E_n', E_n, m_n, and m_s, all of which should be known by the user:

$$\psi = \tan^{-1}\left\{\frac{\sqrt{1-\left[1-\frac{(m_S+m_n)^2}{2m_S m_n}\left(1-\frac{E'_{\mathrm{n}}}{E_{\mathrm{n}}}\right)\right]^2}}{1-\frac{(m_S+m_n)^2}{2m_S m_n}\left(1-\frac{E'_{\mathrm{n}}}{E_{\mathrm{n}}}\right)+\frac{m_n}{m_S}}\right\}. \quad (5.5)$$

It should be noted that in this case, the arctangent must be taken between 0 and π radians instead of the traditional –π/2 and π/2 radians. This allows for proper accounting of neutron backscatter. Table 5.1 employs Eq. 5.5 to provide various examples of the necessary scatter angle required to reduce a D-T neutron to one of several final energies in the laboratory system.

Similarly, given the initial neutron energy and by using conservation of kinetic energy and momentum in the laboratory reference system, the final energy of a neutron undergoing a single elastic scatter off a known nucleus at a specific angle can be determined:

$$E'_{\mathrm{n}} = \frac{E_{\mathrm{n}}}{(m_s+m_n)^2}\left[m_n^2 cos(2\psi) + 2m_n cos\psi\sqrt{m_s^2 - m_n^2 sin^2\psi} + m_s^2\right]. \quad (5.6)$$

For reference, Table 5.2 provides the final energy of a D-T neutron after a single elastic scatter off different nuclei at various angles in the laboratory system. As can be seen from the table, the fraction of energy lost by the neutron drops quickly as the mass of the nucleus increases, even with head-on collisions that result in a π radians backscatter. This limits the nuclei that can be employed in this method, particularly if the desire is to lower the D-T neutron energy below 6 MeV.

By taking advantage of the relationship in Eq. 5.5, altering the angle of the detector relative to the scattering target, and utilizing a scatter target of known composition, a fraction of

the neutrons emitted from the monoenergetic fission source can have their energy reliably varied by the user. This effectively creates a source of neutrons whose energies can be altered to fit specific applications. The method provides additional flexibility during active neutron interrogation based on the scatter target's density, thickness, scatter cross sections, and other properties that affect neutron attenuation. All this can be accomplished without the need for large, expensive accelerator systems.

Materials and Methods

The preliminary investigation of the proposed active neutron interrogation system was simplified in order to establish proof of principle and determine if further research was warranted. Although this method could be applied to neutrons from a D-D or D-T source, simulations focused solely on D-T neutrons since they had a higher energy and provided a wider dynamic range for the scattered neutrons. The initial work was performed using Monte Carlo N-Particle (MCNP)[1] simulations. So as to focus on the underlying physics, the geometry of the first simulations was set up in an idealized manner with a point D-T source emitting neutrons of energy 14.1 MeV in a cone whose apex is $\pi/6$ radians and directed towards the scatter target. A neutron energy cutoff of 0.2 MeV was applied and the number of simulated histories insured a statistical uncertainty of less than 5% per histogram bin.

A cylindrical scattering target was placed in the center of a vacuum. The composition, radius, and depth of the cylinder were varied to test different scattering target materials. Table 5.3 contains the materials tested and their respective scatter target properties. The materials were specifically chosen to contain low atomic number nuclei in order to maximize the energy transfer

[1] computer code Monte Carlo N-Particle Transport version 5 (Los Alamos National Laboratory, Los Alamos, NM 87545, 2006).

on a single elastic scatter, therefore providing a wider dynamic energy range for the scatter neutron source. The scattering material was also chosen so as to minimize the number of nuclei with different atomic masses that it contained. For example, pure graphite, which only contains carbon, would be preferable to ethyl alcohol (C_2H_5OH). However, water and methane (CH_4), which contain both hydrogen and either oxygen or carbon, were explored for the possibility of scattering neutrons at two distinct energies. The thickness of each scatter target simulated was roughly equivalent to two D-T neutron mean free paths.

Within the simulations, a sphere was created 3.048 m from the center of the scattering target. Twelve smaller spheres were arranged equally-spaced in a circle, with their centers on the surface of the larger sphere. The smaller spheres had radii of 0.780 m and were placed in such a way that the surfaces defined by the intersection of the small spheres on the larger sphere were located in positions corresponding to 0, $\pi/6$, $\pi/3$, $\pi/2$, 2 $\pi/3$, $5\pi/6$, and π radians (0°, 30°, 60°, 90°, 120°, 180°) around the center of the sphere. The location associated with π radians correlates to a back scatter of a source neutron in the scattering target, and the location at 0 radians corresponds to a source neutron passing straight through the scattering target without any change in direction. The purpose of these surfaces is to count the number of neutrons that cross them using an F1, or surface current, tally. An example of the simulation geometry can be seen in Fig. 5.1 and found in Appendix A.

A more realistic and thorough set of MCNP simulations were also conducted that contained a source and detector arrangement based on layered, cylindrical design from Whetstone and Kearfott (2013). It consisted of 0.50 m of polyethylene shielding surrounding an isotropic 14.1 MeV source and alternating layers of steel and polyethylene surrounding the detector. There is also a cylindrical target for the neutrons to elastically scatter off. It was

composed of either helium or nitrogen, and consisting of the same dimensions as in the previous simulations. The arrangement was simulated in a room filled with air consisting of a concrete floor, roof, and walls. A list of all materials used in the simulation can be found in Table 5.4. The center of both shield arrangements was placed 2.89 m away from the center of the scattering target. The simulated detector was a 0.1270 m thick cylinder, with a radius of 0.0635 m, and consisted of the organic liquid scintillator EJ-309, which is commonly used for fast neutron detection (Kaplan et al., 2013; Dolan, et al., 2014)[2]. The detector and shield are arranged in such a way as to allow for a $5\pi/6$ radian backscatter off the target while still permitting enough space to allow for both source and detector shielding materials. Enough histories were simulated that the statistical uncertainty of each histogram bin within the peaks was below 10%. The simulated geometry can be seen in Fig. 5.2 and found in Appendix A. The focus of this simulation was to obtain a better estimate of the neutron energy spectra in a non-idealized scenario.

Finally, a separate investigation was done in the laboratory using an MP 320 portable D-D neutron generator[3], two plastic containers each holding 3.8 L of distilled water acting as a scattering target, and a boron triflouride (BF_3) proportional neutron counter. The purpose of the experiment was to determine if the neutron scattering effect could be witnessed in real world conditions. Although the equipment used did not provide neutron energy spectra, by looking at gross counts, it was possible to detect a change in the neutron flux near the detector. By separating the generator and detector with a large amount of shielding, this change in counts was more easily detected.

All three components were set on the concrete floor of the laboratory. As seen in Fig. 5.3, the generator and detector were located next to a concrete wall, which acts as a radiation shield

[2] EJ-309 liquid scintillator (Eljen Technology, Sweetwater, TX 79556).

[3] MP 320 D-D neutron generator (Thermo Fisher Scientific Inc., Waltham, MA 02451).

for personnel in the area during generator operation. The wall turned outward at a right angle, providing an opportunity to place the generator and detector on either side, with a straight line distance between them passing through approximately 0.93 m of concrete. After a background measurement, the generator was turned on, and a gross count in the BF_3 detector was obtained. The two water containers were then placed at the vertex of the right angle, 0.38 m from the generator and 0.91 m from the BF_3 proportional counter. Another gross count was obtained with the scattering target present. The laboratory setup with the water containers can be seen in Fig. 5.4.

Results

The results for the initial simulations can be seen in Fig. 5.5 – 5.10. For each scattering target, the neutron energy spectra at various angles are all combined on a single figure to allow ready visualization of the energy differences between peaks. For the ^{4}He spectra, the 0 and $\pi/6$ radians spectra are included. However, at 0 radians, the peak represents neutrons that were unattenuated, and the $\pi/6$ peak is the result of a small angle and small energy transfer elastic scatter. Therefore, these two peaks are magnitudes larger than the other spectra and do not change significantly for the various scatter targets. The 0 and $\pi/6$ radian spectra are omitted from Fig. 5.6 – 5.10 to simplify the figures and improve readability. Table 5.5 summarizes the results. It lists the peaks and provides an estimate of their full width at half maximum (FWHM) for each spectrum, including 0 and $\pi/6$ radians. It is important to note the scatter plots represent histograms with the data points correlating to the high end of each 0.20 MeV bin. As a result, some peak locations will be shifted slightly to the right. For instance, 14.1 MeV neutrons will create a peak at 14.2 MeV.

For each spectrum, a peak can be seen that correlates to the neutron elastic scatter off a nucleus. The ^{9}Be, ^{12}C, CH_4, and H_2O targets each produced multiple peaks at some scatter angles. This is the result of inelastic neutron scatter that excites the ^{9}Be nucleus to the 2.43 MeV energy level, the ^{12}C nucleus to the 4.43 MeV energy level, and the ^{16}O nucleus to the 6.13 and 7.12 MeV energy levels (National Nuclear Data Center, 2014). The remainder of the energy is distributed between the neutron and nucleus as if it were an elastic scatter.

The results of the realistic simulations can be seen in Fig. 5.11. The helium spectrum contained several peaks, including one at 5.6 MeV. Similarly, the nitrogen spectra contained multiple peaks, with one at 10.8 MeV. When compared to what was predicted by Eq. 5.6 and observed in the idealized simulations, the nitrogen peak was found where it was expected and the helium peak was shifted up 0.2 MeV. However, in both spectra, there were other peaks that were not the result of elastic scatter off the target. These were located at 12.4 and 11.2 MeV.

For the laboratory experiment, a BF_3 tube was used to detect moderated neutrons. The energy deposited in the fill gas, which is independent of the initial neutron energy, was determined and the resultant energy spectra were analyzed. The gross neutron counts within the region of interest were determined while the D-D generator was producing neutrons, both with and without the presence of the water jugs, along with a background count rate. The resultant count rates can be found in Table 5.6. The ratio of the count rate when the water was present versus not present is 1.24 ± 0.02.

Discussion

Uncertainty analysis

Before beginning discussion of the results, it is important to have a thorough understanding of the systematic uncertainty associated with using neutron elastic scatter to reliably change the energy of neutrons. For many of the elastic scatter peaks in Table 5.5, the estimated FWHM was greater than 1 MeV. The peaks can most likely be narrowed through careful optimization of the scatter target dimensions in order to reduce self-attenuation and multiple scatter events. However, there are other systematic issues that also contribute to the FWHM. The final neutron energy, E_n', calculated by Eq. 5.6, is a function of the neutron scatter angle, ψ, which is determined by the initial direction of the neutron and the relative locations of the scatter target and detector. Because the scatter target and detector are not discrete points, but rather consist of a non-negligible volume, the actual scatter angle can vary depending on the location of the interactions within both the scatter target and detector. This ultimately results in single elastic scatter neutrons with a range of energies being detected and contributes to the broadening of the peaks.

A more thorough analysis, similar to the work done on Compton cameras (Ordonez and Chang, 1999), is beyond the scope of this work. However, if it is assumed that the source neutrons originate from a single point and both the scatter target and detector are cylinders, then it is possible to calculate the range in energies of single elastic scatter neutrons that interact in the detector. As seen in Fig. 5.12, a relative coordinate system that describes the points at the edges of the scatter and detector volumes can be determined. In this arrangement, the center of the scatter cylinder, point 6, is located at the origin with both its axis and the neutron point source on the Z axis. The axis of the detector is aligned with the center of the scatter target, forming the

desired scatter angle ψ. The distance between the source and the center of the scatter target is D_1 and the distance between the center of the scatter target and the center of the detector is D_2. The length and radius of the scatter target and detector are L_1, r_1, L_2, and r_2, respectively. Provided these dimensions, which should be fairly simple to determine, and through application of basic trigonometry, the relative coordinates of possible interaction points on the edge of the scatter target and detector can be calculated. The coordinates of points 1 – 19 in Fig. 5.12 can be seen in Table 5.7.

A good first order approximation of the systematic uncertainty associated with the neutron elastic scatter method can be derived using the coordinates found in Table 5.7. The interaction points along the edges of the scatter target and detector will provide the largest deviation in scatter angle when compared to ψ. For instance, a neutron that undergoes a single elastic scatter at point 2 and then interacts in the detector at point 11 will have a different scatter angle than a neutron that scatters at point 2 and interacts in the detector at point 13. The actual scatter angle, ψ_A, of a neutron originating from a point source, scattering somewhere in the scatter target, and being detected somewhere in the detector, can be calculated using the law of cosines:

$$\psi_A = \pi - cos^{-1}\left(\frac{d_1^2+d_2^2-d_0^2}{2d_1d_2}\right). \tag{5.7}$$

As seen in Fig. 5.13, the variables d_0, d_1, and d_2 constitute the three sides of the triangle containing the angle $\pi - \psi_A$, where d_1 is the distance between the point source, located at coordinates (x_0, y_0, z_0), and the interaction in the scatter target, located at (x_1, y_1, z_1), calculated:

$$d_1 = \sqrt{(x_1 - x_0)^2 + (y_1 - y_0)^2 + (z_1 - z_0)^2}. \quad (5.8)$$

Similarly, d_2 is the distance from the scatter location to the point of interaction in the detector, and d_0 is the distance from the point source to the neutron interaction in the detector.

By computing ψ_A for interactions at the edges of the scatter target and detector, the theoretical upper and lower bounds of potential single elastic scatter angles can be calculated. These values can then be substituted into Eq. 5.6 to determine the span of E_n'. Using this method, an estimate of the range of scatter angles and neutron energies in the idealized simulations was made. For simplicity's sake, only the simulation containing a water scatter target was analyzed. Furthermore, the simulated ideal hemisphere detectors were treated as cylinders with their centers 3.048 m from the center of the scatter target, radii of 0.780 m, and lengths approximated as 0.390 m. No other simulation dimensions needed to be altered for the calculation. The range of neutron scatter angles and energies can be found in Table 5.8. Although the realistic simulations were only executed for a single scatter angle of 5π/6 radians, by using the source, water scatter target, and detector dimensions, a similar estimate of the variation in scatter angle and neutron energy was compiled in Table 5.9.

Comparison of Tables 5.8 and 5.9, as well as analysis of the neutron elastic scatter method, demonstrates several ways to minimize systematic uncertainty. Reducing L_1, r_1, L_2, and r_2 creates smaller scatter target and detector volumes for the neutrons to interact in. Similarly, increasing D_1 and D_2 minimizes the solid angle defined by the scatter target and detector, respectively. Although these approaches reduce the range of potential scatter angles, they also decrease the fraction of neutrons that undergo a single elastic scatter in the target and interact in

the detector. This inherent tradeoff between efficiency and uncertainty must be considered when implementing the system.

Simulations

In the idealized elastic scatter simulations, as seen in Fig. 5.5 – 5.10 and Table 5.5, there are easily identifiable peaks that correlate to the expected energy of neutrons that underwent a single elastic scatter event off a nucleus in the scatter target. Even after accounting for the neutron energy resolution in the simulations, the peak locations were not always present where they were predicted to be by Eq. 5.6. However, the calculated peak location almost always fell within the FWHM of the simulated peaks. The wide range of possible scatter angles seen in Table 5.7 explains the large FWHM values of the elastic scatter peaks and the shift of those peaks away from their expected values. In Table 5.5, the three scatter angles with the largest FWHM and greatest difference between the expected and observed neutron energies was consistently $\pi/3$, $\pi/2$, and $2\pi/3$ radians. Due to the geometry, those three arrangements also have the largest range in potential scatter angles in the idealized simulations, leading to less discrete peaks. Changing dimensions of the scatter target and detectors could help reduce these issues.

Another factor to consider is the composition of the scatter target. As seen in Eq. 5.6 and Table 5.2, a smaller scatter target mass gives a wider range of potential neutron energies because more energy can be transferred in a single elastic collision. On the other hand, a larger scatter target mass allows for more precise adjustments. A relatively small change in scatter angle provides a smaller change in neutron energy when compared to a less massive scatter target.

For CH_4 and H_2O, no peaks were observed at energies that would correlate to scatter of a ^1H nucleus. There were not enough single elastic scatters off hydrogen to create a peak that was observable above the multiple scatter background. This is unfortunate, because hydrogen gives

the widest range of possible neutron scatter energies. Unexpectedly, there were several instances when peaks at multiple energies were seen in the scattered neutron spectra. These occurred for ^{9}Be, ^{12}C, CH_4, and H_2O. They were all the result of neutron inelastic scatter off ^{9}Be, ^{12}C, and ^{16}O. The peaks were not observed at all scatter angles, and in most cases, were significantly smaller than the elastic scatter peak. The inelastic scatter and the associated characteristic gamma rays could present a problem, increasing gamma ray background and possibly obscuring the signal when attempting to identify materials based on their characteristic photons. However, the inelastic scatter peaks may also provide an opportunity to further reduce the energy of the neutron beyond what is possible with a single elastic scatter, albeit at a potentially lower intensity.

In general, it would appear that the backscatter peaks at $5\pi/6$ and π radians were narrower compared to other scatter angles. This is a combination of the smaller range of potential scatter angles compared to $\pi/3, \pi/2,$ and $2\pi/3$ radians and the neutrons having to pass through less scattering target material, which provided fewer opportunities to undergo a second, glancing collision that would transfer a small fraction of energy away from the neutron.

In the realistic MCNP simulations, the systematic uncertainty was considerably reduced when compared to earlier arrangements. However, the resulting neutron spectra were significantly more complicated. Even with idealized detectors that identified every incident neutron and had a relatively high degree of energy resolution, the spectra suffered when other materials were introduced. The peaks that did not coincide with either helium or nitrogen were the result of a $5\pi/6$ radian single elastic scatter off ^{16}O and ^{28}Si. These were two of the most prominent nuclides in the concrete, which comprised the floor, ceiling, and walls of the

simulated room. During real world deployment, it is expected that similar peaks from nuclides in the surrounding environement would also be present.

Furthermore, the underlying spectral noise is the result of the large, multiply-scattered neutron background. Not all neutrons that emerge from the source shield opening will undergo an isolated single elastic scatter and enter the detector. Some will interact once or more in the room before reaching the detector. Additionally, other emitted neutrons will pass through the source shield, possibly undergo one or more interactions, and find their way to the detector. The consequence is a large neutron background partially obscuring the elastic scatter neutron peaks. When combined with additional peaks from surrounding media, this background complicates the resultant spectra and any application using this method.

Although not perfect, the simulations support the hypothesis that, at least theoretically, it is possible to reliably reduce the energy of a fraction of neutrons from a monoenergetic source. Provided the user knows the mass of the nuclei in the scatter target and the initial energy of the neutrons, the angle of scatter required for a desired final neutron energy can be determined using Eq. 5.5.

Laboratory experiment

Due to the unlikely nature of a fast neutron interacting in the detector during the laboratory experiment, the BF_3 tube was surrounded by polyethylene to slow the neutrons before they entered the gas detector. This resulted in a complete lack of knowledge of the incoming neutron energy. Although it is promising to observe that the presence of water increased the neutron count rate, without any way to determine the incident neutron energy, it is impossible to know how many of those neutrons underwent a single elastic scatter in the water and how many had multiple interactions. Because the detector was set up at $\pi/2$ radians, any single elastic

scatter neutrons must be from scatter off oxygen. Due to the masses of the two particles, ^{1}H cannot elastically scatter neutrons at that angle.

To confirm the proposed method of varying neutron energies using different scattering target materials and angles, determination of the scattered neutron energies is required. This, unfortunately, cannot be accomplished using gross counts. In future experiments, a different detector is needed that can provide sufficient neutron energy resolution ranging from a fraction of an MeV to tens of MeV in order to identify single elastic scatter neutrons from a monoenergetic source.

Applications and future work

If the method can be refined and the background neutrons that interact in the environment can be eliminated, the single elastic scatter peaks could be used as a source of quasi-monoenergetic neutrons. This is not the only way to create neutrons at specific energies, but by using a compact D-D or D-T source, the system is considerably smaller and cheaper than the particle accelerators typically used. There are several applications that the single elastic scatter system could potentially be used with.

Multiple PFNA, neutron elastic scatter, or neutron transmission measurements could be conducted quickly by changing the scatter target or angle to align the new neutron energy with peaks and valleys in the neutron attenuation cross sections for various isotopes of interest. Observation of the change in the number of neutrons passing through the interrogation target at several carefully chosen energies could provide useful information about its composition. Although the application is outside the scope of this work, neutron imaging could also benefit from the flexibility of a variable energy neutron source. Depending on the density and thickness of the interrogation target, the user may want to lower the neutron energy to improve image

quality. Neutron activation measurements could also be improved by aligning the scattered neutron energy with cross section resonances of interest, increasing the likelihood of interaction and requiring less flux.

Application of the elastic scatter method to neutron transmission and imaging is only feasible if the neutron detection is improved significantly. As seen in the realistic simulations, even with shielding, the detector is still exposed to a large number of neutrons at all energies. If the detector could determine incident neutron energy, as opposed to gross counts, many of the neutrons could be neglected due to having the wrong energy. Instead focus could be paid only to the behavior of the elastic scatter peak in the neutron energy spectrum. Unfortunately, the neutron background in the simulations obscures much of these peaks. Even with ideal energy resolution, the neutrons that interact in the environment must be further discriminated. One way to accomplish this is to use neutron time of flight. If the neutron generator can be pulsed at a significantly high frequency, or if the generator has associated particle imaging, then the neutron time of flight can be determined when the neutron interacts in the detector (Chichester et al., 2007). If the time of flight does not match the expected flight time for a neutron that undergoes a single elastic scatter in the target, then the neutron is neglected. This also provides a method for confirming the neutron energy. Future work will focus on integrating neutron energy and time-of-flight information in to the process.

Conclusions

The neutron elastic scatter method provides added flexibility to monoenergetic D-D and D-T sources and is an alternative to the larger, costlier, and more complicated particle accelerators that are traditionally required to obtain neutrons of specific energies. Although the

method still needs refinement, implementing neutron energy and time-of-flight discrimination should significantly improve the neutron elastic scatter signal. With improvements, the cost, size, portability, and ease of use of the novel, variable energy neutron system may make it a viable accelerator substitute.

Figures

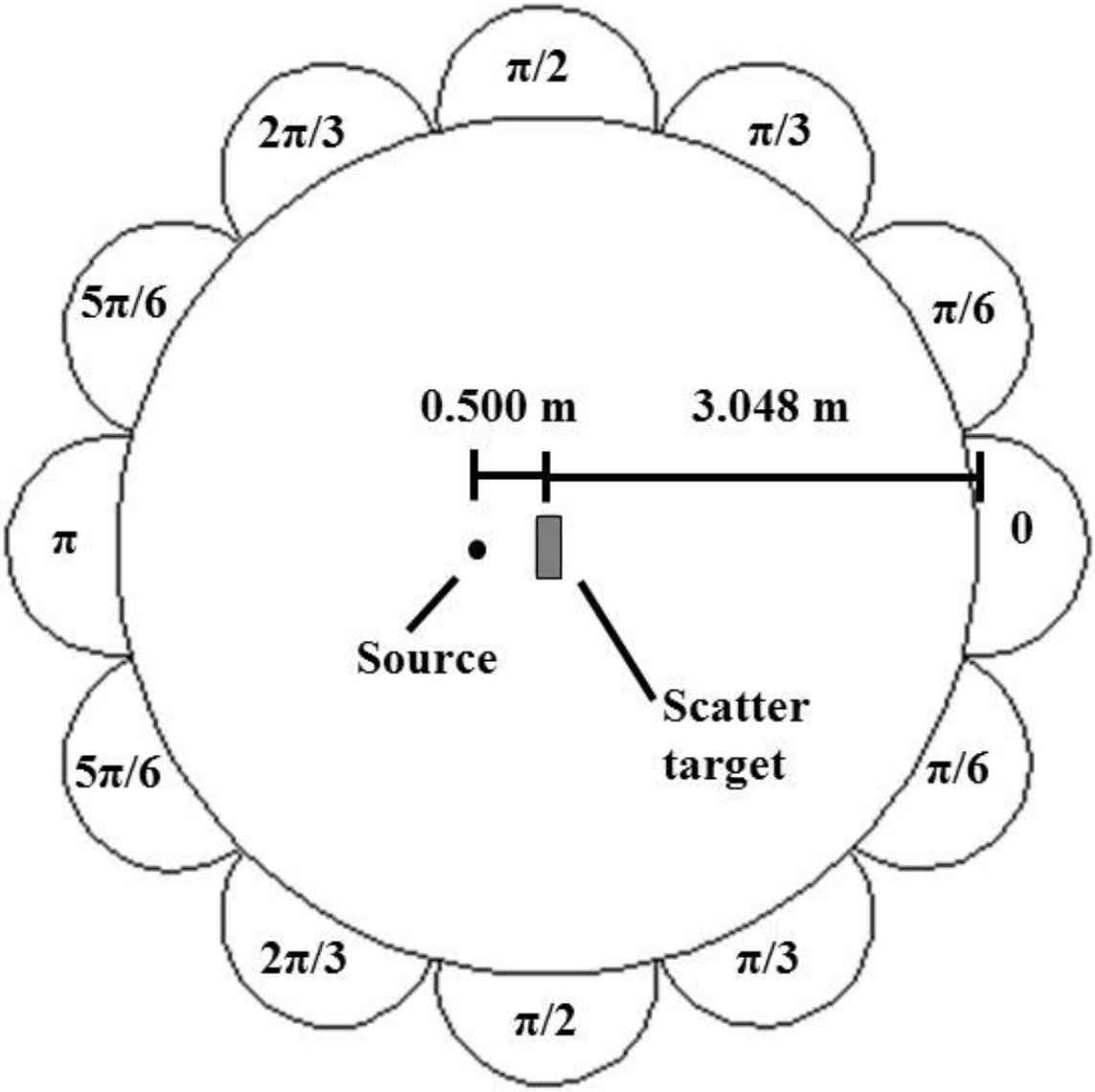

Fig. 5.1: A simulated source and scatter target in a vacuum surrounded by idealized detectors placed at regular intervals to determine the neutron scatter spectra at various solid angles (radians).

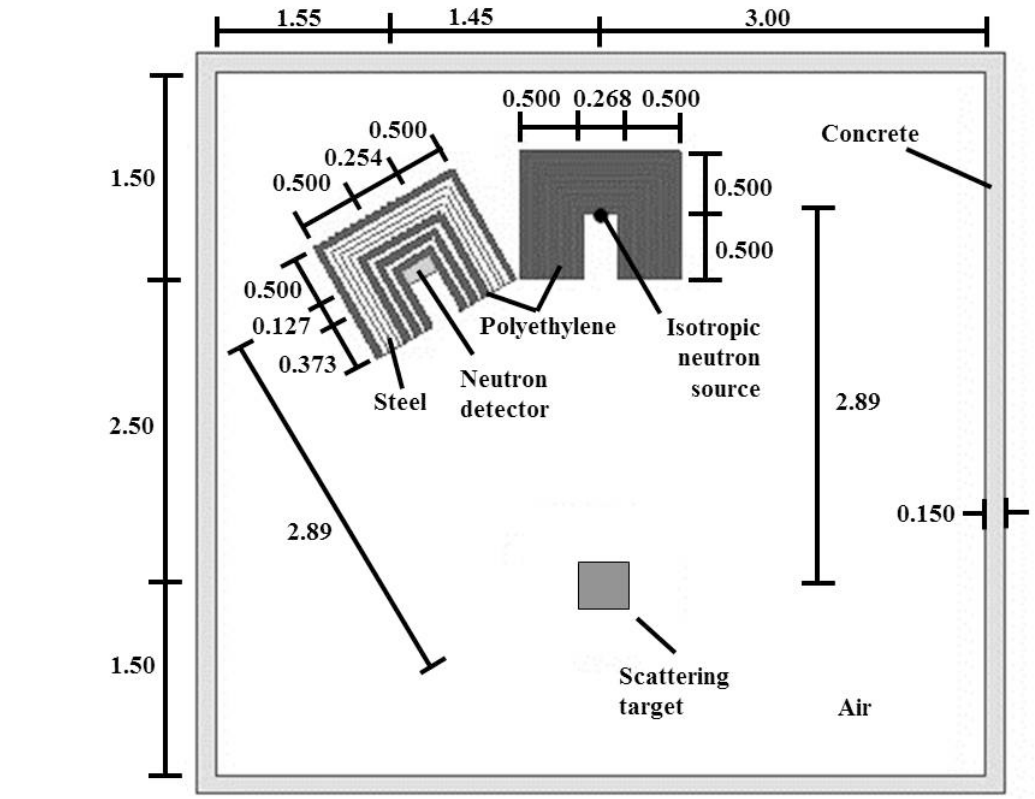

a)

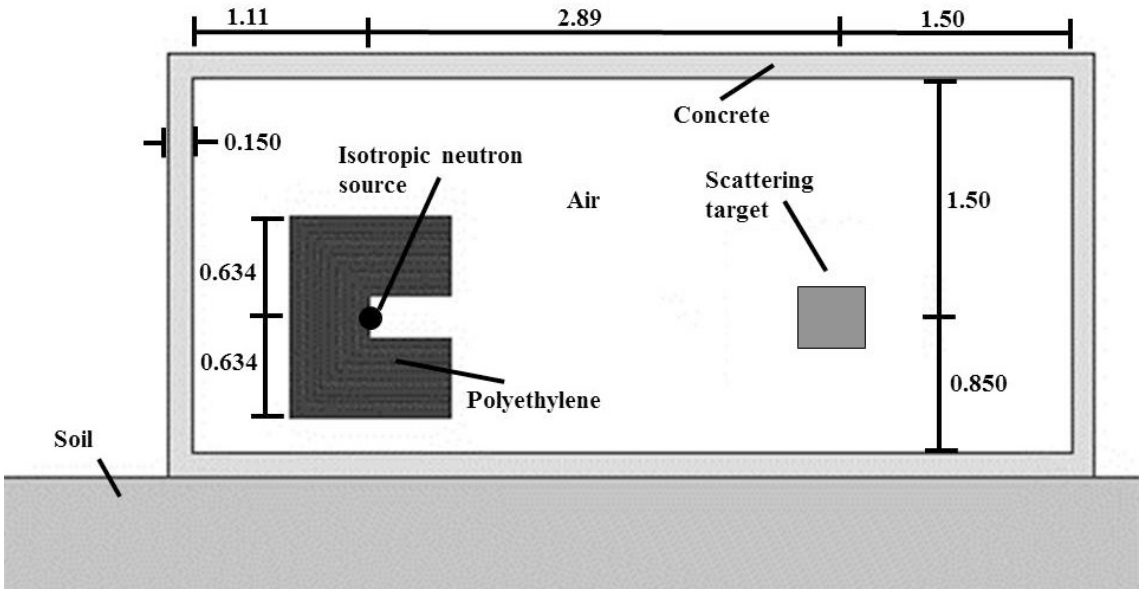

b)

Fig. 5.2: A a) top-down and b) side view of the realistic simulations performed using MCNP. All lengths are in meters.

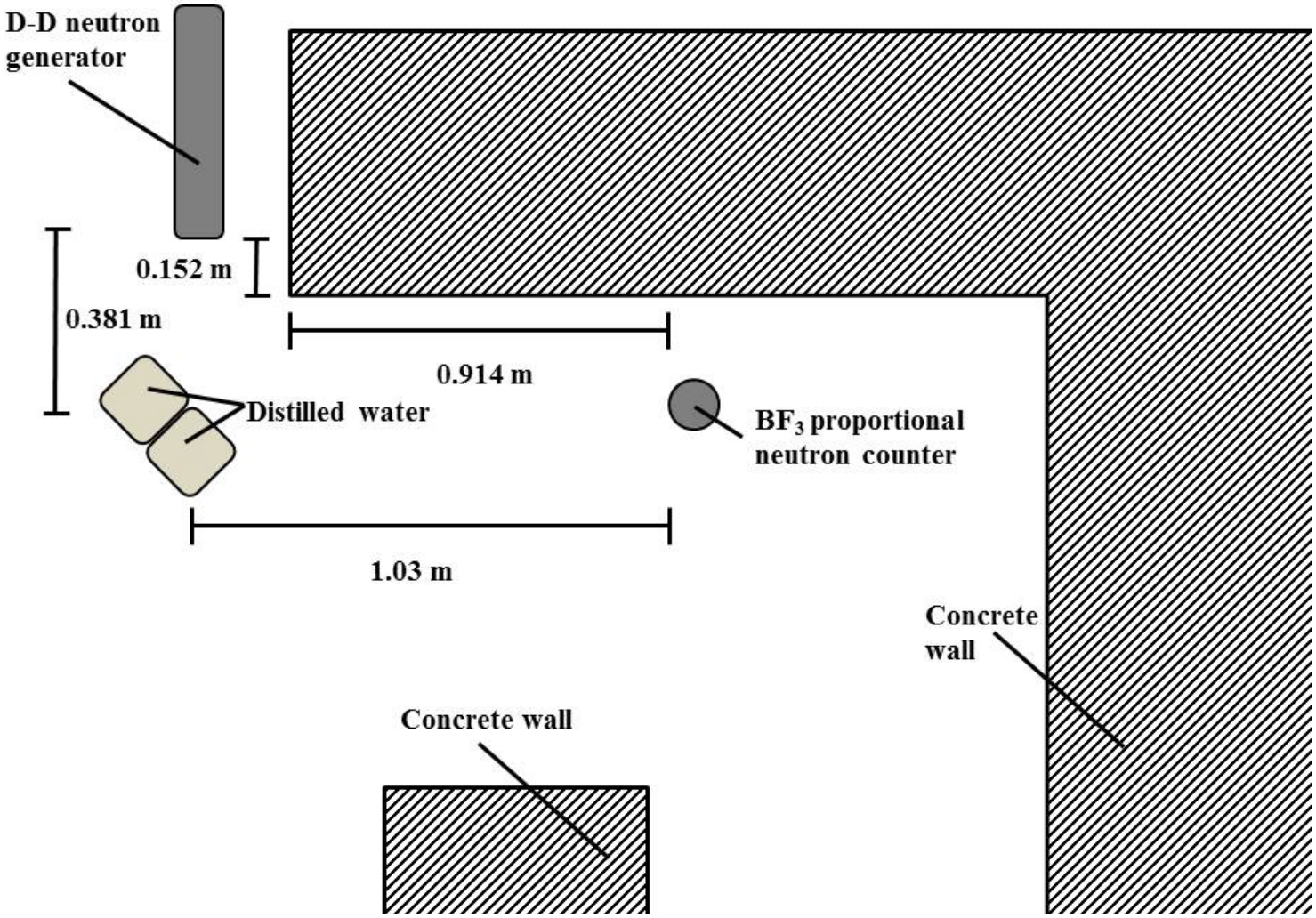

Fig. 5.3: A top-down view of the layout of the neutron scatter experiment performed in the Neutron Science Laboratory at the University of Michigan. The generator created neutrons at 2.5 MeV.

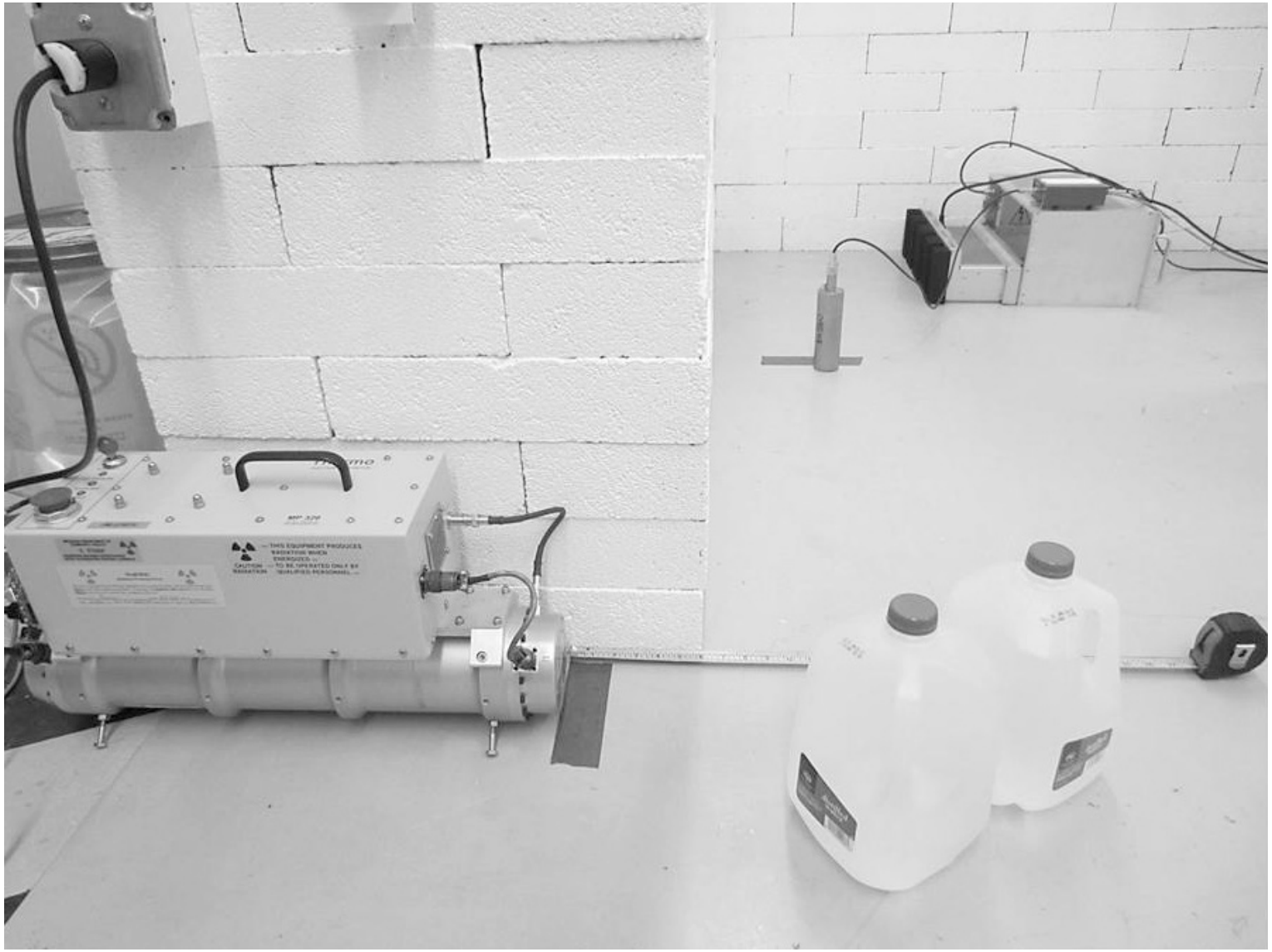

Fig. 5.4: A photograph of the laboratory experiment performed with the D-D neutron generator to the left, scatter target to the right, and BF_3 detector in the back.

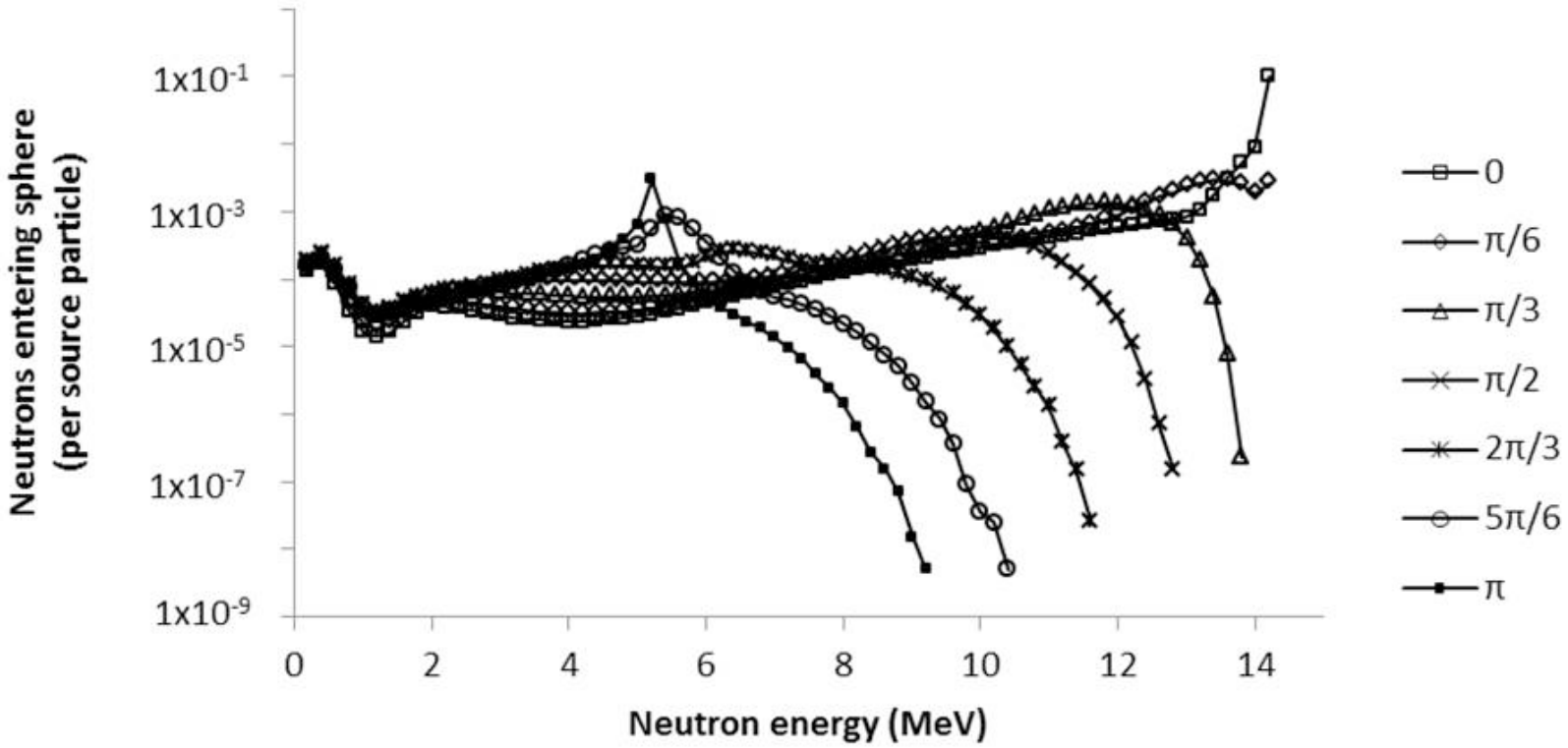

Fig. 5.5: The simulated neutron energy spectra at various angles for a ^{4}He scatter target.

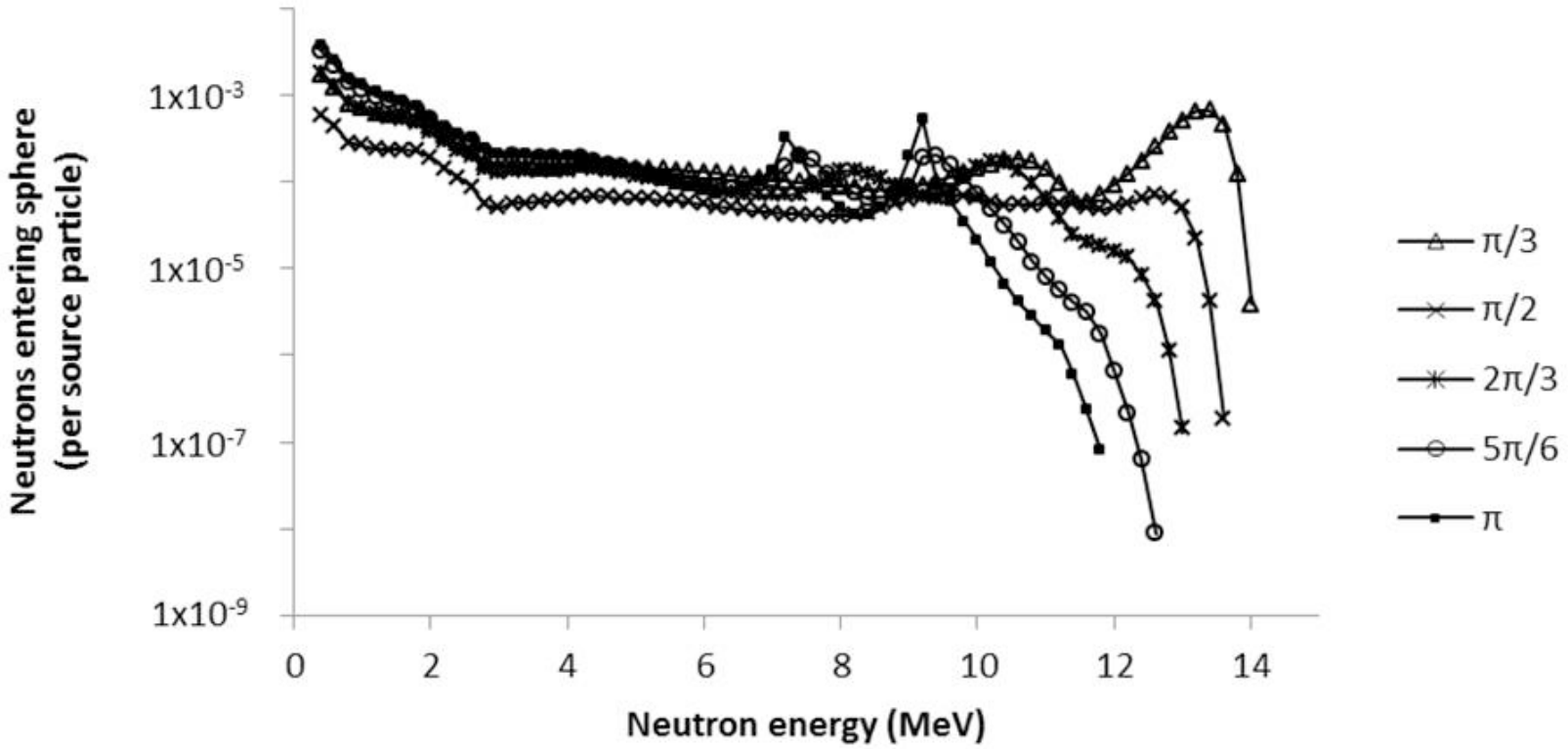

Fig. 5.6: The simulated neutron energy spectra at various angles for a ^{9}Be scatter target.

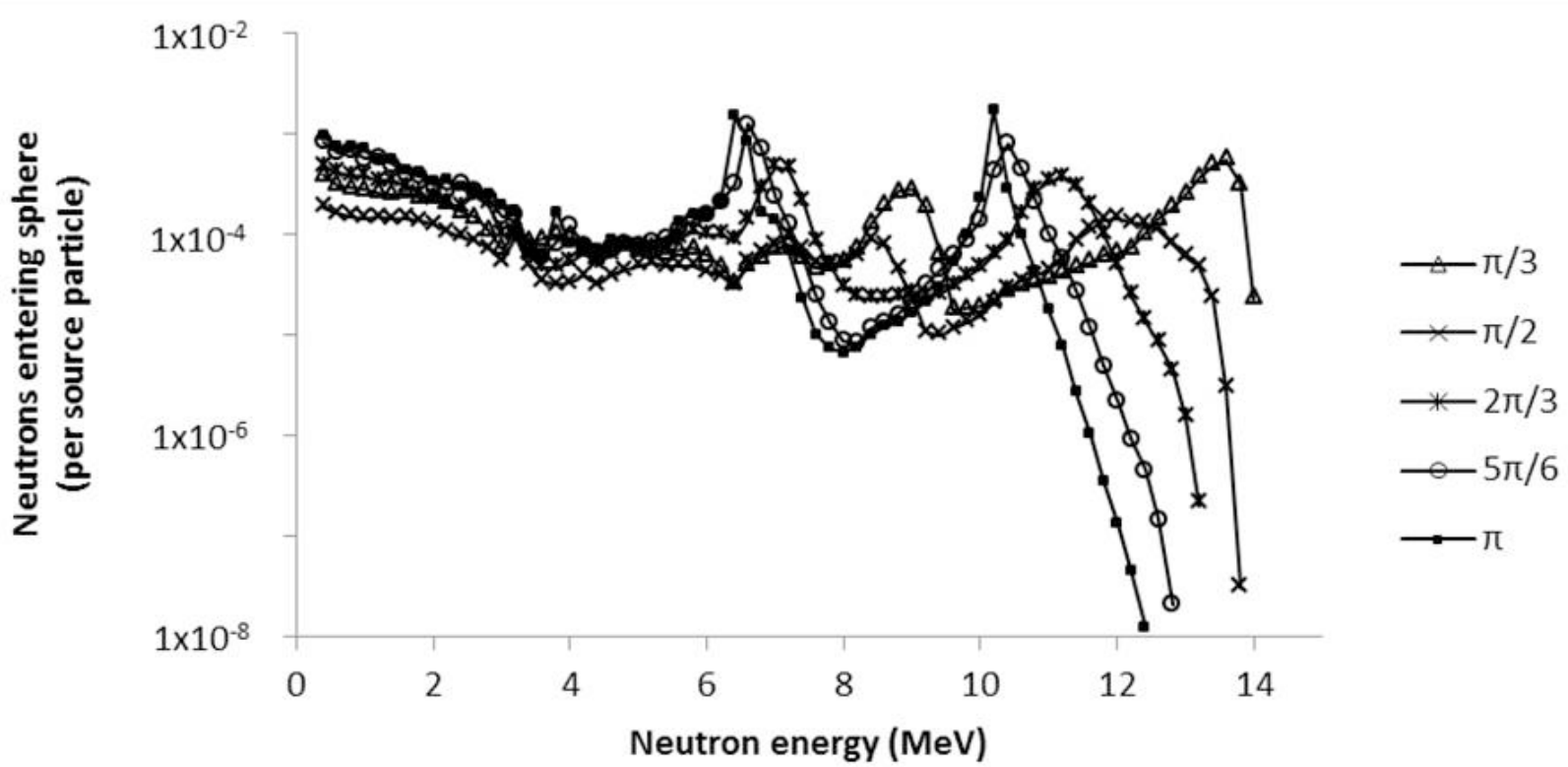

Fig. 5.7: The simulated neutron energy spectra at various angles for a ^{12}C scatter target.

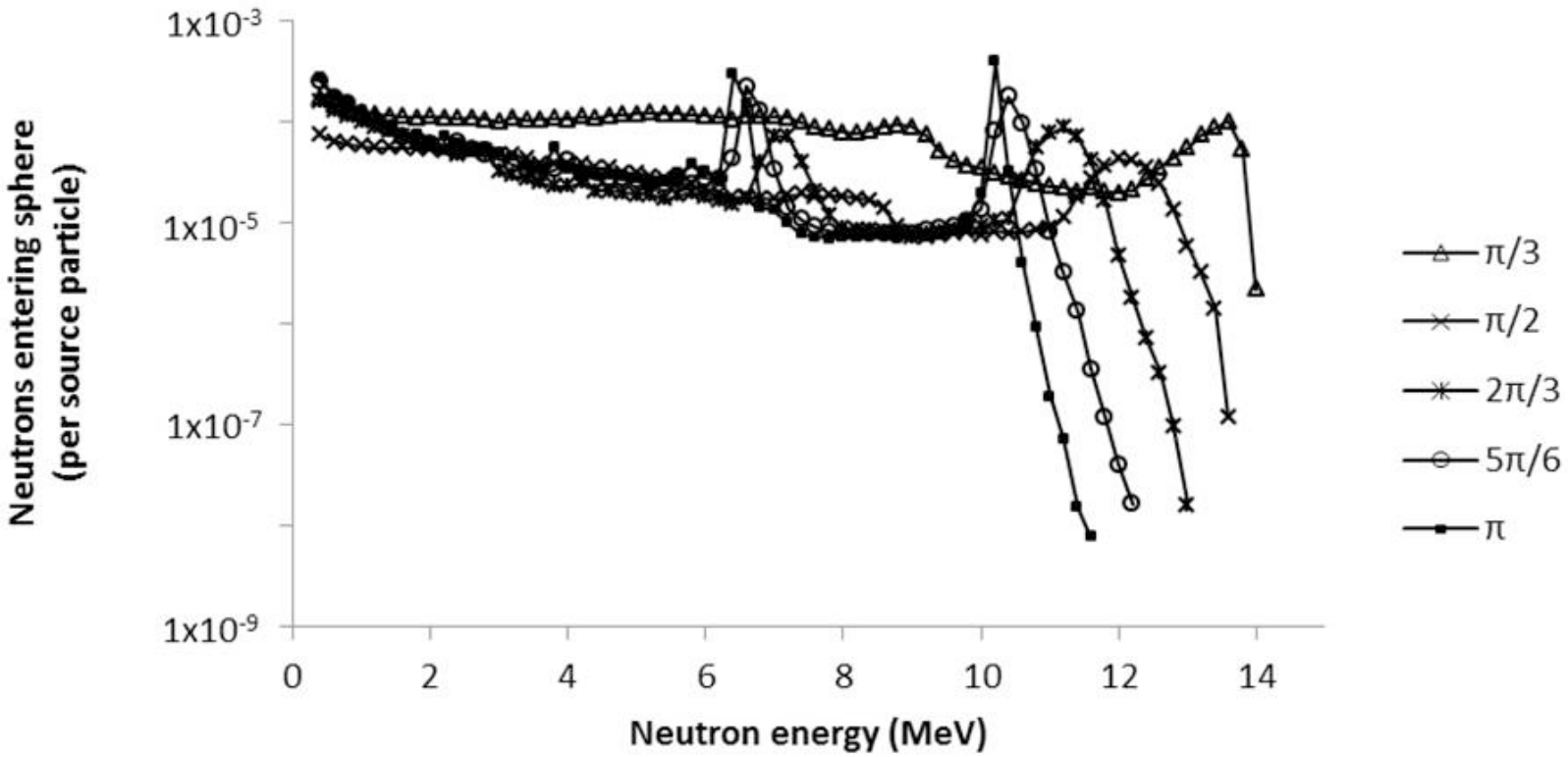

Fig. 5.8: The simulated neutron energy spectra at various angles for a CH_4 scatter target.

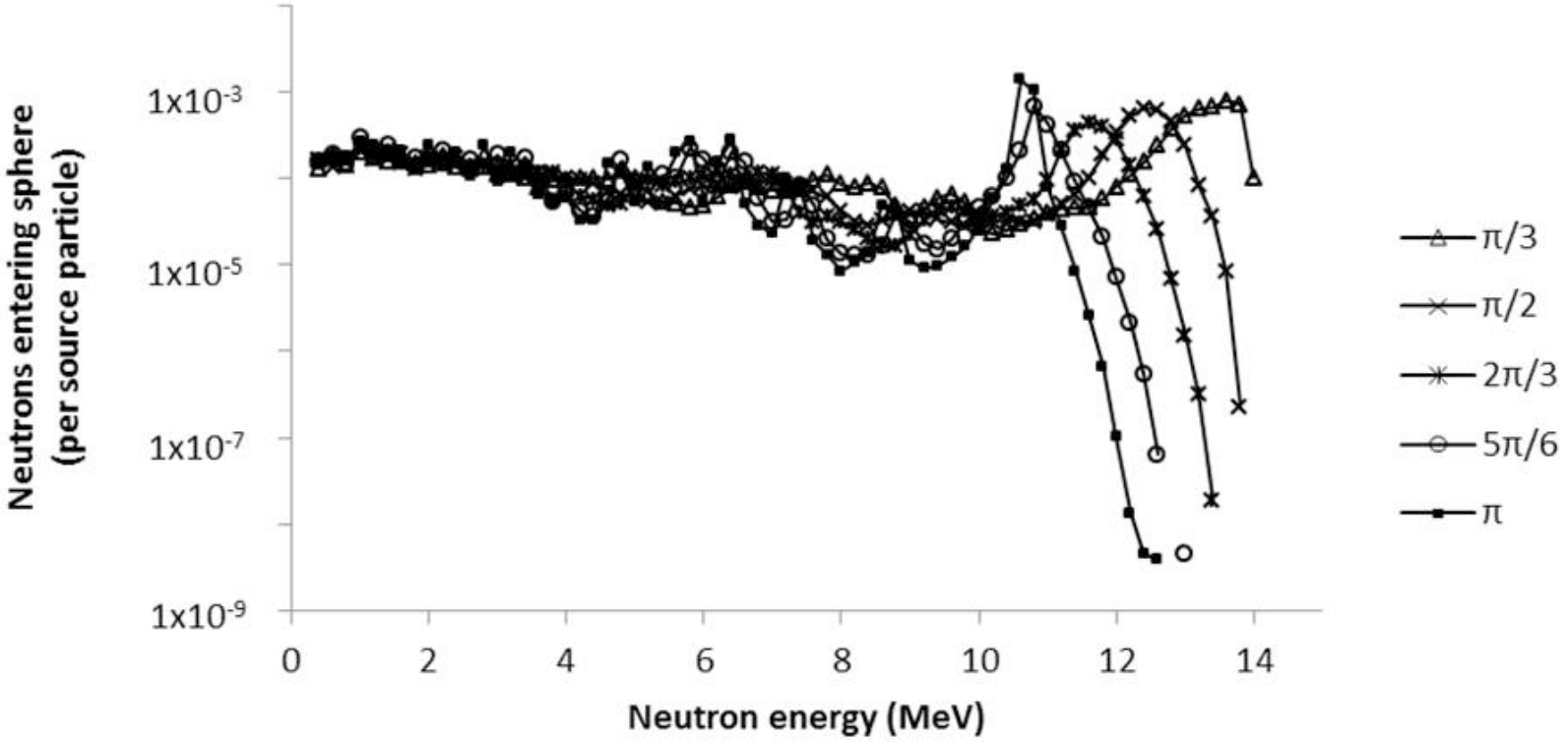

Fig. 5.9: The simulated neutron energy spectra at various angles for a ^{14}N scatter target.

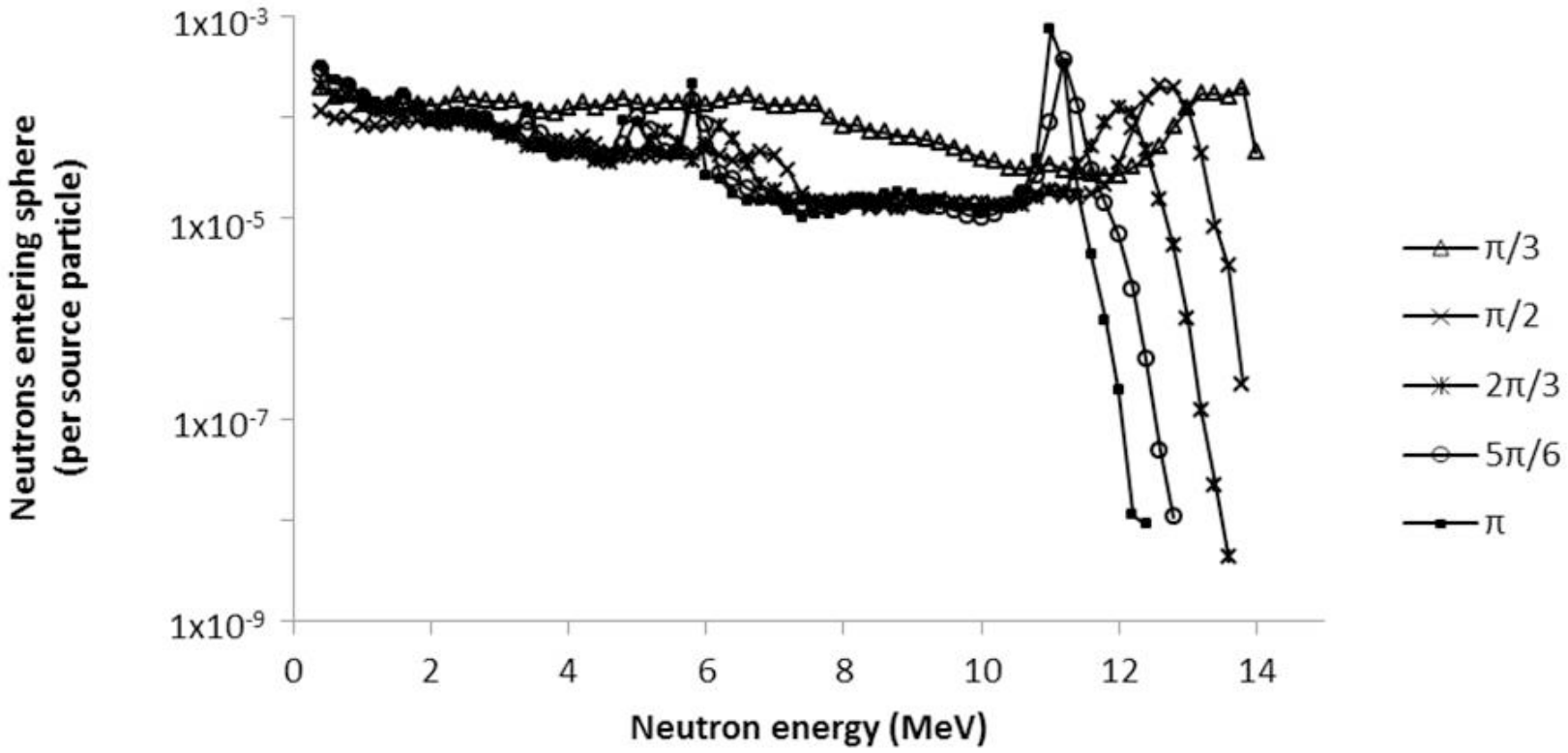

Fig. 5.10: The simulated neutron energy spectra at various angles for an H_2O scatter target.

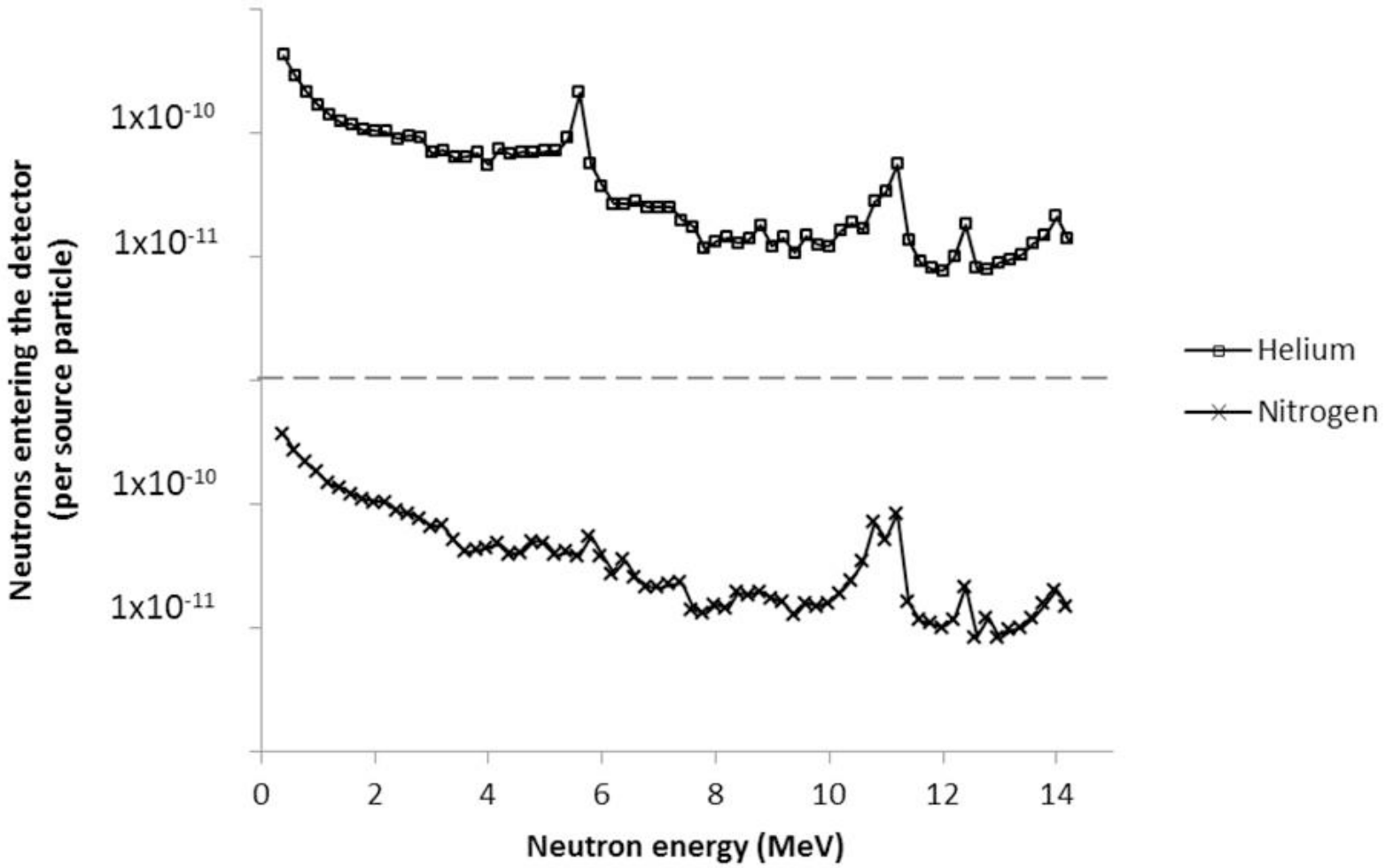

Fig. 5.11: The simulated neutron energy spectra for the realistic scatter arrangement at 5π/6 radians with helium and nitrogen scatter targets.

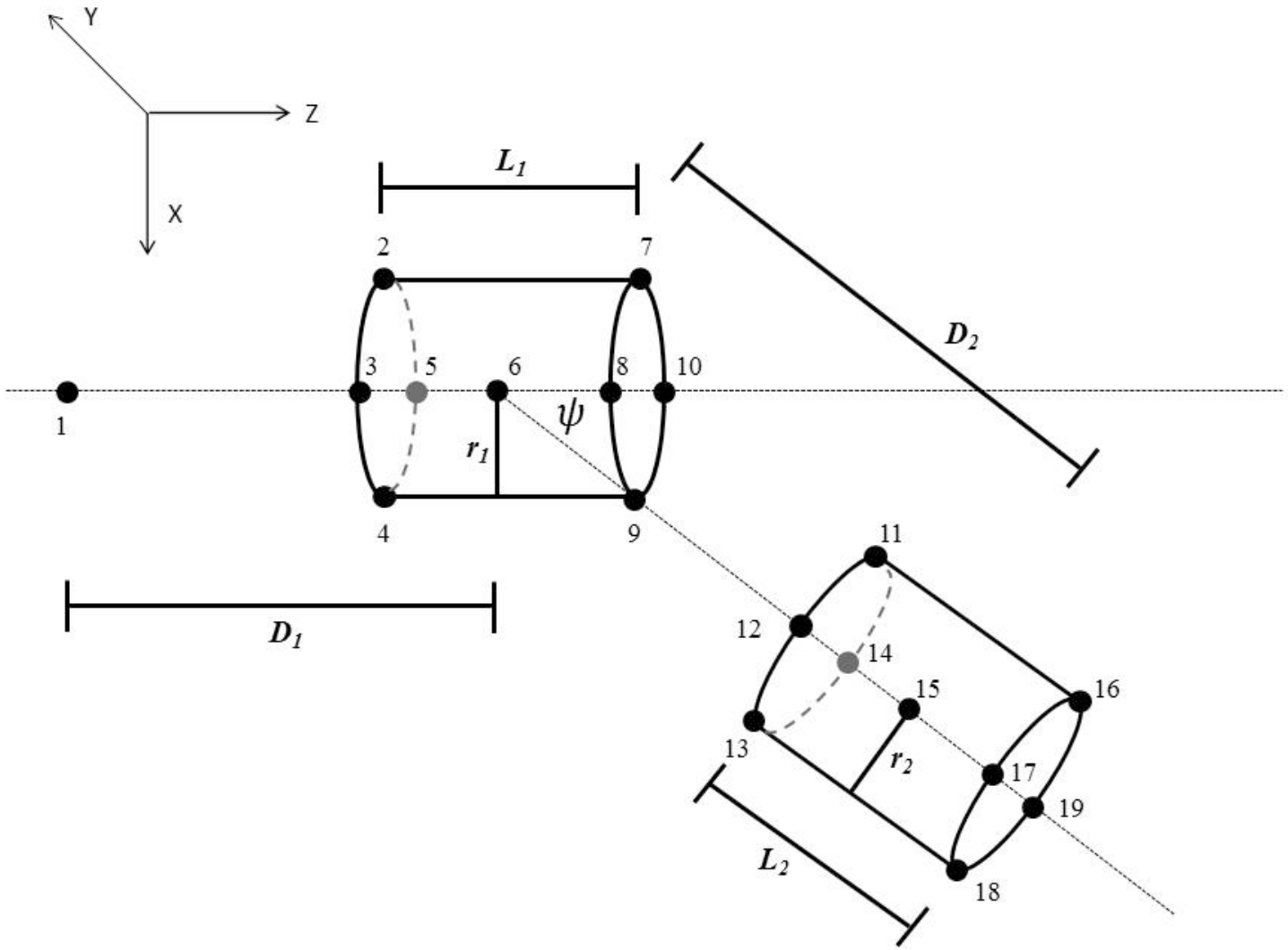

Fig. 5.12: A diagram of the various dimensions and point locations on the source, scatter target, and detector. These relative locations can be used to estimate the range in scatter angles for a given arrangement.

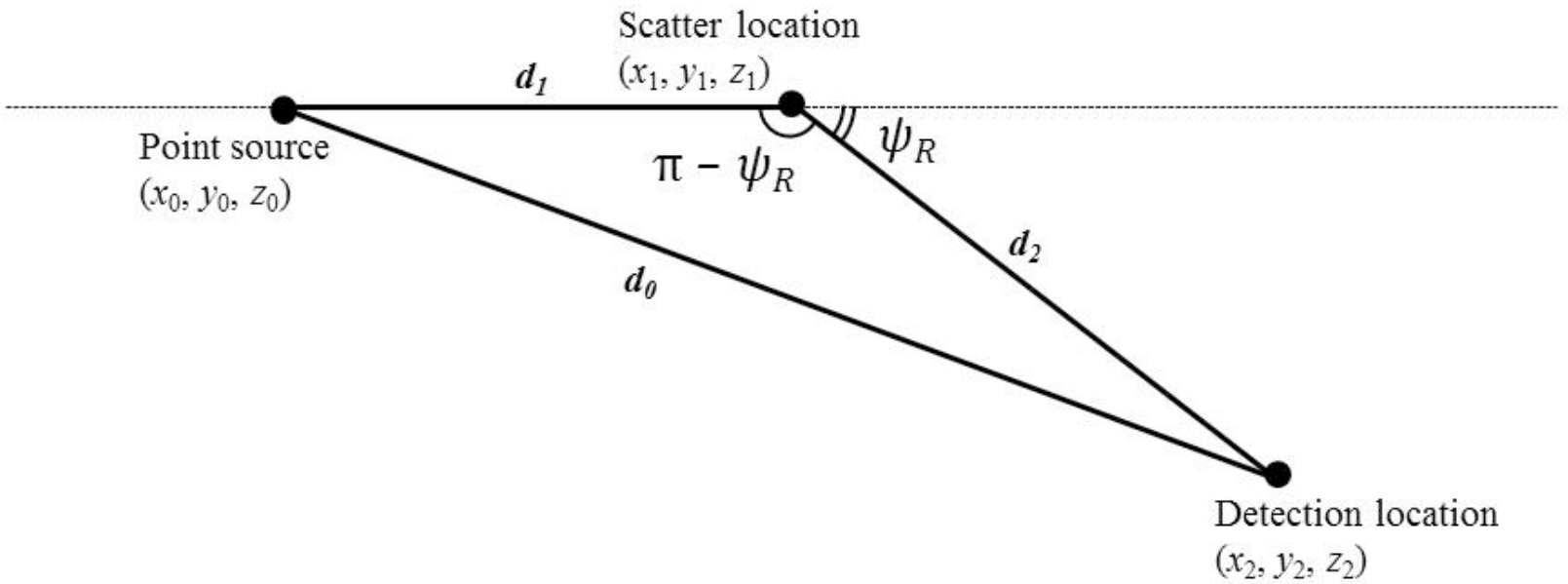

Fig. 5.13: A diagram demonstrating the application of the law of cosines to determine neutron scatter angle.

Tables

Table 5.1: Examples, for various nuclei, of the calculated single elastic scatter angle required, ψ, to achieve a given final neutron energy. The incident neutron has an energy of 14.1 MeV and the angles are provided in the laboratory system of reference.

Necessary D-T scatter angle (degrees) for a given neutron energy (MeV)							
Final neutron energy (MeV)	Nucleus	^{1}H	^{4}He	^{9}Be	^{12}C	^{14}N	^{16}O
	Mass (amu)	1.0078	4.0026	9.0121	12.0000	14.0031	15.9949
12.0		22.7	46.9	73.6	87.5	96.7	106
10.0		32.6	70.7	122			
8.00		41.1	95.7				
6.00		49.3	131				
4.00		57.8					
2.00		67.8					

Table 5.2: The calculated final energies of a 14.1 MeV neutron undergoing single elastic scatter off various nuclei, in the laboratory system, through a range of angles, ψ.

D-T scatter neutron energy in laboratory system (MeV)								
Scatter angle (radians)	Scatter angle (degrees)	Nucleus	^{1}H	^{4}He	^{9}Be	^{12}C	^{14}N	^{16}O
0	0		14.10	14.10	14.10	14.10	14.10	14.10
π/12	15		13.15	13.86	13.99	14.02	14.03	14.04
π/6	30		10.57	13.18	13.68	13.79	13.83	13.86
π/4	45		7.04	12.15	13.20	13.42	13.52	13.59
π/3	60		3.52	10.92	12.60	12.96	13.12	13.24
5π/12	75		0.93	9.64	11.94	12.45	12.67	12.84
π/2	90			8.42	11.26	11.91	12.21	12.43
7π/12	105			7.36	10.62	11.40	11.76	12.03
2π/3	120			6.50	10.06	10.95	11.36	11.67
3π/4	135			5.84	9.60	10.57	11.02	11.37
5π/6	150			5.39	9.27	10.30	10.77	11.14
11π/12	165			5.12	9.06	10.12	10.62	11.00
π	180			5.03	8.99	10.07	10.57	10.95

Table 5.3: The properties of the scatter targets used in the idealized MCNP simulations.

Scatter target	Density (kg m^{-3})	Thickness (m)	Radius (m)
^{4}He	143	0.88	0.30
^{9}Be	1850	0.11	0.20
^{12}C	2250	0.14	0.20
CH_4	416	0.32	0.30
^{14}N	808	0.37	0.20
H_2O	1000	0.20	0.20

Table 5.4: Description of materials simulated for the realistic MCNP scenario.

Material	Elemental makeup (relative abundance)	Elemental makeup (weight %)	Density (kg m^{-3})
Air (McConn et al., 2011)		C (0.001), N (0.755), O (0.231), Ar (0.013)	1.2
Polyethylene	H (4), C (2)		940
Water	H (2), O (1)		1,000
Steel		C (0.2), Fe (99.8)	7,860
EJ-309	H(5), C(4)		960
Helium	He(1)		143
Nitrogen	N(1)		810
Soil (Eckerman and Ryman, 1993)	H (0.2938), C (0.0187), O (0.5045), Al (0.0259), Si (0.1354), K (0.0143), Fe (0.0027)		1,750
Concrete (McConn et al., 2011)		H (0.56), O (49.81), Na (1.71), Mg (0.26), Al (4.57), Si (31.51), S (0.13), K (1.92), Ca (8.29), Fe (1.24)	2,080

Table 5.5: Estimated peak information for the various scatter targets in the idealized simulations. The energy resolution in the simulation was 0.2 MeV.

Scatter angle (radians)	^{4}He				^{9}Be							
	Peak 1				Peak 1				Peak 2			
	Maximum value (neutrons per source particle)	Maximum Energy (MeV)	Expected Energy (MeV)	FWHM (MeV)	Maximum value (neutrons per source particle)	Maximum Energy (MeV)	Expected Energy (MeV)	FWHM (MeV)	Maximum value (neutrons per source particle)	Maximum Energy (MeV)	Expected Energy (MeV)	FWHM (MeV)
0	1.02×10^{-1}	14.2	14.10	0.4	1.06×10^{-1}	14.2	14.10	0.4				
π/6	2.88×10^{-3}	13.4	13.18	1.5	6.17×10^{-3}	14.0	13.68	1.0	3.79×10^{-4}	11.2	11.23	1.2
π/3	1.31×10^{-3}	11.8	10.92	2.4	6.64×10^{-4}	13.4	12.60	1.2	1.81×10^{-4}	10.6	10.34	1.3
π/2	4.47×10^{-4}	9.8	8.42	2.6	7.06×10^{-5}	12.6	11.26	1.2				
2π/3	2.58×10^{-4}	6.4	6.50	1.5	1.74×10^{-4}	10.2	10.06	1.3	1.36×10^{-4}	8.2	8.26	1.2
5π/6	8.77×10^{-4}	5.4	5.39	1.0	1.99×10^{-4}	9.4	9.27	0.9	2.03×10^{-4}	7.4	7.61	0.9
π	3.04×10^{-3}	5.2	5.03	0.4	5.38×10^{-4}	9.2	8.99	0.4	3.31×10^{-4}	7.2	7.38	0.5

Scatter angle (radians)	^{12}C							
	Peak 1				Peak 2			
	Maximum value (neutrons per source particle)	Maximum Energy (MeV)	Expected Energy (MeV)	FWHM (MeV)	Maximum value (neutrons per source particle)	Maximum Energy (MeV)	Expected Energy (MeV)	FWHM (MeV)
0	1.07×10^{-1}	14.2	14.10	0.4				
π/6	6.25×10^{-3}	14	13.79	0.8	6.34×10^{-4}	9.4	9.44	0.8
π/3	5.47×10^{-4}	13.6	12.96	0.9	2.72×10^{-4}	9.0	8.88	0.9
π/2	1.43×10^{-4}	12	11.91	1.8				
2π/3	3.64×10^{-4}	11.2	10.95	1.1	4.63×10^{-4}	7.0	7.50	0.9
5π/6	8.00×10^{-4}	10.4	10.30	0.8	1.23×10^{-3}	6.6	7.05	0.5
π	1.72×10^{-3}	10.2	10.07	0.4	1.48×10^{-3}	6.4	6.90	0.5

Table 5.5 Continued: Estimated peak information for the various scatter targets in the idealized simulations. The energy resolution in the simulation was 0.2 MeV.

Scatter angle (radians)	CH_4								^{14}N			
	Peak 1				Peak 2				Peak 1			
	Maximum value (neutrons per source particle)	Maximum Energy (MeV)	Expected Energy (MeV)	FWHM (MeV)	Maximum value (neutrons per source particle)	Maximum Energy (MeV)	Expected Energy (MeV)	FWHM (MeV)	Maximum value (neutrons per source particle)	Maximum Energy (MeV)	Expected Energy (MeV)	FWHM (MeV)
0	9.89×10^{-2}	14.2	14.10	0.4					1.16×10^{-1}	14.2	14.10	0.4
π/6	2.94×10^{-3}	14.2	13.79	0.6					7.84×10^{-3}	14.0	13.83	0.5
π/3	9.92×10^{-5}	13.6	12.96	0.8					7.87×10^{-4}	13.6	13.12	1.1
π/2	4.27×10^{-5}	12.0	11.91	1.3					6.47×10^{-4}	12.4	12.21	1.3
2π/3	8.71×10^{-5}	11.2	10.95	1.1	7.09×10^{-5}	7.0	7.50	0.6	4.41×10^{-4}	11.6	11.36	0.9
5π/6	1.77×10^{-4}	10.4	10.30	0.4	2.22×10^{-4}	6.6	7.05	0.5	6.75×10^{-4}	10.8	10.77	0.5
π	3.85×10^{-4}	10.2	10.07	0.4	2.91×10^{-4}	6.4	6.90	0.5	1.39×10^{-3}	10.6	10.57	0.6

Scatter angle (radians)	H_2O											
	Peak 1				Peak 2				Peak 3			
	Maximum value (neutrons per source particle)	Maximum Energy (MeV)	Expected Energy (MeV)	FWHM (MeV)	Maximum value (neutrons per source particle)	Maximum Energy (MeV)	Expected Energy (MeV)	FWHM (MeV)	Maximum value (neutrons per source particle)	Maximum Energy (MeV)	Expected Energy (MeV)	FWHM (MeV)
0	1.10×10^{-1}	14.2	14.10	0.4								
π/6	4.31×10^{-3}	14.2	13.86	0.6								
π/3	1.94×10^{-4}	13.8	13.24	1.2								
π/2	2.00×10^{-4}	12.6	12.43	0.9								
2π/3	1.23×10^{-4}	12.0	11.67	0.8	8.02×10^{-5}	6.2	6.59	0.8	7.22×10^{-5}	5.4	5.78	1.0
5π/6	3.63×10^{-4}	11.2	11.14	0.4	1.45×10^{-4}	5.8	6.30	0.5	9.97×10^{-5}	5.0	5.51	0.5
π	7.28×10^{-4}	11.0	10.95	0.5	2.14×10^{-4}	5.8	6.19	0.6	8.97×10^{-5}	4.8	5.42	0.6

Table 5.6: The counts in the region of interest for the laboratory neutron scatter experiment.

Arrangement	Gross counts	Live time (s)	Counts per second
Background	50 ± 7	2247.78	0.022 ± 0.003
Generator with no water scatter target	18,470 ± 140	729.36	25.32 ± 0.19
Generator with water scatter target	2,3070 ± 150	737.22	31.29 ± 0.21

Table 5.7: A list of the relative coordinates for the various points found in Fig. 5.12.

Point	X	Y	Z
1	0	0	$-D_1$
2	$-r_1$	0	$-L_1/2$
3	0	r_1	$-L_1/2$
4	r_1	0	$-L_1/2$
5	0	$-r_1$	$-L_1/2$
6	0	0	0
7	$-r_1$	0	$L_1/2$
8	0	r_1	$L_1/2$
9	r_1	0	$L_1/2$
10	0	$-r_1$	$L_1/2$
11	$(D_2-L_2/2)sin\psi-r_2sin(\pi/2-\psi)$	0	$(D_2-L_2/2)cos\psi+r_2cos(\pi/2-\psi)$
12	$(D_2-L_2/2)sin\psi$	r_2	$(D_2-L_2/2)cos\psi$
13	$(D_2-L_2/2)sin\psi+r_2sin(\pi/2-\psi)$	0	$(D_2-L_2/2)cos\psi-r_2cos(\pi/2-\psi)$
14	$(D_2-L_2/2)sin\psi$	$-r_2$	$(D_2-L_2/2)cos\psi$
15	$D_2sin\psi$	0	$D_2cos\psi$
16	$(D_2+L_2/2)sin\psi-r_2sin(\pi/2-\psi)$	0	$(D_2+L_2/2)cos\psi+r_2cos(\pi/2-\psi)$
17	$(D_2+L_2/2)sin\psi$	r_2	$(D_2+L_2/2)cos\psi$
18	$(D_2+L_2/2)sin\psi+r_2sin(\pi/2-\psi)$	0	$(D_2+L_2/2)cos\psi-r_2cos(\pi/2-\psi)$
19	$(D_2+L_2/2)sin\psi$	$-r_2$	$(D_2+L_2/2)cos\psi$

Table 5.8: An estimate of the variation in scatter angle and scatter energy of neutrons in the idealized simulations.

$\psi_{Expected}$ (radians)	$\psi_{A,Max}$ (degrees)	$\psi_{A,Min}$ (degrees)	$\Delta\ \psi_A$ (radians)	$\Delta\ \psi_A$ (degrees)	$E'n_{,Expected}$ (MeV)	$E'n_{,Max}$ (MeV)	$E'n_{,Min}$ (MeV)	$\Delta E'_n$ (MeV)
0	0.78	0.00	0.78	44.9	14.1	14.1	13.6	0.5
π/6	1.28	0.09	1.19	68.2	13.9	14.1	12.9	1.2
π/3	1.76	0.24	1.52	87.1	13.2	14.1	12.1	2.0
π/2	2.25	0.79	1.47	84.0	12.4	13.6	11.5	2.1
2π/3	2.75	1.35	1.41	80.6	11.7	12.8	11.1	1.7
5π/6	3.13	1.91	1.22	69.7	11.1	11.9	11.0	0.9
π	3.14	2.47	0.67	38.5	11.0	11.3	11.0	0.3

Table 5.9: An estimate of the variation in scatter angle and scatter energy of neutrons given the detector dimensions and the distance between the source and scatter target in the realistic simulations.

$\psi_{Expected}$ (radians)	$\psi_{A,Max}$ (radians)	$\psi_{A,Min}$ (radians)	$\Delta\ \psi_A$ (radians)	$\Delta\ \psi_A$ (degrees)	$E'n_{,Expected}$ (MeV)	$E'n_{,Max}$ (MeV)	$E'n_{,Min}$ (MeV)	$\Delta E'_n$ (MeV)
0	0.17	0.00	0.17	9.5	14.1	14.1	14.1	0.0
π/6	0.69	0.35	0.34	19.7	13.9	14	13.7	0.3
π/3	1.20	0.88	0.32	18.3	13.2	13.5	13	0.5
π/2	1.69	1.44	0.25	14.4	12.4	12.6	12.2	0.4
2π/3	2.18	2.00	0.17	10.0	11.7	11.8	11.6	0.2
5π/6	2.67	2.57	0.10	5.5	11.1	11.2	11.1	0.1
π	3.14	3.12	0.03	1.5	11.0	11.0	11.0	0.0

References

Aleksandrov, V.D., Bogolubov, E.P., Bochkarev, O.V., Korytko, L.A., Nazarov, V.I., Polkanov, Y.G., Ryzhkov, V.I., Khasaev, T.O., 2005. Application of neutron generators for high explosives, toxic agents, and fissile material detection. *Appl. Radiat. Isotopes,* 63 (5-6), 537-543.

Buffler, A., 2004. Contraband detection with fast neutrons. *Radiat. Phys. Chem.*, 71(3-4), 853-861.

Chichester, D.L., Simpson, J.D., Lemchak, M., 2007. Advanced compact accelerator neutron generator technology for active neutron interrogation field work. *J. Radioanal. Nucl. Ch.*, 271 (3), 629-637.

Dolan, J.L., Marcath, M.J., Flaska, M., Pozzi, S.A., Chichester, D.L., Toanin, A., Peerani, P., 2014. Active-interrogation measurements of fast neutrons from induced fission in low-enriched uranium. *Nucl. Instrum. Methods Phys. Res. A*, 738, 99-105.

Eckerman, K.F., Ryman, J.C., 1993. External exposure to radionuclides in air, water, and soil. Oak Ridge National Laboratory, Report No. EPA-402-R-93-081.

Hsu H.H., Kearfott K.J., 1999. Effects of neutron source selection on land-mine detection efficiency. *Nucl. Instrum. Meth. A*, 442 (1-3), 914-918.

Kaplan, A.C., Flaska, M., Enqvist, A., Dolan, J.L., Pozzi, S.A., 2013. EJ-309 pulse shape discrimination performance with a high gamma-ray-to-neutron ratio and low threshold. *Nucl. Instrum. Methods Phys. Res. A*, 729, 463-468.

Knoll, G.F., 2010. Radiation Detection and Measurement, 4th ed. (Wiley, Hoboken, NJ), pp. 19-22.

Lehnert, A.L., Kearfott, K.J., 2010. The detection of explosive materials: review of considerations and methods. *Nucl. Technol.*, 172 (3), 325 – 334.

Lehnert, A.L., Flaska, M., Kearfott, K.J., 2012. D-D neutron-scatter measurements for a novel explosives-detection technique. *Nucl. Instrum. Meth. A*, 693, 195-202.

McConn Jr., R.J., Gesh, C.J., Pagh, R.T., Rucker, R.A., Williams III, R.G., 2011. Compendium of material composition data for radiation transport modeling. Pacific Northwest National Laboratory, Report No. PNNL-15870.

National Nuclear Data Center. 2014. Interactive Chart of the Nuclides level schemes for ^{9}Be, ^{12}C, and ^{16}O. Brookhaven National Laboratory. Online, accessed April 2, 2014. http://www.nndc.bnl.gov/chart/.

Ordonez C.E., Chang W., 1999. Angular uncertainties due to geometry and spatial resolution in Compton cameras. *IEEE T. Nucl. Sci.* 46 (4), 1142-1147.

Overley, J.C., Chmelik, M.S., Rasmussen, R.J., Schofield, R.M.S., Sieger, G.E., Lefevre, H.W., 2006. Explosives detection via fast neutron transmission spectroscopy. *Nucl. Instrum. Meth. B*, 251 (2), 470-478.

Raas, W.L., Blackburn, B., Boyd, E., Hall, J.M., Kohse, G., Lanza, R., Rusnak, B., Watterson, J.I.W., 2005. Neutron resonance radiography for explosives detection: technical challenges. *Nuclear Science Symposium Conference Record, 2005 IEEE*, (1), 129-133.

Sowerby, B.C., Tickner, J.R., 2007. Recent advances in fast neutron radiography for cargo inspection. *Nucl. Instrum. Meth. A*, 580 (1), 799-802.

Strellis, D., Gozani, J., Stevenson, J., 2009. Air cargo inspection using pulsed fast neutron analysis. *International Topical Meeting on Nuclear Research Applications and Utilization of Accelerators*, *Vienna, Austria, May 4-8, 2009*.

Whetstone, Z.D., Kearfott, K.J., 2011. Use of multiple layers of repeating material to effectively collimate an isotropic neutron source. *Nucl. Technol.*, 176 (3), 395 – 413.

Whetstone, Z.D., Kearfott, K.J., 2014. A review of conventional explosives detection using active neutron interrogation. *J. Radioanal. Nucl. Ch.*, 301 (3), 629-639.

CHAPTER 6: EXPERIMENTAL VERIFICATION OF A METHOD TO CREATE A VARIABLE ENERGY NEUTRON BEAM FROM A MONOENERGETIC, ISOTROPIC SOURCE USING NEUTRON ELASTIC SCATTER AND TIME OF FLIGHT

Abstract

An experiment was performed to determine the neutron energy of near-monoergetic deuterium-deuterium (D-D) neutrons that elastically scatter off a hydrogenous target. The experiment used two liquid scintillators to perform time-of-flight (TOF) measurements to determine neutron energy, with the start detector also serving as the scatter target. The stop detector was placed 1.0 m away and at scatter angles of $\pi/6$, $\pi/4$, and $\pi/3$ radians, and 1.5 m at a scatter angle of $\pi/4$ radians. When discrete 1 ns increments were implemented, the TOF peaks had estimated errors between -21.2 and 3.6% relative to their expected locations. Full widths at half maximum (FWHM) ranged between 9.6 and 20.9 ns, or approximately 0.56 to 0.66 MeV. Monte Carlo simulations were also conducted that approximated the experimental setup and had both D-D and deuterium-tritium neutrons. The simulated results had errors between -17.2 and 0.0% relative to their expected TOF peaks when 1 ns increments were applied. The largest D-D and D-T FWHMs were 26.7 and 13.7 ns, or approximately 0.85 and 4.98 MeV, respectively. These values, however, can be reduced through manipulation of the dimensions of the system components. The results encourage further study of the neutron elastic scatter TOF system with

particular interest in application to active neutron interrogation to search for conventional explosives.

Introduction

The work performed in Ch. 5 discussed a method for changing the energy of neutrons from a deuterium-deuterium (D-D) or deuterium-tritium (D-T) source. The ability to reliably change the energy of a near-monenergetic source has applications to many different fields, including active neutron interrogation to search for conventional explosives. The neutron energy could be aligned with resonant reaction peaks or valleys to change the chance of attenuation and elastic scatter or similarly increase the likelihood of producing secondary gamma rays, thereby increasing the detection probability (Overley et al., 2006; Sowerby and Tickner, 2007; Lehnert and Kearfott 2010; Lehnert and Kearfott, 2012; Strellis et al., 2009; Whetstone and Kearfott, 2014; Lehnert and Kearfott, 2014).

By using a target of known composition, it is possible to predict the final energy of monoenergetic neutrons that undergo a single elastic scatter at a variety of angles. As seen in the previous chapter, the final neutron energy, E_n', can be calculated based on the original energy, E_n, the lab frame scatter angle, ψ, the mass of the scatter target nucleus, m_s, and the mass of the neutron, m_n:

$$E'_{\mathrm{n}} = \frac{E_{\mathrm{n}}}{(m_s+m_n)^2}\left[m_n^2 cos(2\psi) + 2m_n cos\psi\sqrt{m_s^2 - m_n^2 sin^2\psi} + m_s^2\right]. \quad (6.1)$$

Conversely, the laboratory frame scatter angle necessary for a desired final neutron energy can be determined using:

$$\psi = \tan^{-1}\left\{\frac{\sqrt{1-\left[1-\frac{(m_S+m_n)^2}{2m_S m_n}\left(1-\frac{E'_{\mathrm{n}}}{E_{\mathrm{n}}}\right)\right]^2}}{1-\frac{(m_S+m_n)^2}{2m_S m_n}\left(1-\frac{E'_{\mathrm{n}}}{E_{\mathrm{n}}}\right)+\frac{m_n}{m_S}}\right\}, \tag{6.2}$$

with the arctangent taken such that ψ ranges between 0 and π radians, with 0 corresponding to an unscattered neutron and π describing a backscatter event (Whetstone and Kearfott, 2015).

In preliminary simulations from Ch. 5, both idealized and more realistic, the neutron elastic scatter method showed promise, resulting in a significant fraction of neutrons that underwent a single elastic scatter and obtained a final energy that was predicted by Eq. 6.1. The proposed method was not without its drawbacks, however. Many of the neutrons created by the source did not undergo a single elastic scatter in the target. Instead, they interacted somewhere else in the environment, creating a relatively large neutron background in the simulated detectors, which obscured the desired signal from the single elastic scatter events. Furthermore, laboratory confirmation of the simulation results was difficult because obtaining scattered neutron energy information proved problematic. The method of fast neutron detection previously employed required slowing of the neutrons in hydrogenous material, thus sacrificing energy information. Although more neutrons were seen by a shielded detector when a scatter target was present, it was not possible to determine how many of those neutrons were from single-neutron elastic scatter.

Fast neutron spectroscopy is essential to observe whether elastic scatter is an effective method of reliably changing neutron energy. With the large background, confirming neutron energy is a good way to discriminate neutrons that did not undergo a single elastic scatter in the target. Unfortunately, determining final neutron energy directly can be problematic because fast

neutrons generally only deposit a fraction of their energy in an elastic scattering detector before scattering out. Alternatively, other popular neutron detectors, such as boron trifluoride (BF_3), depend on the neutron to first be slowed down by passing through moderating material before being absorbed and generating a signal. In both instances, it is very difficult to determine the incident neutron energy.

A standard alternative to energy spectroscopy is neutron time of flight (TOF). The velocity, *v*, of the scattered neutron can be determined by dividing the distance traveled, *d*, by the neutron *TOF*. Assuming a non-relativistic velocity, its energy, E'_n, can be calculated using the kinetic energy equation:

$$E'_n = \frac{1}{2} m_n v^2, \tag{6.3}$$

$$E'_n = \frac{1}{2} m_n \left(\frac{d}{TOF}\right)^2. \tag{6.4}$$

Depending on the timing resolution, this method can provide functional energy information. However, it requires two signals to measure TOF. The start signal can be from either the generator signaling the neutron creation, or from a detector that the neutron interacted in. The stop signal occurs in a detector some distance from the location of the start signal, and indicates the neutron's arrival. The time and distance between pulses can then be used with Eq. 6.4 to confirm the neutron's energy.

Conversely, if the energy of an elastically scattered neutron is calculated via Eq. 6.1, the velocity can be predicted,

$$v = \sqrt{2E'_n/m_n} \tag{6.5}$$

and, provided *d* is known, the *TOF* can be estimated,

$$TOF = \frac{d}{\sqrt{2E'_n/m_n}}. \tag{6.6}$$

Applying neutron TOF allows for discrimination of neutrons that entered the stop detector without first undergoing a single elastic scatter in the target. If the neutrons do not have a start signal or the correct TOF, and hence the correct energy, they can be quickly neglected.

Proposed improvements to laboratory setup

The method for changing the energy of neutrons from a monoenergetic source, originally discussed in Ch. 5, can be enhanced through the application of TOF. The additional information allows the user to determine the scattered neutron energy while also neglecting many of the other neutrons that were obscuring the signal in the earlier simulations. This will create cleaner, more distinct peaks. Furthermore, the proposed improvements can be applied to any monoenergetic source while maintaining the simplistic original design. This is accomplished via adoption of TOF measurement techniques. In the modified system, the neutron elastic scatter target also functions as the TOF detector that generates the start signal.

The resultant source and detector arrangement, known as the variable energy neutron elastic scatter (VENES) system, requires two organic scintillators to be used as fast neutron detectors. The detectors consist of hydrogenous material and generate a light pulse when a neutron imparts energy to a hydrogen atom. As long as it is above the set threshold, the amount of energy deposited and size of the pulse do not matter. They simply act as triggers to signal the

beginning and end of the TOF. The first, or start detector, is placed near the neutron generator. The second, or stop detector, is placed at a predetermined distance and angle away from the start detector. When the generator is turned on, it will act as a near isotropic source of neutrons. Some neutrons will travel towards and interact in the start detector, creating a signal. A fraction of those neutrons will undergo a single elastic scatter and be directed towards the second detector. Some of those neutrons will interact, creating a stop signal. Using Eq. 6.1, the expected scattered neutron energy can be determined and the time for the neutron to travel a set distance can be calculated based on Eq. 6.6.

In addition to providing the start signal, the use of an organic liquid scintillator as the scatter target provides an excellent opportunity to interrogate with neutrons having a wide variety of possible energies. Since a neutron and ^{1}H nucleus have nearly identical masses, the percentage of neutron energy lost through a single elastic scatter can range between 0 and 100% for scatter angles between 0 and roughly $\pi/2$ radians, respectively. This is an advantage over heavier potential scatter nuclei, whose larger masses create an increasingly narrow range of scattered neutron energy options across all scatter angles, limiting applicability.

By using two detectors in coincidence, TOF measurements automatically reduce the neutron background associated with operating an isotropic source. Only neutrons that interact in the start and stop detectors and within a set amount of time are analyzed. A start signal without a stop and a stop signal without a start are automatically discarded. This eliminates source neutrons that bypass the start detector and either interact immediately in the stop detector or interact in the environment before entering the stop detector. Similarly, neutrons that scatter off the start detector at a different angle, never reaching the stop detector, are ignored. Compared to the simulations from Ch. 5, the inherent selection bias of TOF measurements will ultimately

result in cleaner spectra with the neutron noise significantly reduced and a more prominent single elastic scatter peak.

By using the start detector as the scatter target, TOF measurements and neutron energy information will be available. This will not only permit experimental investigation of the use of elastic scatter as a method to reliably vary the energy of neutrons from a monoenergetic source, but also significantly reduce the background of the neutron energy spectra in the VENES system.

Materials and Methods

The experimental work was performed with a portable MP 320 D-D neutron generator[1]. The organic scintillators were both cylindrical canisters containing EJ-309 liquid[2], which has a hydrogen-to-carbon ratio of 1.25. The start detector, which was also the scatter target, was a length of 25.4 mm and had a radius of 12.7 mm and was connected to an H10580 photo-multiplier tube (PMT) assembly[3]. The stop detector was 127 mm long and had a radius of 63.5 mm and was connected to a XP4512B PMT[4]. The start and stop detectors were connected to negative high voltages of roughly -1330 V and -1360 V, respectively. They were each calibrated before measurements with ^{137}Cs attached directly to their faces. A 12-bit, 250-MHz, eight-channel digitizer[5] collected and processed the pulses.

The arrival time of each neutron is determined by its pulse's creation in the detector and subsequent appearance in the digitizer. The digitizer has a timing resolution of 4 ns, but it is possible to reduce this value through a consistent and fairly accurate method of calculating pulse

[1] MP 320 D-D neutron generator (Thermo Fisher Scientific Inc., Waltham, MA 02451).

[2] EJ-309 liquid scintillator (Eljen Technology, Sweetwater, TX 79556).

[3] H10580 PMT assembly (Hamamatsu Photonics K.K., Hamamatsu City, Japan)

[4] XP4512B PMT (Photonis Technologies S.A.S., Merignac, France)

[5] V1720 digitizer (CAEN, Viareggio, Italy)

arrival times. Through a post-processing algorithm, the pulse's maximum voltage is determined based on the digitizer samples acquired in the waveform. In order to minimize interpolation errors, the pulse arrival is defined as the point in time in which its rising edge is at half of the pulse's maximum. This can be estimated by identifying the rising edge data points immediately below and above the half-maximum value and assuming a straight line between them. Through linear interpolation, the pulse time of arrival can be approximated and is no longer limited to a 4 ns resolution. The neutron *TOF* is then simply calculated by subtracting the neutron pulse arrival time in the start detector, t_{start}, from the arrival time in the stop detector, t_{stop}:

$$TOF = t_{stop} - t_{start}. \tag{6.7}$$

The start detector was placed next to the D-D generator, with its face parallel to the side of the generator, centered along the source plane, touching the housing. Throughout the experiment, the stop detector was moved relative to the start detector. Measured from the center of the front face of each detector, it was positioned 1.00 m away at π/6, π/4, and π/3 radians scatter angles. It was also placed at 1.50 m and a π/4 radians scatter angle. When measuring from the center of each detector volume, the distance and scatter angle between the detectors increases by varied amounts, but always less than 0.06 m and 0.011 radians (0.7 degrees). These adjusted values were accounted for when calculating the expected *TOF*. A diagram of the laboratory arrangement can be seen in Fig. 6.1 and 6.2. In order to minimize the effect of the concrete floor on the neutrons, the generator and both detectors were elevated off the ground roughly 1.20 m using a metal frame to hold the generator and a combination of cinderblocks and metal ring stands with clamps to secure the detectors. Extra structural stability was added through generous

application of duct tape. The closest wall was roughly 1.4 m from the center of the neutron generator. Images of the laboratory setup can be seen in Fig. 6.3 – 6.5.

Although the TOF coincidence measurements helped to significantly reduce background, the EJ-309 liquid scintillators also responded to gamma rays, creating coincident pulses in the start and stop detectors. During generator operation, the gamma ray background was significant and needed to be reduced. This was accomplished using a previously developed pulse shape discrimination (PSD) post-processing tool that compared the tail integral of a pulse to its total integral (Flaska and Pozzi, 2007; Pozzi et al., 2009; Kaplan et al., 2014; Detection for Nuclear Nonproliferation Group, 2014a). Generally, in liquid scintillators, the tail integral to total integral ratio is larger for neutrons compared to gamma rays. Through careful selection of parameters within the post processing tool, it is possible to eliminate nearly all gamma ray noise in the signal. In order to capture as many pulses as possible, the threshold settings for both detectors were set at 70 keVee.

After PSD, a MATLAB[6] script was used to calculate the TOF between the start and stop detector and generate a histogram with fixed width Δt. In order to more easily compare the somewhat noisy curves, a line of best fit was generated. Using Eq. 6.4, and assuming d was constant and equal to the distance between the center of the start detector and the center of the stop detector, the TOF histograms were transformed to neutron energy. Given the fixed width of Δt and $E_n' \sim 1/TOF^{1/2}$, the neutron energy histogram bin widths become wider the larger E'_n is. As such, it was necessary to normalize the histogram values by their variable bin widths to obtain an accurate curve. Next, the MATLAB Curve Fitting Tool found the best Gaussian curve to fit the

[6] computer program MATLAB (The MathWorks, Inc., Natick, MA 01760-2098, 2006).

neutron energy peak, based on r^2 value. Finally, the equation of the curve was transformed from neutron energy back to TOF by removing the normalization and using Eq. 6.6.

In an effort to confirm the neutron elastic scatter in the start detector and benchmark the results, Monte Carlo simulations of the experiment were conducted using the modified Monte Carlo N-Particle (MCNP)[7] Transport Code, MCNPX-PoliMi[8]. The modified code allows the user to obtain precise TOF information from the simulated neutrons, providing more accurate and realistic results compared to the original code (Pozzi et al, 2003). The spectra did not require PSD because gamma rays were not simulated. The output files were then post-processed using MCNPX-PoliMi's MPPost[9] to more accurately model the detector response (Miller et al, 2012; Enqvist et al, 2013). The simulation allowed for precise TOF measurements which did not require interpolation and provided much smoother spectra. However, in order to mirror the experimental post-processing algorithm, once the TOF histogram was obtained from MPPost, a process similar to what was employed on the laboratory data was used to determine the best curves to fit the neutron energy, and consequently, TOF peaks.

The simulated geometry included a generator model, which was provided by the MP 320 manufacturer, as well as models of the start and stop detectors, their PMTs, and the associated housing materials (Thermo Fisher Scientific Inc., 2014; Detection for Nuclear Nonproliferation Group, 2014b). The isotropic point source was placed in the generator near the face of the deuterium target and produced neutrons of 2.5 MeV. The center of the generator and both detectors was 1.23 m above a concrete floor. Just as in the experiment, the start detector was

[7] computer code Monte Carlo N-Particle Transport version 5 (Los Alamos National Laboratory, Los Alamos, NM 87545, 2006).

[8] computer code MCNPX-PoliMi v2.0 (Polytechnic of Milan, Milano, Italy and the University of Michigan, Ann Arbor, MI, USA).

[9] computer code MPPost v2.1.0 (University of Michigan, Ann Arbor, MI, USA)

aligned with the source plane, 53 mm from the point source, with the stop detector placed at the same relative distances and scatter angles. The universe extended 3.00 m, with its remaining volume filled with air. The concrete walls and all other objects in the laboratory were neglected.

Further simulations were conducted where the 2.5 MeV source was replaced with a 14.1 MeV source to investigate application of this method to a D-T generator. All other aspects of the simulation and analysis remained unchanged.

Results

The spectra from the detector at 1.0 m and a $\pi/4$ radian scatter angle are shown before and after PSD in Fig. 6.6. The removal of the peak at roughly 3 ns, which is due to a single gamma ray interacting in the start then stop detectors, and the suppression of the background, illustrate the effectiveness of the PSD post processing technique. The oscillating noise introduced into the spectra from the TOF interpolation technique is also visible.

The experimental TOF spectra with their associated lines of best fit can be seen in Fig. 6.7. To better visualize the TOF peaks, each histogram was normalized by the maximum value in the best fit line appearing in Fig. 6.8. Similarly, the simulated D-D TOF spectra are presented in Fig. 6.9 and 6.10 and the simulated D-T TOF spectra are found in Fig. 6.11 and 6.12. The source strength of the experimental D-D generator was not precisely known, but it was assumed to be 2 x 10^6 neutrons per second. All spectra were presented with 1 ns resolution and error bars indicate the statistical uncertainty.

The neutron energy spectra and the associated Gaussian curves for the three sets of data appear in Fig. 6.13 – 6.15. Due to the relationship between *TOF* and E'_n, the widths of the energy bins vary and get larger as E'_n increases. In the tens of keV range, due to the shrinking

bin width and contribution from neutrons that underwent multiple scatters between the start and stop detector, noise and uncertainty dominate the lower energies of the neutron energy spectra. Therefore, that energy range is not shown here. Again, the error bars represent the statistical uncertainty of the histogram values. A quantile-quantile plot was also generated comparing the scattered neutron energy curve to the Gaussian fit. An example from the simulated $\pi/4$ radians D-D scatter at 1.0 m, between approximately 2.4 and 0.7 MeV, can be seen in Fig. 6.16. The shape is typical of all of the Q-Q plots, with most of the points lying near the line $y = x$. This confirms the similarity between the scattered neutron energy spectra and the Gaussian fit. The only deviation was from points near the edge of the curve where the Gaussian distribution broke down due to contributions from interactions other than a single elastic scatter off hydrogen in the start detector.

Due to the noise in the curves, the peak maximum, peak mode, and the full width at half maximum (FWHM) values for the various spectra were determined based on the Gaussian curves fit to the neutron energy spectra and the resultant best fit lines for the TOF spectra. The values from all the spectra can be found in Table 6.1. The approximated experimental FWHM values were between 9.6 to 20.9 ns and 0.56 to 0.66 MeV. The simulated D-D spectra had FWHMs ranging from 11.2 to 25.2 ns and 0.58 to 0.85 MeV. Finally, the simulated D-T spectra had FWHMs between 5.1 to 12.8 ns and 2.71 to 4.98 MeV.

Comparing the experimental and simulated D-D data was difficult due to the variation between peak maxima at the same stop detector location. Therefore, for a visual comparison between the experimental and simulated data, the D-D TOF spectra were normalized by the peak height in Fig. 6.17. The percent differences between the experimental and simulated D-D data for the TOF peak maximum, peak mode, and FWHM are presented in Table 6.2.

Discussion

Experimental data

As seen in Fig 6.6, PSD completely eliminates the gamma ray peak, confirming its effectiveness. Furthermore, the background is reduced by approximately a factor of three. For comparison, when the stop detector was positioned at 1.0 m and $\pi/4$ radians, the maximum peak value was reduced by only 11% after PSD. The remaining background seen in the experimental results is due to coincident neutron measurements between the start and stop detectors. The background is not visible in the simulations because there was only one neutron simulated at a time, eliminating the chance for incidental coincident measurements between two neutrons. All points in the spectra after the peak are a result of a single neutron first interacting in the start detector and eventually, possibly after multiple interactions in the environment, interacting in the stop detector. Although not shown in the figures, the simulations contained some negative TOF values that were the result of a neutron interacting first in the stop detector and then the start detector. As expected, these interactions were much less likely and indiscernible above the background present in the experimental results.

The oscillations present in the experimental TOF data are an artifact of the time linear interpolation process. The rise time of the peaks in both the start and stop detectors appear to be on the order of roughly 4-6 ns, meaning that for a majority of pulses, the digitizer values will jump from at or near baseline to at or near the peak value in a single 4 ns step. In these instances, the rising edge half-maximum time, which is linearly interpolated, will fall roughly halfway between the two points spaced 4 ns apart, creating an approximately 2 ns offset. Therefore, when calculating neutron TOF, the offset, which is present for both the start and stop detector arrival times, is canceled out via subtraction. This leads to a majority of the calculated TOF values

falling near a multiple of 4 ns, hence the oscillation seen in the figures. If the pulse rise time was slower or the digitizer resolution was higher, this would not be a concern as the points along the rising edge would be more evenly distributed. However, since the rise time is so steep, the oscillation is an unavoidable byproduct of interpolation. The process of converting the TOF bins to neutron energy and fitting a Gaussian peak corrects for this oscillation and allows for easier analysis of both peaks.

The TOF experiments performed as expected. As evident in Table 6.1, the TOF peaks were located near the anticipated time. The $\pi/6$ radian scatter had the largest peak maximum, followed by $\pi/4$ radians at 1.0 m, then $\pi/3$ radians. This correlates to the relative attenuation expected by neutrons of decreasing energy. The $\pi/4$ radians scatter at 1.5 m had the lowest maximum due to the increased travel distance and smaller solid angle presented by the stop detector. Similarly, the smaller solid angle for neutron scatter leads to a narrower energy FWHM for the $\pi/4$ radian scatter at 1.5 m when compared to the same angle at 1.0 m. The same does not hold true, however, when looking at the TOF peaks' FWHM. There, the additional travel distance broadens the FWHM at 1.5 m, even though the neutron energy range is actually narrower.

As discussed in Ch. 5, the detected scattered neutrons will have a range of energies and corresponding TOFs due to the non-negligible volume of the start and stop detectors. This, combined with the light creation and collection within the detector, PMT, and associated electronics, contributes to the broadening of the peaks. However, at $\pi/3$ radians the TOF spectra has a feature that is not the result of peak broadening. The initial rise in the peak beginning around 55 ns, seen in Fig. 6.7 and 6.8, is significantly faster than what a neutron that undergoes a single scatter off ^{1}H near $\pi/3$ radians is capable. Instead, multiple interactions with the H and C

nuclei found in the EJ-309 liquid scintillator material induce a pulse in the start detector while still leaving the neutron with enough energy to arrive at the stop detector sooner than expected and alter the leading edge on the TOF spectra. Due to the scattering angle, the threshold on the start detector is too large to detect the neutron scatter off a ^{12}C nucleus at either $\pi/6$ or $\pi/4$ radians and could most likely be adjusted to eliminate the $\pi/3$ neutrons as well.

D-D simulation data

Due to a lack of gamma rays, multiple coincident neutrons, and imprecise TOF interpolations present in the PoliMi spectra, the simulations provide a somewhat idealized representation of the experimental TOF results. However, it is first important to confirm the simulations are properly representing the experiment. Comparing the simulated D-D spectra to the experiment, as seen in Fig 6.16 and Tables 6.1 and 6.2, demonstrates a strong, but not perfect, correlation between the two data sets. Most glaring is the difference in the maximum values of the experimental peaks compared to their simulated counterparts. This is primarily the result of the D-D generator having an imperfect isotropic distribution resulting in nearly twice as many forward directed neutrons than those emitted at $\pi/2$ radians (Csikai, 1987). The generator was assumed to create 2.0×10^6 neutrons per second isotopically, which was the value used when normalizing the experimental spectra. However, the actual flux was most likely more complicated, resulting in the smaller peaks when compared to the simulations.

Interestingly, the ratios of the simulated D-D peak heights are similar to the experimental peak heights. The ratio between the $\pi/6$ and $\pi/4$ radians scatter at 1.0 m is 0.58 for the experimental peaks and 0.55 for the simulated peaks. Comparing $\pi/4$ and $\pi/3$ radians scatter at 1.0 m reveals a ratio of 0.29 and 0.40 for the experimental and simulated peaks, respectively. Finally, the ratio between $\pi/3$ radians scatter at 1.0 m and $\pi/4$ radians scatter at 1.5 m is 0.51

experimental and 0.82 simulated. These are relatively close, especially considering the amount of noise in the experimental spectra and the uncertainty of the precise peak height.

When comparing the simulated TOF peak to experimental peak, the largest percent difference between the spectra modes is 5.2% at π/6 radians. The disagreement in values was not entirely unexpected. Although every care was taken to confirm that the stop detector was set up properly in relation to the start detector, as seen in Eqs. 6.1 and 6.6, even a small deviation in the distance, d, and scatter angles, ψ, between the two detectors can shift the TOF peak by several ns. For example, an uncertainty of $\pm$ 0.03 m and $\pm$ 0.087 radians (5 degrees) results in a TOF uncertainty of $\pm$ 1.5, 1.7, 1.8, and 1.8 ns, for scatters at π/6 radians, π/4 radians, and π/3 radians at 1.0 m, and π/4 radians at 1.5 m, respectively. Another source of discrepancy is the initial energy of the neutron, E_n. Although it was assumed to be 2.5 MeV in the simulation and when calculating the expected TOF of neutrons, the actual value is unknown and may be slightly different due to the operating voltage of the neutron generator.

When comparing the FWHM of the two data sets, although still within the expected range, the simulated data set is consistently larger by 16 – 30%. The volumes of the simulated detectors were the same as their experimental counterparts. However, since they are liquid, it is possible that they were not completely filled and the actual active volume may have been smaller. Alternatively, light collection near the edge of the detectors in the laboratory may have been inefficient, reducing the effective detector size. Also, the post-processing of the simulated data that was meant to mimic the experimental detector response may have broadened the peaks more than expected. Even with the broadened peaks, the π/3 radians scatter spectra also shows a contribution from elastic scatter off ^{12}C in the start detector, similar to the experimental spectra.

Regardless of the minor irregularities between the simulated and experimental data, with the shape and location of the peaks very similar to one another, the simulated results provide an effective representation of the behavior of neutrons in the experiment.

D-T simulation data

Although there were no experimental results to compare to, because of the lack of an appropriate experimental system, the simulated D-T spectra were still very interesting. Due to the higher energy of the neutrons, as seen in Table 6.1, the FWHM of the TOF peaks was considerably narrower than either other data set. However, given that $E'_n \sim 1/TOF^{1/2}$, the energy range of the neutrons interacting in the detector is significantly larger than the D-D neutrons. Furthermore, one of the four energy spectra had peak modes in the same TOF bin as anticipated based on Eq. 6.6., while the spectra from $\pi/4$ and $\pi/3$ at 1.0 m and $\pi/4$ at 1.5 m were within 1, 6, and 2 ns, respectively. This closer fit is not surprising due to the larger range of neutron energies contained in each bin and the shorter TOFs.

Similar to the D-D experiment and simulations, the D-T $\pi/3$ spectra showed contributions from neutrons interacting with ^{12}C. In this case, however, the energy difference was enough to form two separate TOF peaks at approximately 22 and 27 ns. The 22 ns peak correlates to an elastic scatter, while the 27 ns peak correlates to the inelastic scatter that excites the ^{12}C nucleus to the 4.44 MeV energy state (National Nuclear Data Center, 2014). These peaks are relatively small compared to the peak from elastic scatter off the hydrogen nucleus, but contribute to the detector signal. They must either be taken into account in future experiments, or eliminated through higher detector threshold settings.

General observations

The forward shift of nearly all the TOF peaks in all of the data sets, as seen in Table 6.1, is a result of preferential attenuation of the lower energy neutrons present in the spectra. As neutron energies decrease, the probability of the neutron interacting again before reaching the stop detector increases. As a result, a larger proportion of higher energy neutrons are counted, changing the shape of the TOF peak. This effect is strongest in the lower energy neutron spectra, specifically for the experimental and simulated D-D $\pi/3$ radians results. For scattered neutrons with higher energies, whether due to a smaller scatter angle or D-T source neutrons, the proportion of neutrons attenuated is smaller, leading to less of a peak shift.

A potential drawback to the VENES system is the relatively low probability for a neutron created in the generator to interact in both the start and stop detector. As an example, in the simulated D-D spectra for a $\pi/4$ radians scatter at 1.0 m, less than four source neutrons out of every million contribute to the signal between 50 and 100 ns, which is nearly the entire width of the peak and correlates to an energy range of 1.75 MeV. Depending on the source strength, measurement times could be on the order of hours or longer. This is not ideal for many applications. Larger detectors can increase the system's efficiency, but as seen in Ch. 5, will also broaden the TOF peaks and increase the systematic uncertainty. Strong sources or long count times are the only practical solution to correct for this lack of efficiency.

Although the scattered neutrons are not monenergetic, their TOF, and hence energy range, is centered near what was predicted by Eqs. 6.1 and 6.6, confirming it is possible to reliably change the energy of neutrons from a near-monoenergetic source. However, in the current arrangement, the peak neutron energy range, particularly from the D-T source, is likely too wide for many applications. Many of the neutron interaction cross section resonances are a

fraction of an MeV wide and an effective neutron interrogation system should produce neutrons whose energy range is on a similar scale. Fortunately, the energy range of the VENES system can be adjusted. As previously discussed, the energy resolution is dependent on a combination of the distances between the neutron source, start detector, and stop detector as well as the detector volumes. The FWHM, as determined via simulation, is approximately 14 to 40% of the potential neutron energy range estimated using the method discussed in Ch. 5 (Whetstone and Kearfott, 2015).

As an example, using the D-T source and same scatter angles, but increasing the distance between the neutron source location and start detector to 1.0 m, the distance between the start and stop detectors to 2.0 m, and reducing the size of the stop detector to that of the start detector, results in expected neutron energy peaks with approximate FWHM values between 0.26 and 0.48 MeV. This is a 90% reduction in the energy range at each scatter angle compared to the previously simulated arrangement when the larger stop detector was 1.0 m from the start detector. The system dimensions can be adjusted further if a more narrow energy range is desired. Unfortunately, the increase in distance between components and decrease in stop detector volume also results in approximately a six order of magnitude reduction in the expected count rate due to increased geometric attenuation and decreased detector volume.

Another factor in the VENES system's precision is the width of the energy steps possible. Ultimately, this is dependent on the timing resolution of the system and the neutron TOF. As seen in Table 6.1, even though the width of the TOF peak decreases as the scatter energy of the neutrons increases, the energy range of the neutrons per ns time step increases. Adapting Eq. 6.4, the system's scattered neutron energy step, $\Delta E_n'$, can be determined via:

$$\Delta E_n' = \frac{1}{2} m_n d^2 \left[\frac{1}{TOF^2} - \frac{1}{(TOF+\Delta t)^2}\right], \tag{6.8}$$

where Δt is the timing step. Assuming a constant timing step and distance between the start and stop detector, like in the experiment, the scattered neutron energy step will decrease as the TOF gets larger and the timing step becomes a smaller fraction of the neutron TOF. In other words, the energy step of the system improves as the neutron energy decreases. In the absence of improved timing resolution, the energy step can be reduced by increasing the distance between the start and stop detector, which increases the expected TOF for a given neutron energy. This again results in the timing step becoming a smaller proportion of the TOF and improves the energy step of the system across all neutron energies. Again, assuming a distance of 2.0 m between the start and stop detector and a timing step of 1.0 ns, the possible energy step for neutrons scattered at energies near 2.0, 7.5, and 12.0 MeV are approximately 0.04, 0.29, and 0.59 MeV, respectively.

Another potential limit to the precision of the VENES system is the resolution of the stop detector's angle relative to the start detector. For example, adjusting the stop detector's location in order to change the expected scattered neutron energy from 7.5 MeV to 7.6 MeV requires an adjustment of less than 0.0072 radians, or approximately 0.4 degrees. This type of alteration is possible, but requires precise movements with little room for error.

In practice, application of the VENES system will require some flexibility in regards to the energy of the scattered neutrons. The neutron energy peak will likely not be narrow enough, or precise enough, to fit completely in some of the neutron interaction cross section resonances. However, even if the neutron energy peak is wider than the resonance, many of the neutrons will still fall within it, altering the likelihood of interactions. Also, other neutron cross section

resonances are approximately the same size or larger than the potential neutron energy peaks, allowing for precise alignment. Combined, this makes the VENES system a good option for active neutron interrogation.

The simulated results provided a strong approximation of the laboratory setup. Although the peak maximums and FWHM were not precisely replicated, the simulated spectra behavior and peak shapes were consistent with what was seen in the laboratory results. Use of MCNP PoliMi simulations should be continued to further understand the neutron scattering process within the TOF system and help study its use in active neutron interrogation.

Based on experimental results, the new method of elastic scatter, confirmed via TOF measurements, appears to be an effective method of reliably reducing the energy of neutrons to a predetermined value. This was corroborated via simulations of both D-D and D-T neutrons. The VENES system is also portable and much less complicated than the large particle accelerators that are generally used to create neutrons of varying energies. Further study, both via laboratory measurements when possible, and simulations when necessary, is needed to see how this method can be applied to different types of active neutron interrogation, including pulsed fast neutron analysis, neutron elastic scatter, and neutron transmission measurements.

Conclusions

Both the experimental and simulated investigation of neutron elastic scatter of near-monoenergetic neutrons at specific angles were encouraging. The application of TOF measurements allows for both confirmation of the neutron energy and discrimination of source neutrons that did not interact in the scatter target. The VENES system provides a relatively easy means to create neutrons centered around an energy of the user's choosing, which could have

tremendous impact upon active interrogation methods in general. Potential challenges include the relatively low detection rate and, due to the volumes of the start and stop detectors, potentially broad energy range of elastically scattered neutrons. However, these can be partially corrected for with careful selection of the neutron generation rate, detector sizes, and relative component locations.

Future work will focus on the adoption of the VENES system to active neutron interrogation in search for conventional explosives. The potential to change the energy of source neutrons opens up many new avenues of study. Additional experimental and simulation work is needed to characterize the method and understand the effects of inserting an interrogation target.

Figures

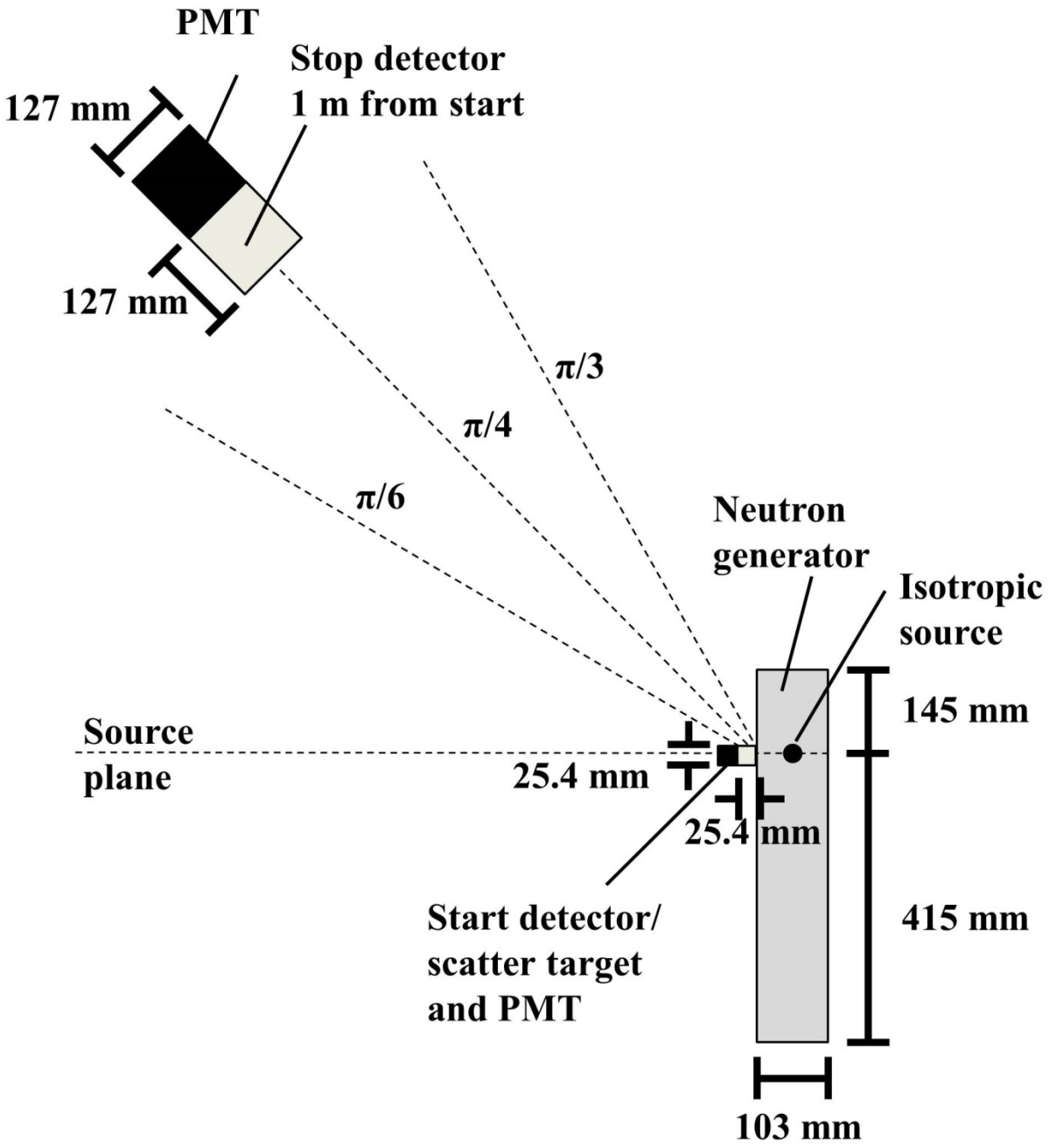

Fig. 6.1: A schematic view of the TOF system used to determine the energy of neutrons elastically scattered off the start detector.

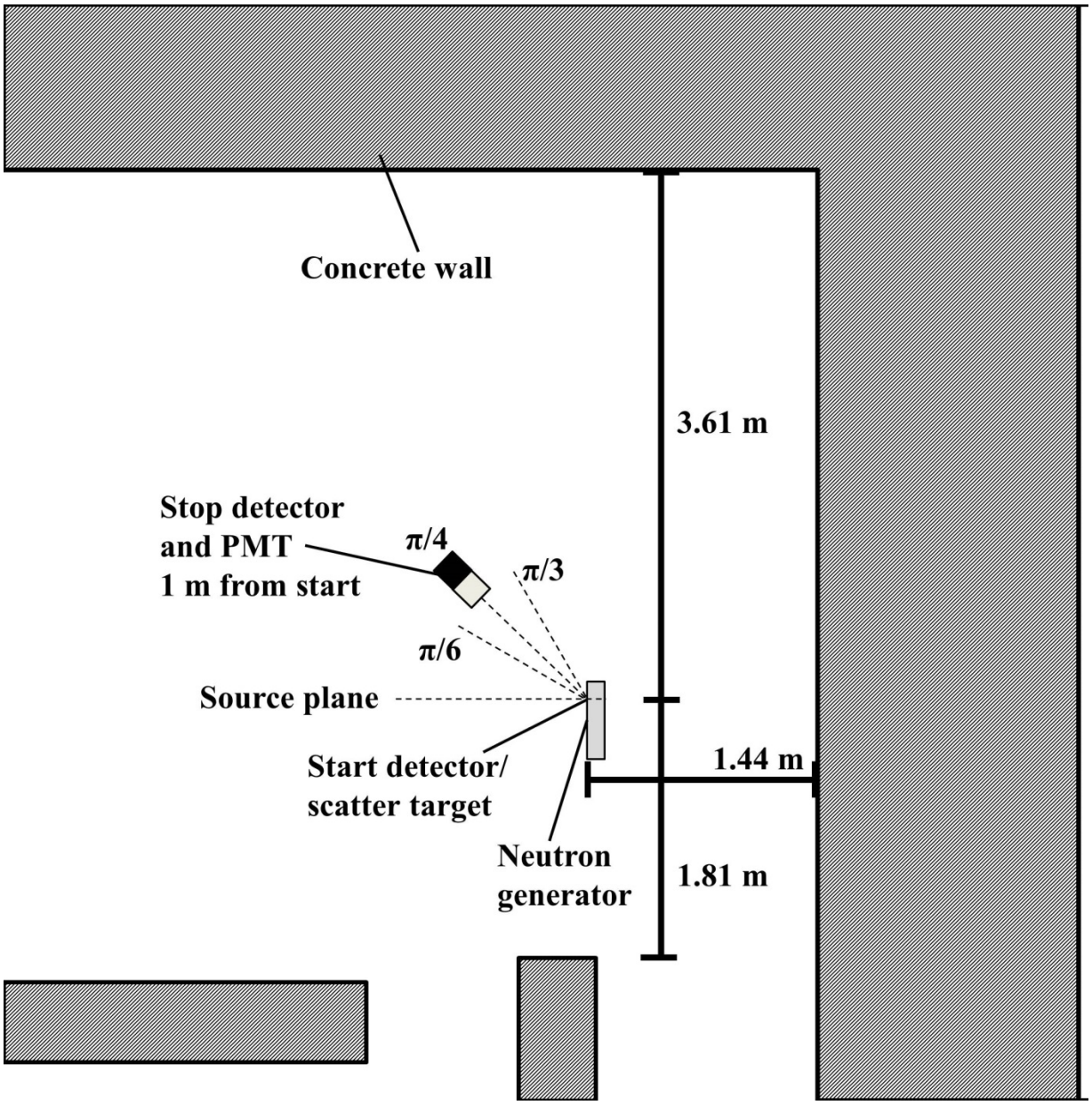

Fig. 6.2: A schematic view of the laboratory setup of the TOF experiment.

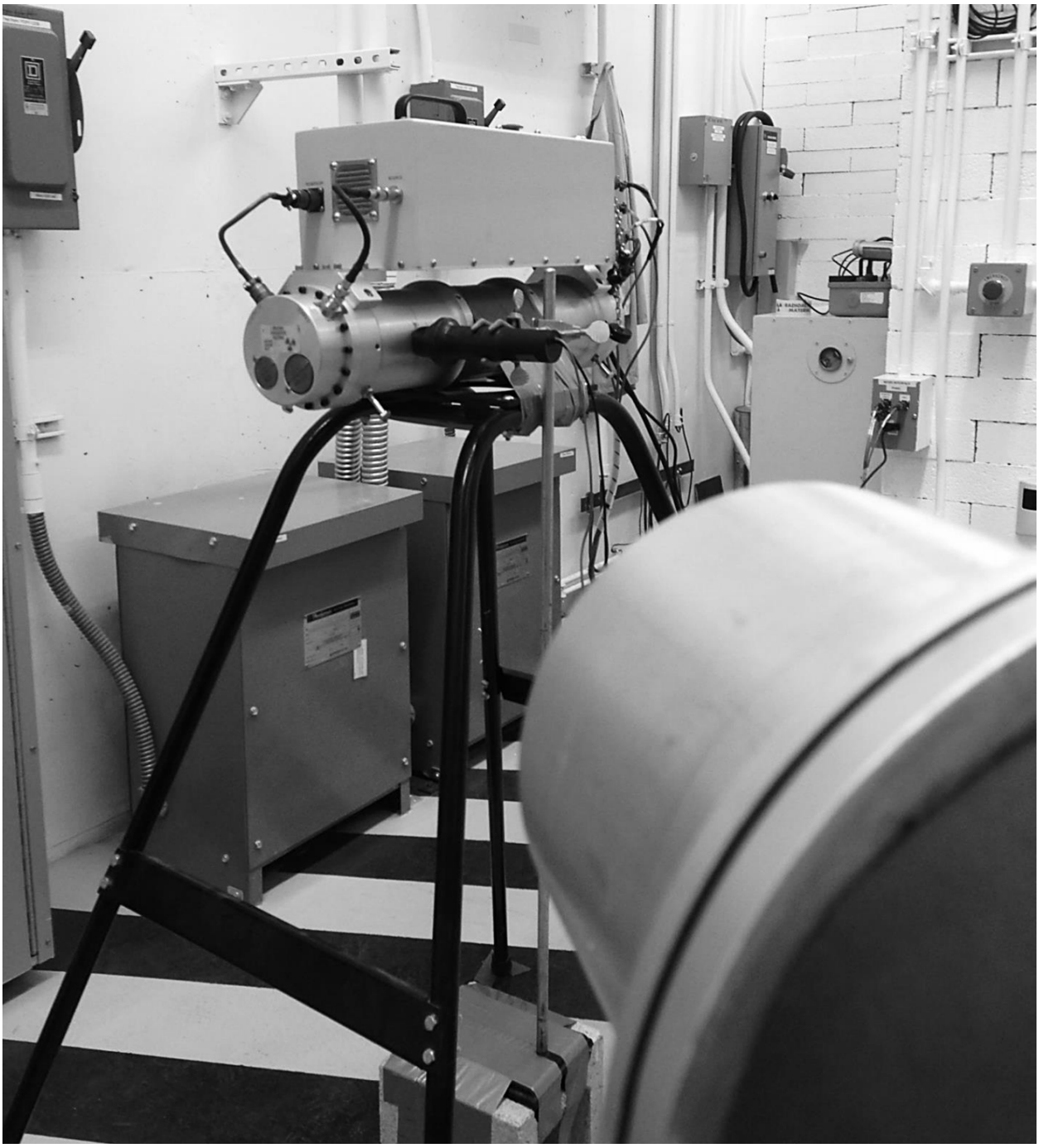

Fig. 6.3: An image from the experimental setup looking down the barrel of the stop detector towards the start detector and D-D neutron generator.

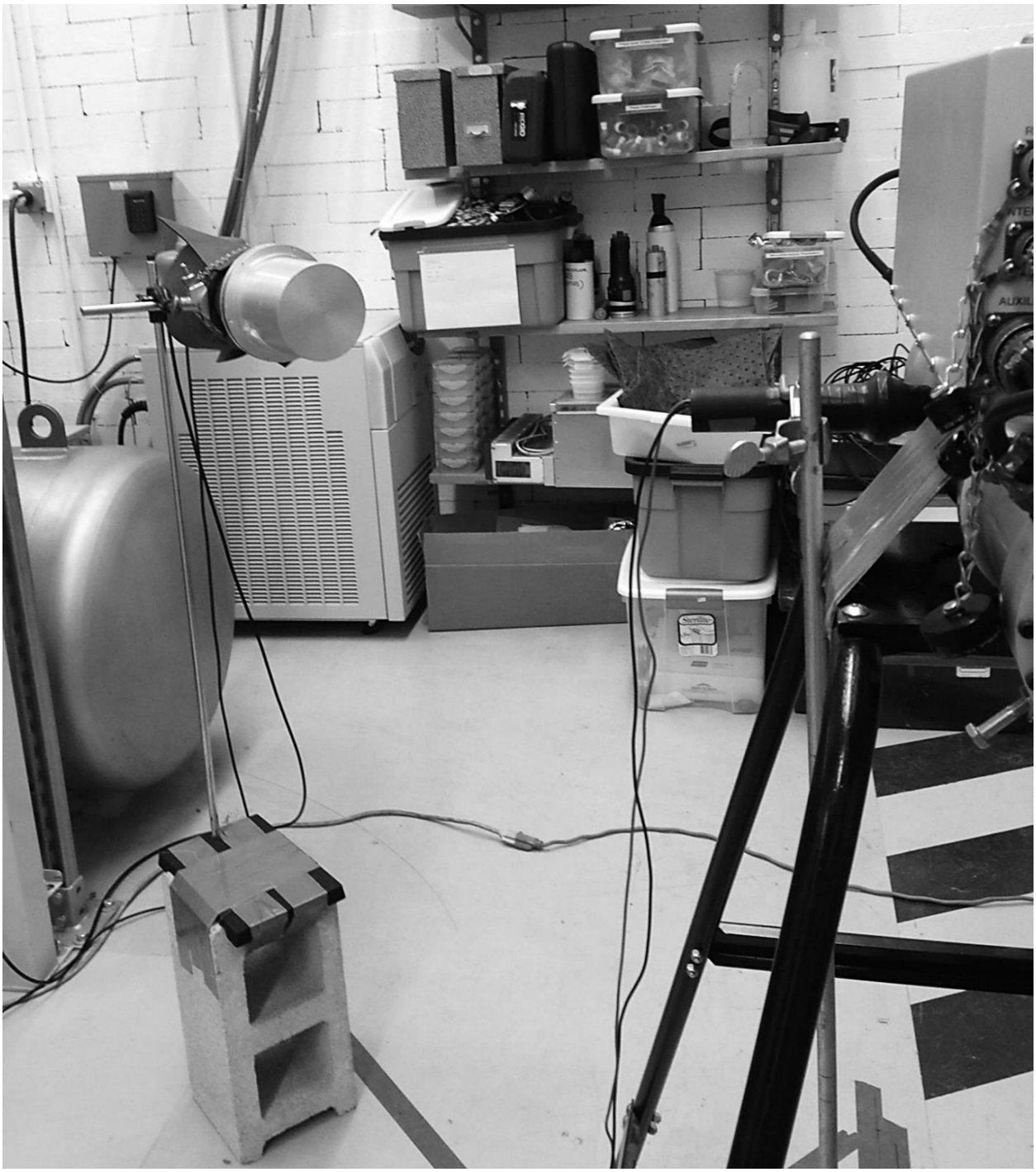

Fig. 6.4: An image from the experimental setup taken perpendicular to the D-D generator cylinder, with the start detector in the foreground and the stop detector in the background. All components have been elevated roughly 1.2 m off the ground.

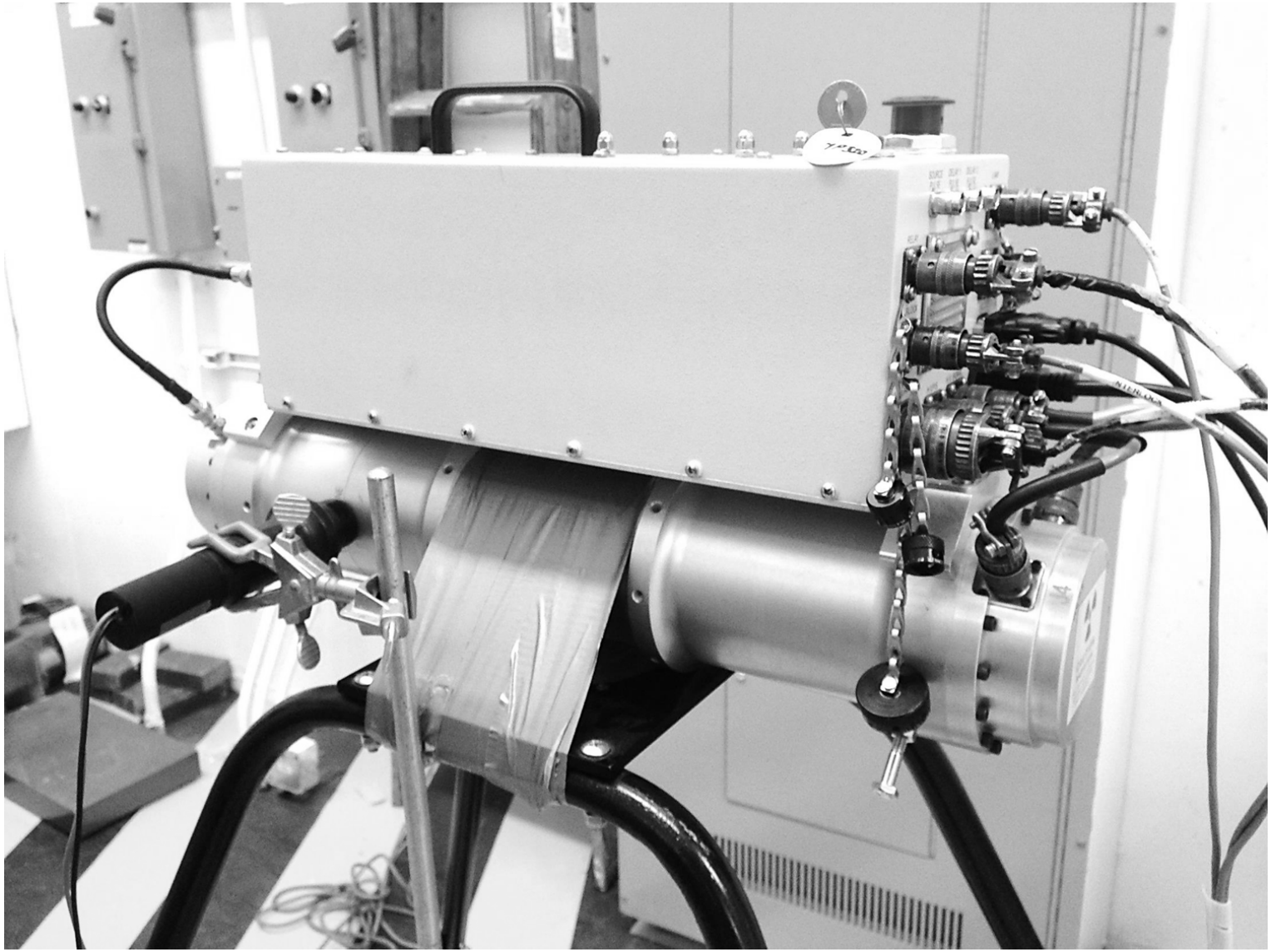

Fig. 6.5: An image of the neutron generator with the start detector in front of it.

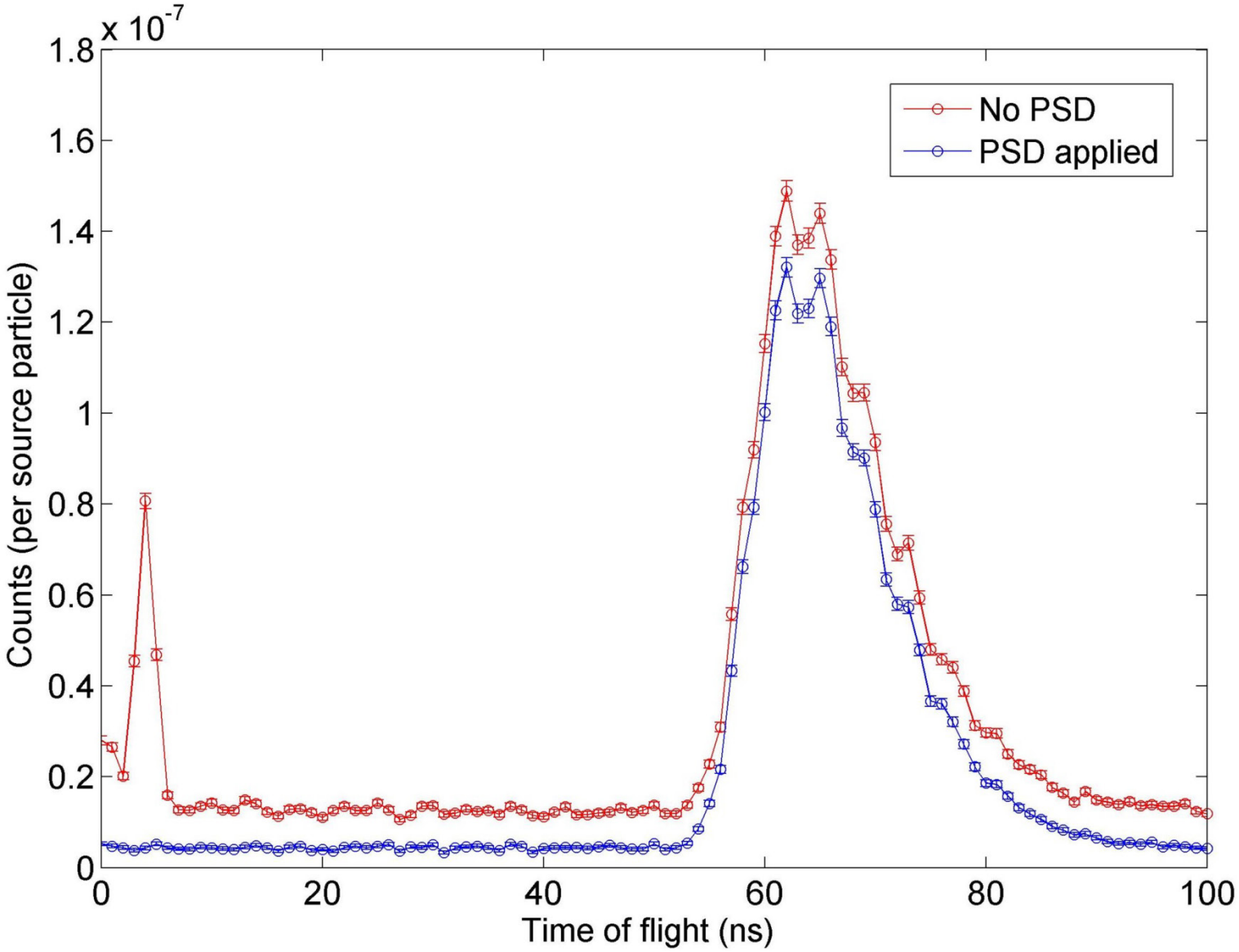

Fig. 6.6: A comparison of the experimental π/4 radians scatter spectra at 1.0 m, both with and without PSD.

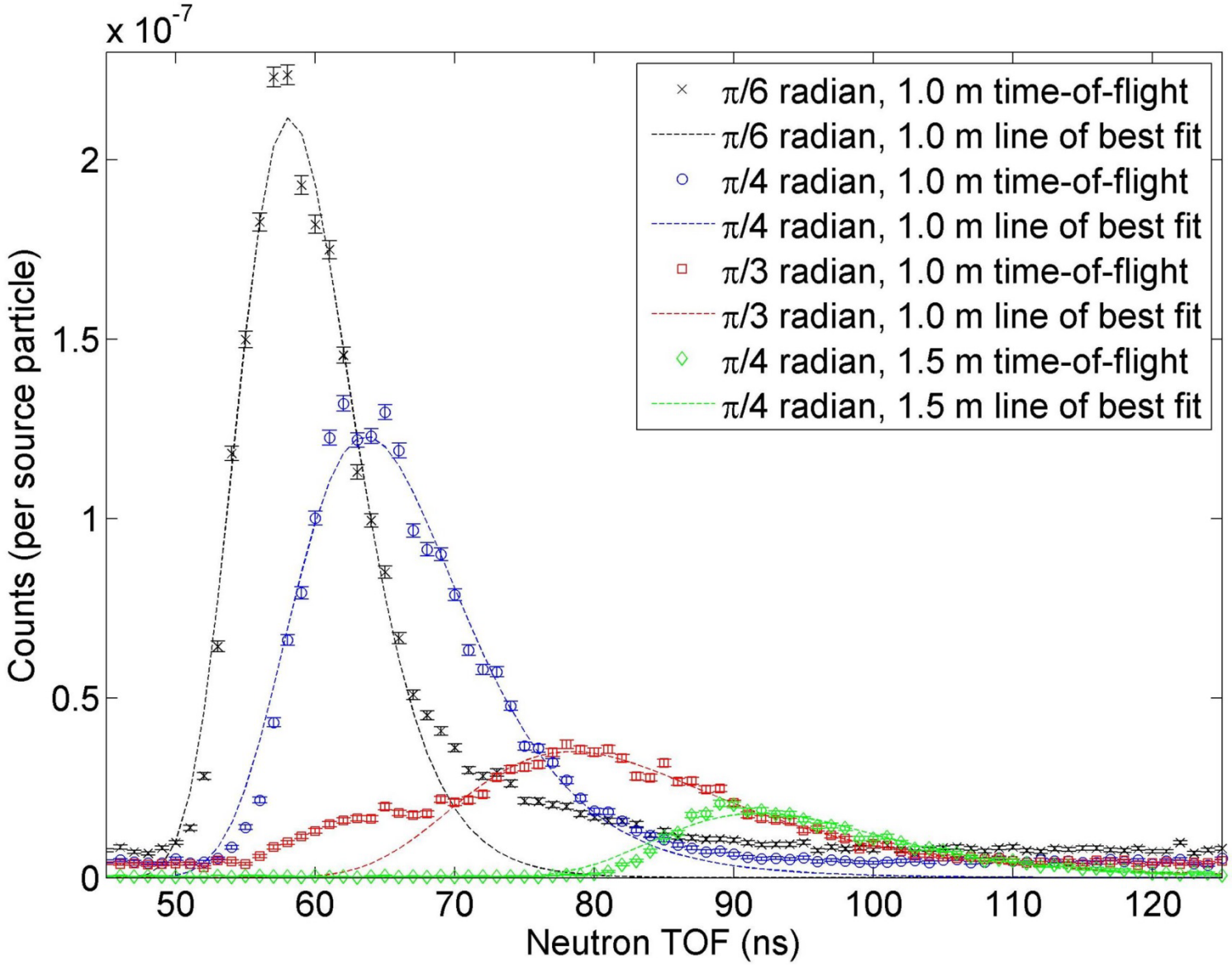

Fig. 6.7: The experimental D-D TOF spectra, including lines of best fit.

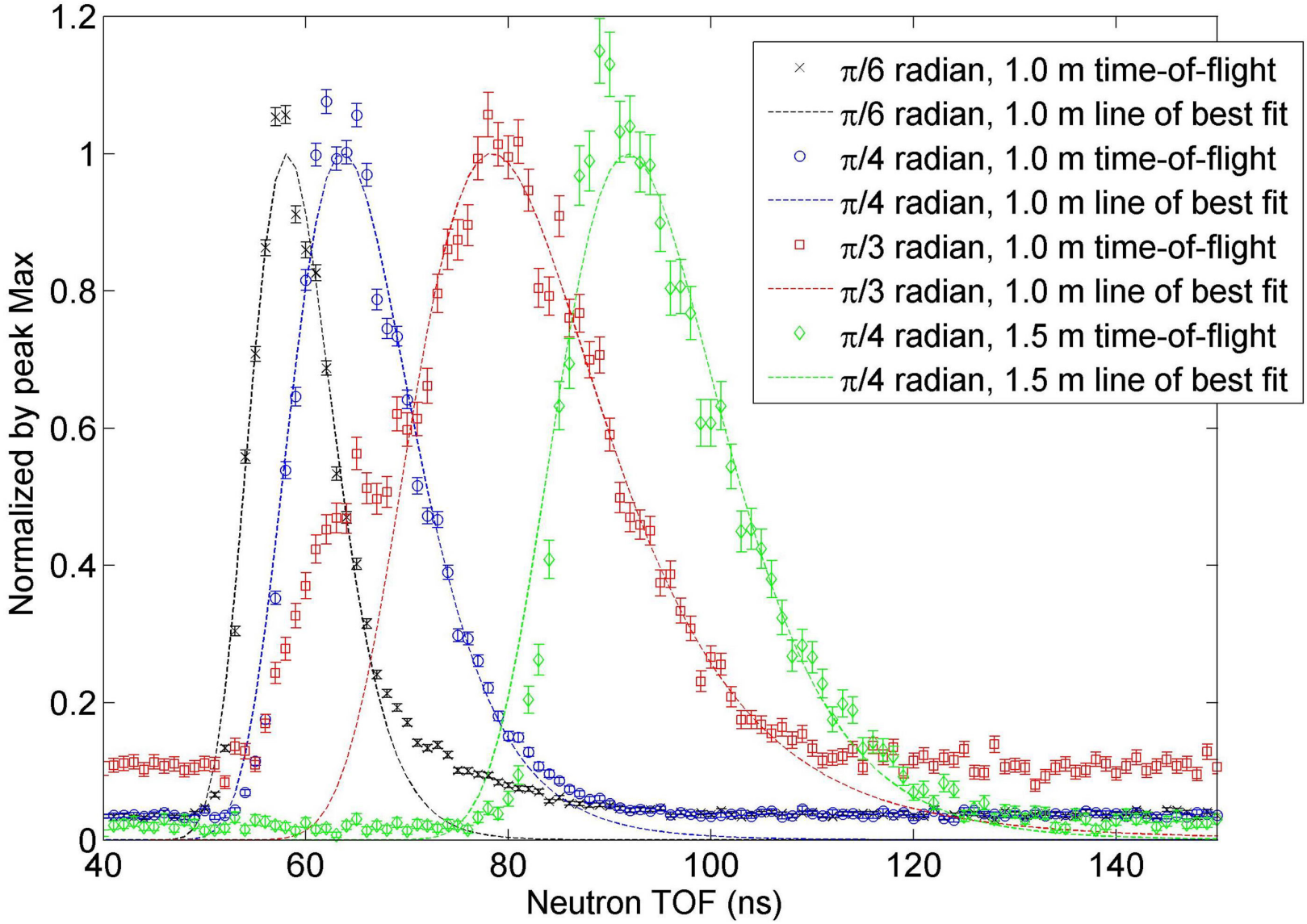

Fig. 6.8: The normalized experimental D-D TOF spectra.

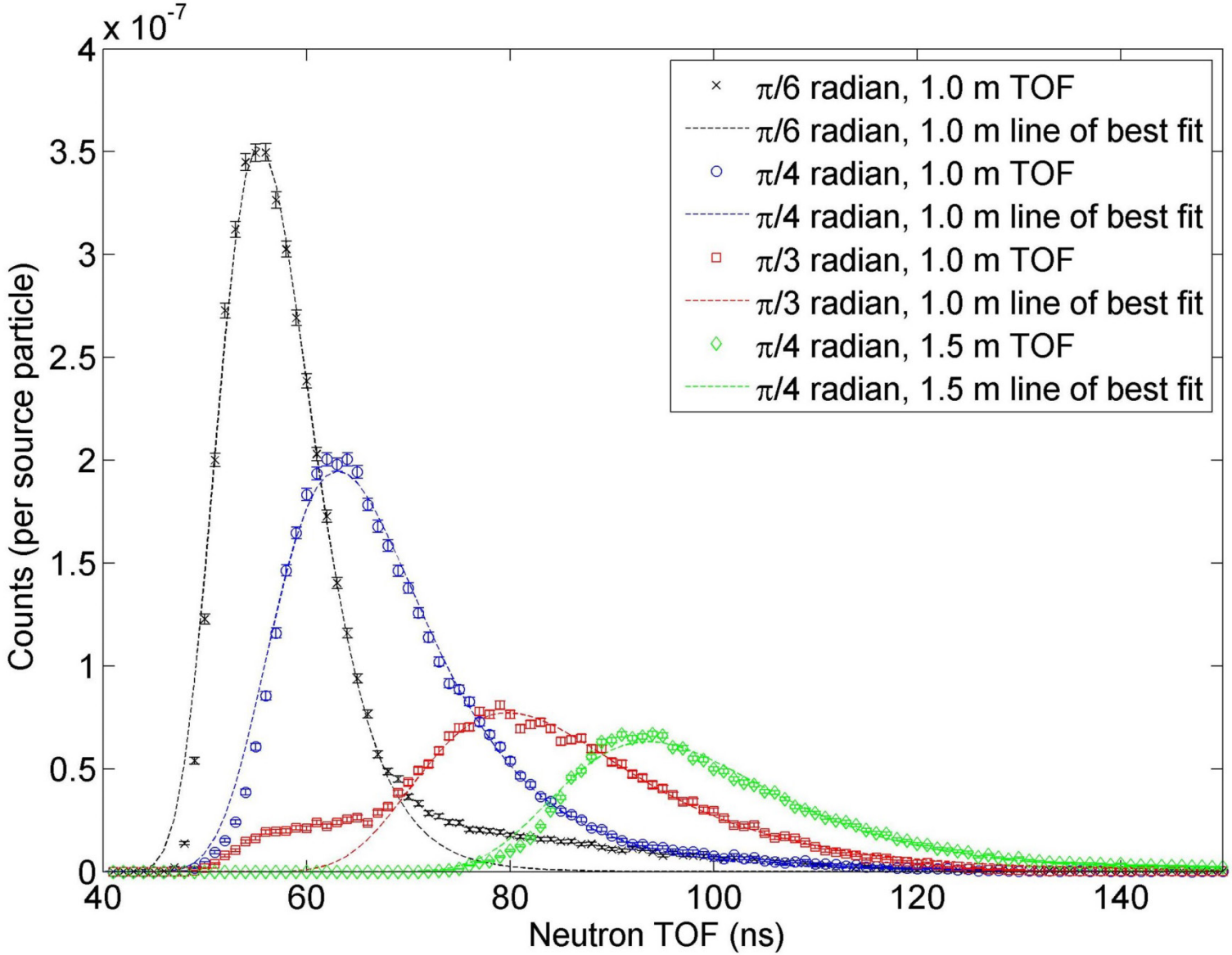

Fig. 6.9: The simulated D-D TOF spectra, including lines of best fit.

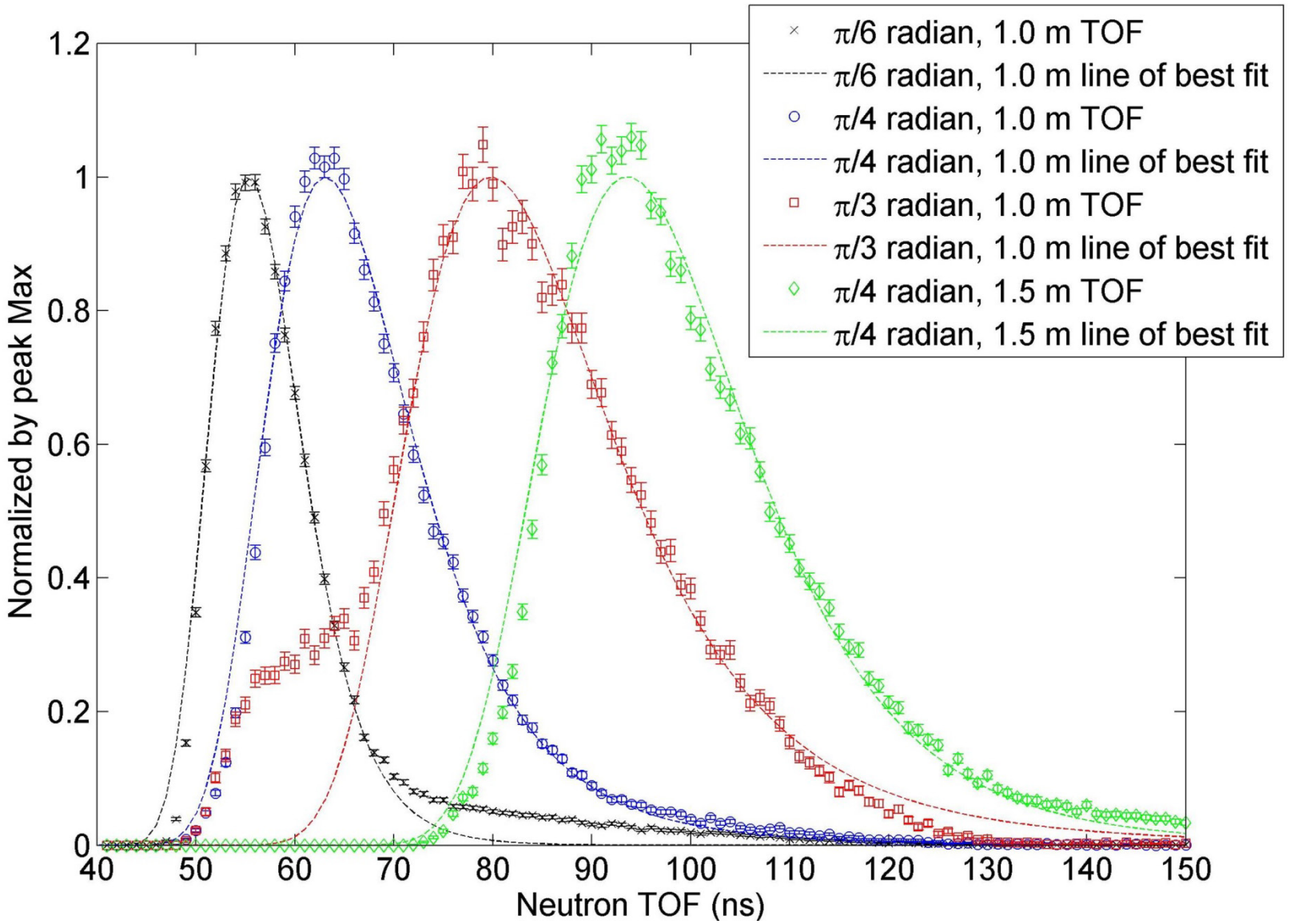

Fig. 6.10: The normalized simulated D-D TOF spectra.

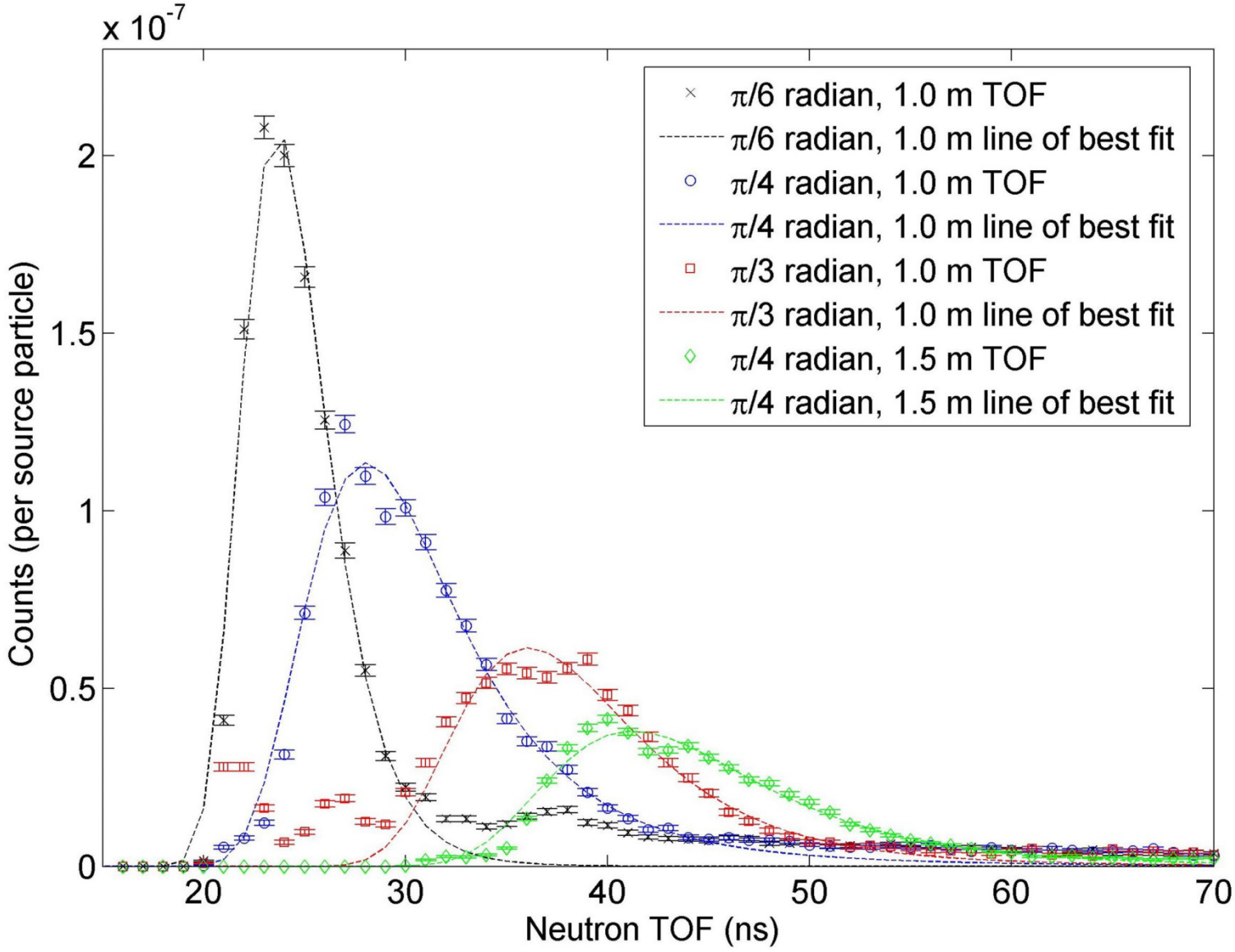

Fig. 6.11: The simulated D-T TOF spectra, including lines of best fit.

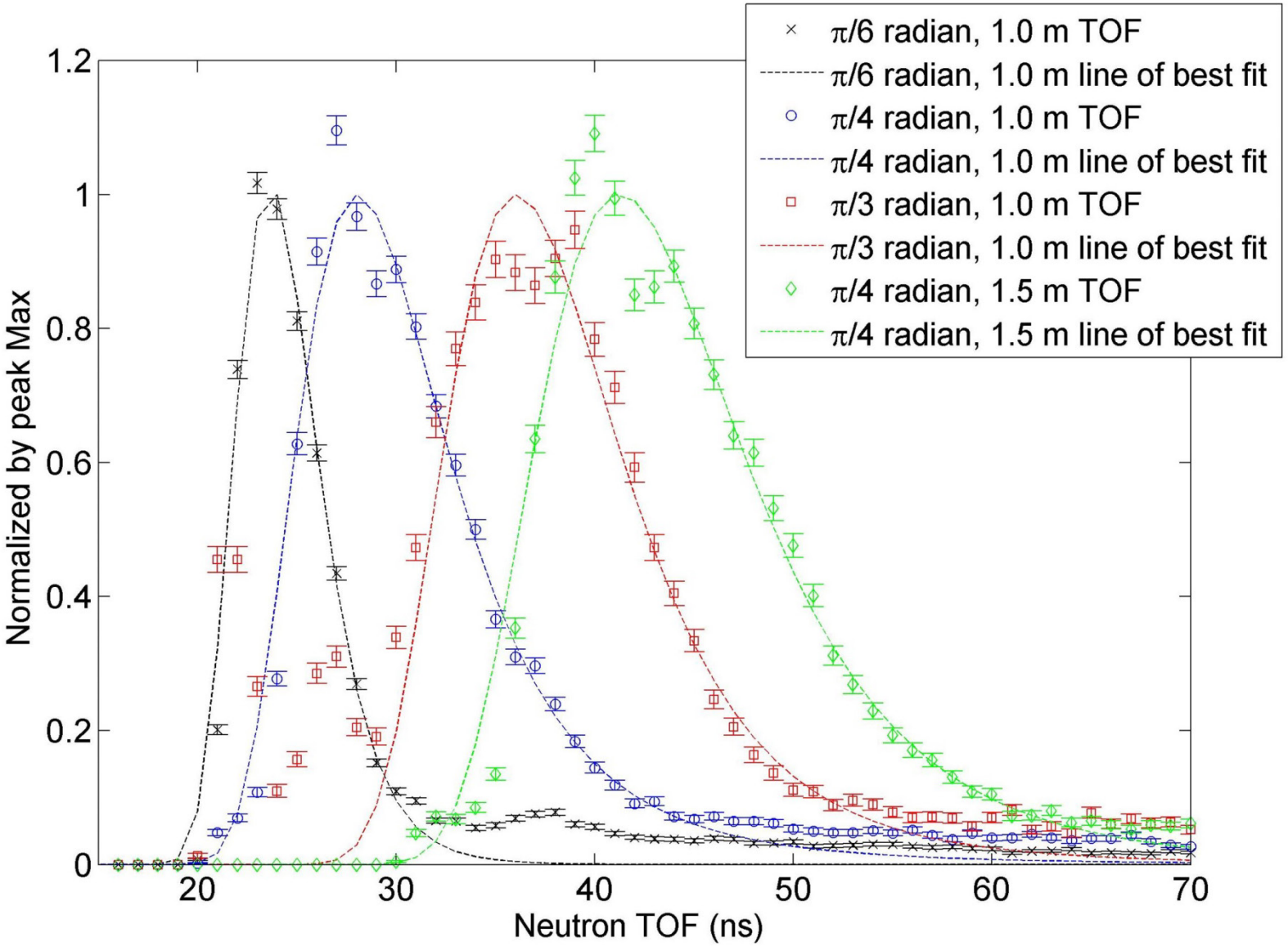

Fig. 6.12: The normalized simulated D-T TOF spectra.

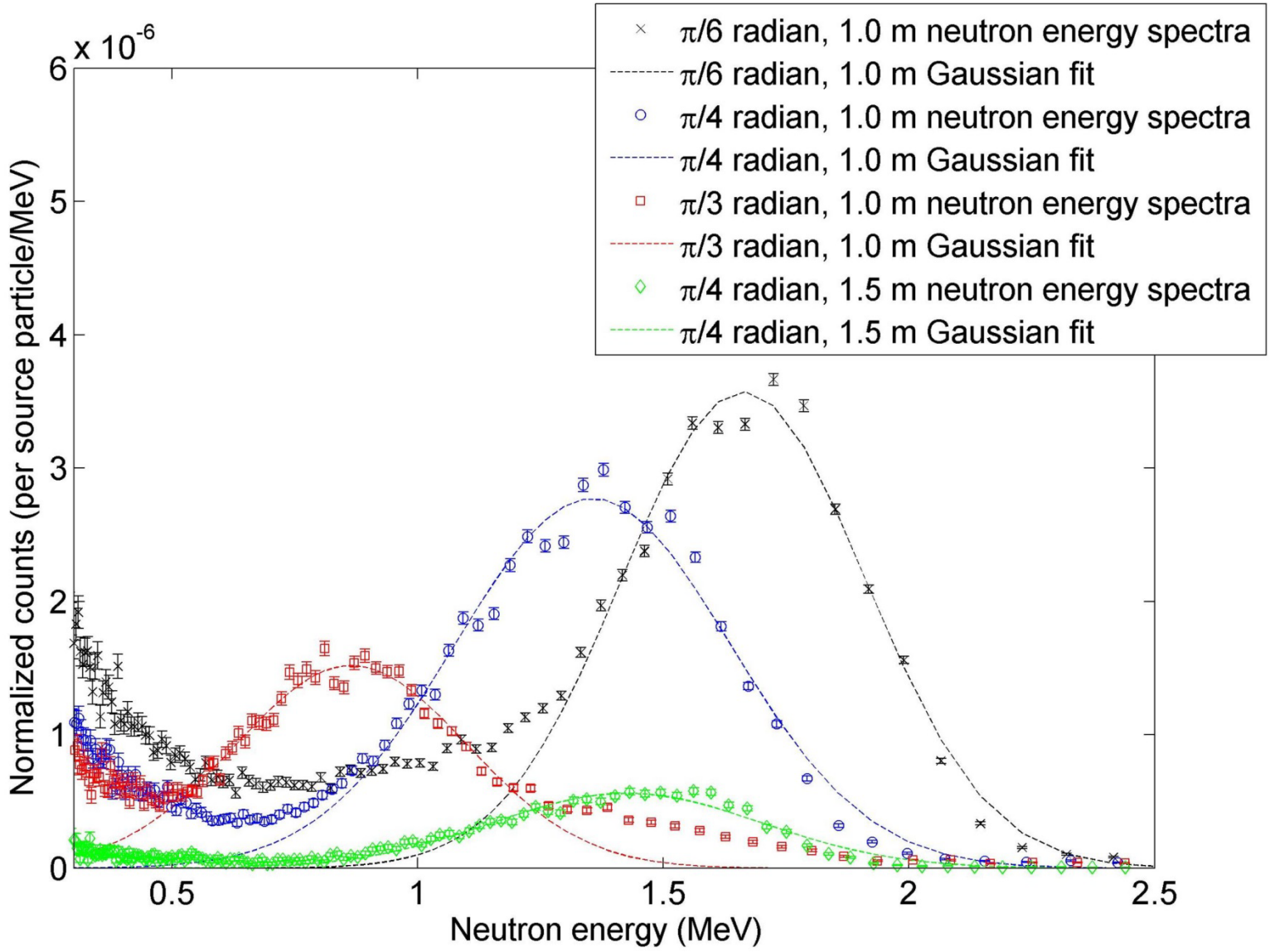

Fig. 6.13: The calculated experimental D-D scattered neutron energy spectra, normalized by the bin width.

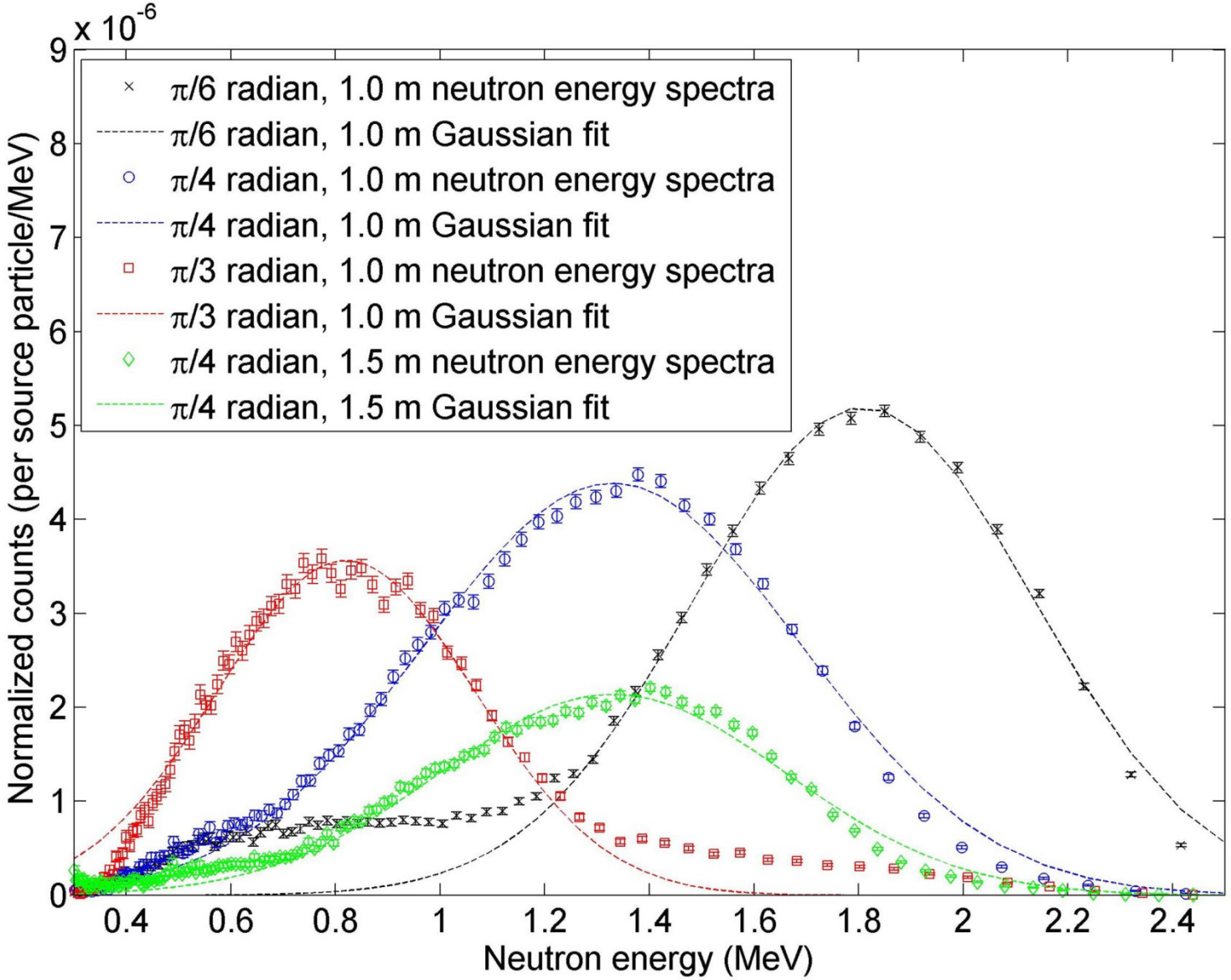

Fig. 6.14: The calculated simulated D-D scattered neutron energy spectra, normalized by the bin width.

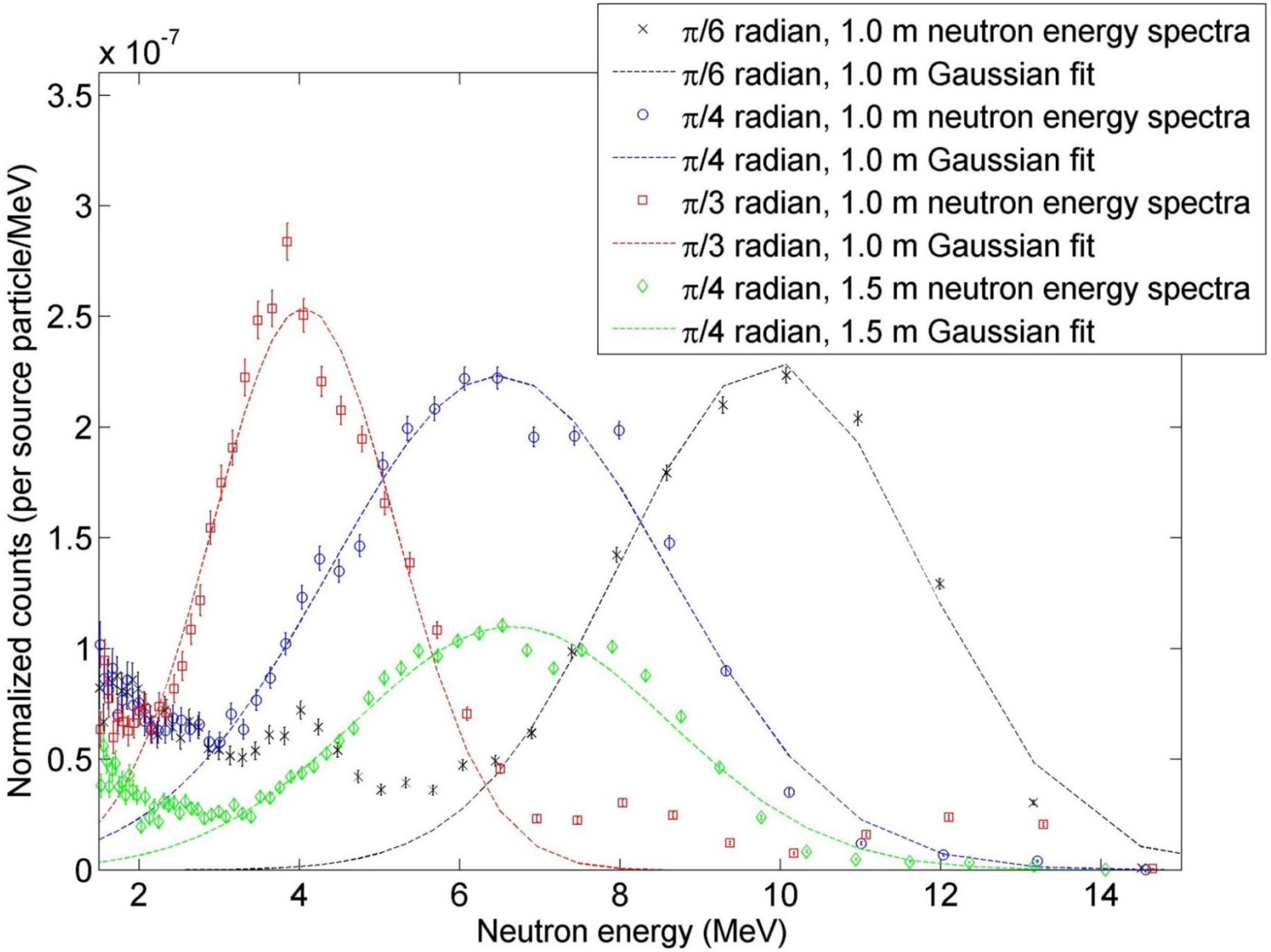

Fig. 6.15: The calculated simulated D-T scattered neutron energy spectra, normalized by the bin width.

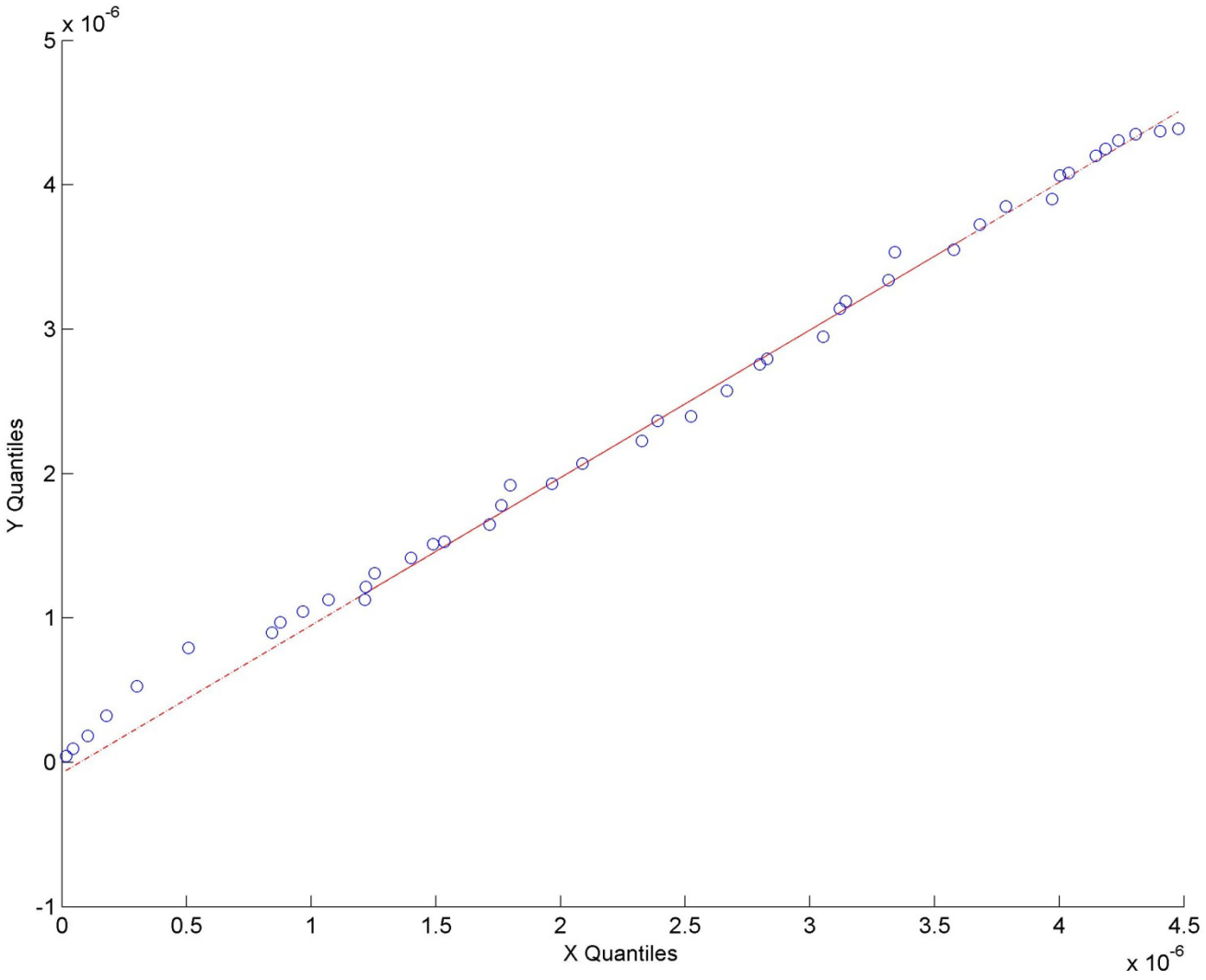

Fig. 6.16: An example quantile-quantile plot comparing scattered neutron energy data to the Gaussian fit. All generated plots had a similar, linear appearance.

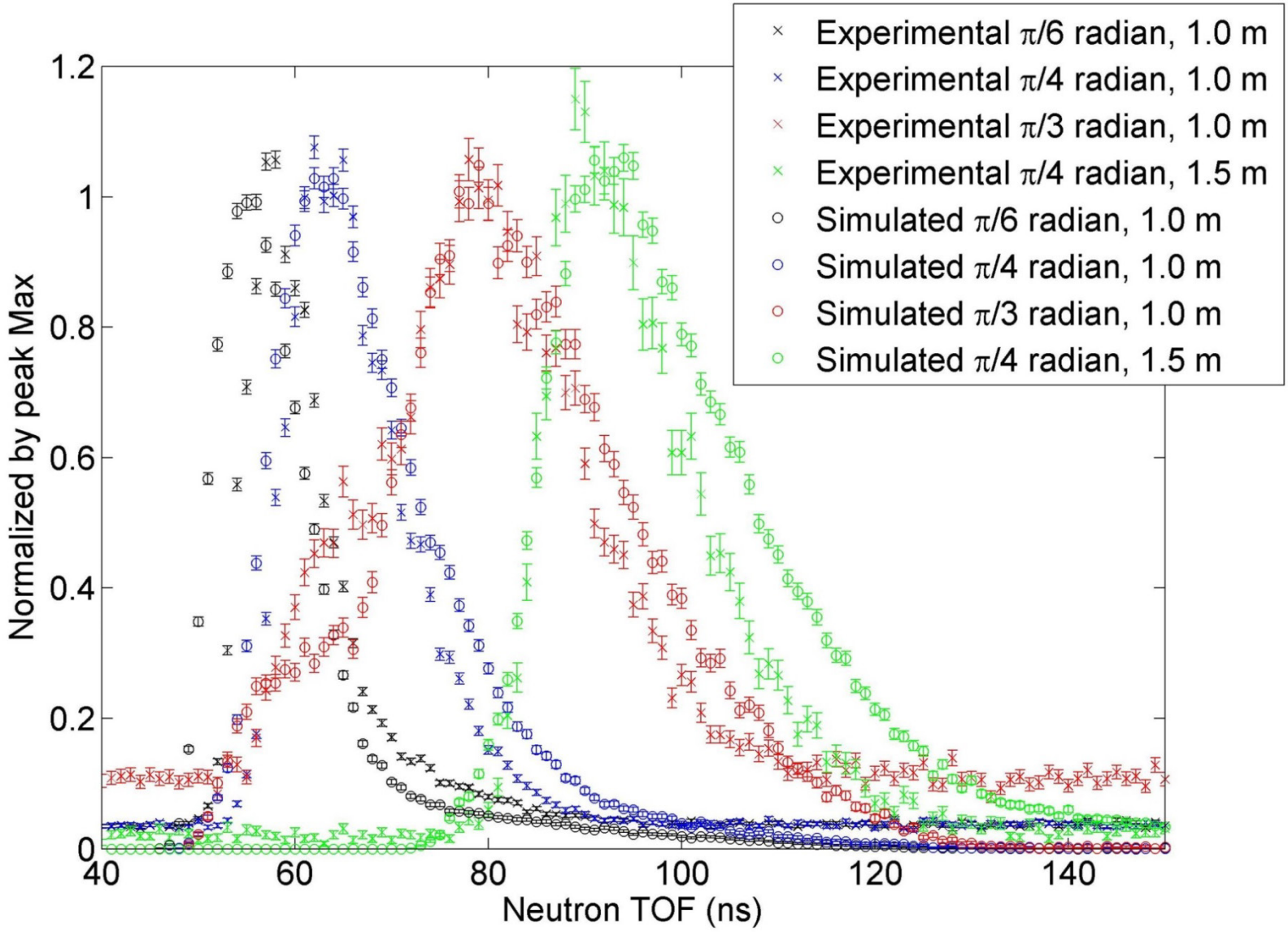

Fig. 6.17: A comparison of the normalized experimental and simulated D-D TOF spectra.

Tables

Table 6.1: The TOF and energy peak information based on the Gaussian curve fit to the energy spectra and transformed to the TOF spectra.

			TOF - line of best fit					Energy - Gaussian fit			
Data set	ψ (radians)	d (m)	Peak maximum (per source particle)	Observed peak mode (ns)	Predicted peak mode (ns)	% difference	Estimated FWHM (ns)	Peak maximum (source particle^{-1} MeV^{-1})	Peak center (MeV)	FWHM (MeV)	r^2
	π/6	1.0 m	2.12×10^{-7}	58	56	3.6	9.6	3.57×10^{-7}	1.66	0.58	0.972
Experimental	π/4	1.0 m	1.23×10^{-7}	64	69	-7.3	14.2	2.77×10^{-6}	1.36	0.66	0.978
D-D	π/3	1.0 m	3.51×10^{-8}	78	99	-21	20.9	1.52×10^{-6}	0.87	0.56	0.944
	π/4	1.5 m	1.80×10^{-8}	92	101	-8.9	19.4	5.62×10^{-7}	1.43	0.65	0.947
	π/6	1.0 m	3.52×10^{-7}	55	56	-1.8	11.2	5.19×10^{-6}	1.81	0.77	0.993
Simulated	π/4	1.0 m	1.94×10^{-7}	63	69	-8.7	18.3	4.37×10^{-6}	1.33	0.85	0.992
D-D	π/3	1.0 m	7.72×10^{-8}	80	99	-19	25.1	3.56×10^{-6}	0.82	0.58	0.978
	π/4	1.5 m	6.32×10^{-8}	94	101	-6.9	25.2	2.14×10^{-6}	1.33	0.78	0.982
	π/6	1.0 m	2.04×10^{-7}	24	24	0.0	5.1	2.30×10^{-7}	9.87	4.40	0.987
Simulated	π/4	1.0 m	1.14×10^{-7}	28	29	-3. 5	9.4	2.23×10^{-7}	6.49	4.98	0.976
D-T	π/3	1.0 m	6.15×10^{-8}	36	42	-14	10.9	2.54×10^{-7}	4.06	2.71	0.948
	π/4	1.5 m	3.80×10^{-8}	41	43	-4.7	12.8	1.10×10^{-7}	6.65	4.63	0.959

Table 6.2: The percent differences between the experimental and simulated D-D data, based on the lines of best fit.

ψ (radians)	d (m)	Peak maximum	Peak mode	Estimated FWHM
π/6	1.0 m	-66.6	5.2	-16.4
π/4	1.0 m	-58.0	1.6	-28.5
π/3	1.0 m	-120	-2.6	-20.1
π/4	1.5 m	-251	-2.2	-30.3

References

Csikai, J., 1987. CRC Handbook of Fast Neutron Generators, Volume 1.(CRC Press, Boca Raton, FL). pp. 9-11.

Detection for Nuclear Nonproliferation Group, University of Michigan, Ann Arbor, MI, 2014a. Personal conversations. February 5-18.

Detection for Nuclear Nonproliferation Group, University of Michigan, Ann Arbor, MI, 2014b. Personal email correspondence. June 9 – 13.

Enqvist, A., Lawrence, C.C., Wieger, B.M., Pozzi, S.A., Massey, T.N., 2013. Neutron light output response and resolution functions in EJ-309 liquid scintillation detectors. *Nucl. Instrum. Methods Phys. Res. A*, 715, 79-86.

Flaska, M., Pozzi, S.A., 2007. Identification of shielded neutron sources with the liquid scintillator BC-501A using a digital pulse shape discrimination method. *Nucl. Instrum. Methods Phys. Res. A*, 577 (3), 654-663.

Kaplan, A.C., Flaska, M., Enqvist, A., Dolan, J.L., Pozzi, S.A., 2013. EJ-309 pulse shape discrimination performance with a high gamma-ray-to-neutron ratio and low threshold. *Nucl. Instrum. Methods Phys. Res. A*, 729, 463-468.

Lehnert, A.L., Kearfott, K.J., 2010. The detection of explosive materials: review of considerations and methods. *Nucl. Technol.*, 172 (3), 325 – 334.

Lehnert, A.L., Flaska, M., Kearfott, K.J., 2012. D-D neutron-scatter measurements for a novel explosives-detection technique. *Nucl. Instrum. Meth. A*, 693, 195-202.

Lehnert, A.L., Kearfott, K.J., 2014. Simulations for developing a flag-based active neutron interrogation method for explosives detection in sea-land cargo containers. *Nucl. Technol.*, 188 (1), 97 – 111.

Miller, E.C., Clarke, S.D., Flaska, M., Pozzi, S.A., Padovani, E., 2012. MCNPX-PoliMi post-processing algorithm for detector response simulations. *J Nucl Mater Manag*, 40 (2), 34-41.

National Nuclear Data Center. 2014. Interactive Chart of the Nuclides level schemes for ^{9}Be, ^{12}C, and ^{16}O. Brookhaven National Laboratory. Online, accessed November 12, 2014. http://www.nndc.bnl.gov/chart/.

Overley, J.C., Chmelik, M.S., Rasmussen, R.J., Schofield, R.M.S., Sieger, G.E., Lefevre, H.W., 2006. Explosives detection via fast neutron transmission spectroscopy. *Nucl. Instrum. Meth. B*, 251 (2), 470-478.

Pozzi, S.A., Clarke, S.D., Flaska, M., Peerani, P., 2009. Pulse-height distributions of neutron and gamma rays from plutonium-oxide samples. *Nucl. Instrum. Methods Phys. Res. A*, 608 (2), 310-315.

Pozzi, S.A., Padovani, E., Marseguerra, M., 2003. MCNP-PoliMi: a Monte-Carlo code for correlation measurements. *Nucl. Instrum. Methods Phys. Res. A*, 513 (3), 550-558.

Sowerby, B.C., Tickner, J.R., 2007. Recent advances in fast neutron radiography for cargo inspection. *Nucl. Instrum. Meth. A*, 580 (1), 799-802.

Strellis, D., Gozani, J., Stevenson, J., 2009. Air cargo inspection using pulsed fast neutron analysis. *International Topical Meeting on Nuclear Research Applications and Utilization of Accelerators*, *Vienna, Austria, May 4-8, 2009*.

Thermo Fischer Scientific Inc., Waltham, MA, 2014. Personal phone and email correspondence. June 17 – 23.

Whetstone, Z.D., Kearfott, K.J., 2014. A review of conventional explosives detection using active neutron interrogation. *J. Radioanal. Nucl. Ch.*, 301 (3), 629-639.

Whetstone, Z.D., Kearfott, K.J., 2015. A method for using neutron elastic scatter to create a variable energy neutron beam from a nearly monoenergetic source. *Radiat. Phys. Chem.*, 112, 21-28.

CHAPTER 7: APPLICATION OF A VARIABLE ENERGY NEUTRON BEAM TO SEARCH FOR CONVENTIONAL EXPLOSIVES USING FAST NEUTRON RESONANCE RADIOGRAPHY

Abstract

Application of the variable energy neutron elastic scatter (VENES) system to fast neutron resonance radiography (FNRR) was investigated for detection of conventional explosives. Preliminary work focused on laboratory measurements of transmission rates using neutrons whose energy had been reduced to roughly 1.25 MeV by the VENES system in conjunction with a deuterium-deuterium (D-D) generator. Transmission ratios varied between 0.0327 $\pm$ 0.0004 and 0.559 $\pm$ 0.003. Monte Carlo simulations were used to benchmark future work, with transmission measurement uncertainties ranging between 73 and -36%. The FNRR method was simulated using a D-D and deuterium-tritium generator to obtain neutrons with energies ranging from 1.0 to 11.8 MeV. Using the least squares method, the elemental composition of nearly all materials tested was correctly identified, with the only exceptions being the misclassification of the presence of less than 0.006 atomic fractions of nitrogen in paper, toluene, and vegetable oil. In general, the largest difference in calculated atomic fraction was 0.013. The results encourage further exploration of FNRR and investigation of methods to improve the VENES system efficiency.

Introduction

Conventional explosives can cause significant damage to people and property. Given the persistent threat of terrorism and relative ease at which explosives can be obtained and used, it is important to continually investigate new and improved explosives detection methods. One field of study is based on active neutron interrogation, which directs neutrons at an unknown target in order to help determine if explosives are present. There are many different approaches to active neutron interrogation that vary in execution, however, they all attempt to identify unique relative elemental concentrations of one or more of the following: hydrogen, carbon, nitrogen, and oxygen (Buffler, 2004; Buffler and Tickner, 2010; Whetstone and Kearfott, 2014). Of particular note is relatively high nitrogen content (Gozani, 1994; National Research Council, 2004).

Traditionally, the neutron sources used in active interrogation are either based on constantly decaying radioactive materials, such as a ^{252}Cf or a combination plutonium and beryllium source, or on particle accelerators that initiate fusion reactions, such as deuterium-deuterium (D-D) or deuterium-tritium (D-T) generators (Knoll, 2010). The neutrons from radioactive decay have a broad energy spectrum, ranging across several MeV, while D-D and D-T generators create nearly monoenergetic neutrons centered on 2.5 and 14.1 MeV, respectively. However, none of these sources may be ideal when trying to determine if an unknown target contains explosive materials.

As seen in Fig. 7.1, the likelihood of neutron-nuclear interactions varies significantly and is uniquely dependent on the incident neutron energy (National Nuclear Data Center, 2015). Many of the largest cross-section resonances occur between 1 and 10 MeV. Therefore, the ideal source is one that has the ability to create nearly monoenergetic neutrons across a range of different energies, allowing the user to tune the neutron energy to what is appropriate for the

application. This can already be accomplished through large particle accelerators, but the systems are significantly more complicated than other neutron sources and carry much higher costs.

Fortunately, an alternative to accelerators has been developed. As discussed in Ch. 5 and 6, elastically scattering nearly monoenergetic D-D or D-T neutrons off a scatter target containing nuclei of known mass, and detecting them at a specific and adjustable angle, results in a source of neutrons with consistent and variable energy (Whetstone and Kearfott, 2015). This can be confirmed via neutron time-of-flight (TOF) measurements. The variable energy neutron elastic scatter (VENES) system described in Ch. 6 uses an organic scintillator as both the scatter target and a start detector to calculate TOF. Some of the source neutrons will elastically scatter off the hydrogen in the scintillator and create a start pulse. Some of these neutrons will then interact in the stop detector, creating the stop pulse. Assuming a single elastic scatter and an unattenuated flight path, the scattered neutron energy, E_n', should correspond to:

$$E'_{\mathrm{n}} = \frac{E_{\mathrm{n}}}{(m_s+m_n)^2}\left[m_n^2 cos(2\psi) + 2m_n cos\psi\sqrt{m_s^2 - m_n^2 sin^2\psi} + m_s^2\right], \tag{7.1}$$

where E_n is the initial neutron energy, m_s is the mass of the scatter nucleus, m_n is the mass of the neutron, and ψ is the scatter angle in the laboratory system (Whetstone and Kearfott, 2015). The scattered neutron energy can be confirmed via the neutron TOF. Compared to accelerators, this method is relatively cheap, compact, and simple.

This new method for tuning neutrons can potentially be applied to a variety of explosives detection active neutron interrogation techniques, including Fast Neutron Resonance Radiography (FNRR). In FNRR, fast neutrons with energies in the MeV range are directed at an

interrogation target and the change in transmission across that energy range provides information as to the composition of the target (Chen et al., 2001; Chen and Lanza; 2002). Fig. 7.1 shows that carbon, nitrogen, and oxygen all have localized regions of high and low attenuation at different energies, while hydrogen's attenuation cross section steadily declines as neutron energy increases. By carefully observing the changes in neutron transmission for neutrons of specific energies, it is possible to determine the elemental densities present in the interrogation target.

One current method of producing neutrons of variable energy for transmission measurements requires accelerating 4.2 MeV deuterons into a beryllium metal target, which creates neutrons with a broad spectrum of energies and whose spectroscopic information is determined via neutron TOF (Overley et al., 2006). Another option necessitates accelerating deuterium ions up to several MeV in a radio-frequency quadrupole (RFQ) accelerator before impact with a deuterium target (Lanza, 2007). This results in neutrons whose final energies, due to conservation of momentum, are functions of the angle of the neutrons' initial flight paths relative to the incident deuterium ion beam. A previously proposed system had possible neutron energies between 1.67 and 5.13 MeV (Raas et al., 2005). By using a D-T neutron generator with the recently developed VENES system, the larger accelerators could be replaced, allowing for more portability and a theoretical range of neutrons between 0 and 14.1 MeV. The preferred neutron energies can be determined through analysis of the total neutron attenuation cross section spectra for all nuclides of interest. Assuming an initial neutron energy, E_n, of 2.5 MeV for a D-D source and 14.1 MeV for a D-T source, and provided the user knows the mass of the nuclides in the scatter target, the necessary scatter angle required for a desired final scatter neutron energy can be calculated with (Whetstone and Kearfott, 2015):

$$\psi = \tan^{-1}\left\{\frac{\sqrt{1-\left[1-\frac{(m_S+m_n)^2}{2m_S m_n}\left(1-\frac{E'_{\mathrm{n}}}{E_{\mathrm{n}}}\right)\right]^2}}{1-\frac{(m_S+m_n)^2}{2m_S m_n}\left(1-\frac{E'_{\mathrm{n}}}{E_{\mathrm{n}}}\right)+\frac{m_n}{m_S}}\right\}. \tag{7.2}$$

Because an interrogation target has unknown concentrations of H, C, N, and O, several transmission measurements are required (Raas et al., 2005). In order to get the greatest theoretical contrast in transmission and accurately determine the mass attenuation coefficients of the elements of interest, transmission measurements should be conducted at energies where there is a large difference between the various nuclides' attenuation cross sections. Adopting the nomenclature from the previous work of other researchers, the neutron count rate in the detector for each measurement should be a function of the product of the mass attenuation cross section and mass thickness for each nuclide (Chen et al., 2001; Chen and Lanza, 2002). This results in a set of equations:

$$\begin{gathered}
a_{1,1}x_1 + a_{1,2}x_2 + a_{1,3}x_3 + \ldots + a_{1,n}x_n = b_1 \\
a_{2,1}x_1 + a_{2,2}x_2 + a_{2,3}x_3 + \ldots + a_{2,n}x_n = b_2 \\
a_{3,1}x_1 + a_{3,2}x_2 + a_{3,3}x_3 + \ldots + a_{3,n}x_n = b_3 \\
\vdots \\
a_{i,1}x_1 + a_{i,2}x_2 + a_{i,3}x_3 + \ldots + a_{i,j}x_j = b_i \\
\vdots \\
a_{m,1}x_1 + a_{m,2}x_2 + a_{m,3}x_3 + \ldots + a_{m,n}x_n = b_m,
\end{gathered} \tag{7.3}$$

where $a_{i,j}$ represents the mass attenuation coefficient at neutron energy i of nuclide j, x_j represents the density thickness of nuclide j, and b_i is the neutron transmission at energy i, as determined by the negative logarithm of the ratio of the neutron count rate in the detector when a transmission target is and is not present. If the values of $a_{i,j}$ are known, least squares fitting is used to find the optimal solution to this set of equations, providing estimates of the mass thickness of each nuclide, with the only constraint being that the number of measurements, and hence number of equations, m, must be larger than the number of nuclides that are being solved for, n. The final result is an estimate of the relative amounts of H, C, N, and O present in the sample.

Compared to the work by Raas et al. (2005), the range in energy of the neutrons produced using the VENES system will be significantly broader due to the systematic uncertainty discussed in Ch. 5 (Whetstone and Kearfott, 2015). This is a result of the varied neutron interaction locations in both the start and stop detector creating an array of neutron scatter angles and energies. Although this system cannot precisely tune the neutron energy to a specific resonance peak or valley, it can still be used to determine the average attenuation across a fairly narrow range of neutron energies.

The VENES system has several advantages over larger accelerators used for neutron transmission measurements. It is much smaller, allowing for its potential use at airports where space is limited and accelerators do not fit (National Research Council, 1999). It also provides a broader range of possible neutron energies than a similar system by Raas et al. (2005), providing access to additional resonance peaks and valleys. Finally, the robustness and ease of use of the generator allows for its use in mobile or static applications by a variety of personnel (Chichester et al., 2007). The purpose of this work is to examine the applicability of the VENES system for use with FNRR when searching for conventional explosives.

Materials and Methods

Neutron transmission measurements

Laboratory experiments, similar to those analyzed in Ch. 6, were performed with the purpose of understanding the neutron transmission properties of several materials within the VENES system. In this experiment, however, transmission targets were placed between the start and stop detectors. The transmission materials consisted of various hydrogenous materials including melamine, which is often used as an explosive surrogate. The experimental setup was nearly identical to the previous chapter. A portable sealed-tube D-D neutron generator[1] served as the source, which was assumed to be isotropic and create 2 x 10^6 neutrons per second. The start detector, which also served as the scatter target, was a 25.4 mm long, 12.7 mm radius cylinder of stilbene[2], which has a hydrogen-to-carbon ratio of 0.714. The detectors were connected to a photo-multiplier tube (PMT) assembly[3]. The two stop detectors were each EJ-309 liquid scintillators[4], with hydrogen-to-carbon ratios of 1.25, contained within 127 mm long cylinders with a 63.5 mm radius and connected to PMTs[5]. The detector assemblies were connected to a 12-bit, 250-MHz, eight-channel digitizer[6] to process the pulses. A ^{137}Cs source was used to calibrate all three detectors before each measurement. In order to keep the Compton edge consistent, the detector voltage was adjusted as needed. The start detector voltage was kept around 1300 V, the stop-1 detector stayed around 1110 V, and the stop-2 detector was kept near 1350 V.

[1] MP 320 D-D neutron generator (Thermo Fisher Scientific Inc., Waltham, MA 02451)

[2] Stilbene crystal (Proteus, Inc., Chagrin Falls, OH 44022)

[3] H10580 PMT assembly (Hamamatsu Photonics K.K., Hamamatsu City, Japan)

[4] EJ-309 liquid scintillator (Eljen Technology, Sweetwater, TX 79556)

[5] XP4512B PMT (Photonis Technologies S.A.S., Merignac, France)

[6] V1720 digitizer (CAEN, Viareggio, Italy)

As seen in Fig. 7.2 and 7.3, the start detector was placed with its front face parallel to and touching the side of the neutron generator, with its cylindrical axis aligned with the center of the generator's beam target, allowing the generator's source plane to bisect the start detector along the cylindrical axis. Two stop detectors, which were both placed at a $\pi/4$ radians scatter angle relative to the start detector, but on opposite sides of the source plane, were used to improve the counting statistics while decreasing measurement time. The stop-1 detector was positioned towards the front of the generator, which was shorter, while the stop-2 detector was positioned closer to the back of the generator, which housed most of the electronics. The distance between the centers of the front faces of the start and stop detectors was 1.00 m. The center of the generator and all detectors were approximately 1.24 m above the concrete floor. The closest wall to the neutron source was approximately 1.4 m away. The stop-2 detector was the closest to a wall at about 1.1 m. The generator was supported by a metal frame and the detectors were attached to metal ring stands that were set on concrete blocks. Identical materials, used as transmission targets, were placed 0.50 m between the start and each stop detector. Photographs of the experiment can be seen in Fig. 7.4-6.

When the generator was powered on and producing D-D neutrons, the same TOF measurements were performed as in Ch. 6. In this setup, only neutrons that interacted in multiple detectors were recorded. The arrival times of the light pulses created from neutron interactions in two separate scintillator detectors were used to determine the TOF of the neutron between those detectors. This provides a strong indication of the neutron's energy after its interaction in the first detector. The leading edge of the light pulse was used to determine timing information for TOF measurements. The digitizer had a sampling period of 4.0 ns, but that was reduced using linear interpolation between light collection data points, resulting in an approximated timing resolution

of 1.0 ns. Measurements were conducted both with no transmission target present and also with commercially available paper, melamine, vegetable oil, or water used as individual transmission targets, with the center of their volume aligned with the stop detectors' cylindrical axis. In the case of the water and vegetable oil, which were irregularly shaped, the larger volume of the base was positioned to be the transmission target. The physical properties of those materials can be seen in Table 7.1.

As in Ch. 6, the results of the measurements were post-processed using pulse shape discrimination (PSD) software in order to eliminate gamma ray pulses from the detector signal and organize the data (Detection for Nuclear Nonproliferation Group, 2014a). A personally developed MATLAB[7] script was then used to calculate the neutron TOF between the start detector and both stop detectors, create a histogram based on the tallied TOF measurements, convert the TOF histogram to a neutron energy histogram, fit a Gaussian curve to the results, and use that curve to generate a line of best fit for the TOF data. An example can be found in Appendix B. The post-processing was necessary due to the nonlinear relationship between neutron energy and TOF: $E_n' \sim 1/TOF^{1/2}$. The TOF line of best fit is then used to determine the histogram maximum, mode, and asymmetric full width at half maximum (FWHM). To maintain consistency, the same region of interest (ROI), based on the unattenuated neutron spectrum, was used to determine neutron counts in the presence of all transmission targets, regardless of the properties of the resultant curve. Once the total coincident neutron count rates for each transmission target was determined in both stop detectors, they were divided by the total unattenuated neutron count rate to calculate the transmission ratios of the various targets.

[7] computer program MATLAB (The MathWorks, Inc., Natick, MA 01760-2098, 2006).

In order to benchmark future simulations, the neutron transmission measurements were simulated using a modified Monte Carlo simulation tool, Monte Carlo N-Particle (MCNP)[8] PoliMi[9]. This allows for precise tracking, on an individual neutron basis, of secondary particles resulting from neutron interactions, and provides an opportunity for accurate TOF simulations. The setup, which contained air and a concrete floor extending a radius of 3.0 m, included a model of the neutron generator provided by the manufacturer and models of the detectors, PMTs, and all the housing materials (Thermo Fisher Scientific Inc., 2014; Detection for Nuclear Nonproliferation Group, 2014b). An example of the MCNP PoliMi input can be found in Appendix A. Simulated neutrons that interacted in the start detector and then made their way to one of the stop detectors had their interaction information saved, including the time of each interaction and the energy deposited. The results of the simulations were post processed using MPPost[10] to more accurately model the light pulses created from neutron interactions in the detectors. The simulated pulses and their timing information were then analyzed by a MATLAB program that performed essentially the same function as the program used on the laboratory data, outputting TOF and estimated neutron energy histograms with associated line of best fit and Gaussian curves. Again, an ROI was determined based on the simulated unattenuated measurement. This was then used to calculate the transmission rates for the various materials.

The initial simulations were conducted with the same positioning for the generator and detectors as in the laboratory and with the same transmission targets, seen in Table 7.2. The elemental ratios and densities for all the materials were obtained from McConn et al. (2011).

---

[8] computer code Monte Carlo N-Particle Transport version 5 (Los Alamos National Laboratory, Los Alamos, NM 87545, 2006).

[9] computer code MCNPX-PoliMi v2.0 (Polytechnic of Milan, Milano, Italy and the University of Michigan, Ann Arbor, MI, USA).

[10] computer code MPPost v2.1.0 (University of Michigan, Ann Arbor, MI, USA)

However, when recreating experiment in MCNP PoliMi, the densities measured in the lab and found in Table 7.1 were used in place of the densities provided. Due to a lack of knowledge of their precise composition, the paper target was approximated as wood and the vegetable oil was approximated as lard. The isotropic point source was placed at the center of the generator on the source plane, using the MCNP built-in D-D Gaussian neutron energy distribution function to approximate the fusion source.

Fast neutron resonance radiography

The next set of MCNP PoliMi simulations was designed to determine if FNRR may be performed using the VENES system. An arrangement similar to the previous simulations was used, with the same generator and detector models. However, the start detector was moved so that it was still aligned along the source plane, but now the center of the detector crystal was 0.25 m from the point source to reduce systematic uncertainty and narrow the neutron energy range. The center of the stop detector was 1.00 m from the center of the start detector and the angle was varied so that the detected scattered neutrons would have energies that aligned with various regions in the carbon, nitrogen, and oxygen total neutron attenuation spectra. The D-T scatter angles were 1.301, 1.208, 1.150, 1.097, 1.047, 0.967, 0.835, 0.736, 0.439 radians, which correspond to neutron energies of 1.00, 1.78, 2.35, 2.94, 3.53, 4.55, 6.35, 7.75, and 11.55 MeV, respectively. To investigate an alternative method of obtaining neutrons at 1.00 and 1.78 MeV, simulations were also run with a D-D source and scatter angles of 0.886 and 0.566 radians.

Again, the built-in functions were used to simulate the Gaussian energy distribution of the D-D and D-T source. However, in order to reduce the required computational resources, the simulated source only produced neutrons that were directed towards the start detector. The neutron point source emitted neutrons in a cone whose apex was 0.140 radians. Assuming that

only neutrons initially directed at the start detector would contribute a signal to the TOF spectrum, this improves simulation run times significantly. All normalized simulated values reported as "per source particle" assume an isotropic source and are corrected by approximately a factor of 820, which is the ratio of 4π steradians to the solid angle defined by the source cone. Compared to isotropic simulations in Ch. 6, there is no significant difference in the peak size or background.

The same calibration and test methods as discussed in Raas et al. (2005) were implemented in these simulations. As seen in Table 7.2, the calibration transmission targets are graphite, polyethylene, water, and melamine. For the purposes of these simulations, it is assumed the calibration targets' thicknesses, densities, and compositions are well known. The first step of the simulated measurements was to obtain the neutron count rates at each scatter angle with no transmission target present. Then, the graphite block was used to estimate carbon's neutron attenuation coefficient at each scatter angle via the new detector count rate. Once these were determined, the polyethylene target was simulated at all scatter angles. Since the carbon attenuation coefficients had already been calculated from the graphite transmission target, it was possible to determine the hydrogen attenuation coefficients via transmission count rates. Once these were estimated, simulated measurements of the water calibration target allowed calculation of the oxygen attenuation coefficients at all angles. Finally, the nitrogen attenuation coefficients were determined via transmission measurements of melamine.

Both the calibration and test transmission targets, which provided a good representation of low atomic number materials and are described in Table 7.2, had a height and width of 0.15 m, were centered along the cylindrical axis of the stop detectors, and were placed 0.50 m from

the center of both the start and stop detector. Every transmission target had a thickness of 0.05 m, which was expected to reduce neutron transmission by approximately a factor of two.

The test transmission targets were simulated at each scatter angle and transmission measurements were performed using a set ROI based on the mode of the unattenuated TOF spectrum. The calculated attenuation coefficients and transmission target count rates were inserted in to Eq. 7.3. The composition, thickness, and density of the transmission targets were treated as unknowns. A MATLAB least squares fitting function was used to determine the relative nuclide abundance in each material tested, with the only constraint being that no values were allowed to be negative.

In order to better understand the effect of counting uncertainty on the determination of atom fractions, random normalized uncertainty with a standard deviation of 5.0% was added to each transmission ratio. The least squares method was again used to estimate the atom fractions of H, C, N, and O. This was repeated 10,000 times for each transmission target and the standard deviation in atom fraction for each nuclide was found.

Results

Neutron transmission measurements

The laboratory transmission measurement data can be seen in Table 7.3, with paper having the highest transmission ratio, and water the lowest. The table also includes the calculated signal-to-noise ratio (SNR). The requirement for a neutron to interact in both the start and stop detector, when combined with gamma ray PSD, results in a greatly reduced signal background. However, there is still some background throughout the entire TOF range that is the result of two different source neutrons coincidentally interacting in both detectors within a several hundred

nanosecond time frame. This background was accounted for when determining transmission ratios.

As illustrated in Fig. 7.7, the mode and FWHM for the unattenuated peak defined the ROI used to determine the total neutron counts in the stop detectors, with only histogram bins completely within the FWHM being used. The ROI was defined as 58 – 73 ns. The individual stop detector TOF spectra are also visible in the figure and vary significantly from one another, having modes of 65 and 62 ns, heights of 9.8×10^{-8} and 6.2×10^{-8} neutrons per source particle, and FWHMs of 16.2 and 14.8 ns, respectively. It was anticipated they would be much closer in shape and size. Their differing peak modes result in an increased FWHM for the combined peak than would otherwise be expected. All count rate determinations were performed based solely on the combined peak FWHM. The TOF spectra for all transmission targets are presented in Fig. 7.8.

The simulated transmission TOF spectra can be seen in Fig. 7.9. The transmission data, which is based on an ROI of 57 – 73 ns, is presented in Table 7.4 and includes a calculation of the differences relative to the laboratory measurements. The SNR was not calculated because only a single neutron was simulated at a time, eliminating the possibility for two coincident neutrons to interact in the start and stop detector within a short time frame. This reduced the simulated system background to zero. All other sources of noise, such as improperly discriminated gamma rays, potential dark current, or contributions from naturally occurring background radiation, were also not present. The transmission results varied significantly compared to the previous measurements. The spectra for the stop-1 and stop-2 detectors were nearly identical, with both having peak modes of 63 ns and peak heights of 1.9×10^{-7} neutrons

per source particle. The estimated FWHM was 17.6 ns for the start-1 detector and 18.0 ns for the stop-2 detector.

Fast neutron resonance radiography

After the initial simulations with no transmission target, it was decided that the D-T scatter at 1.30 and 1.21 radians, which scattered neutrons at energies of approximately 1.00 and 1.78 MeV, respectively, were unsuitable for FNRR measurements, at least in the configuration used. The TOF spectra were much broader than higher energy scattered neutrons, with modes near 35 ns, instead of the predicted 73 and 55 ns. The irregular spectra were composed primarily of contributions from both neutron elastic and inelastic scatter off carbon nuclei in the start detector. When combined with the decreased likelihood of the desired neutrons reaching the detector due to their low energy, the expected TOF peak was not discernable above the noise. This problem persisted, even when the simulated start detector threshold was increased in an attempt to eliminate all contributions from neutron scatter off carbon. As seen in Fig. 7.10, this issue was also evident in the 1.15 radian, 2.35 MeV scatter. However, by increasing the start detector threshold to nearly 2 MeV, the expected TOF peak became much more definitive, allowing for its use in the simulated NRR measurements.

The peak information, at all scatter angles, for the simulations with no transmission target can be seen in Table 7.5. ROIs were applied consistently to each transmission measurement, even if the peak shape had been altered, with the ROI centered around the unattenuated peak mode for each neutron energy. Calculations were performed using count rates from ROIs that contained 1, 3, and 5 histogram bins, with each bin being 1.0 ns wide. The results from the 3 bin calculations are presented here because that width provided better statistics than a single bin, but did not greatly exceed the FWHM for some of the higher energy scattered neutron peaks. The

statistical uncertainty for the 3 bin ROI count rate was below 1.2% for every transmission target simulation. It should be noted that the results from the 1 bin and 5 bin calculations did not vary significantly compared to the 3 bin ROI. The absolute difference between what was presented and the calculated atom fractions for the 1 and 5 bin ROIs was 0.021 or less.

The simulated transmission ratios for the calibration targets can be seen in Table 7.6. These were used to calculate the various cross sections at each neutron energy, as seen in Table 7.7 and provided values for $a_{i,j}$ in Eq. 7.3. The transmission ratios for the test targets, which were used as b_i, are presented in Table 7.8. A least squares fit determined the optimal values for x_j, estimating the total elemental composition and density of the transmission target. The results of those calculations can be found in Table 7.9. The atom fraction estimated standard deviations, after randomized uncertainty was added to the transmission ratios, can be seen in Table 7.10.

Discussion

Neutron transmission measurements

There were some discrepancies between the measured transmission data and the simulations. One issue complicating the stop-2 signal was that the ring stand and clamp holding the start detector in place was positioned between it and the stop-2 detector, as seen in Fig. 7.6. This material was not modeled in the MCNP simulations presented. When a 10 mm sheet of iron was modeled in roughly the same location, the stop-2 peak was similarly depressed, but the peak mode was unchanged. The difference between the stop-1 and stop-2 modes was most likely due to slight variations in their locations relative to the start detector. As explained in Ch. 6, even though every effort was taken to accurately measure the placement of the stop detectors, a

difference of a couple centimeters or a fraction of a radian can result in a TOF difference of multiple nanoseconds.

Similarly, although the dimensions and mass of the transmission targets could be measured directly, it was more difficult knowing precisely what was in the containers. Vegetable oil and paper had to be approximated as their closest counterparts, wood and lard, respectively, because accurate descriptions of their compositions could not be found. In conjunction with this, each transmission target had different types of containers, which were not modeled. They were all some type of plastic, but the water and vegetable oil containers were fairly thin, while melamine's container was thicker. As seen in Fig. 7.1, misrepresenting the H, C, and O composition can result in significantly different transmission ratios at 1.25 MeV. Fortunately, FNRR can correct for some of these issues, since it uses multiple measurements of the same target to determine its composition. To a degree, unknown quantities that are not canceled out by the transmission ratios will become a constant factor in the calculations and should not negatively affect the system of equations or its ability to be solved by the least squares method.

The inherent background suppression of TOF measurements provides a strong SNR for transmission targets with lower density thickness. However, there are still some coincident neutron contributions to the TOF background. The continued decrease in SNR as the target density thickness increased was not unexpected, but it indicates a limit to the effectiveness of transmission measurements, particularly at lower neutron energies. Further reduction in the coincident neutron background could be possible with application of previously demonstrated shielding material around the neutron generator or stop detectors (Whetstone and Kearfott, 2011).

Fast neutron resonance radiography

The results of the FNRR simulations were very encouraging. The method, when paired with the VENES system, managed to correctly identify nearly all the elements present in each transmission target. The only minor exception was the 0.003 nitrogen atomic fraction missed in the paper target. The largest absolute difference between the calculated and actual atomic fraction was only 0.013 for all targets. Just as promising, the only nuclide that was not present and misidentified was nitrogen with erroneous 0.006 and 0.005 estimated atomic fractions in the toluene and vegetable oil targets, respectively. This lack of misidentification is especially important for limiting false alarms. Fortunately, the average nitrogen atomic fraction in conventional explosives is over 0.20, so the size of the differences seen in the simulations should not be of major concern (National Research Council, 2004). The method also correctly identified the density thickness of the transmission target, which could be information that is valuable to personnel searching for contraband.

Preliminarily, there was concern that the relatively broad energy spectrum from the scattered neutrons seen in Ch. 6 would not be precise enough to align with the resonance peaks of interest. This appears to be unfounded. Many of the tested neutron energy regions of the attenuation cross sections were roughly consistent across a fairly broad range, allowing for some variation while still interacting with the peaks and valleys of the attenuation spectrum. Furthermore, the method for calculating the individual cross sections was not limited to neutrons of a single energy. Without any additional work or calculations, the method provided an accurate cross section that was precisely weighted to the neutron energy spectrum presented by the VENES system. This allowed it to essentially self-correct for any neutron energy variation encountered during measurements at a given scatter angle.

Even though the investigated system included air, ground, generator and detector housings, and realistic detector responses and neutron energy spectra, it is important to remember that the calculated atom fractions are the result of simulations. Ch. 6 helped confirm that MCNP PoliMi could accurately model the shape of the TOF peaks and the basic behaviors of neutrons produced via VENES. However, measurements in the real world can have additional sources of uncertainty, such as poor counting statistics or systematic issues. Although some of this may be corrected for when calculating count rate ratios, the laboratory results will almost certainly be different than the more idealized simulated results.

As seen in Table 7.10, the random perturbations inserted into each of the transmission ratios used in the system of linear equations led to significant standard deviations. This is not entirely unexpected, as the inclusion of nine different uncertainties will make estimation of the atomic fractions via least squares method more difficult. The deviation in atom fraction values resulting from uncertainties of this magnitude could potentially obscure the relatively high characteristic nitrogen and oxygen content of explosives. This analysis illustrates the need for careful and accurate neutron counting when implementing the VENES system. Reducing the neutron energy spectra at a given angle via smaller detector volumes, or placing larger distances between the detectors, may limit the deviation introduced by the uncertainty. The smaller neutron energy range would allow for a tighter focus on the resonant attenuation peaks and valleys, leading to greater differentiation between the cross sections of the nuclides and provide more contrast at the different neutron energies. This, unfortunately, would come at the cost of counting efficiency.

Calculations were also performed using only neutrons derived from the D-T source, meaning that the equations pertaining to transmission measurements at 1.00 and 1.78 MeV were

not included. The results were nearly identical, with the magnitude of the atom fraction differences being the same as those presented here. This would allow for implementation of FNRR with the VENES system using a single neutron source. The primary drawback is that when introducing uncertainty to the transmission measurements, the standard deviation of the atom fraction uncertainty increases anywhere between 0.005 and 0.111. This is not unexpected, given that the number of equations used for least squares fitting has been reduced, but must be accounted for when determining how to implement the system.

Future work

As seen in the earlier neutron transmission laboratory experiment, measurements are always more complicated in the real world. Still, the accuracy with which the simulated VENES system was able to accurately identify atomic ratios when paired with FNRR warrants further investigation.

The primary drawback to this method is the relatively low efficiency of the VENES system due to the requirement that source neutrons must first interact in the start detector before they can contribute to the stop detector signal. The simulated count rates in the largest TOF histogram bins ranged between 10^{-8} and 10^{-10} counts per source neutron. Given that the source strength of the MP 320 D-T generator is approximately 1 x 10^{8} neutrons per second, count times in this arrangement could last on the order of minutes to hours at each scatter angle. Fortunately, several D-T generators with increased neutron output are being developed. Currently, generators of various sizes with outputs ranging between 10^{12} and 10^{13} D-T neutrons per second are being advertised (Phoenix Nuclear Labs, 2015). Additionally, Lawrence Berkeley National Laboratory has patented a fusion generator design that can theoretically produce up to 10^{14} or more D-T neutrons per second (Leung, 2005; Lawrence Berkeley National Laboratory, 2015). Improved

neutron output rates at or near this magnitude would help decrease count times while accommodating some decreased efficiency associated with the reduction of systematic uncertainties.

In addition to finding a stronger neutron source or increasing the ROI, the count time can be decreased by modifying the simulated setup and reducing the distance between detectors or increasing the detector size. This would improve detection efficiency, but also further broaden the neutron energy spectrum. Given the preliminary results, this may be an acceptable tradeoff. Similarly, multiple start and stop detectors could be used at once, provided the slight variation in scatter angle and neutron energies between different detectors does not significantly impact the nuclide detection capabilities. Additional research is necessary to determine the limits of detector size and positioning relative to the scattered neutron energy spectrum.

Not all potential interrogation targets are composed entirely of H, C, N, and O, so future work is warranted to see how the method responds to other nuclides. Perhaps, as was suggested previously, a fifth generic nuclide should be included in Eq. 7.3 that has a set cross section and is treated as an amalgam of all other elements (Chen et al., 2001). Alternatively, this method could work as secondary screening after a primary method, such as x-ray interrogation, has flagged suspicious hydrogenous material.

Conclusions

As seen in the neutron transmission measurements, the VENES system has many qualities that allow it to work well with FNRR. It can discriminate signals from many of the background neutrons, produce neutrons over a broader range of energy than other systems previously tested, and is relatively cheap, robust, and portable.

The preliminary results from simulated VENES FNRR measurements show an excellent agreement between the calculated and actual elemental abundances. Further investigation of this method should continue, with particular focus paid to confirming the simulated results via laboratory measurements, increasing the system's efficiency, and determining how the system responds to materials containing elements in addition to H, C, N, and O.

Figures

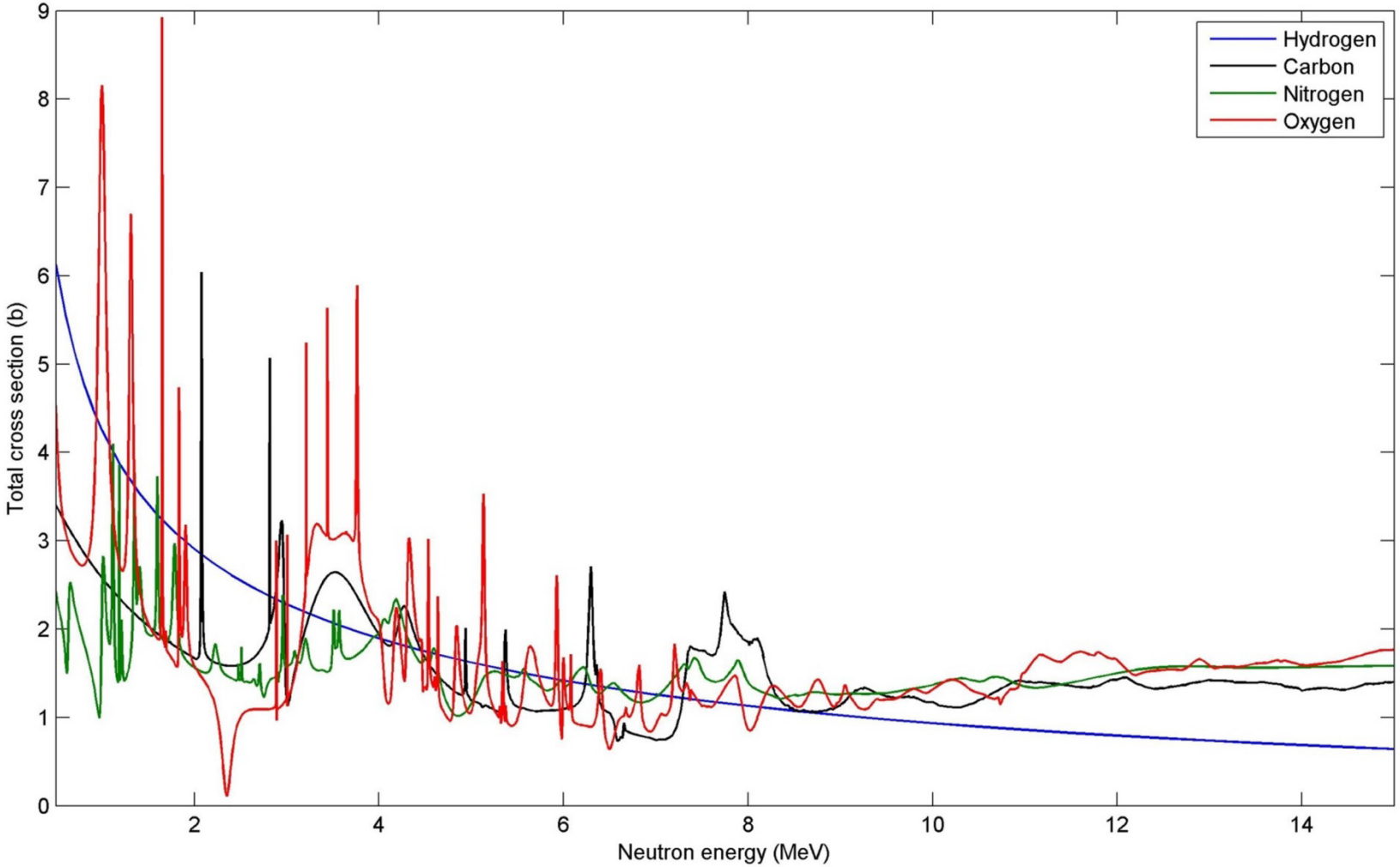

Fig. 7.1: The attenuation cross sections for ^{1}H, C, ^{14}N, and ^{16}O between 0 and 15 MeV (NNDC, 2015).

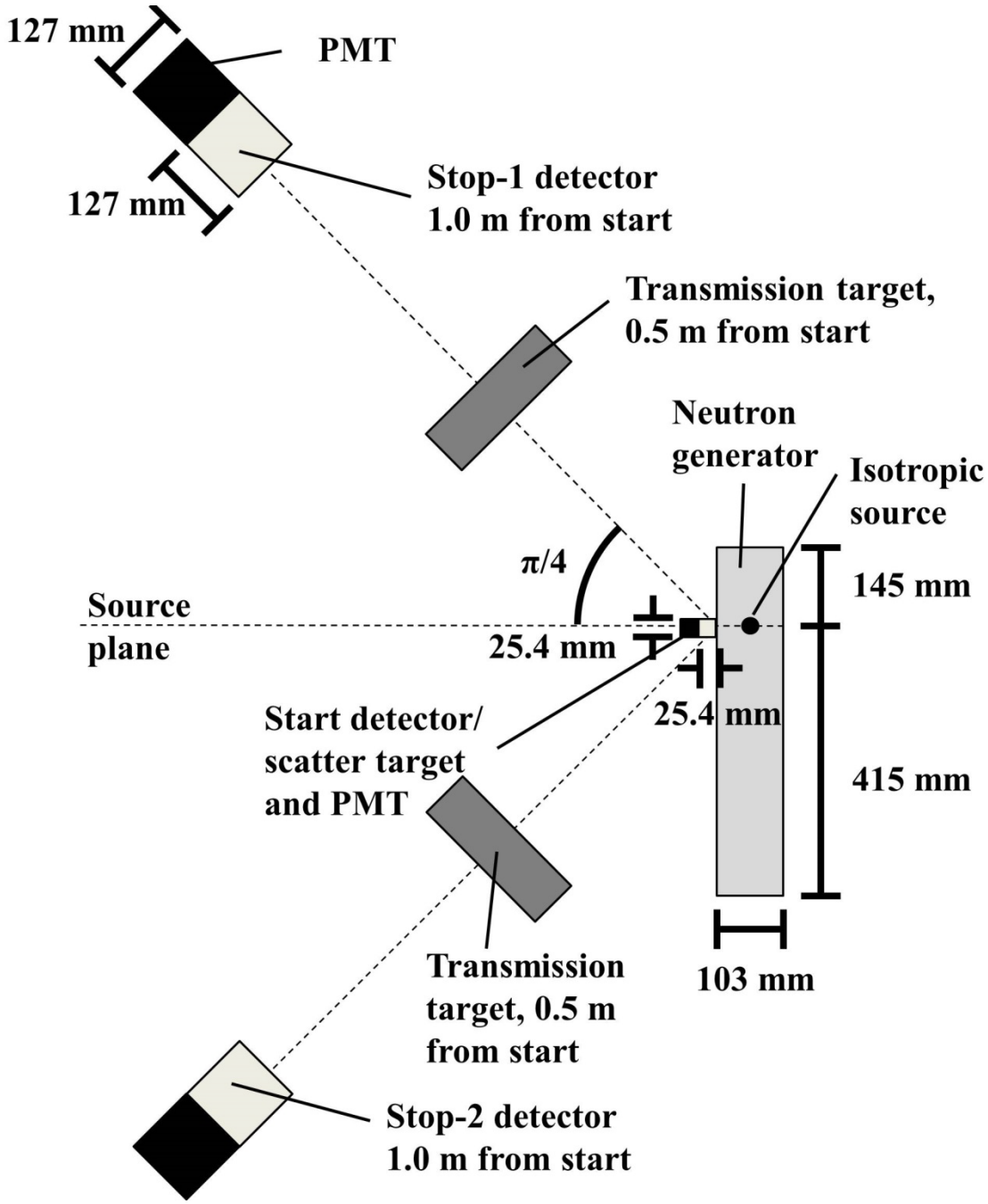

Fig. 7.2: A close, top-down view of the arrangement for the neutron transmission measurements.

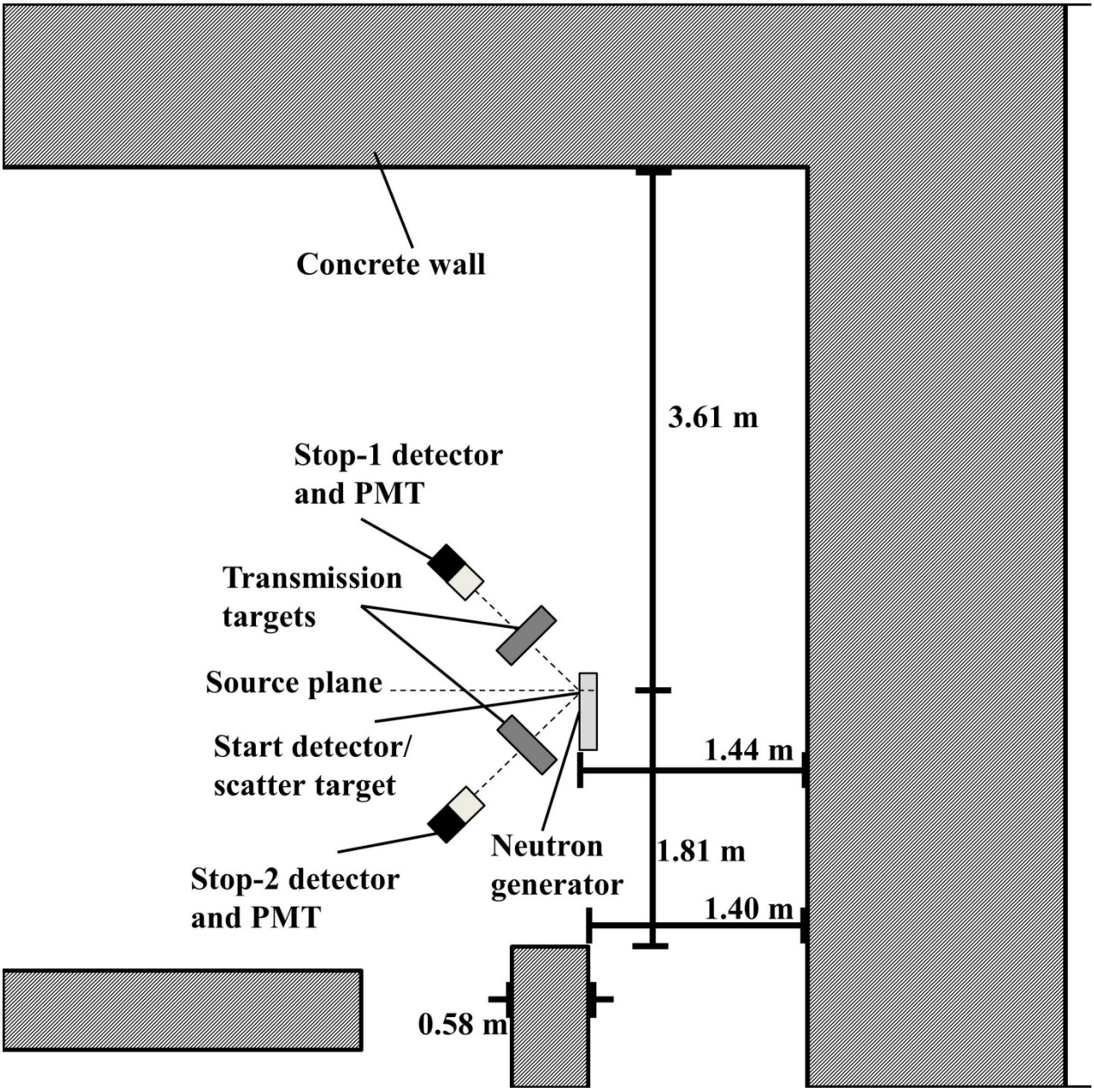

Fig. 7.3: A broad, top-down view of the laboratory arrangement for the neutron transmission measurements.

Fig. 7.4: A picture of the laboratory setup for the unattenuated neutron transmission measurements, with the stop-1 detector in the foreground and start detector and D-D generator to the left.

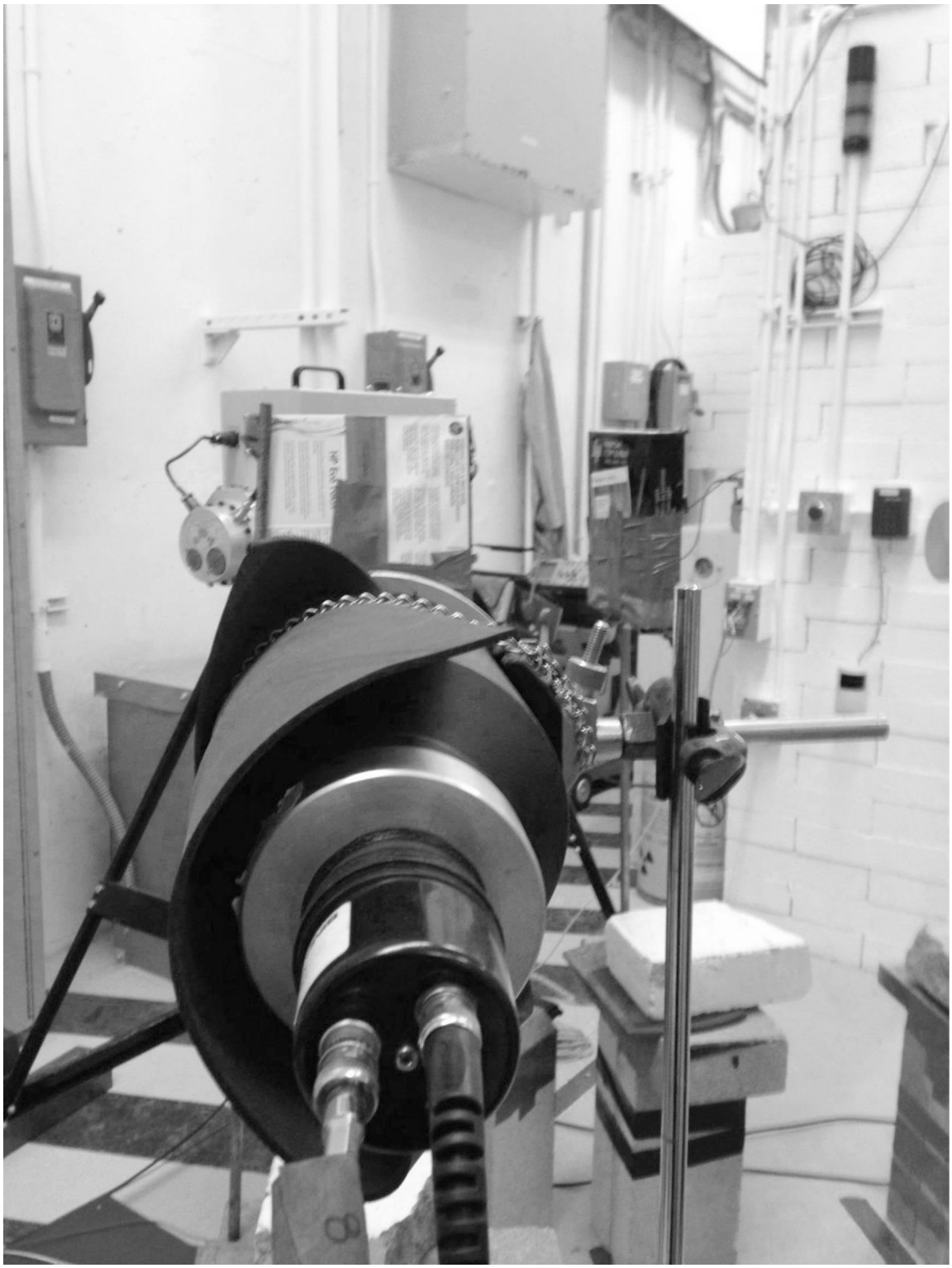

Fig. 7.5: A picture of the laboratory setup for the paper neutron transmission measurements, behind the stop-1 detector, facing the paper transmission target and D-D generator.

Fig. 7.6: A picture of the laboratory setup for the vegetable oil neutron transmission measurements, with the stop-2 detector in the foreground and start detector and D-D generator located to the right.

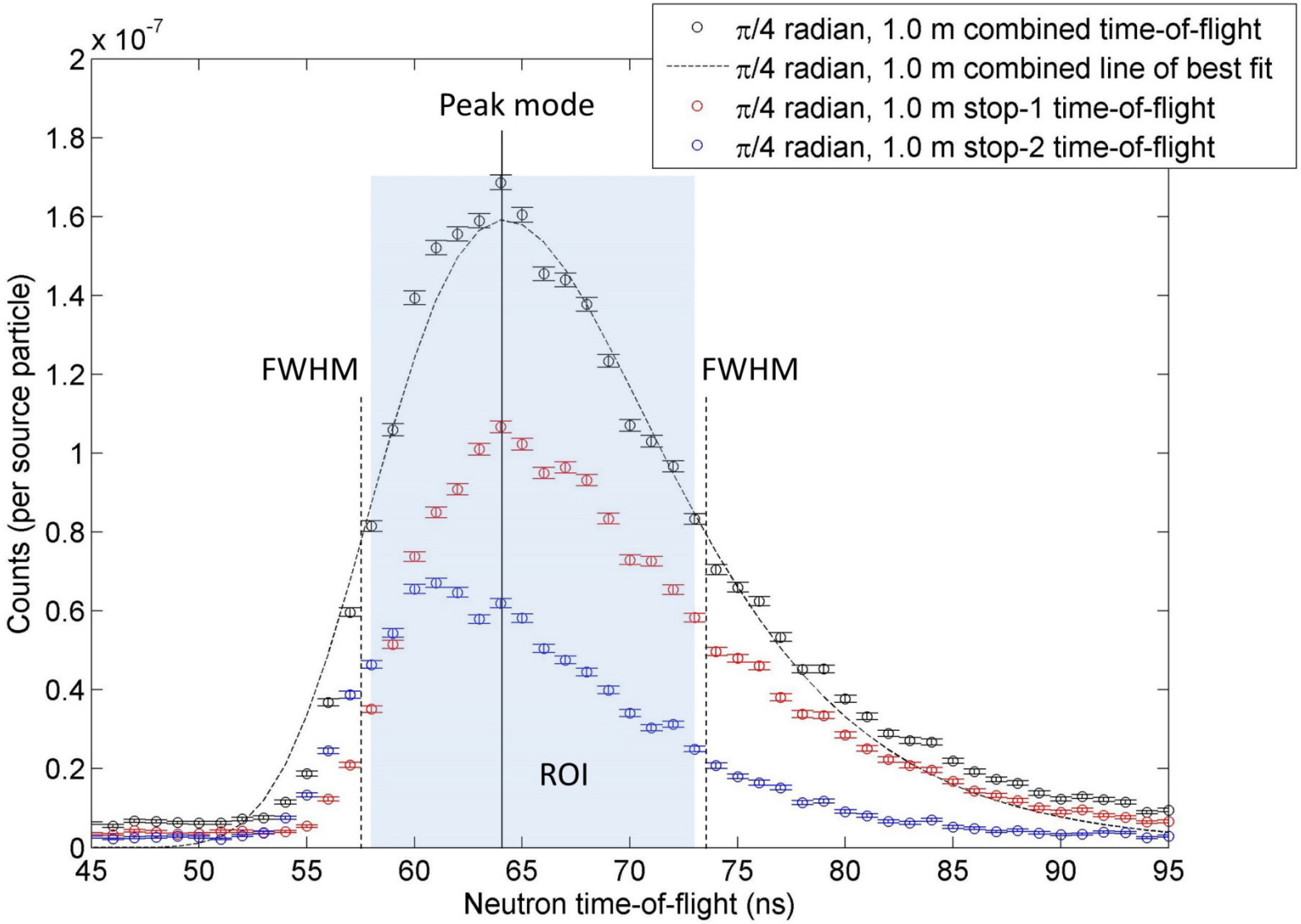

Fig. 7.7: The TOF spectra from the unattenuated laboratory neutron transmission measurement. It illustrates how the ROI was determined and the discrepancy between the two stop detector spectra.

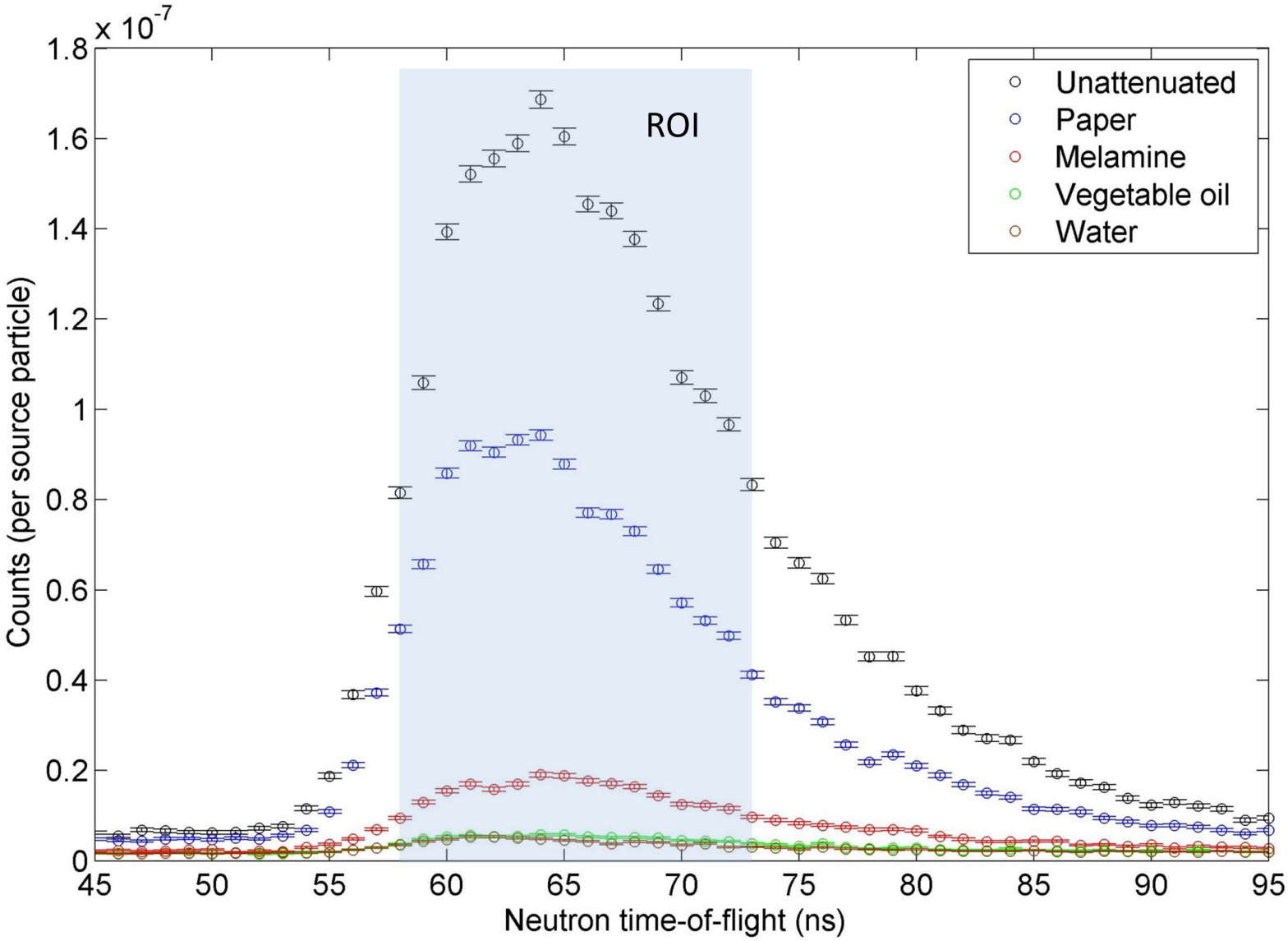

Fig. 7.8: The combined TOF spectra for the various neutron transmission measurements performed in the laboratory.

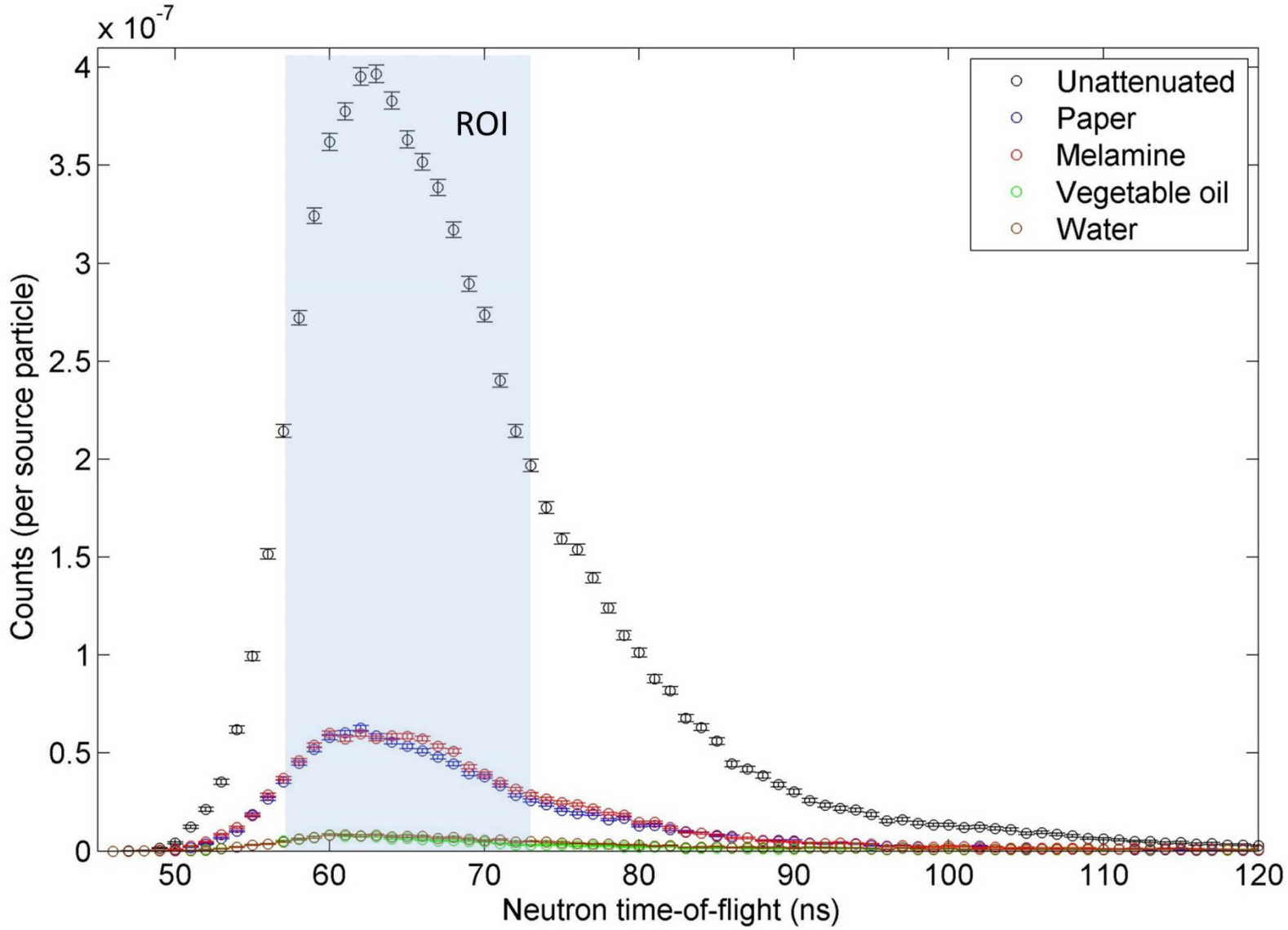

Fig. 7.9: The combined TOF spectra for the various simulated neutron transmission measurements.

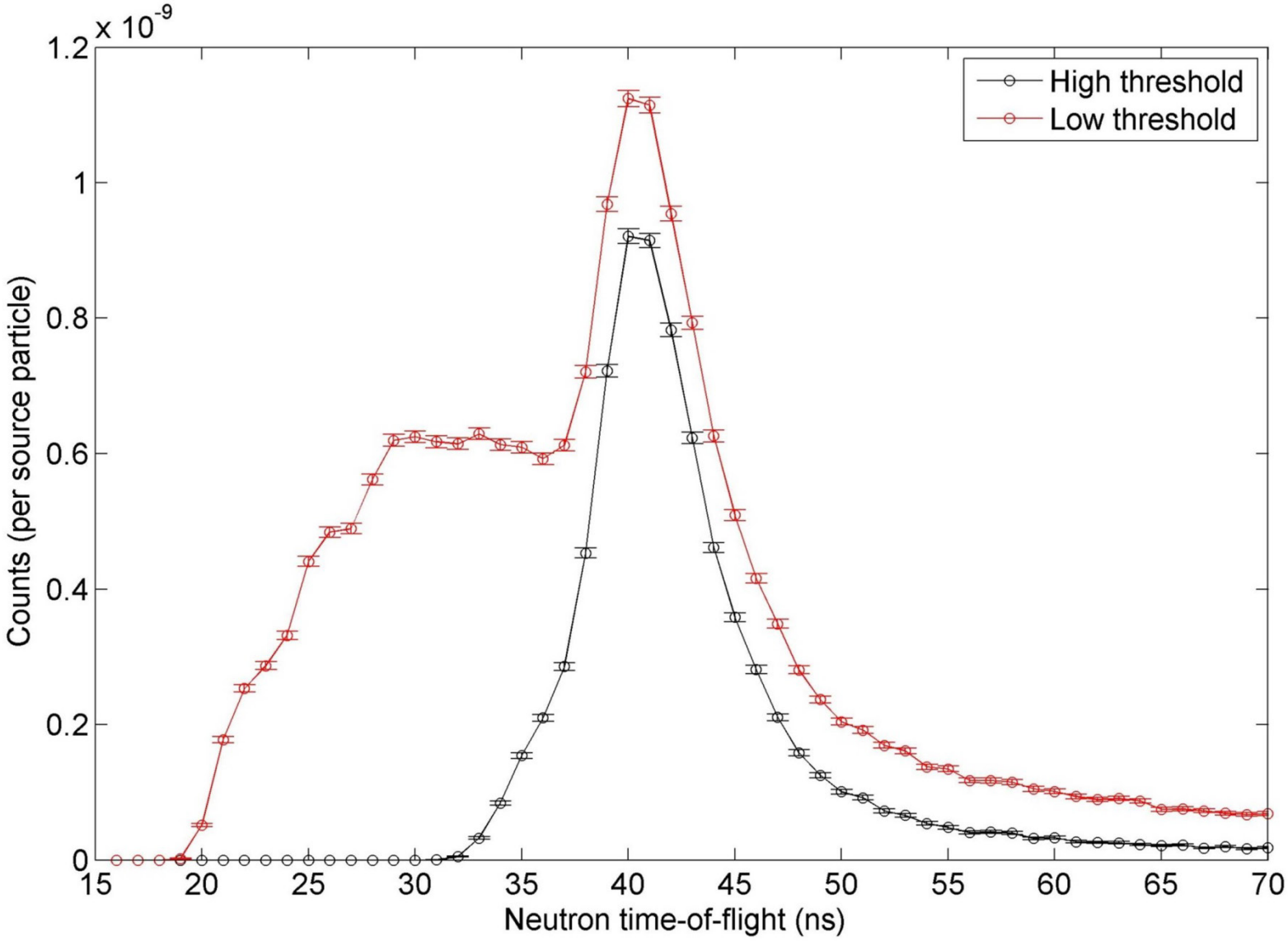

Fig. 7.10: The simulated unattenuated TOF spectra of roughly 2.4 MeV neutrons with a high and low start detector threshold.

Tables

Table 7.1: The physical properties of the transmission targets used in the laboratory measurements.

Transmission target	Depth (mm)	Width (mm)	Height (mm)	Density (kg/m^3)
Paper	49	216	279	757
Melamine	120	120	200	868
Vegetable oil	137	151	140	959
Water	145	145	92	1000

Table 7.2: The elemental composition of the simulated transmission targets for both the neutron transmission and FNRR measurements. The densities provided were used during the FNRR simulations (McConn et al., 2011).

Transmission target	Atom fractions				Density (kg/m^3)
	H	C	N	O	
Test material					
Acetone	0.600	0.300	0	0.100	790
Ammonium nitrate	0.444	0	0.222	0.333	1720
Methanol	0.667	0.167	0	0.167	791
Sucrose	0.489	0.267	0	0.244	850
Paper	0.464	0.324	0.003	0.209	757
Toluene	0.533	0.467	0	0	867
Vegetable oil	0.621	0.345	0	0.034	959
Calibration material					
Graphite	0	1.000	0	0	1700
Polyethylene	0.667	0.333	0	0	930
Water	0.667	0	0	0.333	1000
Melamine	0.389	0.278	0.333	0	1350

Table 7.3: Results from the laboratory D-D transmission measurements.

Transmission target	Total counts	ROI Counts per minute	% uncertainty	Ratio	% uncertainty	SNR	% uncertainty
None	96549	248	0.32	-	-	24.9	1.2
Paper	83067	138	0.35	0.559	0.47	19.8	1.1
Melamine	17956	28.5	0.75	0.115	0.81	8.5	1.7
Vegetable oil	9695	9.50	1.0	0.0384	1.1	3.6	1.7
Water	8254	8.09	1.1	0.0327	1.1	3.2	1.8

Table 7.4: Results from the simulated D-D neutron transmission measurements.

Transmission target	ROI counts per source particle	% uncertainty	Ratio	% uncertainty	% difference vs laboratory data
None	5.31×10^{-6}	0.31	-	-	-
Paper	7.90×10^{-7}	0.56	0.149	0.64	73.4
Melamine	8.28×10^{-7}	0.55	0.156	0.63	-35.5
Vegetable oil	9.72×10^{-8}	1.60	0.0183	1.6	52.3
Water	1.12×10^{-7}	1.49	0.0212	1.5	35.2

Table 7.5: Unattenuated peak information for simulated FNRR measurements.

E_n' (MeV)	Predicted peak mode (ns)	Observed peak mode (ns)	ROI counts per particle	% Uncertainty	Estimated FWHM (ns)
D-D					
1.00	72.3	70	9.45×10^{-8}	0.11	12.3
1.78	54.2	54	2.28×10^{-7}	0.07	6.8
D-T					
2.35	47.2	40	2.55×10^{-9}	0.69	6.7
2.94	42.2	39	1.43×10^{-8}	0.29	6.7
3.53	38.5	38	3.29×10^{-8}	0.19	7.2
4.55	33.9	34	5.17×10^{-8}	0.15	6.7
6.35	28.7	29	7.81×10^{-8}	0.12	4.7
7.75	26.0	26	9.40×10^{-8}	0.11	3.6
11.55	21.3	22	1.12×10^{-7}	0.10	2.4

Table 7.6: The simulated neutron transmission ratios across a 3.0 ns ROI for the calibration materials.

	Calibration material transmission ratios							
En' (MeV)	Graphite	% uncertainty	Polyethylene	% uncertainty	Water	% uncertainty	Melamine	% uncertainty
1.00	0.343	0.6	0.123	1.0	0.108	1.1	0.259	0.7
1.78	0.457	0.3	0.218	0.5	0.276	0.4	0.329	0.4
2.35	0.525	1.2	0.390	1.3	0.483	1.2	0.490	1.2
2.94	0.441	0.5	0.306	0.9	0.359	0.8	0.408	0.8
3.53	0.395	0.4	0.296	0.6	0.334	0.6	0.394	0.5
4.55	0.501	0.3	0.373	0.4	0.433	0.4	0.451	0.4
6.35	0.643	0.2	0.485	0.4	0.541	0.4	0.554	0.4
7.75	0.547	0.2	0.484	0.5	0.576	0.5	0.542	0.5
11.55	0.602	0.4	0.582	0.4	0.614	0.4	0.603	0.4

Table 7.7: Calculated attenuation cross sections at various energies, based on simulated transmission measurements of calibration targets and a 3.0 ns ROI.

	Attenuation cross sections (b)			
E_n'	H	C	N	O
1.00	3.99	2.51	1.61	5.33
1.78	2.90	1.84	1.97	1.90
2.35	1.60	1.51	1.29	1.15
2.94	2.01	1.92	1.62	2.12
3.53	1.96	2.18	1.66	2.64
4.55	1.66	1.62	1.64	1.69
6.35	1.30	1.03	1.29	1.08
7.75	1.11	1.42	1.32	1.09
11.55	0.76	1.19	1.26	1.40

Table 7.8: The simulated neutron transmission ratios across a 3.0 ns ROI for the interrogation materials.

	Test material transmission ratios							
En' (MeV)	Acetone	% uncertainty	Ammonium nitrate	% uncertainty	Methanol	% uncertainty	Paper	% uncertainty
1.00	0.103	1.1	0.220	0.8	0.168	0.9	0.324	0.6
1.78	0.253	0.5	0.361	0.4	0.319	0.4	0.500	0.3
2.35	0.448	1.2	0.533	1.2	0.509	1.2	0.648	1.1
2.94	0.322	0.9	0.439	0.8	0.407	0.8	0.547	0.7
3.53	0.292	0.6	0.422	0.5	0.389	0.5	0.523	0.5
4.55	0.382	0.4	0.506	0.4	0.476	0.4	0.612	0.3
6.35	0.492	0.4	0.611	0.4	0.581	0.4	0.707	0.4
7.75	0.515	0.5	0.608	0.5	0.595	0.5	0.696	0.4
11.55	0.534	0.5	0.678	0.4	0.659	0.4	0.738	0.4

	Test material transmission ratios					
En' (MeV)	Sucrose	% uncertainty	Toluene	% uncertainty	Vegetable oil	% uncertainty
1.00	0.262	0.7	0.247	0.7	0.147	0.9
1.78	0.449	0.4	0.359	0.4	0.257	0.5
2.35	0.611	1.1	0.514	1.2	0.431	1.3
2.94	0.502	0.7	0.430	0.8	0.340	0.8
3.53	0.476	0.5	0.414	0.5	0.326	0.6
4.55	0.570	0.4	0.496	0.4	0.408	0.4
6.35	0.672	0.4	0.606	0.4	0.521	0.4
7.75	0.666	0.5	0.582	0.5	0.516	0.5
11.55	0.708	0.4	0.666	0.4	0.603	0.4

Table 7.9: The calculated elemental composition of the simulated interrogation targets using a 3.0 ns ROI.

	Atom fractions								Total density thickness (kg/m^2)	% difference
Transmission target	H	% difference	C	% difference	N	% difference	O	% difference		
Acetone	0.597	0.5	0.303	-1.1	0.000	NA	0.099	0.5	39.9	-1.09
Ammonium nitrate	0.455	-2.3	0.000	NA	0.213	4.0	0.332	0.4	84.2	2.04
Methanol	0.668	-0.2	0.160	4.2	0.000	NA	0.172	-3.2	39.7	-0.27
Paper	0.453	2.3	0.331	-2.1	0.000	100.0	0.216	-3.2	39.0	-2.94
Sucrose	0.482	1.4	0.262	1.6	0.000	NA	0.256	-4.6	43.5	-2.41
Toluene	0.520	2.5	0.474	-1.6	0.006	NA	0.000	NA	44.7	-3.18
Vegetable oil	0.617	0.6	0.340	1.4	0.005	NA	0.038	-10.1	48.6	-1.40

Table 7.10: The atomic fraction standard deviation for each nuclide after a normal, randomized uncertainty distribution with 5.0% standard deviation was introduced to each neutron transmission ratio in Eq. 7.3.

	Atom fraction standard deviation			
Transmission target	H	C	N	O
Test material				
Acetone	0.101	0.128	0.096	0.070
Ammonium nitrate	0.077	0.087	0.085	0.054
Methanol	0.094	0.090	0.067	0.064
Paper	0.138	0.158	0.116	0.098
Sucrose	0.122	0.132	0.097	0.085
Toluene	0.087	0.141	0.108	0.050
Vegetable oil	0.074	0.115	0.090	0.051
Calibration material				
Graphite	0.038	0.128	0.105	0.036
Melamine	0.076	0.152	0.127	0.043
Polyethylene	0.064	0.103	0.080	0.038
Water	0.068	0.034	0.029	0.055

References

Buffler, A., 2004. Contraband detection with fast neutrons. *Radiat. Phys. Chem.*, 71(3-4), 853-861.

Buffler, A., Tickner, J., 2010. Detecting contraband using neutrons: challenges and future directions. *Radiat. Meas.*, 45 (10), 1186 – 1192.

Chen, G., Lanza, R.C., 2002. Fast neutron resonance radiography for elemental imaging: theory and applications. *IEEE T. on Nucl. Sci.*, 49 (4), 1919-1924.

Chen, G., Lanza, R.C., Hall, J., 2001. Fast neutron resonance radiography for security applications. *AIP Conf. Proc.*, 576, 1109-1112.

Chichester, D.L., Simpson, J.D., Lemchak, M., 2007. Advanced compact accelerator neutron generator technology for active neutron interrogation field work. *J. Radioanal. Nucl. Ch.*, 271 (3), 629-637.

Detection for Nuclear Nonproliferation Group, University of Michigan, Ann Arbor, MI, 2014a. Personal conversations. February 5-18.

Detection for Nuclear Nonproliferation Group, University of Michigan, Ann Arbor, MI, 2014b. Personal email correspondence. June 9-13.

Gozani, T., 1994. Novel applications of fast neutron interrogation methods. *Nucl. Instrum. Meth. A*, 353 (1-3), 635-640.

Knoll, G.F., 2010. Radiation Detection and Measurement, 4th ed. (Wiley, Hoboken, NJ), pp. 19-22.

Lanza, R., 2007. Nuclear techniques for explosive detection: current prospects and requirements for future development. *Proceedings of an IAEA Technical Meeting: combined devices for humanitarian demining and explosives*, *November 13-17, 2006*.

Lawrence Berkeley National Laboratory, 2015. Compact Neutron Generators IB-1764. Online, accessed May 14, 2015. http://ipo.lbl.gov/lbnl1764/.

Leung, K., 2005. Cylindrical neutron generator. U.S. Patent No. 6,907,097.

McConn Jr., R.J., Gesh, C.J., Pagh, R.T., Rucker, R.A., Williams III, R.G., 2011. Compendium of material composition data for radiation transport modeling. Pacific Northwest National Laboratory, Report No. PNNL-15870.

National Nuclear Data Center. 2015. Evaluated Nuclear Data Files for ^{1}H, C, ^{14}N, and ^{16}O. Brookhaven National Laboratory. Online, accessed February 16, 2015. http://www.nndc.bnl.gov/exfor/endf00.jsp.

National Research Council, 1999. The Practicality of Pulsed Fast Neutron Transmission Spectroscopy for Aviation Security. (National Academies Press, Washington, DC), pp. 2-3.

National Research Council, 2004. Existing and Potential Standoff Explosives Detection Techniques. (National Academies Press, Washington, DC), pp. 58-59.

Overley, J.C., Chmelik, M.S., Rasmussen, R.J., Schofield, R.M.S., Sieger, G.E., Lefevre, H.W., 2006. Explosives detection via fast neutron transmission spectroscopy. *Nucl. Instrum. Meth. B*, 251 (2), 470-478.

Phoenix Nuclear Labs, 2015. Multiple product webpages. Online, accessed May 14, 2015. http://phoenixnuclearlabs.com/product/high-yield-neutron-generator/; http://phoenixnuclearlabs.com/product/mid-yield-neutron-generator/; http://phoenixnuclearlabs.com/product/low-yield-neutron-generator/.

Raas, W.L., Blackburn, B., Boyd, E., Hall, J.M., Kohse, G., Lanza, R., Rusnak, B., Watterson, J.I.W., 2005. Neutron resonance radiography for explosives detection: technical challenges. *Nuclear Science Symposium Conference Record, 2005 IEEE*, (1), 129-133.

Thermo Fischer Scientific Inc., Waltham, MA, 2014. Personal phone and email correspondence. June 17-23.

Whetstone, Z.D., Kearfott, K.J., 2011. Use of multiple layers of repeating material to effectively collimate an isotropic neutron source. *Nuc. Technol.*, 176 (3), 395 – 413.

Whetstone, Z.D., Kearfott, K.J., 2014. A review of conventional explosives detection using active neutron interrogation. *J. Radioanal. Nucl. Ch.*, 301 (3), 629-639.

Whetstone, Z.D., Kearfott, K.J., 2015. A method for using neutron elastic scatter to create a variable energy neutron beam from a nearly monoenergetic source. *Radiat. Phys. Chem.*, 112, 22-28.

CHAPTER 8: PRELIMINARY INVESTIGATION INTO ALTERNATIVE APPLICATIONS AND ARRANGEMENTS FOR THE VARIABLE ENERGY NEUTRON ELASTIC SCATTER TIME-OF-FLIGHT SYSTEM

Abstract

Several Monte Carlo simulations were conducted to investigate application of the variable energy neutron elastic scatter (VENES) system to active neutron interrogation methods to search for conventional explosives. Both fast neutron analysis (FNA) and neutron backscatter simulations were performed with the VENES system serving as the source of tagged neutrons. The results of the preliminary simulations are encouraging and demonstrate clear neutron TOF dependence, allowing for discrimination of approximately 85% and 96% of the noise associated with undesirable neutron interactions during time-tagged VENES FNA and neutron backscatter measurements, respectively. Application of previous shielding designs to the VENES system was also investigated in order to evaluate its effectiveness in reducing total neutron flux in the stop detector. The simulated flux from a D-T source was reduced by approximately a factor of four after application of 0.20 m thick of either pure polyethylene or layered steel and polyethylene shielding material around the generator. Combined VENES active neutron interrogation methods and alternative source, detector, and interrogation target arrangements were also discussed. Although the VENES system is relatively inefficient, especially when conducting FNA and neutron backscatter measurements, the benefits of its adaptability and tagged neutron variability provide motivation to continue its development.

Introduction

The work in Ch. 7 demonstrated via simulation that the newly developed variable energy neutron elastic scatter (VENES) system can be applied to fast neutron resonance radiography (FNRR). However, as discussed in Ch. 2, there are other methods of active neutron interrogation used to search for the unique ratios of H, C, N, and O found in conventional explosives that may also benefit from the variable energy, time-tagged neutrons provided by the VENES system (Whetstone and Kearfott, 2014).

The ability to adjust the scattered neutron energy, combined with the portability and ease of use of the VENES system, permits potential application to a variety of active neutron interrogation methods. Similar to associated particle imaging (API), the system notes the time the source neutron interacts in the start detector/scatter target, allowing for application of a timing window when searching for secondary radiation (Chichester et al., 2005).

One active interrogation method the VENES system could be applied to is fast neutron analysis (FNA), where the interrogating neutrons inelastically scatter off the nuclei of the unknown material, creating characteristic gamma rays that are unique to the nuclides present. The inelastic collisions of interest occur in C, N, and O. The cross sections for all these interactions are significantly smaller than the total attenuation cross sections and have thresholds above 2 MeV. Furthermore, like total attenuation cross sections, they also vary with neutron energy, but instead trend upwards as energy increases. By measuring the flux of the characteristic gamma rays at one or more neutron energies, an estimate of the relative amounts of C, N, and O can be determined (Sudac et al., 2011). The characteristic gamma ray energy for inelastic scatter is: 4.43 MeV for ^{12}C; 1.64, 2.31, and 5.11 MeV for ^{14}N; and 6.13 MeV for ^{16}O (Buffler, 2004).

FNA using the VENES system can be conducted independently, or in conjunction with FNRR measurements, as a second form of verification. If used with FNRR, FNA can be applied during some or all of the fixed neuron energy interrogations, as long as the scattered neutron energy is above the inelastic scatter threshold for each nuclide. The only component that would need to be added is a gamma ray detector facing the interrogation target. Depending on the size of the interrogation target, the inelastic scatter gamma ray signal may be significantly smaller than the transmission signal, resulting in either longer count times, or more statistical uncertainty associated with the photon signature. However, this could be somewhat counteracted by detecting gamma rays at multiple neutron energies, since the photon energy does not change and the inelastic scatter cross sections are fairly consistent above their thresholds.

Another benefit of using the VENES system for FNA measurements is that the start detector/scatter target provides timing information that can be used to discriminate much of the undesirable signal that results from secondary gamma rays produced via neutron interactions in the environment (Sudac et al., 2011). These tagged neutrons can then be used for FNA. Gamma rays that are detected within a certain timing window after a neutron interaction in the start detector would be counted, resulting in a cleaner signal for analysis.

The VENES system could also serve as the source of neutrons for the explosives detection method designed by Lehnert and Kearfott (2105). In addition to searching for transmission neutrons and characteristic gamma rays via FNA, the system also detects elastically scattered neutrons at various angles. The information gathered from the gamma ray and neutron detectors is then used to form flags that are evaluated by an algorithm, which ultimately helps characterize the unknown material within a cargo container as inert or a threat. The flexibility of VENES, which allows for selection of the incident neutron energy via manipulation of the scatter

angle used, provides the opportunity to choose new neutron energies where there is greater contrast between interaction probabilities of the various nuclides of interest. This is a significant improvement compared to the deuterium-tritium generator originally suggested.

The flags that are used for identification include both total backscatter neutron counts, as well as those above certain energy thresholds determined via pulse height distributions (PHDs) within organic liquid scintillators (Lehnert and Kearfott, 2014). Substituting time-of-flight (TOF) measurements for PHD measurements, provided the interrogation target is small enough to limit TOF uncertainties to a reasonable magnitude, may increase the method's efficiency. This is because many neutrons of a given energy do not create pulse heights equivalent to their energy, resulting in their possible discrimination, whereas TOF measurements are the same, regardless of the energy deposited in the stop detector.

Unfortunately, there are some potential drawbacks to using VENES in conjunction with Lehnert and Kearfott's (2014) flag based explosives detection method. Neutron TOF is an indirect measurement of energy and is dependent on distance traveled between the start and stop detectors. This, when combined with the systematic uncertainty associated with the VENES system discussed in Ch. 5, means that differentiation of elastic scatter peaks from C, N, and O will most likely be difficult (Whetstone and Kearfott, 2015). For instance, D-T neutrons that initially have their energy reduced by the VENES system to 7.75 MeV, then backscatter off the target material at an angle of $5\pi/6$ radians, have final energies of 5.7, 5.9, and 6.1 MeV when scattering off of C, N, and O, respectively. Without small detector volumes and relatively large distances between detectors limiting systematic uncertainty to less than 0.1 MeV, the "monoenergetic" neutron peaks proposed by Lehnert and Kearfott (2014) will not be possible. However, the threshold measurements are still possible using neutron TOF as a means of

discriminating neutrons that interacted multiple times in the environment or interrogation target and have longer TOFs.

The VENES system could also be improved by the addition of shielding to the system. As seen in the laboratory measurements of Ch. 7, minimizing the signal-to-noise ratio (SNR) is important when trying to determine transmission through an interrogation target, particularly when the transmission rate is low. The SNR effectively limits the maximum density thickness of material that can be interrogated. Any reduction in SNR has the potential to improve fast neutron resonance radiography measurements. The nature of TOF measurements allows the system to discriminate many of the neutrons that interact in the start detector, interact somewhere in the environment, and eventually find their way to the stop detector. The primary cause of the existing SNR appears to be from coincident neutrons, previously emitted by the source, interacting in the stop detector within the timing window of a different source neutron interacting in the start detector. Therefore, source shielding that limits the emission isotropic of neutrons at angles other than towards the start detector should reduce the SNR. As discussed in Ch. 3, it also has the added benefit of reducing the potential dose rate to any nearby personnel (Whetstone and Kearfott, 2011).

Detector shielding, similar to what was presented in Ch. 4, could also benefit the VENES system. Depending on the gamma ray detector used in FNA, it may be necessary to protect it from the high neutron flux near the generator, or secondary gamma rays generated from neutron interactions in locations other than the interrogation target. Similarly, backscatter stop detectors used during NES will be close to the isotropic neutron source and start detector, necessitating significant neutron shielding to allow differentiation between the backscatter signal and system noise.

The work presented in this chapter focuses on initial evaluations of FNA and neutron backscatter as future applications for the VENES system, as well as application of previously designed source and detector shielding methods. Additionally, discussion of alternative source and detector arrangements to maximize system efficiency is included.

Materials and Methods

All investigations were performed using Monte Carlo methods via Monte Carlo N-Particle (MCNP)[1] PoliMi[2]. This allowed for precise accounting of all particle interactions and realistic TOF measurements. Similar to previous chapters, the source was assumed to be an isotropic point source within a sealed-tube neutron generator[3] (Thermo Fisher Scientific Inc., 2014). It was modeled using the MCNP built-in Gaussian fusion neutron energy distributions. However, in order to reduce simulation time, the simulated source only emitted neutrons directed towards the start detector. All values reported as per source particle assume an isotropic source and are normalized by the inverse of the solid angle fraction defined by the neutron beam cone. The universe was a sphere with a 4.0 m radius and the environment consisted of air with a concrete floor (McConn et al., 2011). The center of the detectors and source were located 1.23 m above the floor.

The simulated neutron detectors were either a liquid organic scintillator[4] that was a 127.0 mm long cylinder with a 63.5 mm radius, or a plastic organic scintillator[5] that was 25.4 mm long

[1] computer code Monte Carlo N-Particle Transport version 5 (Los Alamos National Laboratory, Los Alamos, NM 87545, 2006).

[2] computer code MCNPX-PoliMi v2.0 (Polytechnic of Milan, Milano, Italy and the University of Michigan, Ann Arbor, MI, USA).

[3] MP 320 D-T neutron generator (Thermo Fisher Scientific Inc., Waltham, MA 02451)

[4] EJ-309 liquid scintillator (Eljen Technology, Sweetwater, TX 79556)

[5] Stilbene crystal (Proteus, Inc., Chagrin Falls, OH 44022)

with a 12.7 mm radius. Both models included photomultiplier tube assemblies and associated detector housing (Detection for Nuclear Nonproliferation Group, 2014). The start detector, which was used to determine the beginning of a neutron's TOF after the neutron interacted in it, was aligned facing the generator, with its cylindrical axis parallel to the floor and coincident with the generator source plane. It was placed with the center of its detector volume 0.25 m away from the isotropic point source, which was located at the front center of the accelerator beam target. The stop detector, whose pulse signaled the end of the TOF measurement, was moved around depending on the simulated application.

Results from the simulations were post processed via MPPost[6] to better estimate the light response function of the scintillators and help determine simulated TOF measurements. Personally developed MATLAB[7] scripts were then used to analyze the results.

FNA

Similar to the FNRR measurements in Ch. 7, the FNA simulations consisted of the plastic organic scintillator as the start detector. The neutron TOF stop detector was a liquid organic scintillator and was located 1.0 m from the start detector at an angle, ψ, such that neutrons that underwent a single elastic scatter in the start detector and were directed towards the stop detector would have an incident energy of roughly 7.75 MeV. This is above the threshold for the characteristic gamma rays of C, N, and O. The D-T source emitted neutrons in a cone whose apex subtended a solid angle of 0.0153 steradians. A transmission target that was 0.30 m tall, 0.30 m wide, and 0.20 m thick was placed halfway between the detectors.

[6] computer code MPPost v2.1.0 (University of Michigan, Ann Arbor, MI, USA)

[7] computer program MATLAB (The MathWorks, Inc., Natick, MA 01760-2098, 2006).

In order to examine the possibility of FNA application to the VENES system, an inorganic sodium iodine, or NaI(Tl), scintillator, based on the work by Sudac et al. (2009), was simulated 0.50 m from the center of the interrogation target. Since it was assumed the production of secondary gamma rays is isotropic, the gamma ray detector could be located at any angle. It was initially placed at an angle of $3\pi/4$ radian backscatter to provide a full view of the interrogation target while allowing for use of collimation material to shield it from neutrons and secondary gamma rays in the generator and start detector. However, this required placing the gamma ray detector closer to the generator and start detector and the resultant increase in flux, even with collimating material present, dominated the gamma ray spectra. The detector signal was much cleaner at the $\pi/4$ radian forward scatter position, due to geometric attenuation, and no collimating material was needed. This detector location was used for all FNA simulations. The simulated NaI(Tl) detector had a large volume to increase the fraction of gamma rays detected. It was a cylinder facing the interrogation target with a length and radius of 0.20 m. It had 0.500 atom fractions of sodium and iodine and a density of 3,667 kg m^{-3} (McConn et al., 2011). A timing window was used to limit the gamma ray signal, increasing the likelihood that they were from an interaction in the interrogation target. It should be noted that although a NaI(Tl) detector was used in the simulations, similar TOF principles could be applied to any gamma ray spectrometer, provided it has sufficient timing resolution and can be used near a neutron source.

Ammonium nitrate, melamine, methanol, polyethylene, and sucrose were all simulated as interrogation targets, as was an arrangement where there was no interrogation target present (McConn et al., 2011). A schematic of the setup can be seen in Fig. 8.1.

Neutron backscatter

Several simulations were run to examine the ability of the VENES system to detect elastic neutron backscatter. The interrogation target was placed 1.00 m from the start detector. A backscatter/stop detector was placed 1.00 m from the interrogation target at a scatter angle of $5\pi/6$ radians relative to the expected incident neutron path. The distance between the interrogation target and detectors was chosen in order to provide a longer flight path over which neutrons of varying energies could potentially be distinguished via TOF. It also allowed for discrimination of neutrons that interacted in the start detector and traveled towards the stop detector without first interacting in the interrogation target. Those neutrons have a shorter TOF compared to neutrons that scattered off the interrogation target.

The larger liquid organic scintillator was used as the start and stop detector. The larger start detector increased the likelihood of source neutrons being directed towards the interrogation target, but also broadened the possible energy of the scattered neutrons. To account for the increased size of the start detector, the apex of the emitted neutron cone was increased to 0.3790 steradians. The interrogation target was nearly the same as in the FNA simulations, but 0.10 m thick. The location of the interrogation target was varied such that initially scatter neutrons had expected energies of 3.53 and 7.75 MeV. The neutron energies were chosen because of their broad, relatively constant, contrasting attenuation scatter cross sections for C, N, and O. The simulated arrangements included melamine and methanol interrogation targets, as well as an arrangement with no interrogation target present (McConn et al., 2011).

It was quickly discovered that neutrons that interacted in the start detector and not in the interrogation target, instead either first scattering off the floor or traveling directly towards the stop detector, dominated the simulated TOF signal. Adjusting threshold settings in MPPost did

not sufficiently solve the problem. Therefore, a shield was added that surrounded the stop detector. This significantly reduced the contribution from neutrons that did not interact with the interrogation target and allowed for investigation of the neutron backscatter method. Since gamma ray signal was not a concern, 0.20 m thick polyethylene shield was used. It extended 0.10 m beyond the front face of the stop detector to limit the detector's field of view. An example of the simulated arrangement can be seen in Fig. 8.2.

Shielding

An arrangement similar to the FNA simulations was used to evaluate the neutron shields' effectiveness. The variations in design included removal of the NaI(Tl) and interrogation targets and increasing the distance between the center of the generator and start detector from 0.25 m to 0.27 m. This was done to permit 0.20 m of detector shielding to be applied, while keeping the start detector outside of the shield volume. The shield surrounded the generator and was 0.20 m thick at all locations. The only exception was a cylinder of air with a radius of 70 mm that extended from the edge of the generator, along the source plane, to the edge of the shield closest to the start detector. This provided an unshielded path for source neutrons initially directed at the start detector. The generator, shield, and detector setup can be seen in Fig. 8.3. The source neutron cone present in previous simulations was replaced with an isotropic source to provide a better approximation of the neutron flux surrounding the generator.

Since the neutron TOF background is primarily the result of pulses from two different, coincident neutron interactions in the start and stop detector, it was assumed that the relative flux in the stop detector would provide a good approximation of the TOF background during simulation. The total flux average over the volume of the stop detector was estimated using an F4 tally in MCNP. The detector flux was determined without a generator shield, a shield

consisting entirely of polyethylene, and a layered shield that was modeled after the layered shield from Ch. 3, with an inner 0.05 m layer of polyethylene, then 0.05 m of steel, then 0.05 m of polyethylene, and finally an outer layer 0.05 m of steel (Whetstone and Kearfott, 2011). One set of simulations was conducted both with a D-T source and the stop detector at a scatter angle of 0.967 radians relative to the start detector, resulting in scattered neutrons with an approximate energy of 4.53 MeV. The other set had a deuterium-deuterium (D-D) source with the stop detector at 0.566 radians and neutrons with expected scatter energies of 1.78 MeV.

Results

After simulations, the FNA results were processed. The total number of counts in the gamma ray detector versus the combined neutron and gamma ray TOF can be seen in Fig. 8.4. The time required for a neutron to elastically scatter off a hydrogen nucleus in the start detector, inelastically scatter in the interrogation target, and then have the characteristic gamma ray reach the stop detector is about 14 ns. The earlier peak at 4 ns is a result of the creation of characteristic gamma rays in the start detector. The peak around 22 ns is from interactions in the neutron generator. The final peak is from neutrons interacting in the floor. Based on the expected gamma ray arrival time and Fig. 8.4, the TOF region of interest (ROI) for examining the gamma ray spectra was 11 to15 ns. The resultant spectra for all the interrogation targets can be seen in Fig. 8.5 with a simulated gamma ray energy resolution of 0.020 MeV.

The backscatter TOF spectra can be seen in Fig. 8.6 and 8.7. For neutrons initially scattered at 7.75 MeV, the expected TOF is approximately 56 ns, assuming elastic scatters in the center of the start detector, interrogation target, and stop detector. This corresponds to the peak seen in the figure. A similar peak is present around 80 ns in the spectra for neutrons initially

scattered at 3.53 MeV. The large peak centered near 20 ns is from neutrons that interacted in the start and stop detectors without first scattering in the interrogation target. After accounting for the TOF signal when no interrogation target is present, melamine to methanol ratios were calculated using the counts in the neutron backscatter peaks. The ROI was 60 to 70 ns for the 7.75 MeV scattered neutrons and 72 to 82 ns for the 3.53 MeV scattered neutrons. The resultant values were 0.495 ± 0.018 and 0.516 ± 0.016, respectively.

The total average flux in the stop detector was estimated for both sets of shielding simulations. The results can be seen in Table 8.1. With a D-D source, the flux in the stop detector was reduced by 91% and 97% for the layered and pure polyethylene shield designs, respectively. Both shields reduced the detector flux from a D-T source by approximately 75%.

Discussion

VENES applications

The VENES system provides an alternative means of generating tagged neutrons for active interrogation, using readily available equipment while also providing the means to change the expected energy of those tagged neutrons. This flexible solution can potentially be applied to a wide variety of explosives detection methods.

The simulations using tagged neutrons from the VENES system for FNA and neutron backscatter measurements were encouraging. Without thorough optimization of the detector setup or laboratory measurements to help benchmark the simulations, it is difficult to draw any specific conclusions from the work. However, general trends can be observed. In the FNA simulations, the distinct TOF distribution of total gamma ray counts provides an opportunity for discrimination. By using the combined TOF of the scattered neutron and secondary gamma ray,

the noise in the signal can be reduced. This allows for better contrast between the gamma ray spectra for the assorted interrogation targets. The differences in peak occurrence and magnitude amongst the gamma ray spectra, seen in Fig. 8.5, demonstrate a potential method for confirming the presence of explosive materials. The method has had success previously using a generator with API (Sudac et al., 2009; Sudac et al., 2011). As seen in Fig. 8.4, the VENES system appears to be an adaptable means of generating tagged neutrons to narrow the gamma ray detector timing window. The simulated arrangement avoids many secondary gamma rays from neutron interactions in locations other than the interrogation target, reducing noise in the time-tagged gamma ray spectra by approximately 80 – 90%. This number would be different in laboratory measurements due to the nearly isotropic source and coincident gamma rays created by neutron interactions in the environment, but the overall signal will still be improved. The method could possibly be refined through implementation of PHD in the start detector. Since the neutron energy deposited in the detector should be its initial energy minus its scattered energy, the signal in the gamma ray detector could be further discriminated if the start detector pulse height does not correlate to a neutron scatter towards the interrogation target.

Similarly, the obvious neutron backscatter TOF peaks seen in Fig. 8.6 and 8.7 confirm potential application of the VENES system for neutron backscatter measurements and offer a viable alternative to PHD when measuring neutron backscatter (Lehnert and Kearfott, 2015). As seen in the TOF spectra, there is a clear difference between the number of detected neutrons for the two interrogation targets. The distinction occurs in the peaks centered near the expected TOF for a neutron that undergoes single elastic scatter in both the start detector and interrogation target. In its current arrangement, and by utilizing the ROI, approximately 95 – 98% of the time-tagged neutrons would be discriminated, eliminating much of the signal that was a result of one

or more neutron scattering events in locations other than the interrogation target. Again this number would vary in practice due to coincident neutrons in the stop detector. However, the system will still be able to distinguish single backscatter events from most of the other neutrons detected. The neutron signal within the timing window can be analyzed, either for a change in total backscatter events or, if the interrogation target was small and the start or stop detector were sufficiently far away, to search for characteristic peaks in the TOF spectra. If this method were successfully adapted, it would allow for determination of neutron interrogation explosives detection flags without the need for direct measurement of neutron energy.

Unfortunately, compared to FNRR measurements, the detection efficiency for both FNA and neutron backscatter measurements using the VENES system is relatively low. This is a consequence of searching for secondary radiation and has always been true, regardless of the neutron source used. However, given that the VENES system efficiency is already comparatively less than other sources, such as linear accelerators or API generators, use of the VENES system for FNA and neutron backscatter measurements would most likely only be justifiable in certain scenarios, such as when long count times are allowed, a powerful neutron source is available, or there are no readily accessible alternatives to produce tagged neutrons.

Another option would be to combine the FNA and neutron backscatter methods with other measurements, similar to what was suggested by Lehnert and Kearfott (2015). In their system, nearly monoenergetic neutrons from a sealed-tube D-T source are used to conduct neutron transmission, FNA, and neutron backscatter measurements in order to determine whether an interrogation target was a threat or benign. Additional detectors can be applied to the VENES FNRR method explored in Ch. 7 to allow for a comparable setup, permitting FNA and neutron backscatter measurements during each transmission measurement. This system would be an

improvement over previous work because tagged neutrons can now have their energy reliably varied without the need for a large particle accelerator. This permits the opportunity for multiple measurements at different neutron energies in order to gain additional information about the interrogation target.

Further work is needed to determine how the ability to vary the energy of the tagged neutrons during FNA or neutron backscatter measurements can best be utilized. Given that the neutron interaction cross sections fluctuate with neutron energy, it may be possible to find an optimum combination of incident neutron energies that helps in determining the relative elemental abundances of the interrogation target. Conversely, it may be that FNA and neutron backscatter measurements are simply used as a secondary check for FNRR measurements, helping to confirm the presence of a nuclide, or eliminate some ambiguity during analysis.

Deployed system suggestions

Although it provides flexibility in choosing incident neutron energy, the VENES system reduces the usable neutron production rate compared to the same D-D or D-T source in a traditional setup. Given that many active neutron interrogation applications need to be conducted quickly, this could be a serious concern. Fortunately, the VENES arrangement previously presented can be improved.

The shield designs discussed in Ch. 3, and adapted for simulation here, significantly reduce the neutron flux in the stop detector. As seen in Table 8.1, for D-D neutrons, the polyethylene source shield was approximately three times more effective at reducing neutron flux in the stop detector compared to the steel and polyethylene layered shield. However, when a D-T generator was simulated, the detector fluxes were similar. Therefore, in the current arrangement, a polyethylene shield is the better choice. It is lighter than, and at least as effective

as, the layered design. However, as discussed in Ch. 3, this may not always be the case with thicker shields or if dose rates to surrounding personnel are a concern.

The reduced stop detector flux will improve the SNR and permit shorter count times with better statistics. In the current arrangement, source shield space was limited by the start detector location. In future applications, additional shielding material could be possible. However, the tradeoffs between increased system size and mass compared to improvements in the SNR must be carefully weighed. The transmission stop detector could also have detector shielding applied, but given that it is essentially facing the neutron source and start detector, it is unlikely that shielding around its side and back would have as significant an impact as the source shielding.

In all the laboratory measurements and simulations discussed, a single start detector was used to scatter neutrons and a single stop detector was placed at the predetermined distance and scatter angle. On occasion, a second stop detector was placed at the same scatter angle and distance in a symmetric location to improve counting statistics. In both instances, the single start detector presented a relatively small volume in which the source neutrons could elastically scatter.

Enlarging the start detector volume would increase the likelihood of source neutron interactions, but as discussed in Ch. 5, also increase the systematic uncertainty related to the scattered neutron energies. This can be avoided, however, by using an array of smaller start detectors arranged to create a single large scatter target. The location of each scattered neutron interaction would be known more precisely than in a single large detector, minimizing uncertainty while still increasing the relative likelihood of interactions. The face of the detector would be pointed up with the PMT and detector housing directed at the ground, removing them from the desired flight path of the scattered neutrons. This allows for the start detectors to be

tightly packed in a horizontal plane. Similarly, an array of relatively small stop detectors can be used to create a large target for transmission neutrons without sacrificing systematic uncertainty. This arrangement would also be beneficial if attempting to determine a two-dimensional elemental map of a large interrogation object. It would allow smaller, discretized transmission measurements of the interrogation target (Raas et al., 2005). Additionally, the VENES system arrangement could benefit from the symmetry associated with the nearly isotropic nature of neutron generation and elastic scatter. This would permit for the placement of multiple start and stop detectors around a single neutron generator, resulting in interrogation of multiple objects at the same time.

A permanent VENES system would also benefit from an arrangement that would assist in quickly changing the stop detector and interrogation target location relative to the scatter target. This can be done with a set of tracks allowing for their quick rotation about the center of the system. The stop detector and transmission target can then be locked in place to assure an accurate scatter angle and assumed neutron travel distance. A schematic drawing of the proposed arrangement, with arrays for the start and stop detectors, FNA and neutron backscatter detectors, and source and detector shields, can be seen in Fig. 8.8. An alternative FNRR arrangement can be seen in Fig. 8.9. In it, the stop detector and interrogation target location are fixed and multiple start detectors are positioned independently. Source neutrons interacting in each start detector must undergo elastic collisions at different angles to arrive in the stop detectors. This permits for interrogation at multiple neutron energies simultaneously, and potentially quicker evaluations. For the first VENES arrangement, there will be slight variations in scatter angle and neutron path. In the second arrangement, the neutron paths through the interrogation target vary significantly based on their scatter angle. These variations will have to be accounted for when

interrogating unknown targets, but if properly addressed, the VENES efficiency could be considerably increased.

Ultimately, application of the VENES system will be determined through evaluation of the tradeoffs between the ability to vary the incident neutron energy and the reduction in efficiency associated with the preliminary neutron elastic scatter. For FNRR, where no other portable systems exist that can change the incident neutron energy, the reduction in efficiency should be acceptable. FNA and neutron backscatter measurements, on the other hand, are inherently less efficient, making use of the VENES system for those individual measurements less likely. However, as discussed previously, the approximately two order of magnitude increases to the SNR through TOF discrimination and source shielding will improve the detector signal. Improvements to overall system efficiency, via optimization of detector arrangements, and potentially new explosives detection flags at different incident energies will also benefit the VENES system. This should allow for FNA and neutron backscatter measurements to be conducted in conjunction with the multiple transmission measurements necessary for FNRR.

Conclusions

Optimized source, detector, and interrogation target placement, combined with appropriate shielding, can make the VENES system, in certain circumstances, a viable alternative to other neutron sources. Preliminary investigation has explored the potential to apply the VENES system to several explosives detection methods. The ease of use of the system, combined with the commercial availability and relatively low cost of its components, allows for adaptation of the VENES system to a variety of applications. Furthermore, when compared to

traditional sealed-tube D-T and D-D generators, the flexibility of the tagged neutron energy provides many additional opportunities for exploration via active neutron interrogation.

In simulations, the VENES system showed promise for use with both FNA and neutron backscatter measurements. Even with careful detector and shield placement, the inherent inefficiency of the system may limit the practical application of FNA and neutron backscatter as standalone approaches. However, combining FNA and neutron backscatter with FNRR measurements conducted by the VENES system could create a viable alternative to current active neutron interrogation methods. This would increase the potential information available to investigators, and provide a secondary confirmation of the interrogation object's composition. The ability to change the tagged neutron energy allows for the development of new detection methods and algorithms not previously available with traditional sealed-tube neutron generators. Further work is warranted to investigate implementation of the VENES system with current active neutron interrogation methods.

Figures

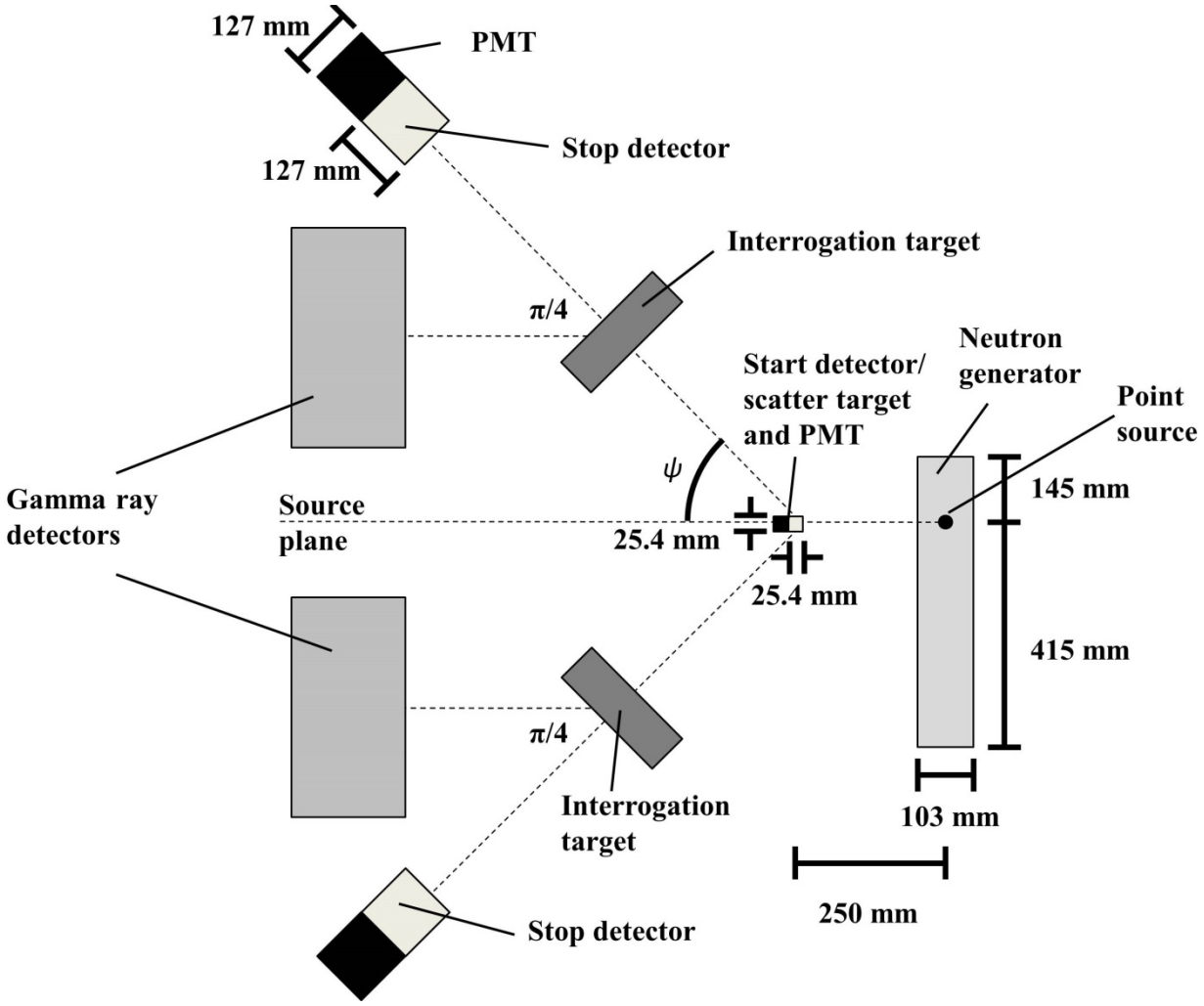

Fig. 8.1: A top-down view representing the geometry used in the FNA simulations.

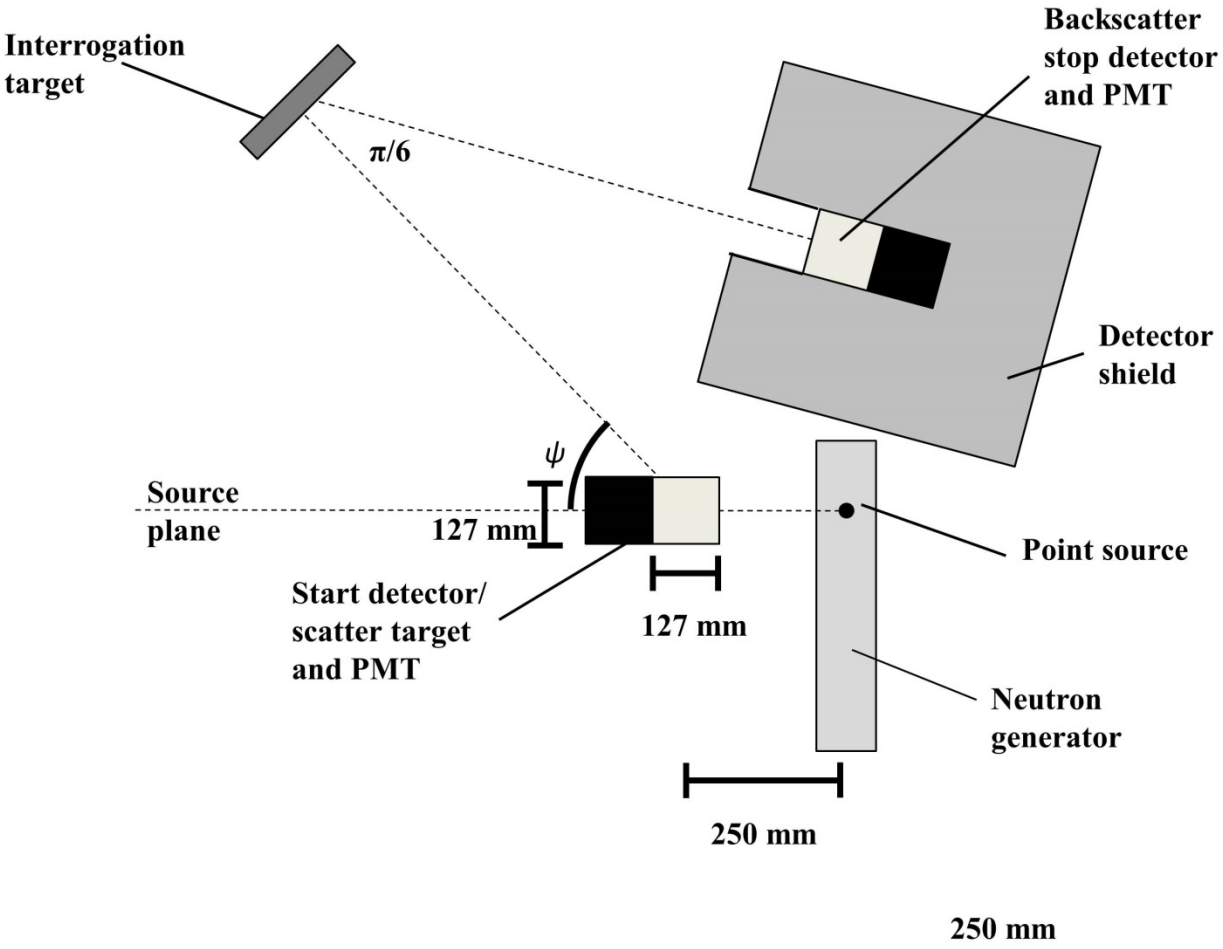

Fig. 8.2: A top-down view representing the geometry used in the neutron backscatter simulations.

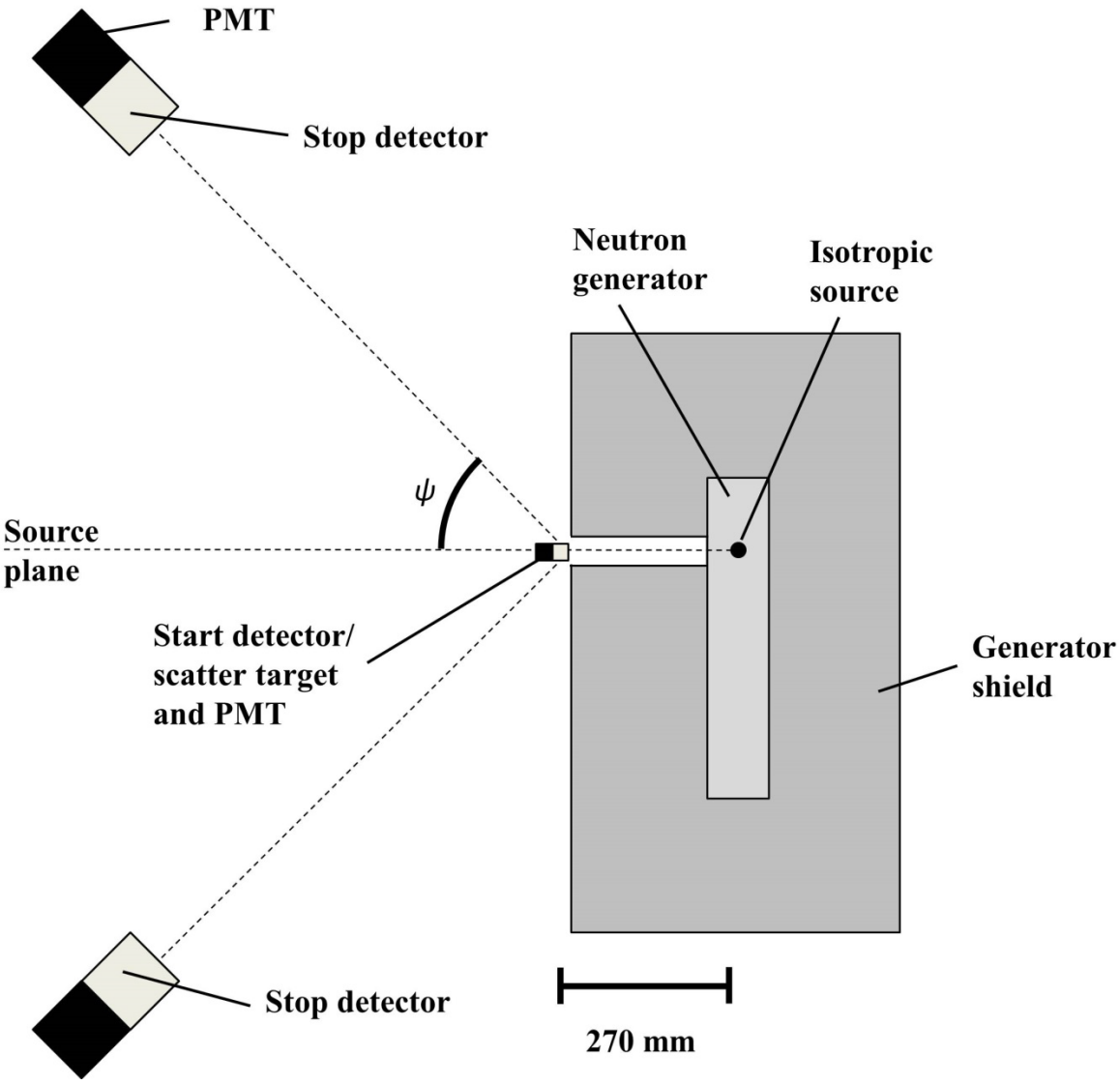

Fig. 8.3: A top-down view representing the geometry used in the generator shielding simulations.

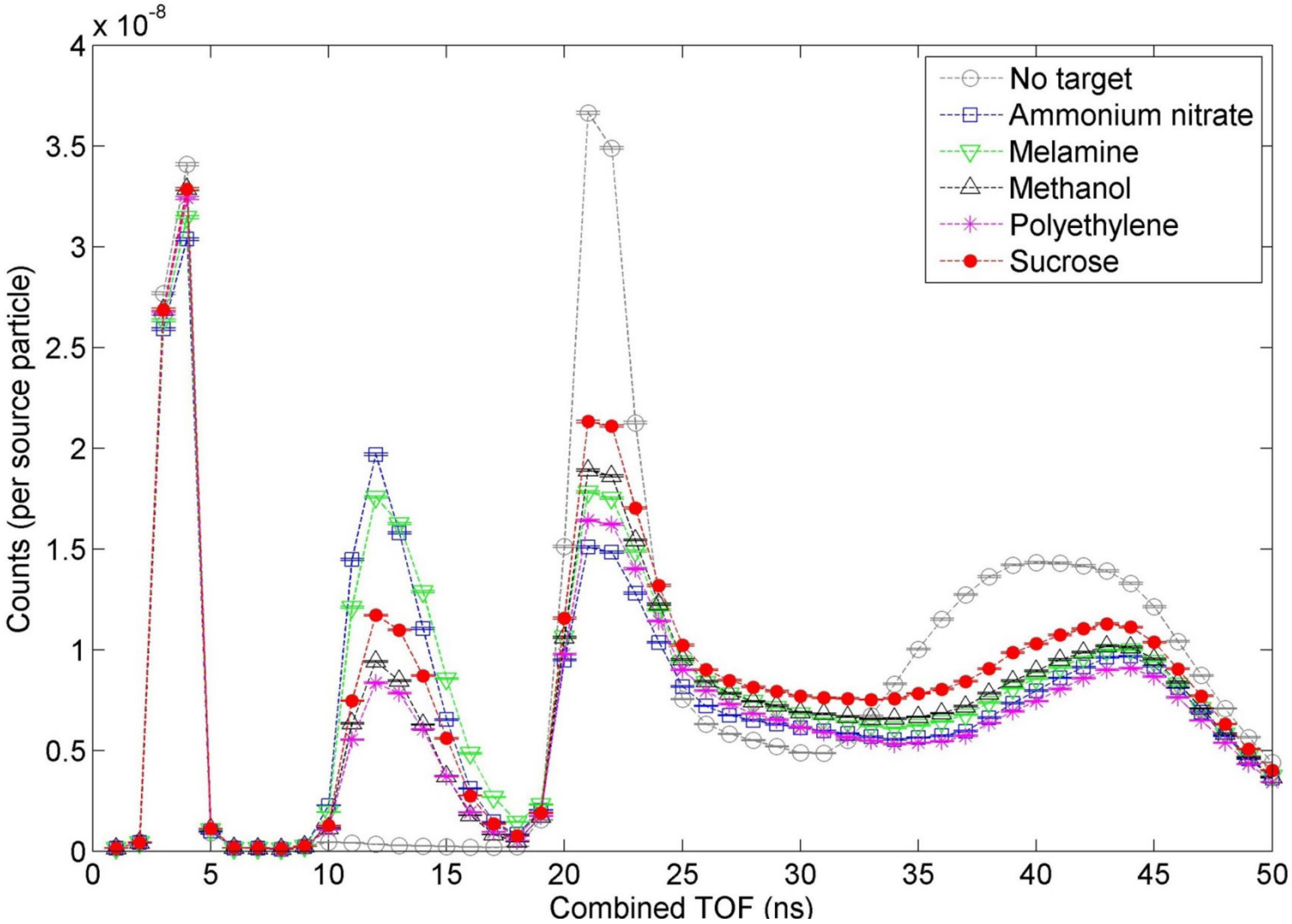

Fig. 8.4: The simulated TOF distribution for total gamma ray counts in a single NaI(Tl) detector.

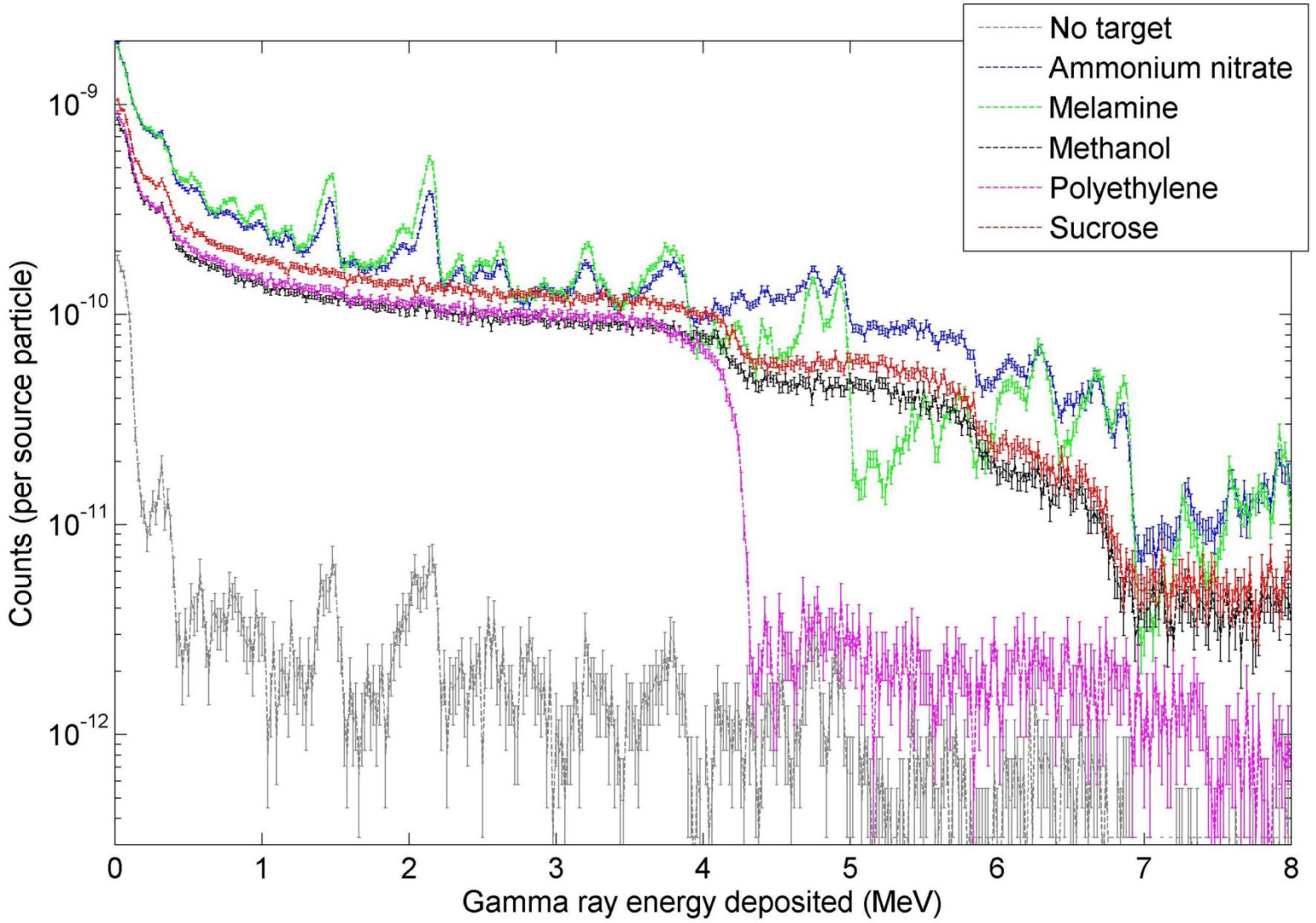

Fig. 8.5: The simulated gamma ray energy spectra in a single NaI(Tl) detector for multiple different interrogation targets using a TOF ROI from 11 – 15 ns.

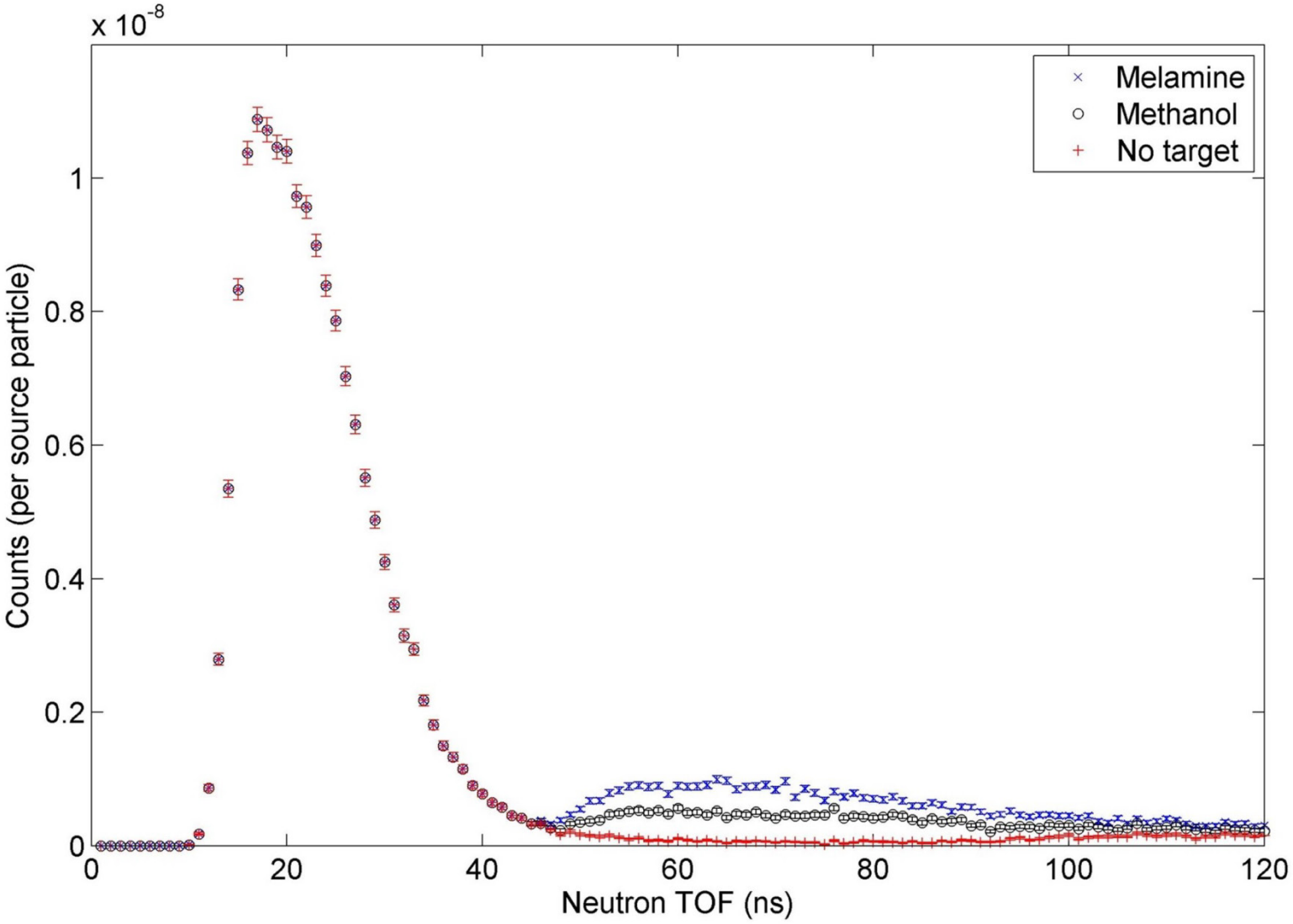

Fig. 8.6: The neutron backscatter TOF spectra with neutrons initially scattered at approximately 7.78 MeV.

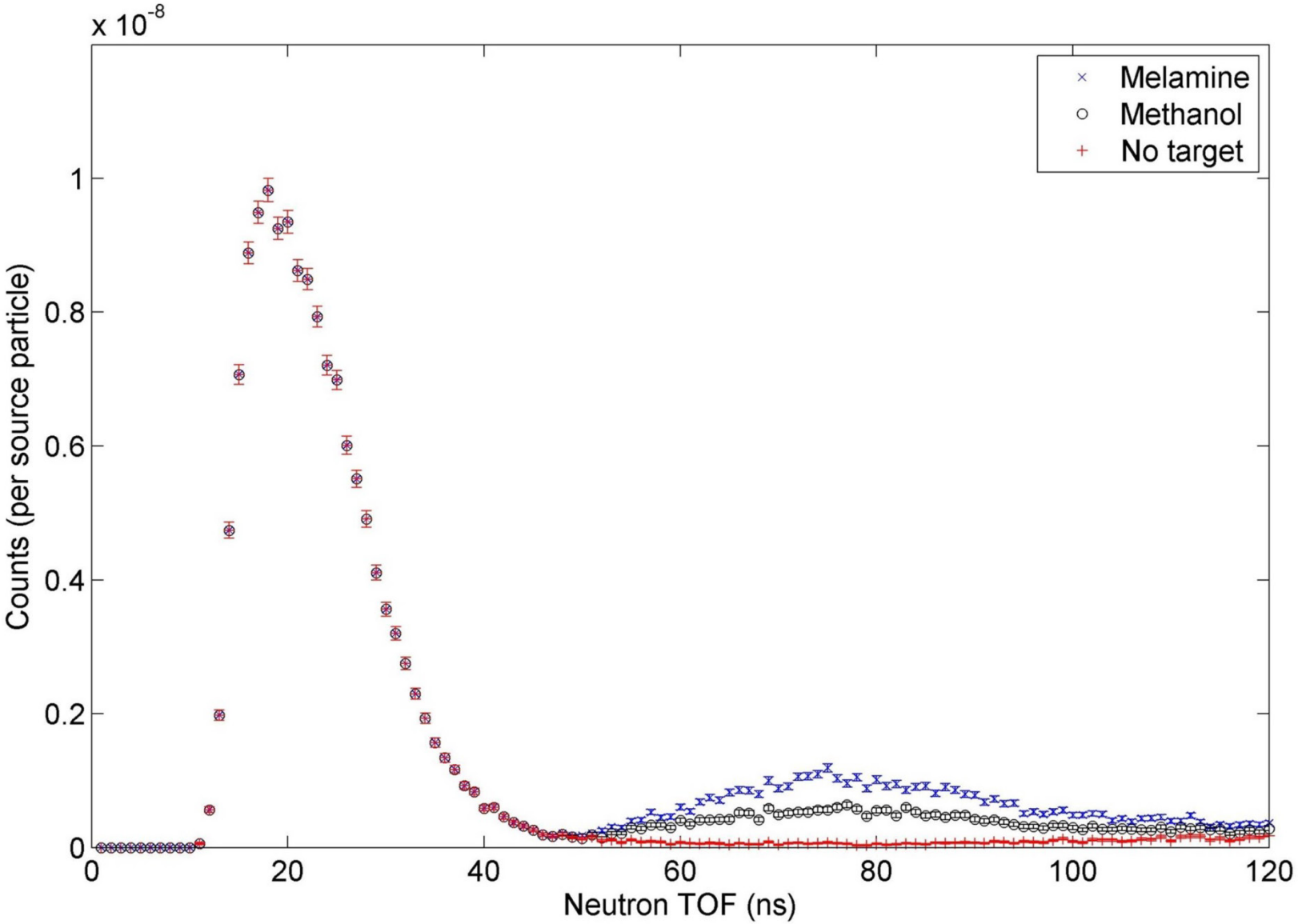

Fig. 8.7: The neutron backscatter TOF spectra with neutrons initially scattered at approximately 3.53 MeV.

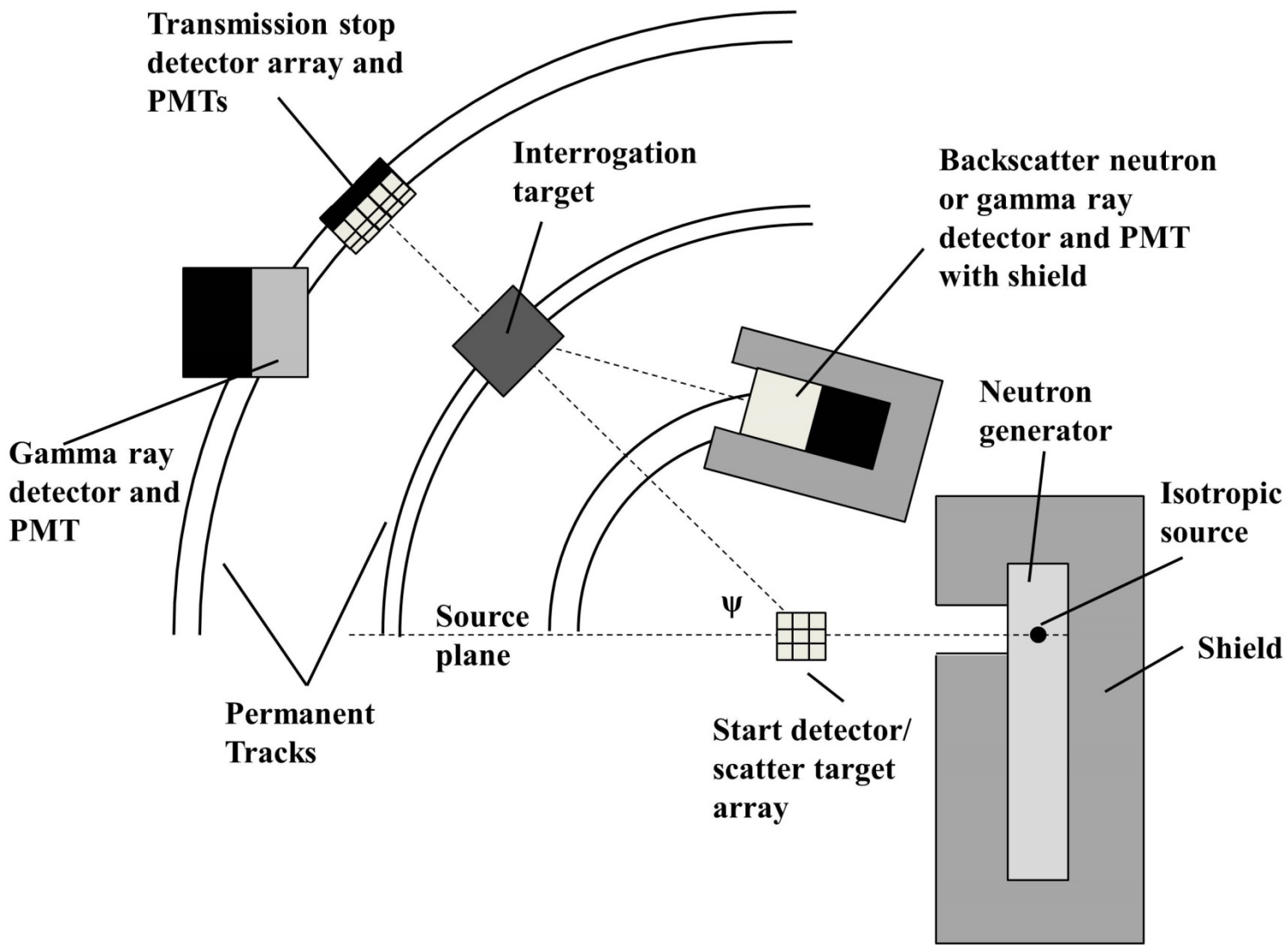

Fig. 8.8: A proposed VENES system arrangement with tracks that allows for quick, precise rotation of the interrogation target and stop detectors about the start detector.

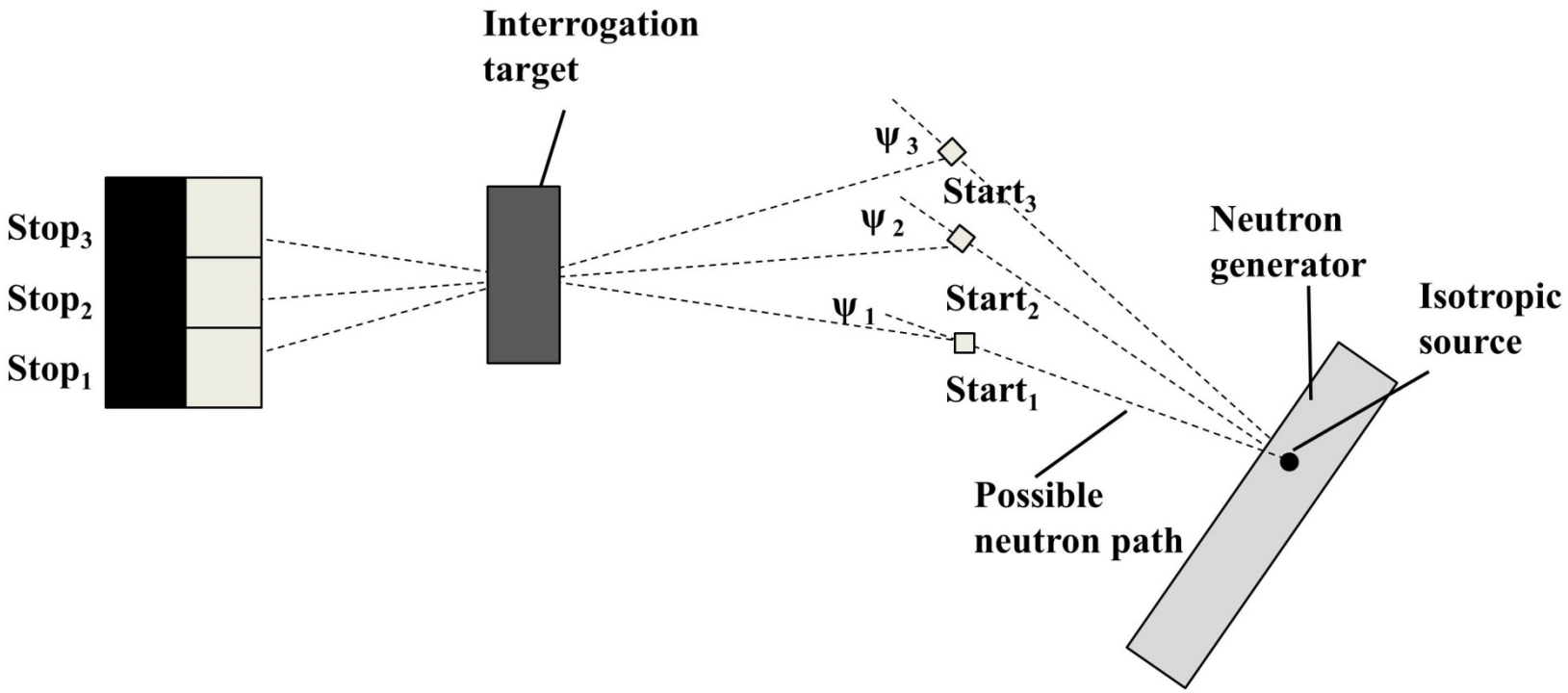

Fig. 8.9: An alternative VENES system arrangement that allows for simultaneous measurements at multiple neutron energies using several start detectors at different locations.

Table

Table 8.1: The estimated average flux in the stop detector for two different generator shields and neutron sources, as determined by an MCNP PoliMi F4 tally. Statistical uncertainties were all below 1%.

Source	Shield arrangement	Average simulated neutron flux (mm^{-2} source $particle^{-1}$)
D-D	Unshielded	5.11×10^{-8}
	Layered	4.67×10^{-9}
	Polyethylene	1.52×10^{-9}
D-T	Unshielded	6.21×10^{-8}
	Layered	1.34×10^{-8}
	Polyethylene	1.58×10^{-8}

References

Buffler, A., 2004. Contraband detection with fast neutrons. *Radiat. Phys. Chem.*, 71(3-4), 853-861.

Chichester, D., Lemchak, M., Simpson, J., 2005. The API 120: A portable neutron generator for the associated particle technique. *Nucl. Instrum. Meth. B,* 241 (1-4), 753-758.

Detection for Nuclear Nonproliferation Group, University of Michigan, Ann Arbor, MI, 2014. Personal email correspondence. June 9-13.

McConn Jr., R.J., Gesh, C.J., Pagh, R.T., Rucker, R.A., Williams III, R.G., 2011. Compendium of material composition data for radiation transport modeling. Pacific Northwest National Laboratory, Report No. PNNL-15870.

Raas, W.L., Blackburn, B., Boyd, E., Hall, J.M., Kohse, G., Lanza, R., Rusnak, B., Watterson, J.I.W., 2005. Neutron resonance radiography for explosives detection: technical challenges. *Nuclear Science Symposium Conference Record, 2005 IEEE*, (1), 129-133.

Sudac, D., Matika, D., Valkovic, V., 2009. Detection of explosives in objects on the bottom of the sea. AIP Conf. Proc., 1099, 574-577.

Sudac, D., Vlakovic, V., Nad, K., Obhodas, J., 2011. The underwater detection of TNT explosive. *IEEE T. on Nucl. Sci.*, 58 (2), 547 – 551.

Thermo Fischer Scientific Inc., Waltham, MA, 2014. Personal phone and email correspondence. June 17-23.

Whetstone, Z.D., Kearfott, K.J., 2011. Use of multiple layers of repeating material to effectively collimate an isotropic neutron source. *Nuc. Technol.*, 176 (3), 395 – 413.

Whetstone, Z.D., Kearfott, K.J., 2014. A review of conventional explosives detection using active neutron interrogation. *J. Radioanal. Nucl. Ch.*, 301 (3), 629-639.

Whetstone, Z.D., Kearfott, K.J., 2015. A method for using neuton elastic scatter to create a variable energy neutron beam form a nearly monoenergetic source. *Radiat. Phys. Chem.*, Accepted for publication.

CHAPTER 9: CONCLUSIONS AND FUTURE WORK

Research Summary

The use of conventional explosives against people and property continues to be a serious threat. As discussed in Ch. 2, there are a variety of methods used to search for hidden explosives, including several different active neutron interrogation techniques. Despite its advantages, such as the relatively high penetrability of neutrons and the ability to determine the elemental composition of objects, active neutron interrogation has failed to find wide-spread deployment. This is, in part, a consequence of the complications associated with shielding neutrons and either a lack of variability in neutron energy, or alternatively, large, complicated, and expensive neutron production equipment. Improvements in traditional active neutron interrogations systems can have wide-spread benefits across several explosives detection techniques. The research presented in this work explored new designs for generator and detector shielding, as well as developed a novel method for altering the energy of neutrons from a nearly monoenergetic source. The purpose was to design an adaptable active neutron interrogation system using currently available technology that was relatively simple and could be applied to several different explosives detection methods.

Initial research, presented in Ch. 3, evaluated many different neutron shielding designs, via Monte Carlo simulation, to help limit the unattenuated emission of nearly isotropic source neutrons and reduce the flux and potential dose to personnel around the generator. The final design was a multi-layered steel and polyethylene shield that reduced the estimated dose

opposite the shield opening by roughly two orders of magnitude. The work was expanded in Ch. 4, with a similar simulated shielding design applied to detectors in an active neutron interrogation system. The layered design helped limit the field of view and reduce the neutron and photon flux in detectors by several orders of magnitude. The chapter also contained discussion of a way to design and build the generator and detector shields which allowed for portability and adjustability with quick construction and disassembly via modular implementation of the various shield layers.

The work in Ch. 5 focused on developing a new method by which it was possible to reliably change the energy of neutrons. Current generators produce neutrons clustered around a single energy and either cannot have that energy adjusted, such as with sealed-tube deuterium-deuterium and deuterium-tritium generators, or are large accelerators that are costly and difficult to operate. Given that the likelihood of neutron-nucleus interactions are dependent on the nuclide and vary significantly with neutron energy, the added flexibility of a variable energy neutron source provides significantly more options for active interrogation applications. The method, which employs a portable sealed-tube generator as the source, produces neutrons within a specific energy range via single elastic scatter off a target containing nuclides of known mass. The neutron's final energy is determined by the scatter nuclide mass and neutron scatter angle, allowing for the user to choose their interrogating neutron energy. This is accomplished via manipulation of the composition of the scatter target and the interrogation object's location relative to the incident direction of source neutrons on the scatter target. The elastic scatter method showed promise in idealized simulations with multiple scatter targets. However, more realistic simulations and a laboratory experiment revealed accurate neutron energy information would be required to properly discriminate source neutrons that interacted elsewhere in the

environment. Furthermore, analysis of the systematic uncertainty associated with the discrete volumes of the scatter target and neutron detector revealed limits to the precision of the scattered neutron energy.

The idea of using elastic scatter to reliably change neutron energy was further expanded in Ch. 6. In order to confirm the scattered neutron energy and help discriminate neutrons that did not interact in the scatter target, an organic scintillator time-of-flight (TOF) spectrometry system was adapted to serve as both the scatter target and neutron detector for active interrogation applications. A single organic scintillator served a dual purpose as both the TOF start detector and scatter target, providing accurate timing information and signaling when neutrons scattered off its hydrogen nuclei. If the scattered neutrons were then detected by the stop detector, their TOF and approximate energy could be determined. This was confirmed in both laboratory measurements and simulations. Neutrons that were detected in the stop detector and did not have a corresponding signal in the start detector were neglected, greatly improving the stop detector signal. By using the variable energy neutron elastic scatter (VENES) system, it became possible to identify scattered neutrons of specific energies and use them for active neutron interrogation applications. The energy range of scattered neutrons identified by the stop detector was dependent on the distances between the source, start detector/scatter target, and stop detector as well as the volume of the detectors. Increased energy precision was possible, but came with the consequence of decreased system efficiency.

In Ch. 7, the VENES system was applied to the fast neutron resonance radiography (FNRR) method of active neutron interrogation. Due to the differing neutron attenuation cross sections for H, C, N, and O in the 1 to 14 MeV range, it is possible to determine the atomic fractions of unknown targets by measuring the neutron transmission rates through the

interrogation target at various energies. Traditionally, large particle accelerators are used to generate near-monoenergetic neutrons. Laboratory experiments and simulations were conducted to determine if the VENES system could be a viable alternative. The results were promising, with simulated elemental composition estimates accurate to within several hundredths of an atom fraction. As expected, the introduction of measurement uncertainty increased the average error in the estimated atom fractions, emphasizing the need for precise measurements. The signal-to-noise ratio of the VENES system during transmission measurements was also explored, revealing the existence of an upper density thickness limit for interrogation objects.

Finally, in Ch.8, alternative active neutron interrogation applications for the VENES system were explored. Preliminary investigations showed a significant TOF dependence for both fast neutron analysis (FNA) and neutron backscatter when using neutrons from the VENES system. Although both methods require neutrons to interact in the interrogation target, resulting in a reduction in efficiency, they can be combined with a VENES FNRR measurement system to provide additional, independent methods of investigation. It was also demonstrated that the use of source and detector shields can reduce the neutron flux in the stop detector, with the ultimate goal of improving the signal-to-noise ratio.

In general, the VENES system improves active neutron interrogation methods that search for conventional explosives. The flexibility in potential neutron energy expands the avenues of investigation for established interrogation techniques while also providing accurate neutron energy and timing information. The VENES system is also a strong alternative to large, expensive accelerator sources when neutrons of specific and varied energies are required. It may have a lower efficiency compared to other sources, but the VENES system's portability and ease of use may allow it to fit certain applications, such as mobile inspections or situations where

space is limited. Furthermore, it can be constructed with readily available, relatively inexpensive components, expanding the potential reach of active neutron interrogation techniques for explosives detection.

Future Work

There are three general directions on which further research should focus. The first is refining the VENES system. The equipment simulated and tested in the laboratory proved the system works. However, it still needs to be optimized. Alternative detectors and neutron sources should be explored. Similarly, relative detector sizes and locations need to be tested to help characterize and evaluate the variation in scattered neutron energy and correlated tradeoffs in system efficiency. Finally, testing in realistic scenarios should be conducted to better understand sources of measurement uncertainty.

Many aspects of the VENES system will need to be adjusted, based on the particular application. Therefore, it is important to further investigate how the system can be applied to various active neutron interrogation scenarios. Simulated FNRR measurements were encouraging, but actual measurements must be conducted to determine the viability of combining VENES with FNRR. Both FNA and neutron backscatter measurements also showed promise with preliminary simulations, but much more work is needed to determine if use of the VENES system, given its relatively low efficiency, is appropriate for these active interrogation methods. If so, laboratory measurements must be performed in order to optimize the detector signal, with particular emphasis on determining the ideal energies required for scattered neutrons incident on the interrogation target. All methods should be tested with a variety of interrogation materials and inhomogeneous arrangements.

Finally, alternative applications for the VENES system could be explored. This work has focused on improving active neutron interrogation methods to find conventional explosives. However, these same techniques could be applied to search for narcotics, which tend to also be comprised of light nuclides and have unique elemental ratios. There are other fields that may benefit from an inexpensive, portable, easy-to-use neutron source that can vary the energy of its neutrons and perform TOF spectroscopy. One example would be neutron imaging. The flexibility of the VENES system could be ideal for imaging objects of various dimensions and adjusting the scattered neutron energy based on the object's size and density. Alternatively, it could be transported to image more permanent objects that cannot be easily moved themselves. Further research should be conducted to find additional applications for the VENES system.

APPENDICES

Appendix A: Example Monte Carlo Simulation Inputs

Isotropic neutron source shield evaluation

```
c Cylindrical shielding geometry w/ alternating layers of steel and polyethylene
1 1 -0.0012 -1 2 -3 imp:n=1 imp:p=1 $opening
2 2 -0.94 -1 2 3 -5 imp:n=1 imp:p=1 $polyethylene cylinder
3 2 -0.94 -2 4 -5 imp:n=1 imp:p=1 $polyethylene plate
4 3 -7.86 -1 4 5 -7 imp:n=1 imp:p=1 $steel cylinder
5 3 -7.86 -4 6 -7 imp:n=1 imp:p=1 $steel plate
6 2 -0.94 -1 6 7 -9 imp:n=1 imp:p=1 $polyethylene cylinder
7 2 -0.94 -6 8 -9 imp:n=1 imp:p=1 $polyethylene plate
8 3 -7.86 -1 8 9 -11 imp:n=1 imp:p=1 $steel cylinder
9 3 -7.86 -8 10 -11 imp:n=1 imp:p=1 $steel plate
10 2 -0.94 -1 10 11 -13 imp:n=1 imp:p=1 $polyethylene cylinder
11 2 -0.94 -10 12 -13 imp:n=1 imp:p=1 $polyethylene plate
12 3 -7.86 -1 12 13 -15 imp:n=1 imp:p=1 $steel cylinder
13 3 -7.86 -12 14 -15 imp:n=1 imp:p=1 $steel plate
50 1 -0.0012 -50 imp:n=1 imp:p=1
52 1 -0.0012 -52 imp:n=1 imp:p=1
54 1 -0.0012 -54 imp:n=1 imp:p=1
56 1 -0.0012 -56 imp:n=1 imp:p=1
58 1 -0.0012 -58 imp:n=1 imp:p=1
70 1 -0.0012 -70 imp:n=1 imp:p=1
72 1 -0.0012 -72 imp:n=1 imp:p=1
74 1 -0.0012 -74 imp:n=1 imp:p=1
76 1 -0.0012 -76 imp:n=1 imp:p=1
78 1 -0.0012 -78 imp:n=1 imp:p=1
1000 1 -0.0012 -1000 #(-1 14 -15) 50 52 54 56 58
            70 72 74 76 78 imp:n=1 imp:p=1
1001 0 1000 imp:n=0 imp:p=0

1 py 50
2 py 0.0001
3 cy 16
4 py -5
```

```
5 cy 21
6 py -30
7 cy 46
8 py -35
9 cy 51
10 py -40
11 cy 56
12 py -45
13 cy 61
14 py -50
15 cy 66
50 sy 150 25
c 51 s 0 138.58 57.40 25
52 s 0 106.066 106.066 25
c 53 s 0 57.40 138.58 25
54 sz 150 25
c 55 s 0 -57.40 138.58 25
56 s 0 -106.066 106.066 25
c 57 s 0 -138.58 57.40 25
58 sy -150 25
70 sy 500 25
72 s 0 353.55 -353.55 25
74 sz -500 25
76 s 0 -353.55 -353.55 25
78 sy -500 25
1000 so 1000

mode p n
m1 6012 .0001 7014 .755 8016 .232 18000 .013  $air
m2 1001 4 6000 2 $polyethylene
m3 26000 -.998 8016 -0.002 $1018 steel
sdef POS=0 0 0 PAR=1 ERG=14.1
nps 10000000
de715: 2.5E-8 1E-7 1E-6 1E-5 1E-4 1E-3 0.01 0.02 0.05 0.1 0.2 0.5 1 1.5 2 3 4 5
      6 7 8 10 14 17 20
df715: 19E-12 22.2E-12 22.4E-12 18.4E-12 14.2E-12 12.4E-12 19E-12 39.8E-12
      101.2E-12 192E-12 302E-12 558E-12 728E-12 750E-12 738E-12 836E-12 878E-12
      804E-12 830E-12 888E-12 928E-12 962E-12 1040E-12 1280E-12 1320E-12
f715:n 0 150 0   0
c
de725: 0.01 0.015 0.02 0.03 0.04 0.05 0.06 0.08 0.1 0.15 0.2 0.3 0.4 0.5 0.6 0.8
      1 1.5 2 3 4 5 6 8 10
df725: 0.077E-12 0.85E-12 1E-12 0.79E-12 0.63E-12 0.54E-12 0.50E-12 0.53E-12
      0.61E-12 0.89E-12 1.2E-12 1.8E-12 2.38E-12 2.93E-12 3.44E-12 4.38E-12
```

5.2E-12 7E-12 8.6E-12 11.2E-12 13.6E-12 15.7E-12 17.9E-12 22.3E-12
26.4E-12
f725:p 0 150 0 0
de735: 2.5E-8 1E-7 1E-6 1E-5 1E-4 1E-3 0.01 0.02 0.05 0.1 0.2 0.5 1 1.5 2 3 4 5
6 7 8 10 14 17 20
df735: 19E-12 22.2E-12 22.4E-12 18.4E-12 14.2E-12 12.4E-12 19E-12 39.8E-12
101.2E-12 192E-12 302E-12 558E-12 728E-12 750E-12 738E-12 836E-12 878E-12
804E-12 830E-12 888E-12 928E-12 962E-12 1040E-12 1280E-12 1320E-12
f735:n 0 106.066 106.066 0
c
de745: 0.01 0.015 0.02 0.03 0.04 0.05 0.06 0.08 0.1 0.15 0.2 0.3 0.4 0.5 0.6 0.8
1 1.5 2 3 4 5 6 8 10
df745: 0.077E-12 0.85E-12 1E-12 0.79E-12 0.63E-12 0.54E-12 0.50E-12 0.53E-12
0.61E-12 0.89E-12 1.2E-12 1.8E-12 2.38E-12 2.93E-12 3.44E-12 4.38E-12
5.2E-12 7E-12 8.6E-12 11.2E-12 13.6E-12 15.7E-12 17.9E-12 22.3E-12
26.4E-12
f745:p 0 106.066 106.066 0
de755: 2.5E-8 1E-7 1E-6 1E-5 1E-4 1E-3 0.01 0.02 0.05 0.1 0.2 0.5 1 1.5 2 3 4 5
6 7 8 10 14 17 20
df755: 19E-12 22.2E-12 22.4E-12 18.4E-12 14.2E-12 12.4E-12 19E-12 39.8E-12
101.2E-12 192E-12 302E-12 558E-12 728E-12 750E-12 738E-12 836E-12 878E-12
804E-12 830E-12 888E-12 928E-12 962E-12 1040E-12 1280E-12 1320E-12
f755:n 0 0 150 0
c
de765: 0.01 0.015 0.02 0.03 0.04 0.05 0.06 0.08 0.1 0.15 0.2 0.3 0.4 0.5 0.6 0.8
1 1.5 2 3 4 5 6 8 10
df765: 0.077E-12 0.85E-12 1E-12 0.79E-12 0.63E-12 0.54E-12 0.50E-12 0.53E-12
0.61E-12 0.89E-12 1.2E-12 1.8E-12 2.38E-12 2.93E-12 3.44E-12 4.38E-12
5.2E-12 7E-12 8.6E-12 11.2E-12 13.6E-12 15.7E-12 17.9E-12 22.3E-12
26.4E-12
f765:p 0 0 150 0
de775: 2.5E-8 1E-7 1E-6 1E-5 1E-4 1E-3 0.01 0.02 0.05 0.1 0.2 0.5 1 1.5 2 3 4 5
6 7 8 10 14 17 20
df775: 19E-12 22.2E-12 22.4E-12 18.4E-12 14.2E-12 12.4E-12 19E-12 39.8E-12
101.2E-12 192E-12 302E-12 558E-12 728E-12 750E-12 738E-12 836E-12 878E-12
804E-12 830E-12 888E-12 928E-12 962E-12 1040E-12 1280E-12 1320E-12
f775:n 0 -106.066 106.066 0
c
de785: 0.01 0.015 0.02 0.03 0.04 0.05 0.06 0.08 0.1 0.15 0.2 0.3 0.4 0.5 0.6 0.8
1 1.5 2 3 4 5 6 8 10
df785: 0.077E-12 0.85E-12 1E-12 0.79E-12 0.63E-12 0.54E-12 0.50E-12 0.53E-12
0.61E-12 0.89E-12 1.2E-12 1.8E-12 2.38E-12 2.93E-12 3.44E-12 4.38E-12
5.2E-12 7E-12 8.6E-12 11.2E-12 13.6E-12 15.7E-12 17.9E-12 22.3E-12
26.4E-12

```
f785:p 0 -106.066 106.066   0
de795: 2.5E-8 1E-7 1E-6 1E-5 1E-4 1E-3 0.01 0.02 0.05 0.1 0.2 0.5 1 1.5 2 3 4 5
       6 7 8 10 14 17 20
df795: 19E-12 22.2E-12 22.4E-12 18.4E-12 14.2E-12 12.4E-12 19E-12 39.8E-12
       101.2E-12 192E-12 302E-12 558E-12 728E-12 750E-12 738E-12 836E-12 878E-12
       804E-12 830E-12 888E-12 928E-12 962E-12 1040E-12 1280E-12 1320E-12
f795:n 0 -150 0   0
c
de805: 0.01 0.015 0.02 0.03 0.04 0.05 0.06 0.08 0.1 0.15 0.2 0.3 0.4 0.5 0.6 0.8
       1 1.5 2 3 4 5 6 8 10
df805: 0.077E-12 0.85E-12 1E-12 0.79E-12 0.63E-12 0.54E-12 0.50E-12 0.53E-12
       0.61E-12 0.89E-12 1.2E-12 1.8E-12 2.38E-12 2.93E-12 3.44E-12 4.38E-12
       5.2E-12 7E-12 8.6E-12 11.2E-12 13.6E-12 15.7E-12 17.9E-12 22.3E-12
       26.4E-12
f805:p 0 -150 0   0
```

Realistic shielding simulation with detector rotated π/2 radians relative to source shield opening

```
c Cylindrical detector shielding geometry w/ alternating layers of steel
c and polyethylene and polyethylene source shield
c
c ------DETECTOR AND SHIELDING -------
c
1 1 -0.0012 -1 imp:n=32 imp:p=32 $opening
2 2 -0.94 1 12 -2 imp:n=32 imp:p=32 $polyethylene cylinder
3 3 -7.86 2 -3 imp:n=32 imp:p=32 $steel cylinder
4 2 -0.94 3 -4 imp:n=16 imp:p=16 $polyethylene cylinder
5 3 -7.86 4 -5 imp:n=16 imp:p=16 $steel cylinder
6 2 -0.94 5 -6 imp:n=8 imp:p=8 $polyethylene cylinder
7 3 -7.86 6 -7 imp:n=8 imp:p=8 $steel cylinder
8 3 -7.86 7 -8 imp:n=4 imp:p=4 $steel cylinder
9 3 -7.86 8 -9 imp:n=4 imp:p=4 $steel cylinder
10 3 -7.86 9 -10 imp:n=2 imp:p=2 $steel cylinder
11 2 -0.94 10 -11 imp:n=2 imp:p=2 $polyethylene cylinder
12 4 -0.959 -12 imp:n=32 imp:p=32
c
c -------------------------------------
c
20 5 -0.808 -20 imp:n=1 imp:p=1 $Scatter material
c
c ----- SOURCE SHIELDING -----------
c
101 1 -0.0012 -101 imp:n=1 imp:p=1 $opening
102 2 -0.94 101 -102 imp:n=1 imp:p=1 $polyethylene cylinder
103 2 -0.94 102 -103 imp:n=1 imp:p=1 $steel cylinder
104 2 -0.94 103 -104 imp:n=1 imp:p=1 $polyethylene cylinder
105 2 -0.94 104 -105 imp:n=1 imp:p=1 $steel cylinder
106 2 -0.94 105 -106 imp:n=1 imp:p=1 $polyethylene cylinder
107 2 -0.94 106 -107 imp:n=1 imp:p=1 $steel cylinder
108 2 -0.94 107 -108 imp:n=1 imp:p=1 $steel cylinder
109 2 -0.94 108 -109 imp:n=1 imp:p=1 $steel cylinder
110 2 -0.94 109 -110 imp:n=1 imp:p=1 $steel cylinder
111 2 -0.94 110 -111 imp:n=1 imp:p=1 $polyethylene cylinder
c
c -------------------------------------
c
500 6 -1.75 -500 -1000 imp:n=1 imp:p=1 $ground
501 7 -2.08 -501 imp:n=1 imp:p=1 $concrete
502 7 -2.08 -502 imp:n=1 imp:p=1 $concrete
503 7 -2.08 -503 imp:n=1 imp:p=1 $concrete
```

```
504 7 -2.08 -504 imp:n=1 imp:p=1 $concrete
505 7 -2.08 -505 imp:n=1 imp:p=1 $concrete
506 7 -2.08 -506 imp:n=1 imp:p=1 $concrete
1001 1 -0.0012 11 20 111 -510 imp:n=1 imp:p=1
1002 1 -0.0012 500 511 -1000 imp:n=1 imp:p=1
1003 0 1000 imp:n=0 imp:p=0

c
c ------DETECTOR AND SHIELDING -------
c
1 RCC 0 50 0    0  -37.3 0    12.7
2 RCC 0 50 0    0  -55 0    17.7
3 RCC 0 50 0    0  -60 0   22.7
4 RCC 0 50 0    0  -65 0   27.7
5 RCC 0 50 0    0  -70 0   32.7
6 RCC 0 50 0    0  -75 0   37.7
7 RCC 0 50 0    0  -80 0   42.7
8 RCC 0 50 0    0  -85 0   47.7
9 RCC 0 50 0    0  -90 0   52.7
10 RCC 0 50 0   0  -95 0   57.7
11 RCC 0 50 0   0 -100 0   62.7
12 RCC 0 12.7 0   0 -12.7 0    12.7
c
c -------------------------------------
c
20 SY     100               25
c
c ----- SOURCE SHIELDING -----------
c
101 RCC 0 100 65    0  0 50   13.4
102 RCC 0 100 65    0  0 55   18.4
103 RCC 0 100 65    0  0 60   23.4
104 RCC 0 100 65    0  0 65   28.4
105 RCC 0 100 65    0  0 70   33.4
106 RCC 0 100 65    0  0 75   38.4
107 RCC 0 100 65    0  0 80   43.4
108 RCC 0 100 65    0  0 85   48.4
109 RCC 0 100 65    0  0 90   53.4
110 RCC 0 100 65    0  0 95   58.4
111 RCC 0 100 65    0  0 100  63.4
c
c ----- SOURCE SHIELDING -----------
c
500 px -100
```

```
501 RPP -100 150  -215 415  -165 -150
502 RPP -100 150  -215 415  400 415
503 RPP -100 150  -215 -200  -150 400
504 RPP -100 150   400 415  -150 400
505 RPP  150 165   -215 415  -165 415
506 RPP -100 -85   -200 400  -150 400
510 RPP -85 150   -200 400   -150 400
511 RPP -100 165   -215 415  -165 415
1000 so 1000

mode p n
Print 10 40 50 100 110 126 140
m1 6012 .0001 7014 .755 8016 .232 18000 .013  $air
m2 1001 4 6000 2 $polyethlene
m3 26000 -.998 8016 -0.002 $1018 steel
m4 1001 5 6000 4 $EJ-309
m5 7014 1 $Nitrogen
m6 1001 0.2938 6012 0.0187 8016 0.5045 13027 0.0259 14028 &
0.1354 19000 0.0143 26056 0.0027 $ soil EPA GR 12 standard
m7 1001.42c -0.0056   8016.42c -0.4981   14000.42c -0.3151   20000.42c
    -0.0829   11023.42c -0.0171   12000.42c -0.0026   13027.42c -0.0457
    16032.42c -0.0013   19000.42c -0.0192   26000.42c -0.0124 $concrete
sdef POS=0 100 114.999 PAR=1 ERG=2.5
nps 2000000000
E0 .000000025 .001 .01 .1 .2 .4 .6 .8 1 69I 15 20
f14:n 12
f24:p 12
```

Ideal neutron scatter simulation

```
c Scatter off graphite block
11 0 -11 50 imp:n=1 imp:p=1
12 0 -12 50 imp:n=1 imp:p=1
13 0 -13 50 imp:n=1 imp:p=1
14 0 -14 50 imp:n=1 imp:p=1
15 0 -15 50 imp:n=1 imp:p=1
16 0 -16 50 imp:n=1 imp:p=1
17 0 -17 50 imp:n=1 imp:p=1
18 0 -18 50 imp:n=1 imp:p=1
19 0 -19 50 imp:n=1 imp:p=1
20 0 -20 50 imp:n=1 imp:p=1
21 0 -21 50 imp:n=1 imp:p=1
22 0 -22 50 imp:n=1 imp:p=1
30 1 -2.25 -30 imp:n=1 imp:p=1
50 0 30 -50 imp:n=1 imp:p=1
100 0 -100 #11 #12 #13 #14 #15 #16 #17 #18 #19 #20
     #21 #22 50 imp:n=1 imp:p=1
101 0 100 imp:n=0 imp:p=0

11 sz 304.8 78
12 s 152.4 0 263.965 78
13 s 263.965 0 152.4 78
14 sx 304.8 78
15 s 263.965 0 -152.4 78
16 s 152.4 0 -263.965 78
17 sz -304.8 78
18 s -152.4 0 -263.965 78
19 s -263.965 0 -152.4 78
20 sx -304.8 78
21 s -263.965 0 152.4 78
22 s -152.4 0 263.965 78
30 RCC -7 0 0    14 0 0    20
50 so 304.8
100 so 1000 $the universe

Print 10 40 50 100 110 126 140
mode n
m1 6012 1 $carbon
sdef POS=-50 0 0 PAR=1 ERG=14.1 VEC=1 0 0 DIR=D1
si1 H 0.966 1   $cosine of angle needed
sp1 0 1
nps 100000000 $number of histories
```

e0 .2 .4 .6 .8 1 69l 15 20
cut:n j 0.2
f111:n 11
f121:n 12
f131:n 13
f141:n 14
f151:n 15
f161:n 16
f171:n 17
f181:n 18
f191:n 19
f201:n 20
f211:n 21
f221:n 22

```
c Cylindrical detector shielding geometry w/ alternating layers of steel
c and polyethylene and polyethylene source shield
c
c ------DETECTOR AND SHIELDING -------
c
1 1 -0.0012 -1 imp:n=32 imp:p=32 $opening
2 2 -0.94 1 12 -2 imp:n=32 imp:p=32 $polyethylene cylinder
3 3 -7.86 2 -3 imp:n=32 imp:p=32 $steel cylinder
4 2 -0.94 3 -4 imp:n=16 imp:p=16 $polyethylene cylinder
5 3 -7.86 4 -5 imp:n=16 imp:p=16 $steel cylinder
6 2 -0.94 5 -6 imp:n=8 imp:p=8 $polyethylene cylinder
7 3 -7.86 6 -7 imp:n=8 imp:p=8 $steel cylinder
8 3 -7.86 7 -8 imp:n=4 imp:p=4 $steel cylinder
9 3 -7.86 8 -9 imp:n=4 imp:p=4 $steel cylinder
10 3 -7.86 9 -10 imp:n=2 imp:p=2 $steel cylinder
11 2 -0.94 10 -11 imp:n=2 imp:p=2 $polyethylene cylinder
12 4 -0.959 -12 imp:n=32 imp:p=32 $detector
c
c -------------------------------------
c
20 5 -0.808 -20 imp:n=1 imp:p=1 $Scatter material
c
c ----- SOURCE SHIELDING -----------
c
101 1 -0.0012 -101 imp:n=1 imp:p=1 $opening
102 2 -0.94 101 -102 imp:n=1 imp:p=1 $polyethylene cylinder
103 2 -0.94 102 -103 imp:n=1 imp:p=1 $steel cylinder
104 2 -0.94 103 -104 imp:n=1 imp:p=1 $polyethylene cylinder
105 2 -0.94 104 -105 imp:n=1 imp:p=1 $steel cylinder
106 2 -0.94 105 -106 imp:n=1 imp:p=1 $polyethylene cylinder
107 2 -0.94 106 -107 imp:n=1 imp:p=1 $steel cylinder
108 2 -0.94 107 -108 imp:n=1 imp:p=1 $steel cylinder
109 2 -0.94 108 -109 imp:n=1 imp:p=1 $steel cylinder
110 2 -0.94 109 -110 imp:n=1 imp:p=1 $steel cylinder
111 2 -0.94 110 -111 imp:n=1 imp:p=1 $polyethylene cylinder
c
c -------------------------------------
c
500 6 -1.75 -500 -1000 imp:n=1 imp:p=1 $ground
501 7 -2.08 -501 imp:n=1 imp:p=1 $concrete
502 7 -2.08 -502 imp:n=1 imp:p=1 $concrete
503 7 -2.08 -503 imp:n=1 imp:p=1 $concrete
```

```
504 7 -2.08 -504 imp:n=1 imp:p=1 $concrete
505 7 -2.08 -505 imp:n=1 imp:p=1 $concrete
506 7 -2.08 -506 imp:n=1 imp:p=1 $concrete
1001 1 -0.0012 11 20 111 -510 imp:n=1 imp:p=1
1002 1 -0.0012 500 511 -1000 imp:n=1 imp:p=1
1003 0 1000 imp:n=0 imp:p=0

c
c ------DETECTOR AND SHIELDING -------
c
1 1 RCC 0 50 0    0  -37.3 0    6.35
2 1 RCC 0 50 0    0  -55 0    11.35
3 1 RCC 0 50 0    0  -60 0   15.35
4 1 RCC 0 50 0    0  -65 0   21.35
5 1 RCC 0 50 0    0  -70 0   25.35
6 1 RCC 0 50 0    0  -75 0   31.35
7 1 RCC 0 50 0    0  -80 0   35.35
8 1 RCC 0 50 0    0  -85 0   41.35
9 1 RCC 0 50 0    0  -90 0   45.35
10 1 RCC 0 50 0   0  -95 0   51.35
11 1 RCC 0 50 0   0 -100 0   55.35
12 1 RCC 0 12.7 0   0 -12.7 0    6.35
c
c ---------------------------------------
c
20 RCC   0 100 -18.5   0 0 37         20
c
c ----- SOURCE SHIELDING -----------
c
101 RCC 0 100 239.2    0  0 50   13.4
102 RCC 0 100 239.2    0  0 55   18.4
103 RCC 0 100 239.2    0  0 60   23.4
104 RCC 0 100 239.2    0  0 65   28.4
105 RCC 0 100 239.2    0  0 70   33.4
106 RCC 0 100 239.2    0  0 75   38.4
107 RCC 0 100 239.2    0  0 80   43.4
108 RCC 0 100 239.2    0  0 85   48.4
109 RCC 0 100 239.2    0  0 90   53.4
110 RCC 0 100 239.2    0  0 95   58.4
111 RCC 0 100 239.2    0  0 100  63.4
c
c ----------------------------------
c
500 px -100
```

```
501 RPP -100 150  -215 415  -165 -150
502 RPP -100 150  -215 415  400 415
503 RPP -100 150  -215 -200  -150 400
504 RPP -100 150   400 415  -150 400
505 RPP  150 165   -215 415  -165 415
506 RPP -100 -85   -200 400  -150 400
510 RPP -85 150   -200 400   -150 400
511 RPP -100 165   -215 415  -165 415
1000 so 1000

mode n
Print 10 40 50 100 110 126 140
m1 6012 -.0001 7014 -.755 8016 -.232 18000 -.013  $air
m2 1001 4 6000 2 $ polyethylene
m3 26000 -.998 8016 -0.002 $1018 steel
m4 1001 5 6000 4 $EJ-309
m5 7014 1 $Nitrogen
m6 1001 0.2938 6012 0.0187 8016 0.5045 13027 0.0259 14028 &
    0.1354 19000 0.0143 26056 0.0027 $ soil EPA GR 12 standard
m7 1001.42c -0.0056   8016.42c -0.4981   14000.42c -0.3151   20000.42c
    -0.0829   11023.42c -0.0171   12000.42c -0.0026   13027.42c -0.0457
    16032.42c -0.0013   19000.42c -0.0192   26000.42c -0.0124 $concrete
sdef POS=0 100 289.199 PAR=1 ERG=D1
SP1 -4  -14.1  -1
nps 10000000000
cut:n j 0.2
*tr1 0 -44.6 250.45   0 90 90   90 60 150
e0 .2 .4 .6 .8 1 69I 15 20
f14:n 12
```

```
Laboratory D-T FNRR Experiment with generator and detector models and 7.75 MeV neutron
C scatter
C
C max line length
C
C  CELLS ----------------------------------------------------------------------
c
c ************************* Neutron Lab ***************************************
c
8  1 -2.08   -15 -5080                          imp:N,P=1 $ floor
c 20      27 -7.87      -20                      imp:N,P=1 $ Steel plate representing ring stand and
clamps
121   3   -1.70  120 -121 122 -123 124 -125    trcl=3 imp:N,P=1 $ Transmission target, stop-1
122   3   -1.70  120 -121 122 -123 124 -125    trcl=5 imp:N,P=1 $ Transmission target, stop-2
35 2 -0.0012 -5080 15
    #201 #203 #204 #206 #207 #208 #209 #210 #211 #218 #219 #213 #214 #215
    #216 #217 #221 #222 #223
    #401 #403 #404 #406 #407 #408 #409 #410 #411 #418 #419 #413 #414 #415
    #416 #417 #421 #422 #423
    #306 #307 #309
    #121 #122 (904914:906907:-905901) $ #301 #303 #304 #308
                                        imp:N,P=1  $ Name 122B
c
c *************Stop 1 5"x5" EJ-309 Liquid Scintillation Detector*****************
C
201     21   -2.70    201 -202  -209          trcl=3 imp:N,P=1      $ Al endcap
203     21   -2.70    202 -232  208  -209      trcl=3 imp:N,P=1      $ Al external wall
204     21   -2.70    203 -205   209  -212     trcl=3 imp:N,P=1      $ Al wall
206     23   -0.935   202 -232  -208          trcl=3 imp:N,P=1      $ detector
207     25   -2.23    232 -205  -209          trcl=3 imp:N,P=1      $ pyrex window
208     21   -2.70    204 -214  212 -213      trcl=3 imp:N,P=1      $ Al ring
209     21   -0.001   205 -231 -210           trcl=3 imp:N,P=1      $ PMT big
210      2   -0.0012  205 -231  210 -211      trcl=3 imp:N,P=1      $ air around PMT
211     26   -8.747   205 -221  211 -212      trcl=3 imp:N,P=1      $ mu metal wall
218     21   -0.001   231 -227 -234           trcl=3 imp:N,P=1      $ PMT small
219      2   -0.0012  231 -221  219 -211      trcl=3 imp:N,P=1      $ air around PMT
221     26   -8.747   215 -227  219 -220      trcl=3 imp:N,P=1      $ mu metal wall
222      2   -0.0012  221 -227  234 -219      trcl=3 imp:N,P=1      $ air around PMT
213     21   -0.001   227 -217 -219           trcl=3 imp:N,P=1      $ air or Al in tube
214     21   -2.70    216 -227  220 -235      trcl=3 imp:N,P=1      $ Al wall
223     21   -2.70    227 -217  219 -235      trcl=3 imp:N,P=1      $ Al wall
215     21   -2.70    217 -218 -235          trcl=3 imp:N,P=1      $ Al endcap
```

```
216     2   -0.0012  221 -215  219 -228       trcl=3 imp:N,P=1      $ air around PMT
217     26   -8.747   221 -215  219  228 -229  trcl=3 imp:N,P=1      $ mu metal wall
C
c **************Stop 2 5"x5" EJ-309 Liquid Scintillation Detector*****************
C
401     21   -2.70    201 -202  -209          trcl=5 imp:N,P=1      $ Al endcap
403     21   -2.70    202 -232  208  -209     trcl=5 imp:N,P=1      $ Al external wall
404     21   -2.70    203 -205   209  -212    trcl=5 imp:N,P=1      $ Al wall
406     23   -0.935   202 -232  -208          trcl=5 imp:N,P=1      $ detector
407     25   -2.23    232 -205  -209          trcl=5 imp:N,P=1      $ pyrex window
408     21   -2.70    204 -214  212 -213      trcl=5 imp:N,P=1      $ Al ring
409     21   -0.001   205 -231 -210           trcl=5 imp:N,P=1      $ PMT big
410     2   -0.0012  205 -231  210 -211       trcl=5 imp:N,P=1      $ air around PMT
411     26   -8.747   205 -221  211 -212      trcl=5 imp:N,P=1      $ mu metal wall
418     21   -0.001   231 -227 -234           trcl=5 imp:N,P=1      $ PMT small
419     2   -0.0012  231 -221  219 -211       trcl=5 imp:N,P=1      $ air around PMT
421     26   -8.747   215 -227  219 -220      trcl=5 imp:N,P=1      $ mu metal wall
422     2   -0.0012  221 -227  234 -219       trcl=5 imp:N,P=1      $ air around PMT
413     21   -0.001   227 -217 -219           trcl=5 imp:N,P=1      $ air or Al in tube
414     21   -2.70    216 -227  220 -235      trcl=5 imp:N,P=1      $ Al wall
423     21   -2.70    227 -217  219 -235      trcl=5 imp:N,P=1      $ Al wall
415     21   -2.70    217 -218 -235          trcl=5 imp:N,P=1      $ Al endcap
416     2   -0.0012  221 -215  219 -228       trcl=5 imp:N,P=1      $ air around PMT
417     26   -8.747   221 -215  219  228 -229  trcl=5 imp:N,P=1      $ mu metal wall
c
c ****************Start 1 1"x1" Stilbene Scintillation Detector*******************
C
306     28   -1.16     302 -332 -308          trcl=7 imp:N,P=1      $ Stilbene detector
307     25   -2.23     332 -305 -310          trcl=7 imp:N,P=1      $ pyrex window
309     21   -0.001    305 -331 -310          trcl=7 imp:N,P=1      $ PMT big
C
C *******MP 320 Neutron Spectrum and Energy ***************************************
c
C Removed at request of the manufacturer
C
5002 0 5080 imp:p=0 imp:n=0

C
c SURFACES -----------------------------------------------------------------
C
c ************************** Neutron Lab ***************************************
c
15 pz    -123       $floor line
```

```
c 20 BOX   -1.8 -10 -2   -0.707 -0.707 0   0 0 4   -11.3 11.3 0 $ Steel barrier, represents ring
stand and clamp
120 PX -52.5       $ transmission target
121 PX -47.5       $ transmission target
122 PY -7.5        $ transmission target
123 PY  7.5        $ transmission target
124 PZ -7.5        $ transmission target
125 PZ  7.5        $ transmission target
c
c ****************5"x5" EJ-309 Liquid Scintillation Detector*******************
c (Some surfaces may not be used or may be repeated)
c
201     PX   0
202     PX   0.16002
203     PX   11.8
204     PX   12.6
232     PX   12.67
205     PX   13.35
208     CX   6.33998
209     CX   6.5
210     CX   6.35
C     Surface cards for the PMT
211     CX   6.8984
212     CX   7
213     CX   8.2
214     PX   14.6
231     PX   21.95
215     PX   32.2
216     PX   34.7
227     PX   35.4
217     PX   37.63998
218     PX   37.8
234     CX   4.2
219     CX   4.3984
220     CX   4.5
235     CX   4.7
221     PX   29.3
C     Surface cards for the conical part of the PMT
228     KX   37.3  0.743162901
229     KX   37.42 0.743162901
c
c ****************1"x1" Stilbene Scintillation Detector*********************
c (Some surfaces may not be used or may be repeated)
c
```

```
301      PX   0
302      PX   0.16
303      PX   2.065
304      PX   2.70
332      PX   2.70
305      PX   3.45
308      CX   1.27
309      CX   1.43
310      CX   1.77
C      Surface cards for the PMT
312      CX   1.93
313      CX   2.43
314      PX   3.335
331      PX   13.54
c
C *******MP 320 Neutron Spectrum and Energy ***********************************
c
c Removed at the request of the manufacturer
c
5080 so 300

C
c ANALYSIS ----------------------------------------------------------------
C
MODE N
dbcn 13j
PRDMP 2j 1 4
nps 1e9
print 10 40 50 100 110 126 140
SDEF POS 0 25 0  ERG=D1  PAR=1 VEC= 0 -1 0 DIR=D2
SP1 -4  -14.1  -1                  $Gaussian fusion distribution for DT
sI2  H 0.99756 1                    $cosine of half angle needed (4 degress), = 1/83.1888 of
isotropic source
sP2  0 1
C
c ************************** Neutron Lab ***************************************
c
m1    1001.42c       -0.0056  $ concrete
     8016.42c       -0.4981 14000.42c       -0.3151 20000.42c       -0.0829
     11023.42c      -0.0171 12000.42c       -0.0026 13027.42c       -0.0457
     16032.42c      -0.0013 19000.66c       -0.0192 26000       -0.0124
m2    6012.42c       -0.0001  $ air
     8016.42c       -0.2097 7014.70c        -0.7809 18000.42c       -0.0093
m3    6012.42c        1.00    $ graphite
```

```
c
c
c ****************5"x5" and 1"x1" EJ-309 Liquid Scintillation Detector***********
C
m21     13027.70c   1        $ Al
m23      1001.66c   0.555
        6000.70c   0.445     $ EJ-309 liquid scintillator
m24      7014.70c   1        $ nitrogen
m25      5011.70c  -0.040064
        8016.70c  -0.539562
       11023.70c  -0.028191
       13027.70c  -0.011644
       14000.21c  -0.377220
       19000.66c  -0.003321  $ pyrex
m26     28000.50c   0.8
       42000.66c   0.05
       14000.21c   0.005
       29063.70c   0.0002
       26056.70c   0.1448    $ mu-metal
m27     26056.70c   1        $ iron
M28     1001.70c  .4615      $ Stilbene
       6012.42c  .5385
       PLIB = 04p
c
C *******MP 320 Neutron Spectrum and Energy ************************************
C
c Removed at the request of the manufacturer
c
C ------------------------------------------------------------
C                        Translations
c ------------------------------------------------------------
c
*tr3   62.85   -69.88  0     47.85  137.85  90    42.15  47.85  90  $ Stop 1 5x5 EJ 309 detector
*tr5  -62.85   -69.88  0     132.15  137.85  90    42.15 132.15  90  $ Stop 3 5x5 EJ 309 detector
*tr7    0       1.27  0      90      180    90     0     90     90  $ Start 1 1x1 Stilbene detector
*tr9    0       25    0      90      90     0     j      j      j   0  90 90   $ Generator translation
c
c ======Advanced Options=========
c
PHYS:P 0 1 1 0 1
c EMCPF: Upper Energy Limit for Detailed Phys
c IDES:  Electron Production by Photons 0/1: will produce e- in MODE E or Brem photons
c        in the case of a thick target brem model/will not as per
c NOCOH: Coherent Scattering 0/1:will/will not
```

```
c ISPN:  Photonuclear Reactions 1/0/-1 biased/none/analog
c NODOP: Doppler Broadening 0/1:will/will not
c
PHYS:N J 20
c
CUT:P 2J 0
c Time - Lower Energy Cutoff - Weight
c
Cut:N J 0.01
c
c =========PoliMi Options==========
c
IPOL  0 1 1 1 J 2 3 306 206 406
c
c (1) Neutron-photon source type, with correct multiplicity
c (2) Neutrons from induced fission
c (3) Photon correlation
c (4) Time delay in photon emission following a fission event
c (5) Not used
c (6) Collisions print out only for histories with events giving energy
c     released in at least N det cells
c (7) Number of cells for which collision data printout is required
c (8) Cell numbers for collision data printout
c
RPOL J 2e-3
c (1) neutron rxn energy cutoff
c (2) photon Rxn energy cutoff
FILES 21 DUMN1
```

Appendix B: Data Analysis

MATLAB input to process experimental time-of-flight data

```
%*******************************************
% DualRead TOF Data Preparation              *
% TWO Stop Detectors                         *
% By Zach Whetstone                          *
% 04/16/2015                                 *
%*******************************************

clear all

% Start the clock
tic;

%%%%%%%%%%%%%% USER INPUT REQUIRED - CHANGE AS NEEDED %%%%%%%%%%%%%%%%%%%%

CreateNewHistogram = 1; % 1 if YES, anything else if NO. If yes, the TOF data
% will be used to create a new histogram based on values entered below
CreateNewGaussFit = 1;  % 1 if YES, anything else if NO. If yes, program will
% iteratvely find the best Gaussian fit to energy data based on values
% entered below
FstBRStart = 0; % start of first TOF range to estimate background (ns)
FstBrStop = 25; % end of first TOF range to estimate background (ns)
SndBRStart = 225; % start of second TOF range to estimate background (ns)
SndBrStop = 250; % end of second TOF range to estimate background (ns)
dt = 1;      % fixed pulse time step (ns), if loading saved histograms, must
% match their bin width, otherwise, set as needed for new histogram

%******* Needed if creating a new histogram ***********
nrfolders = 13; % number of folders with TOF data sets
MeasTimePerFold = 30; %Measurement time per data set/folder (minutes)
tofMin= -150;   %(ns), if loading saved histograms, must match
tofMax= 350;   %(ns), if loading saved histograms, must match
St1Offset = -44.0;  %(ns)
St2Offset = -39.3; %(ns)
sizeSt1TOF = 141468; % Estimate of the size of the Stop1 data set, used to
% preallocate
sizeSt2TOF = 87669; % Estimate of the size of the Stop2 data set, used to
% preallocate
NPS = 2e6; %neutrons per second from the generator
d = 105.54; %distance between center of start and stop detectors (cm)

%******* Needed if creating a new Gaussian fit ***********
AGuess = 1e-7; % Guess at height of combined data Gaussian curve
BGuess = 1.38; % Guess at center energy location of Gaussian curve
CGuess = 0.40; % Guess at width of energy Gaussian curve

BInterval = 0.01; % Iterative steps for guessed b values
BWidth = 0.4; % Width of b values tested... BGuess +/- BWidth/2
CInterval = 0.01; % Iterative steps for guessed c values
CWidth = 0.2; % Width of c values tested... CGuess +/- CWidth/2
```

```
GaussStart = 54; % Begining of Gaussian Fit Data in TOF histograms
GaussStop = 78; % End of Gaussian Fit Data in TOF histograms

%******* Predetermined Gaussian variables ***********
% To be filled in after successful Gaussian fit
% Stop 1
aSt1 = 2.4145e-6; % a1 = a in Gaussian dist
bSt1 = 1.27; % b1 = b in Gaussian dist
cSt1 = 0.42; % c1 DOES NOT = c in Gaussian dist. c = c1/2^0.5

% Stop 2
aSt2 = 1.3276e-6;
bSt2 = 1.40;
cSt2 = 0.44;

% Total
aTot = 3.6590e-6;
bTot = 1.32;
cTot = 0.44;

%%%%%%%%%%%%%%%%%%%% END USER INPUT SECTION %%%%%%%%%%%%%%%%%%%%%%%%%%%%%%%


%%%%%%%%%%%%%%%%%%%%%%%%%%%%%%%%%%%%%%%%%%%%%%%%%%%%%%%%%%%%%%%%%%%%%%%%%%%%
% Reading and organizing of PSD data
%%%%%%%%%%%%%%%%%%%%%%%%%%%%%%%%%%%%%%%%%%%%%%%%%%%%%%%%%%%%%%%%%%%%%%%%%%%%

MeasTime = nrfolders * MeasTimePerFold;
SourceParticles = MeasTime*60*NPS;

if CreateNewHistogram == 1

    Det1TOF = zeros(1,sizeSt1TOF);
    Det2TOF = zeros(1,sizeSt2TOF);
    TOFticker1 = 0;
    TOFticker2 = 0;

    for xxx = 1 : nrfolders
        current_path = pwd;
        detector0 = 'timed0';
        detector1 = 'timed1';
        detector2 = 'timed2';
        file_name0 = [current_path '\' num2str(xxx) '\' detector0];
        file_name1 = [current_path '\' num2str(xxx) '\' detector1];
        file_name2 = [current_path '\' num2str(xxx) '\' detector2];
        start = importdata(file_name0);
        stop1 = importdata(file_name1);
        stop2 = importdata(file_name2);
        nrpulses0 = size(start,1);
        nrpulses1 = size(stop1,1);
        nrpulses2 = size(stop2,1);
        aaa = 1;
```

```
        for bbb = 1 : nrpulses0
            if start(bbb,1) ~= -999
                while stop1(aaa,4) ~= start(bbb,4)
                    aaa = aaa + 1;
                    if aaa > nrpulses1
                        aaa = bbb;
                        break
                    end
                end
                if stop1(aaa,4) == start(bbb,4) && stop1(aaa,1) ~= -999
                    TOFticker1 = TOFticker1 + 1;
                    Det1TOF(TOFticker1) = stop1(aaa,1) -
start(bbb,1)+St1Offset;
                end
            end
        end

        aaa = 1;

        MaxPulses = max(nrpulses0,nrpulses2);
        MinPulses = min(nrpulses0,nrpulses2);

        for ccc = 1 : nrpulses0
            if start(ccc,1) ~= -999
                while stop2(aaa,4) ~= start(ccc,4)
                    aaa = aaa + 1;
                    if aaa > nrpulses2
                        aaa = ccc;
                        break
                    end
                end
                if stop2(aaa,4) == start(ccc,4) && stop2(aaa,1) ~= -999
                    TOFticker2 = TOFticker2 + 1;
                    Det2TOF(TOFticker2) = stop2(aaa,1) -
start(ccc,1)+St2Offset;
                end
            end
        end
        fprintf('\n   Folder %1.0f of %2.0f finished in %3.2f
minutes\n',xxx,nrfolders,cputime/60)

    end

    TotTOF = zeros(1,TOFticker1+TOFticker2);
    TotTOF(1,1:TOFticker1)=Det1TOF(1,1:TOFticker1);
    TotTOF(1,TOFticker1+1:TOFticker1+TOFticker2)=Det2TOF(1,1:TOFticker2);

    xaxis= tofMin:dt:tofMax;

    [St1TOF,xaxis] = hist(Det1TOF,xaxis);
    [St2TOF,xaxis] = hist(Det2TOF,xaxis);
    [TotTOF,xaxis] = hist(TotTOF,xaxis);

    saving_path = [current_path '\'];
```

```
    name = 'St1_TOF';
    saving_path_name = [saving_path name ];
    save(saving_path_name, 'St1TOF');

    name = 'St2_TOF';
    saving_path_name = [saving_path name ];
    save(saving_path_name, 'St2TOF');

    name = 'Tot_TOF';
    saving_path_name = [saving_path name ];
    save(saving_path_name, 'TotTOF');

else
    load('St1_TOF.mat');
    load('St2_TOF.mat');
    load('Tot_TOF.mat');
    xaxis= tofMin:dt:tofMax;
end

St1TOFPercentUncer = (St1TOF.^0.5)./St1TOF;
St1TOF = St1TOF/SourceParticles;
St1TOFUncert = St1TOF.*St1TOFPercentUncer;

St2TOFPercentUncer = (St2TOF.^0.5)./St2TOF;
St2TOF = St2TOF/SourceParticles;
St2TOFUncert = St2TOF.*St2TOFPercentUncer;

TotTOFPercentUncer = (TotTOF.^0.5)./TotTOF;
TotTOF = TotTOF/SourceParticles;
TotTOFUncert = TotTOF.*TotTOFPercentUncer;

%%%%%%%%%%%%%%%%%%%%%%%%%%%%%%%%%%%%%%%%%%%%%%%%%%%%%%%%%%%%%%%%%%%%%%%%%%%%%%%
% Converting TOF data to neutron energy data
%%%%%%%%%%%%%%%%%%%%%%%%%%%%%%%%%%%%%%%%%%%%%%%%%%%%%%%%%%%%%%%%%%%%%%%%%%%%%%%

MaxX = max(xaxis); % ns
MinX = min(xaxis); % ns
xaxisE(1) = 0.5*1.675e-27*((d/dt)^2*1e14/1.602e-19*1e-6);
start = abs(MinX)/dt+1;
xTOFGauss = dt:dt:MaxX;

for xxx = 1:(MaxX/dt) % output(Max,1)
    xaxisE(xxx) = 0.5*1.675e-27*((d/(dt*xxx))^2*1e14/1.602e-19*1e-6);
% Convert TOF bins to Energy (MeV)
end

St1E(1) = St1TOF(start+1)/xaxisE(1);
St1EUncert(1) = St1TOFUncert(start+1)/xaxisE(1);
St2E(1) = St2TOF(start+1)/xaxisE(1);
St2EUncert(1) = St2TOFUncert(start+1)/xaxisE(1);
TotE(1) = TotTOF(start+1)/xaxisE(1);
TotEUncert(1) = TotTOFUncert(start+1)/xaxisE(1);

for yyy = 2:(MaxX/dt) % output(Max,1)
```

```
    St1E(yyy) = St1TOF(start+yyy)/(xaxisE(yyy-1) - xaxisE(yyy));
% Normalize bins by their width
    St1EUncert(yyy) = St1TOFUncert(start+yyy)/(xaxisE(yyy-1) - xaxisE(yyy));
    St2E(yyy) = St2TOF(start+yyy)/(xaxisE(yyy-1) - xaxisE(yyy));
% Normalize bins by their width
    St2EUncert(yyy) = St2TOFUncert(start+yyy)/(xaxisE(yyy-1) - xaxisE(yyy));
    TotE(yyy) = TotTOF(start+yyy)/(xaxisE(yyy-1) - xaxisE(yyy));
% Normalize bins by their width
    TotEUncert(yyy) = TotTOFUncert(start+yyy)/(xaxisE(yyy-1) - xaxisE(yyy));

end

%%%%%%%%%%%%%%%%%%%%%%%%%%%%%%%%%%%%%%%%%%%%%%%%%%%%%%%%%%%%%%%%%%%%%%%%%%%%
% Gaussian fitting of neutron energy data
%%%%%%%%%%%%%%%%%%%%%%%%%%%%%%%%%%%%%%%%%%%%%%%%%%%%%%%%%%%%%%%%%%%%%%%%%%%%

if CreateNewGaussFit == 1
    xaxisFit = transpose(xaxisE(GaussStart:GaussStop));
    BInterval2 = 0.001;
    BWidth2 = 0.02;
    CInterval2 = 0.001;
    CWidth2 = 0.02;

    xxx = 1;
    count = 0;
    iterations = BWidth/BInterval*CWidth/CInterval+400;
    Parameters = zeros(iterations,12);

    yFitSt1 = transpose(St1E(GaussStart:GaussStop));
    yFitSt2 = transpose(St2E(GaussStart:GaussStop));
    yFitTot = transpose(TotE(GaussStart:GaussStop));

    for BTemp1 = (BGuess-BWidth/2):CInterval:(BGuess+BWidth/2)
        for CTemp1 = (CGuess-CWidth/2):CInterval:(CGuess+CWidth/2)
            optionsStop = fitoptions('gauss1', 'StartPoint', [AGuess BTemp1
CTemp1]);
            optionsTot = fitoptions('gauss1', 'StartPoint', [AGuess/2 BTemp1
CTemp1]);
            [GaussSt1,GoFSt1] = fit(xaxisFit,yFitSt1,'gauss1',optionsStop); %
get parameters for Gaussian fit and Goodness of Fit data
            [GaussSt2,GoFSt2] = fit(xaxisFit,yFitSt2,'gauss1',optionsStop);
            [GaussTot,GoFTot] = fit(xaxisFit,yFitTot,'gauss1',optionsTot);
            Parameters(xxx,1:3) = coeffvalues(GaussSt1);
            Parameters(xxx,4) = GoFSt1.rsquare;
            Parameters(xxx,5:7) = coeffvalues(GaussSt2);
            Parameters(xxx,8) = GoFSt2.rsquare;
            Parameters(xxx,9:11) = coeffvalues(GaussTot);
            Parameters(xxx,12) = GoFTot.rsquare;
            xxx = xxx + 1;
        end
    end

    %------------- Stop1 ----------------
    [~,Row] = max(Parameters(:,4));
```

```
    ABestSt1 = Parameters(Row,1);
    BSt1_2 = Parameters(Row,2);
    CSt1_2 = Parameters(Row,3);
    yyy = xxx;

    for BTemp2 = (BSt1_2-BWidth2/2):BInterval2:(BSt1_2+BWidth2/2)
        for CTemp2 = (CSt1_2-CWidth2/2):CInterval2:(CSt1_2+CWidth2/2)
            options = fitoptions('gauss1', 'StartPoint', [ABestSt1 BTemp2
CTemp2]);
            [GaussSt1,GoFSt1] = fit(xaxisFit,yFitSt1,'gauss1',options);
% get parameters for Gaussian fit and Goodness of Fit data
            Parameters(xxx,1:3) = coeffvalues(GaussSt1);
            Parameters(xxx,4) = GoFSt1.rsquare;
            yyy = yyy + 1;
        end
    end

    [St1RSqd,Row] = max(Parameters(:,4));
    aSt1 = Parameters(Row,1);
    bSt1 = Parameters(Row,2);
    cSt1 = Parameters(Row,3);
    ESt1FWHM = cSt1*2^0.5*(2*log(2))^0.5; % accounting for c = c1/2^0.5

    %------------- Stop2 ----------------
    [~,Row] = max(Parameters(:,8));
    ABestSt2 = Parameters(Row,5);
    BSt2_2 = Parameters(Row,6);
    CSt2_2 = Parameters(Row,7);
    yyy = xxx;

    for BTemp2 = (BSt2_2-BWidth2/2):BInterval2:(BSt2_2+BWidth2/2)
        for CTemp2 = (CSt2_2-CWidth2/2):CInterval2:(CSt2_2+CWidth2/2)
            options = fitoptions('gauss1', 'StartPoint', [ABestSt2 BTemp2
CTemp2]);
            [GaussSt2,GoFSt2] = fit(xaxisFit,yFitSt2,'gauss1',options);
% get parameters for Gaussian fit and Goodness of Fit data
            Parameters(xxx,5:7) = coeffvalues(GaussSt2);
            Parameters(xxx,8) = GoFSt2.rsquare;
            yyy = yyy + 1;
        end
    end

    [St2RSqd,Row] = max(Parameters(:,8));
    aSt2 = Parameters(Row,5);
    bSt2 = Parameters(Row,6);
    cSt2 = Parameters(Row,7);
    ESt2FWHM = cSt2*2^0.5*(2*log(2))^0.5; % accounting for c = c1/2^0.5

    %------------- Total ----------------
    [~,Row] = max(Parameters(:,8));
    ABestTot = Parameters(Row,5);
    BTot_2 = Parameters(Row,6);
    CTot_2 = Parameters(Row,7);
    yyy = xxx;
```

```
    for BTemp2 = (BTot_2-BWidth2/2):BInterval2:(BTot_2+BWidth2/2)
        for CTemp2 = (CTot_2-CWidth2/2):CInterval2:(CTot_2+CWidth2/2)
            options = fitoptions('gauss1', 'StartPoint', [ABestTot BTemp2
CTemp2]);
            [GaussSt2,GoFSt2] = fit(xaxisFit,yFitTot,'gauss1',options);
% get parameters for Gaussian fit and Goodness of Fit data
            Parameters(xxx,9:11) = coeffvalues(GaussTot);
            Parameters(xxx,12) = GoFTot.rsquare;
            yyy = yyy + 1;
        end
    end

    [TotRSqd,Row] = max(Parameters(:,12));
    aTot = Parameters(Row,9);
    bTot = Parameters(Row,10);
    cTot = Parameters(Row,11);
    ETotFWHM = cTot*2^0.5*(2*log(2))^0.5; % accounting for c = c1/2^0.5;

    X = zeros(4,6);
    GaussianEnergyValues = num2cell(X);

    GaussianEnergyValues{1,1} = 'Data Set';
    GaussianEnergyValues{1,2} = 'a';
    GaussianEnergyValues{1,3} = 'b';
    GaussianEnergyValues{1,4} = 'c';
    GaussianEnergyValues{1,5} = 'FWHM';
    GaussianEnergyValues{1,6} = 'r^2';

    GaussianEnergyValues{2,1} = 'Stop 1';
    GaussianEnergyValues{2,2} = aSt1;
    GaussianEnergyValues{2,3} = bSt1;
    GaussianEnergyValues{2,4} = cSt1;
    GaussianEnergyValues{2,5} = ESt1FWHM;
    GaussianEnergyValues{2,6} = St1RSqd;

    GaussianEnergyValues{3,1} = 'Stop 2';
    GaussianEnergyValues{3,2} = aSt2;
    GaussianEnergyValues{3,3} = bSt2;
    GaussianEnergyValues{3,4} = cSt2;
    GaussianEnergyValues{3,5} = ESt2FWHM;
    GaussianEnergyValues{3,6} = St2RSqd;

    GaussianEnergyValues{4,1} = 'Combined';
    GaussianEnergyValues{4,2} = aTot;
    GaussianEnergyValues{4,3} = bTot;
    GaussianEnergyValues{4,4} = cTot;
    GaussianEnergyValues{4,5} = ETotFWHM;
    GaussianEnergyValues{4,6} = TotRSqd;

    GaussianEnergyValues

end

%%%%%%%%%%%%%%%%%%%%%%%%%%%%%%%%%%%%%%%%%%%%%%%%%%%%%%%%%%%%%%%%%%%%%%%%%%%%
% Create Gaussian curves and lines of best fit
```

```
%%%%%%%%%%%%%%%%%%%%%%%%%%%%%%%%%%%%%%%%%%%%%%%%%%%%%%%%%%%%%%%%%%%%%%%%%%%%

St1EGauss(1) = aSt1*exp(-((xaxisE(1)-bSt1)/cSt1)^2);
St1TOFGauss(1) = aSt1*exp(-(((0.5*1.675e-27*(d/xTOFGauss(1))^2*1e14/1.602e-
19*1e-6)-bSt1)/cSt1)^2)*xaxisE(1);

St2EGauss(1) = aSt2*exp(-((xaxisE(1)-bSt2)/cSt2)^2);
St2TOFGauss(1) = aSt2*exp(-(((0.5*1.675e-27*(d/xTOFGauss(1))^2*1e14/1.602e-
19*1e-6)-bSt2)/cSt2)^2)*xaxisE(1);

TotEGauss(1) = aTot*exp(-((xaxisE(1)-bTot)/cTot)^2);
TotTOFGauss(1) = aTot*exp(-(((0.5*1.675e-27*(d/xTOFGauss(1))^2*1e14/1.602e-
19*1e-6)-bTot)/cTot)^2)*xaxisE(1);

for yyy = 2:(MaxX/dt) % output(Max,1)
    St1EGauss(yyy) = aSt1*exp(-((xaxisE(yyy)-bSt1)/cSt1)^2);
    St1TOFGauss(yyy) = aSt1*exp(-(((0.5*1.675e-
27*(d/xTOFGauss(yyy))^2*1e14/1.602e-19*1e-6)-bSt1)/cSt1)^2)*(xaxisE(yyy-1) -
xaxisE(yyy)); % Convert Energy Gauss Dist. to TOF Gauss Dist.
    St2EGauss(yyy) = aSt2*exp(-((xaxisE(yyy)-bSt2)/cSt2)^2);
    St2TOFGauss(yyy) = aSt2*exp(-(((0.5*1.675e-
27*(d/xTOFGauss(yyy))^2*1e14/1.602e-19*1e-6)-bSt2)/cSt2)^2)*(xaxisE(yyy-1) -
xaxisE(yyy)); % Convert Energy Gauss Dist. to TOF Gauss Dist.
    TotEGauss(yyy) = aTot*exp(-((xaxisE(yyy)-bTot)/cTot)^2);
    TotTOFGauss(yyy) = aTot*exp(-(((0.5*1.675e-
27*(d/xTOFGauss(yyy))^2*1e14/1.602e-19*1e-6)-bTot)/cTot)^2)*(xaxisE(yyy-1) -
xaxisE(yyy)); % Convert Energy Gauss Dist. to TOF Gauss Dist.
end

% Stop 1
NormSt1TOF = St1TOF/max(St1TOFGauss); % normalized yaxis
NormSt1TOFUncert = St1TOFUncert/max(St1TOFGauss);
% adjust error bars for normalized yaxis
NormSt1TOFGauss = St1TOFGauss/max(St1TOFGauss);

% Stop 2
NormSt2TOF = St2TOF/max(St2TOFGauss); % normalized yaxis
NormSt2TOFUncert = St2TOFUncert/max(St2TOFGauss);
% adjust error bars for normalized yaxis
NormSt2TOFGauss = St2TOFGauss/max(St2TOFGauss);

% Total
NormTotTOF = TotTOF/max(TotTOFGauss); % normalized yaxis
NormTotTOFUncert = TotTOFUncert/max(TotTOFGauss);
% adjust error bars for normalized yaxis
NormTotTOFGauss = TotTOFGauss/max(TotTOFGauss);

%%%%%%%%%%%%%%%%%%%%%%%%%%%%%%%%%%%%%%%%%%%%%%%%%%%%%%%%%%%%%%%%%%%%%%%%%%%%
% Estimate FWHM of TOF lines of best fit
%%%%%%%%%%%%%%%%%%%%%%%%%%%%%%%%%%%%%%%%%%%%%%%%%%%%%%%%%%%%%%%%%%%%%%%%%%%%

St1FrstBckgrnd = mean(St1TOF((FstBRStart+100)/dt:(FstBrStop+100)/dt));
St1SndBckgrnd = mean(St1TOF((SndBRStart+100)/dt:(SndBrStop+100)/dt));
St2FrstBckgrnd = mean(St2TOF((FstBRStart+100)/dt:(FstBrStop+100)/dt));
St2SndBckgrnd = mean(St2TOF((SndBRStart+100)/dt:(SndBrStop+100)/dt));
```

```
TotFrstBckgrnd = mean(TotTOF((FstBRStart+100)/dt:(FstBrStop+100)/dt));
TotSndBckgrnd = mean(TotTOF((SndBRStart+100)/dt:(SndBrStop+100)/dt));

[St1TOFGaussMax, St1PeakTOF] = max(St1TOFGauss);
St1TOFHalfMax = (St1TOFGaussMax+(St1FrstBckgrnd+St1SndBckgrnd)/2)/2;
[St2TOFGaussMax, St2PeakTOF] = max(St2TOFGauss);
St2TOFHalfMax = (St2TOFGaussMax+(St2FrstBckgrnd+St2SndBckgrnd)/2)/2;
[TotTOFGaussMax, TotPeakTOF] = max(TotTOFGauss);
TotTOFHalfMax = (TotTOFGaussMax+(TotFrstBckgrnd+TotSndBckgrnd)/2)/2;

for zzz = 1:(size(xaxisE,2) - 1)

    if St1TOFGauss(zzz) <= St1TOFHalfMax && St1TOFGauss(zzz+1) >=
St1TOFHalfMax
        St1TOFFWHM1 = xTOFGauss(zzz) + dt*(St1TOFHalfMax-
St1TOFGauss(zzz))/(St1TOFGauss(zzz+1)-St1TOFGauss(zzz));
% linear interpolation to estimate TOF at FWHM
    end
    if St1TOFGauss(zzz) >= St1TOFHalfMax && St1TOFGauss(zzz+1) <=
St1TOFHalfMax
        St1TOFFWHM2 = xTOFGauss(zzz) + dt*(St1TOFHalfMax-
St1TOFGauss(zzz))/(St1TOFGauss(zzz+1)-St1TOFGauss(zzz));
% linear interpolation to estimate TOF at FWHM
    end

    if St2TOFGauss(zzz) <= St2TOFHalfMax && St2TOFGauss(zzz+1) >=
St2TOFHalfMax
        St2TOFFWHM1 = xTOFGauss(zzz) + dt*(St2TOFHalfMax-
St2TOFGauss(zzz))/(St2TOFGauss(zzz+1)-St2TOFGauss(zzz));
% linear interpolation to estimate TOF at FWHM
    end
    if St2TOFGauss(zzz) >= St2TOFHalfMax && St2TOFGauss(zzz+1) <=
St2TOFHalfMax
        St2TOFFWHM2 = xTOFGauss(zzz) + dt*(St2TOFHalfMax-
St2TOFGauss(zzz))/(St2TOFGauss(zzz+1)-St2TOFGauss(zzz));
% linear interpolation to estimate TOF at FWHM
    end

    if TotTOFGauss(zzz) <= TotTOFHalfMax && TotTOFGauss(zzz+1) >=
TotTOFHalfMax
        TotTOFFWHM1 = xTOFGauss(zzz) + dt*(TotTOFHalfMax-
TotTOFGauss(zzz))/(TotTOFGauss(zzz+1)-TotTOFGauss(zzz));
% linear interpolation to estimate TOF at FWHM
    end
    if TotTOFGauss(zzz) >= TotTOFHalfMax && TotTOFGauss(zzz+1) <=
TotTOFHalfMax
        TotTOFFWHM2 = xTOFGauss(zzz) + dt*(TotTOFHalfMax-
TotTOFGauss(zzz))/(TotTOFGauss(zzz+1)-TotTOFGauss(zzz));
% linear interpolation to estimate TOF at FWHM
    end
end

St1TOFFWHM = St1TOFFWHM2 - St1TOFFWHM1;
St2TOFFWHM = St2TOFFWHM2 - St2TOFFWHM1;
TotTOFFWHM = TotTOFFWHM2 - TotTOFFWHM1;
```

```
Y = zeros(4,4);
TOFLineOfBestFitValues = num2cell(Y);

TOFLineOfBestFitValues{1,1} = 'Data Set';
TOFLineOfBestFitValues{1,2} = 'Peak Max';
TOFLineOfBestFitValues{1,3} = 'Peak Mode';
TOFLineOfBestFitValues{1,4} = 'Est FWHM';

TOFLineOfBestFitValues{2,1} = 'Stop 1';
TOFLineOfBestFitValues{2,2} = St1TOFGaussMax;
TOFLineOfBestFitValues{2,3} = St1PeakTOF;
TOFLineOfBestFitValues{2,4} = St1TOFFWHM;

TOFLineOfBestFitValues{3,1} = 'Stop 2';
TOFLineOfBestFitValues{3,2} = St2TOFGaussMax;
TOFLineOfBestFitValues{3,3} = St2PeakTOF;
TOFLineOfBestFitValues{3,4} = St2TOFFWHM;

TOFLineOfBestFitValues{4,1} = 'Combined';
TOFLineOfBestFitValues{4,2} = TotTOFGaussMax;
TOFLineOfBestFitValues{4,3} = TotPeakTOF;
TOFLineOfBestFitValues{4,4} = TotTOFFWHM;

TOFLineOfBestFitValues

%%%%%%%%%%%%%%%%%%%%%%%%%%%%%%%%%%%%%%%%%%%%%%%%%%%%%%%%%%%%%%%%%%%%%%%%%%%%%%%
% Plotting of data
%%%%%%%%%%%%%%%%%%%%%%%%%%%%%%%%%%%%%%%%%%%%%%%%%%%%%%%%%%%%%%%%%%%%%%%%%%%%%%%

figure(1)
h = errorbar(xaxis,TotTOF,TotTOFUncert,'ok','MarkerSize',5);
errorbar_tick(h,1,'UNITS')
hold on;
plot(xTOFGauss,TotTOFGauss,'--k')
h = errorbar(xaxis,St1TOF,St1TOFUncert,'or','MarkerSize',5);
errorbar_tick(h,1,'UNITS')
plot(xTOFGauss,St1TOFGauss,'--r')
h = errorbar(xaxis,St2TOF,St2TOFUncert,'ob','MarkerSize',5);
errorbar_tick(h,1,'UNITS')
plot(xTOFGauss,St2TOFGauss,'--b')
axis([-200 300 0 1.2*max(TotTOF)])%adjust once Gauss figured out
set(gca,'FontSize',14)
set(gca,'FontName','Arial')
xlabel('time of flight (ns)')
ylabel('Counts (per source particle)')
legend('\pi/4 radian, 1.0 m combined time-of-flight','\pi/4 radian, 1.0 m
combined line of best fit',...
       '\pi/4 radian, 1.0 m stop-1 time-of-flight','\pi/4 radian, 1.0 m stop-
1 line of best fit',...
       '\pi/4 radian, 1.0 m stop-2 time-of-flight','\pi/4 radian, 1.0 m stop-
2 line of best fit')
hold off;

figure(2)
```

```
h = errorbar(xaxisE,TotE,TotEUncert,'ok','MarkerSize',5);
errorbar_tick(h,.02,'UNITS')
hold on;
plot(xaxisE,TotEGauss,'--k')
h = errorbar(xaxisE,St1E,St1EUncert,'or','MarkerSize',5);
errorbar_tick(h,.02,'UNITS')
plot(xaxisE,St1EGauss,'--r')
h = errorbar(xaxisE,St2E,St2EUncert,'ob','MarkerSize',5);
errorbar_tick(h,.02,'UNITS')
plot(xaxisE,St2EGauss,'--b')
axis([0 3 0 1.1*max(TotE)])%adjust once Gauss figured out
set(gca,'FontSize',14)
set(gca,'FontName','Arial')
xlabel('Neutron energy (MeV)')
ylabel('Normalized counts (per source particle/MeV)')
legend('\pi/4 radian, 1.0 m combined neutron energy spectra','\pi/4 radian,
1.0 m combined Gaussian fit',...
       '\pi/4 radian, 1.0 m stop-1 neutron energy spectra','\pi/4 radian, 1.0
m stop-1 Gaussian fit',...
       '\pi/4 radian, 1.0 m stop-2 neutron energy spectra','\pi/4 radian, 1.0
m stop-2 Gaussian fit')
hold off;

size(Det1TOF)
size(Det2TOF)

% Stop the clock
elapsed_time=toc;
mod_elapsed_time=elapsed_time/60;
fprintf('\n\n   The total data-processing time is %6.2f
min.\n',mod_elapsed_time)
```